

2010

# Surface adsorption and pore-level properties of mineral and related systems of relevance to the recycling of paper

Gribble, Christopher Mark

<http://hdl.handle.net/10026.1/315>

---

<http://dx.doi.org/10.24382/4236>

University of Plymouth

---

*All content in PEARL is protected by copyright law. Author manuscripts are made available in accordance with publisher policies. Please cite only the published version using the details provided on the item record or document. In the absence of an open licence (e.g. Creative Commons), permissions for further reuse of content should be sought from the publisher or author.*

## **Copyright statement**

This copy of the thesis has been supplied on condition that anyone who consults it is understood to recognise that its copyright rests with its author and that no quotation from the thesis and no information derived from it may be published without the author's prior consent.

Signed.....

Christopher M. Gribble

**SURFACE ADSORPTION AND PORE-LEVEL  
PROPERTIES OF MINERAL AND RELATED SYSTEMS  
OF RELEVANCE TO THE RECYCLING OF PAPER**

A thesis submitted to the University of Plymouth in partial fulfilment for the degree of

**DOCTOR OF PHILOSOPHY**

Christopher Mark Gribble B.Sc. (Hons)

Environmental and Fluid Modelling Group

Centre for Research in Earth Sciences

School of Geography, Earth and Environmental Sciences

University of Plymouth

This research has been funded by Omya Development AG and the HEIF 3 programme.

## **Supervisory team**

**Professor G. Peter Matthews**

Environmental and Fluid Modelling Group

School of Geography, Earth and Environmental Sciences

University of Plymouth

Plymouth

Devon

PL4 8AA

UK

Tel: 01752 584798

[P.Matthews@plymouth.ac.uk](mailto:P.Matthews@plymouth.ac.uk)

**Dr Andrew Turner**

School of Geography, Earth and Environmental Sciences

University of Plymouth

Plymouth

Devon

PL4 8AA

UK

Tel: 01752 584570

[A.Turner@plymouth.ac.uk](mailto:A.Turner@plymouth.ac.uk)

**Dr Joachim Schoelkopf**

Head of RD-MS  
Omya Development AG  
Baslerstrasse 42  
CH-4665 Oftringen  
Switzerland  
Tel: +41 62 789 2229

[Joachim.Schoelkopf@omya.com](mailto:Joachim.Schoelkopf@omya.com)

**Dr Patrick A. C. Gane**

Head of Research and Development

Omya Development AG  
Baslerstrasse 42  
CH-4665 Oftringen  
Switzerland  
Tel: +41 62 789 2422

[Patrick.Gane@omya.com](mailto:Patrick.Gane@omya.com)

# Abstract

**By Christopher Mark Gribble**

**Surface adsorption and pore-level properties of mineral and related systems of relevance to the recycling of paper.**

There is a significant problem for the paper recycling industry known as “stickies”. “Stickies” are tacky species, present in recycled paper and coated broke, derived from coating formulations, adhesives, etc. They impact negatively on paper quality and cause web runnability problems by deposit build-up. To sustain recycling, stickies are controlled by adsorbing them onto minerals added to the recycled stock. So the aim of the project was to characterise non-porous and porous minerals suitable for paper-making, and then use the knowledge gained to improve the adsorption of stickies.

The pore level properties of the minerals used to control stickies are highly relevant in regulating adsorption of the stickies. Levels of pore architecture were investigated by characterising filter media with porosimetry, porometry, electron microscopy and modelling the combined results. Seven samples were studied, with pore size distributions ranging from simple unimodal to complicated bimodal. Porometry, porosimetry and SEM, individually can only determine primary pore architecture. A combination of experimental and modelling techniques allows a full characterisation of pore architecture from primary to quaternary levels.

Calcium carbonates can be modified to change the pore architecture, which affects properties such as wetting. Their pore architecture was investigated to understand why some modified calcium carbonates do not show two distinct wetting rates. The investigation implied a significant surface area could be attributed to nano rugosity. The nano rugosity was responsible for the enhanced wetting of a sample. A zero length column was used to study diffusion and desorption of benzene with calcium carbonate. Desorption and diffusion coefficients for calcium carbonate systems were calculated from the corrected concentration versus time measurements. They showed how the pore architecture affects diffusion and desorption. By comparing the experimental results with a pore network simulation, it was possible to deduce the relative effect of surface diffusion.

The adsorption of stickies onto different mineral grades was investigated using a novel proxy method to determine equilibrium constants and adsorption isotherms. The results were then used to understand the influence of particle size on the adsorption behaviour, with three mechanisms proposed. The equilibrium constant and adsorption isotherm data also allowed comparisons between hydrophilic and hydrophobic adsorption onto grades of talc. Recommendations are made for the optimum use of minerals for the removal of stickies, and for in-situ methods for monitoring and optimising removal.

# Table of contents

Copyright statement .....	I
Title page.....	II
Supervisory team.....	III
Abstract .....	V
Table of contents .....	VI
Table of figures .....	XII
Table of tables .....	XX
Table of equations .....	XXII
Acknowledgements .....	XXVI
Author's declaration.....	XXVII
Conferences and presentations .....	XXVIII
Publications .....	XXVIII
Nomenclature .....	XXIX
1 Introduction .....	1
1.1 Structure of the thesis.....	1
1.2 The collaborative basis and aim of this research project .....	2
1.3 Theory and literature review .....	2
1.3.1 Porous media.....	3
1.3.1.1 Experimental methods to characterise porous media.....	5
1.3.1.1 Modelling of porous materials .....	6
1.3.1.1 Mercury porosimetry and porometry modelling .....	6
1.3.1.2 Characterisation of pore architecture .....	9
1.3.1.3 Gas adsorption modelling .....	11

1.3.1.4 Barrett, Joyner and Halenda (BJH) algorithm.....	13
1.3.1.5 Calculation of pore size distribution using the BJH algorithm. ....	15
1.3.1.6 Pore-Cor Research Suite modelling .....	20
1.3.1.7 Compressibility correction (Gane, Kettle et al., 1996) .....	25
1.3.1.8 Diffusion algorithm (Laudone, Matthews et al., 2008).....	27
1.3.2 Zero length column .....	29
1.3.3 Mineralogy .....	31
1.3.3.1 Bentonite .....	31
1.3.3.2 Talc.....	33
1.3.3.3 Calcium carbonate.....	34
1.3.3.4 Ground calcium carbonate .....	35
1.3.3.5 Modified calcium carbonate (Ridgway, Gane et al., 2004) .....	36
1.3.4 Wettability.....	38
1.3.4.1 Wetting fluid properties .....	39
1.3.4.2 Wenzel wetting equation.....	42
1.3.4.3 Cassie-Baxter equation.....	43
1.3.5 Stickies .....	45
1.3.5.1 Equilibrium .....	46
1.3.5.2 Adsorption.....	46
1.3.5.3 Adsorption isotherms .....	47
1.3.5.4 Freundlich equation.....	47
1.3.5.5 Langmuir equation .....	48
1.3.5.6 Dubinin-Radushkevich equation(Rouquerol, Rouquerol et al., 1999)....	48
2 Techniques .....	51
2.1 Characterisation of porous materials.....	51
2.1.1. Scanning electron microscopy (SEM) and image analysis .....	51
2.1.2. Mercury intrusion porosimetry (MIP).....	53
2.1.3. Porometry .....	56
2.1.4. Particle size distribution.....	57



2.2. Physicochemical process differences due to void structure .....	59
2.2.1. High performance liquid chromatography (HPLC) .....	59
2.2.2. Zero length column (ZLC) .....	61
2.3. Effect of surface rugosity on wetting .....	64
2.3.1. Gas adsorption.....	64
2.3.2. Wetting experiment.....	67
2.4. Adsorption characteristics of mineral particles in paper recycling .....	70
2.4.1. Turbidity.....	70
2.4.2. Chemical oxygen demand (COD).....	72
2.4.3. Gravimetric analysis.....	72
2.4.4. Dissolved organic carbon (DOC).....	72
2.4.4.1. Total dissolved nitrogen (TDN) .....	73
2.4.5. Elemental analysis.....	74
2.4.6. Zeta potential.....	75
3 Elucidation of void space architecture of filters by comparison and modelling of porometry, porosimetry and microscopy (Gribble, Matthews <i>et al.</i> , 2010b).....	77
3.1 Introduction .....	77
3.1.1 Theoretical considerations regarding porosimetry and porometry .....	79
3.1.2 The network model .....	86
3.2 Materials.....	87
3.3 Experimental and modelling methods.....	87
3.3.1 Mercury porosimetry.....	87
3.3.2 Porometry .....	88
3.3.3 Scanning electron microscopy and image analysis .....	89
3.3.4 Pore-Cor Research Suite modelling .....	89
3.4 Results .....	90
3.5 Discussion and conclusion .....	102
3.5.1 Highlights .....	104
4 Wetting and absorption properties of calcium carbonate.....	105

4.1 Introduction .....	105
4.2 Experimental .....	106
4.2.1 Minerals.....	106
4.2.2 Materials.....	108
4.2.3 Hexadecane wetting experiment .....	108
4.2.4 Mercury porosimetry.....	109
4.2.5 Gas adsorption desorption isotherms .....	109
4.3 Results and discussion.....	110
4.3.1 Wetting.....	116
4.4 Conclusion.....	119
4.4.1 Highlights .....	120
5 Use of a zero length column to investigate diffusion and desorption in calcium carbonates.....	121
5.1 Theory .....	122
5.1.1 Pore-Cor Research Suite modelling .....	124
5.2 Methodology .....	125
5.2.1 Refinement of the zero length column design.....	125
5.2.2 Materials.....	128
5.2.3 Instrumentation .....	128
5.2.4 Fluids.....	129
5.2.5 Detector calibration.....	129
5.3 Method for diffusion and sorption studies .....	130
5.4 Computer modelling of diffusion.....	131
5.5 Results and discussion.....	132
5.5.1 Qualitative results.....	132
5.5.2 Quantitative analysis of results. ....	133
5.5.3 Pore-Cor RS diffusion simulation.....	135
5.6 Conclusions .....	138
5.6.1 Highlights .....	139

6 Equilibrium coefficients for the adsorption of colloidal stickies onto mineral suspensions to improve paper recycling .....	140
6.1 Introduction .....	140
6.1.1 Background theory .....	141
6.2 Experimental .....	144
6.2.1 Materials and minerals .....	144
6.2.2 Methods .....	146
6.2.3 Artificial sticky preparation .....	146
6.2.4 Turbidity .....	147
6.2.5 Chemical oxygen demand .....	147
6.2.6 Gravimetric analysis .....	148
6.2.7 Dissolved organic carbon and total dissolved nitrogen analysis .....	148
6.2.8 Elemental analysis .....	148
6.3 Results and discussion .....	148
6.3.1 Aqueous phase – turbidity .....	149
6.3.2 Aqueous phase – chemical oxygen demand .....	151
6.3.3 Aqueous phase – gravimetric analysis .....	152
6.3.4 Aqueous phase – dissolved organic carbon analysis (DOC) and total dissolved nitrogen analysis (TDN) .....	154
6.3.5 Technique comparison .....	162
6.3.6 Equilibrium constants .....	163
6.3.7 Limitations on adsorption and the assumption of linearity ( $K_{eq}$ ) .....	165
6.4 Conclusions .....	169
6.4.1 Highlights .....	170
7 Adsorption of surfactant-rich stickies onto mineral surfaces (Gribble, Matthews <i>et al.</i> ) .....	171
7.1 Introduction .....	171
7.2 Materials .....	174
7.2.1 Minerals .....	174

7.2.2 Stickies .....	177
7.3 Experimental methods.....	177
7.3.1 Sticky preparation .....	177
7.3.2 Dissolved organic carbon analysis .....	178
7.3.3 Elemental analysis.....	179
7.3.4 Turbidity.....	179
7.3.5 Zeta potential.....	179
7.3.6 Data presentation and analysis .....	179
7.4 Results and discussion.....	180
7.4.1 Adsorption of fatty acid ester defoamer on mineral surfaces .....	182
7.4.2 Adsorption of acrylic acid ester copolymer on mineral surfaces.....	187
7.4.3 pH, conductivity, zeta-potential and turbidity.....	191
7.5 Conclusions .....	194
7.5.1 Highlights (Gribble, Matthews <i>et al.</i> , 2010a) .....	195
8 Overview .....	196
8.1 Future work .....	200
Appendix A – Pore – Cor RS stochastic generation data for mercury porosimetry and porometry of filter media .....	203
Appendix B – equilibrium constants for all systems in Chapter 6.....	206
Appendix C – Calibration curves for dissolved organic carbon data for Chapter 6 .....	209
Appendix D – Fitting of ARIAN isotherm equations to raw adsorption isotherm data. .....	213
References .....	217

## Table of figures

Figure 1-1 Representation of a porous medium showing isolated pores, pores and connecting throats (Laudone, 2005).....	4
Figure 1-2 Schematic of various porous media types (Schoelkopf, 2002) .....	4
Figure 1-3 Bundle of capillaries model for porous medium (Laudone, 2005) .....	7
Figure 1-4 Attempt to describe tortuosity within the one-dimensional model of a porous medium (Matthews, 2000) .....	8
Figure 1-5 Three dimensional network model of a porous material (Pan, Davis <i>et al.</i> , 1995) .....	8
Figure 1-6 Pore identification from a two-dimensional image and erosion of the pore space as presented in Toivakka and Nyfors (2001) .....	9
Figure 1-7 BET plot for a modified calcium carbonate .....	12
Figure 1-8 A pore filled with condensed fluid has three distinct zones.....	15
Figure 1-9 Simulated Pore-Cor network representation showing cylindrical throat and cubic pore representation arranged in a three dimensional Cartesian array.....	21
Figure 1-10 SEM image of bentonite.....	32
Figure 1-11 Structure of montmorillonites, in the water layer different cations are found such as sodium, magnesium or lithium (Luckham and Rossi, 1999).....	32
Figure 1-12 Schematic of the chemical structure of talc. The top and bottom layers are silicates, and the middle is magnesium hydroxide.....	33
Figure 1-13 Scanning Electron Micrograph of talc, note the layers of platelets which allow for delamination. ....	34
Figure 1-14 Calcite (from <a href="http://www.ggl.ulaval.ca">http://www.ggl.ulaval.ca</a> ).....	35
Figure 1-15 SEM image of a ground calcium carbonate with no identifiable internal porosity as seen with modified calcium carbonate. ....	36

Figure 1-16 SEM image of a “Roses” structure modified calcium carbonate, which is nano-dimensioned surface edge-like structures of high aspect ratio formed on micro-particles. ....	37
Figure 1-17 SEM image of a “Eggs” structure modified calcium carbonate, which is an internally nano-porous calcium carbonate. ....	37
Figure 1-18 SEM image of “Golf balls” modified calcium carbonate structure, which is a description of sub micrometre pores contained within a micro-particle cake.....	38
Figure 1-19 Influence of different phase interactions (L = liquid, S = solid) and their effect on contact angle. ....	42
Figure 1-20 Diagram showing the differences between Wenzel wetting and Cassie-Baxter wetting. The diagram shows the Wenzel wetting filling the surface features and Cassie-Baxter wetting sitting on top of the features. ....	43
Figure 2-1 Photograph of a Micromeritics AutoPore III 9420 mercury porosimeter, showing the twin ports for mounting the penetrometer containing the sample for analysis over progressive pressure ranges.....	55
Figure 2-2 Photograph of a Porvair Porometer 4 (Amey, Stott <i>et al.</i> , 2008), showing the sample holder in the central unit of the apparatus, with the pressure application pipe and reservoir leading from it.....	57
Figure 2-3 Schematic of a static light scattering system for measuring particle size distribution. ....	58
Figure 2-4 Selection of HPLC procedures (Skoog, Holler <i>et al.</i> , 2006).....	60
Figure 2-5 Basic schematic indicating flow of mobile phase through an HPLC system (Skoog, Holler <i>et al.</i> , 2006).....	61
Figure 2-6 Schematic of zero length column and how it is integrated into an HPLC system (Ruthven and Stapleton, 1993a).....	63
Figure 2-7 Schematic design of ZLC cell in detail. (A) Threaded inlet for male connector (1.06 cm x 0.75 cm i.d.); (B) orifice between threaded inlet and truncated cone (0.5 cm x 0.23 cm i.d.); (C) truncated cone ( $h = 0.1$ cm; $d_B = 2.3$ cm; $d_T = 0.23$ cm); (D) replaceable frit (micrometre size 10 $\mu$ m); (E) filter; (F) space for shallow	

bed (0.1 cm x 2.5 cm i.d.); (G) O-ring; (H) bolt; (I) male connector. (Zabka and Rodrigues, 2007) .....	64
Figure 2-8 Photograph of the Gemini 2360 surface area analyser and FlowPrep 060. The vessel for sample exposure to the adsorbing gas is shown in the left-hand unit of the apparatus. ....	66
Figure 2-9 Schematic showing the layout of the Gemini series of surface area analysers (Micromeritics, 2006). ....	67
Figure 2-10 Schematic of the equipment used to create tablets from mineral suspensions / slurries (Ridgway, Gane <i>et al.</i> , 2004) .....	68
Figure 2-11 Schematic of the equipment used to measure absorption into the mineral samples (Schoelkopf, Ridgway <i>et al.</i> , 2000).....	69
Figure 2-12 Photograph of the Shimadzu TOC-5000A coupled to the autosampler ASI-5000A.....	73
Figure 2-13 Photograph of the Carlo-Erba EA-1110 CHNS elemental analyser, with the sample mount seen on top of the analytical instrumentation. ....	75
Figure 3-1. Schematic graph showing how extrapolated porometry data should compare with mercury intrusion data, and how mercury porosimetry and porometry data are interpreted using the capillary bundle model. ....	81
Figure 3-2. Comparison of how mercury porosimetry and porometry probe the pore architecture of schematic structures with simple quaternary level pore architecture. Mercury for standard porosimetry is applied in the direction of the black and grey arrows, and for shielded mercury porosimetry in the direction of the grey arrows only. Air, for porometry, is applied in the direction of the black arrows. Porometry would not be able to differentiate between the four different structures. ....	82
Figure 3-3. a) SEM image of surface of stainless steel filter 3AL3 and b) SEM cross-section of stainless steel filter 3AL3: both with 10 $\mu$ m scale bars.....	92
Figure 3-4. Pore size distribution of stainless steel mesh filter 3AL3 determined by mercury porosimetry, porometry and pore size distribution modelled by Pore-Cor. The same units are used on the primary and secondary y-axes on all graphs, the differences in scale being chosen to illustrate the features more clearly. ....	93

Figure 3-5. SEM images of fine and coarse surfaces of Porvair stainless steel sinter: a) fine features, with 10 $\mu\text{m}$ scale bar, and b) coarse features, with 100 $\mu\text{m}$ scale bar.....	94
Figure 3-6. Pore size distributions of a 3 $\mu\text{m}$ rated Porvair stainless steel sinter using mercury porosimetry, shielded mercury porosimetry, and SEM and image analysis.....	95
Figure 3-7. a) SEM image of Aegis stainless steel sinter, with 5 $\mu\text{m}$ scale bar, b) SEM image of glass fibre filter, with 10 $\mu\text{m}$ scale bar.....	96
Figure 3-8. Pore size distribution of Aegis stainless steel sinter determined using mercury porosimetry, image analysis and a pore size distribution calculated using Pore-Cor.....	97
Figure 3-9. Pore size distribution of a 0.7 $\mu\text{m}$ filtration-rated Fisherbrand glass fibre filter determined experimentally using mercury porosimetry and porometry, and by modelling the experimental data. ....	98
Figure 3-10 a) SEM image of grade 1 filter paper, with 50 $\mu\text{m}$ scale bar, b) SEM image of cellulose nitrate membrane, with 5 $\mu\text{m}$ scale bar. ....	99
Figure 3-11. Pore size distribution of grade 1 filter paper determined by mercury porosimetry and porometry, together with Pore-Cor modelling of mercury porosimetry and porometry. ....	100
Figure 3-12. Pore size distribution of a Whatman cellulose nitrate membrane filter determined by mercury porosimetry and porometry, together with the pore size distribution determined by modelling the porometry and mercury porosimetry data with Pore-Cor. ....	101
Figure 3-13 SEM image of 1 $\mu\text{m}$ -rated track etch membrane, with 5 $\mu\text{m}$ scale bar.....	102
Figure 3-14. Pore size distribution for a Whatman track etch membrane determined using image analysis, mercury porosimetry and porometry with a pore size distribution calculated by the Pore-Cor model for porometry and mercury porosimetry. ....	102
Figure 4-1 Scanning electron micrograph of GCC. ....	107
Figure 4-2 Scanning electron micrograph of DP MCC. ....	107
Figure 4-3 Scanning electron micrograph of HSA MCC.....	108



Figure 4-4. Graph comparing pore volume against diameter for MCC calculated from mercury porosimetry results using the Laplace equation.....	111
Figure 4-5. Adsorption desorption average isotherms with nitrogen for calcium carbonate systems. The error bars represent two times the standard deviation from six replicates. ....	112
Figure 4-6. Adsorption desorption average isotherms with <i>n</i> -butane for calcium carbonate systems. The error bars represent two times the standard deviation from four replicates. ....	113
Figure 4-7 Pore size distribution of DP MCC, determined using the BJH algorithm to analyse the average desorption curve for both adsorbates. ....	114
Figure 4-8 Pore size distribution of HSA MCC, determined using the BJH algorithm to analyse the average desorption curve for both adsorbates. ....	115
Figure 4-9 Pore area of MCCs determined using the BJH algorithm, with the sum of the individual pore areas being similar to the BET specific surface area. ....	116
Figure 4-10. Chart showing differences in absorption behaviour of three calcium carbonate systems.....	117
Figure 4-11 Schematic representation of the differences between the calcium carbonate systems. The GCC has no internal porosity, where both MCC minerals have macropores present. The DP MCC additionally has significant quantities of micropores and the HSA MCC has nanopores and nanorugosity on the surface of its pores. ....	119
Figure 5-1 Photograph of the initial design of the zero length column used in this investigation. ....	125
Figure 5-2 Cross sectional schematic of zero length column. Not to Scale.....	126
Figure 5-3 An exploded schematic of the zero length column, showing how the sample (stationary phase) interacts with the mobile phase. Not to scale .....	127
Figure 5-4 Photograph of final constructed zero length column. The internal diameter of the entry and exit tubes is 0.12mm.....	127
Figure 5-5 Zero length column calibration curve for benzene concentration. The error bars represent two times the standard deviation from three replicates. ....	130

Figure 5-6 Graph showing the justification for using a centrally weighted moving average function on a section of raw concentration data. For clarity, the smoothed data has been displaced downwards, as shown by the secondary axis. ....	131
Figure 5-7 Graph of the zero length column results of time versus the natural log of the benzene concentration divided by the initial benzene concentration. The data presented is average data obtained from a minimum of three replicates. ....	133
Figure 5-8 Three dimensional representation of DP MCC after 100 seconds of diffusion has taken place. The cubes represent pores in the sample and the cylinders represent throats connecting the pores. With the $x$ , $y$ and $z$ axes identified.....	135
Figure 5-9 Graph showing the differences in bulk diffusion rate for the two different modified calcium carbonate grades, simulated using the diffusion algorithm of Pore-Cor RS.....	137
Figure 6-1 Schematic highlighting how the equilibrium adsorption behaviour is modified by mineral concentration. ....	143
Figure 6-2 Graph showing how the different techniques of measuring fatty acid ester defoamer concentration varied when compared with the dissolved organic carbon analysis. The turbidity and chemical oxygen demand show a good correlation over a smaller concentration range from $0.05 - 0.5 \text{ g dm}^{-3}$ . The gravimetric results for this sample did not have enough data to generate a comparison best fit line. The total dissolved nitrogen analysis is not applicable to this sticky as nitrogen is not present..	156
Figure 6-3 Graph showing how the different techniques of measuring acrylic acid ester copolymer concentration varied when compared with dissolved organic carbon analysis. The total dissolved nitrogen data are not relevant as the results obtained are very inconsistent. The turbidity and chemical oxygen demand results show a correlation with the dissolved organic carbon analysis over a limited concentration range. ....	157
Figure 6-4 Comparison of dissolved organic carbon analysis with turbidity and chemical oxygen demand. The results for the turbidity did not agree with the dissolved organic carbon or chemical oxygen demand analysis, due to incomplete removal of mineral, which affects the less turbid mixtures proportionally more. ....	158
Figure 6-5 Comparison of all aqueous techniques with the dissolved organic carbon results. The reporting of values by total dissolved nitrogen analysis is unexpected as	

polyvinyl acetate <i>per se</i> does not have nitrogen, which explains the lower $R^2$ value obtained, but not that some reporting of nitrogen appears to be present. ....	159
Figure 6-6 Comparison of how the styrene butadiene latex concentration determined using all investigated techniques has a very good correlation with the dissolved organic carbon results. The turbidity, chemical oxygen demand and gravimetric results have a smaller concentration range than the dissolved organic carbon, but they overlap well. The total dissolved nitrogen results have a very good correlation with the dissolved organic carbon analysis of about 99.5 %, which indicates that the technique can be used successfully when nitrogen is present in the sticky even at low concentrations, as it is in this case. ....	160
Figure 6-7 Comparison of techniques for the colophonium. The turbidity results were affected by the low starting turbidity for colophonium resin alone. The chemical oxygen demand and gravimetric analyses have a good correlation with the dissolved organic carbon analysis at high initial concentrations. ....	161
Figure 6-8 Average equilibrium constants for all experimental systems investigated, calculated from the dissolved organic carbon and elemental analysis carbon data. The error bars represent double the standard deviation determined from a minimum of three replicates of elemental analysis and dissolved organic carbon analysis. ....	164
Figure 6-9 Schematic representation of how adsorption can vary dependent on the diameter of the mineral particle or sticky species. The concentration of mineral is always in excess, Figure 6-1a.....	166
Figure 7-1 a) SEM image of LSA MCC with 8 $\mu\text{m}$ scale bar shown. b) SEM image of LSA MCC with 2 $\mu\text{m}$ scale bar shown. ....	175
Figure 7-2 a) SEM image of HSA MCC with 8 $\mu\text{m}$ scale bar shown. b) SEM image of HSA MCC with 2 $\mu\text{m}$ scale bar shown. ....	175
Figure 7-3 Adsorption of the fatty acid ester defoamer onto LSA and HSA talc. ....	183
Figure 7-4 Adsorption of the fatty acid ester defoamer onto LSA and HSA talc, after correction for specific surface area. ....	183
Figure 7-5 Adsorption of fatty acid ester defoamer onto LSA MCC and HSA MCC..	184

Figure 7-6 Schematic showing a possible mechanism for the adsorption of a fatty acid ester defoamer onto LSA and HSA surface area talc, respectively. For clarity, the size of the ester molecule has been enlarged relative to the talc. ....	185
Figure 7-7 Schematic showing proposed adsorption mechanism for a fatty acid ester defoamer onto modified calcium carbonate (MCC) or a completely hydrophilic mineral. For clarity, the size of the ester molecule has been enlarged relative to the MCC. ....	187
Figure 7-8 Adsorption of acrylic acid ester copolymer onto LSA and HSA talc. ....	188
Figure 7-9 Adsorption of an acrylic acid ester copolymer onto LSA and HSA-talc corrected for the specific surface area of the talc. ....	188
Figure 7-10 Adsorption of an acrylic acid ester copolymer onto LSA MCC and HSA MCC. ....	189
Figure 7-11 Schematic showing proposed adsorption mechanism for an acrylic acid ester copolymer onto LSA and HSA talc. For clarity, the size of the ester molecule has been enlarged relative to the talc. ....	190
Figure 7-12 Schematic showing proposed adsorption mechanism for acrylic acid ester copolymer onto modified calcium carbonate or a hydrophilic mineral. For clarity, the size of the ester molecule has been enlarged relative to the MCC. ....	191
Figure 7-13 Mean zeta potentials of the supernatant suspensions before adsorption of a fatty acid ester defoamer and acrylic acid ester copolymer, and after adsorption onto the minerals shown and deposition of the mineral / adsorbate species by centrifuging. The sticky suspension being adsorbed was $0.5 \text{ g dm}^{-3}$ , which saturates the mineral. The error bars indicate the standard deviation of the zeta potential distribution at 50 % of the maximum height of the distribution. ....	193
Figure 8-1 Schematic of a possible packing arrangement for a gas adsorbing onto a modified calcium carbonate. ....	201

## Table of tables

Table 1-1 Classification of stickies.....	46
Table 3-1. Ranges of void size distributions, and summary of conclusions .....	91
Table 4-1 Surface area of minerals determined using BET equation with a relative pressure range up to $0.03 P / P_0$ .....	113
Table 4-2 Hexadecane absorption rates for the ground calcium carbonate and dual porous modified calcium carbonate. The high surface area modified calcium carbonate is not listed as the curve for the high surface area modified calcium carbonate is not linear with $t^{0.5}$ , so no continuous gradient can be defined.....	118
Table 5-1 Properties of minerals used during investigation.....	128
Table 5-2 Table of gradient and intercept values calculated using the linear region of the desorption curve. ....	134
Table 6-1 Stickies used in investigation.....	144
Table 6-2 Summary of mineral properties. ....	146
Table 6-3 Turbidities expressed as percentage change on adding $2 \text{ g dm}^{-3}$ of respective mineral to the stickies shown bold for three concentrations of sticky. Cells highlighted in yellow indicate an increase in turbidity. The error range indicates two times the standard deviation from three replicates. ....	150
Table 6-4 Chemical oxygen demand expressed as percentage change on adding $2 \text{ g dm}^{-3}$ of the respective mineral to the stickies shown bold for three concentrations of sticky. Cells highlighted in yellow indicate an increase in chemical oxygen demand. The error range indicates two times the standard deviation from three replicates.....	151
Table 6-5 Non volatile organic residue expressed as percentage change on adding $2 \text{ g dm}^{-3}$ of the respective mineral to the stickies shown bold for three concentrations of sticky. Cells highlighted in yellow indicate an increase in non volatile organic residue. The error range indicates two times the standard deviation from three replicates, and highlights the lack of precision. ....	153

Table 6-6 Advantages and disadvantages of the studied techniques to evaluate sticky removal.....	162
Table 6-7 Table of $R^2$ values to indicate that the results used to generate the equilibrium constants are within the linear range. The top line value indicates the adsorbed $R^2$ value and the bottom line value indicates the aqueous $R^2$ . ....	167
Table 7-1 Details of minerals used in this investigation. ....	176
Table 7-2 Comparison of regression coefficient $R^2$ and significance $p$ values of the gradient for fatty acid ester defoamer (FAED) and acrylic acid ester copolymer (AAEC) isotherms. ....	181
Table 7-3 Table of Dubinin-Radushkevich characteristic energies. ....	182

## Table of equations

Equation 1-1 .....	12
Equation 1-2 .....	12
Equation 1-3 .....	13
Equation 1-4 .....	13
Equation 1-5 .....	13
Equation 1-6 .....	13
Equation 1-7 .....	16
Equation 1-8 .....	16
Equation 1-9 .....	17
Equation 1-10 .....	17
Equation 1-11 .....	17
Equation 1-12 .....	18
Equation 1-13 .....	18
Equation 1-14 .....	18
Equation 1-15 .....	19
Equation 1-16 .....	19
Equation 1-17 .....	19
Equation 1-18 .....	19
Equation 1-19 .....	19
Equation 1-20 .....	20
Equation 1-21 .....	20
Equation 1-22 .....	22

Equation 1-23.....	23
Equation 1-24.....	23
Equation 1-25.....	23
Equation 1-26.....	23
Equation 1-27.....	23
Equation 1-28.....	24
Equation 1-29.....	24
Equation 1-30.....	24
Equation 1-31.....	24
Equation 1-32.....	24
Equation 1-33.....	25
Equation 1-34.....	25
Equation 1-35.....	26
Equation 1-36.....	26
Equation 1-37.....	26
Equation 1-38.....	27
Equation 1-39.....	28
Equation 1-40.....	28
Equation 1-41.....	28
Equation 1-42.....	29
Equation 1-43.....	40
Equation 1-44.....	41
Equation 1-45.....	41
Equation 1-46.....	42



Equation 1-47.....	43
Equation 1-48.....	44
Equation 1-49.....	47
Equation 1-50.....	48
Equation 1-51.....	48
Equation 1-52.....	49
Equation 1-53.....	49
Equation 1-54.....	49
Equation 1-55.....	49
Equation 1-56.....	49
Equation 2-1.....	53
Equation 2-2.....	70
Equation 2-3.....	71
Equation 3-1.....	79
Equation 3-2.....	80
Equation 3-3.....	80
Equation 3-4.....	80
Equation 3-5.....	80
Equation 3-6.....	83
Equation 3-7.....	83
Equation 3-8.....	84
Equation 5-1.....	122
Equation 5-2.....	123
Equation 5-3.....	123

Equation 5-4.....	123
Equation 5-5.....	123
Equation 5-6.....	124
Equation 5-7.....	130
Equation 6-1.....	141
Equation 6-2.....	142
Equation 6-3.....	142
Equation 7-1.....	172
Equation 7-2.....	173
Equation 7-3.....	173
Equation 7-4.....	174
Equation 7-5.....	181

## **Acknowledgements**

I wish to thank all of my supervisors for this research project, Prof. Peter Matthews, Dr. Andrew Turner, Dr Joachim Schoelkopf and Dr. Patrick Gane. Their support, friendship and encouragement have been phenomenal throughout this project, and without them the study would not have been possible.

I also wish to express my gratitude to my research colleagues, Dr. Giuliano Laudone, Dr Deborah Holtham and Dr. John Price, Daniel Gantenbein and Stuart Mills. Their friendship, assistance and support have been invaluable throughout this research project.

I also wish to thank Dr. Paul Sutton, Dr. Jeremy Clark, Andy Arnold and Andrew Tonkin for their invaluable expertise, on different instrumentation.

Many thanks to Dr. Cathy Ridgway and Dr. Dan Gerard for the assistance, and useful discussions, during my visits to Omya, in Switzerland. I also thank all the staff in Omya, who I had the pleasure of dealing with. You made me most welcome, and it is a phenomenal place to work.

To my parents and family, I thank you for all your love, understanding, encouragement and support and I dedicate this work to you.

## **Author's declaration**

At no time during the registration for the degree of Doctor of Philosophy has the author been registered for any other University award.

This study was financed with the aid of a studentship from both Omya Development AG and the HEIF 3 Programme.

Seminars and conferences were regularly attended throughout the period of study at which research was presented. Consultation with other institutions occurred and several publications are to be prepared

Word Count: 42,531 words

Signed.....

Date.....

Christopher M. Gribble

## Conferences and presentations

PTS – CTP Deinking Symposium, Leipzig (Germany); 15<sup>th</sup> – 17<sup>th</sup> April 2008

7<sup>th</sup> International Paper and Coating Chemistry Symposium, Hamilton, Ontario (Canada); 10<sup>th</sup> – 12<sup>th</sup> June 2009 – *A Model Description of Adsorption of Surfactant-Rich Stickies onto Hydrophobic Mineral Surfaces*. Oral Presentation

## Publications

Gribble, C. M., Matthews, G. P., Gantenbein, D., Turner, A., Schoelkopf, J. & Gane, P. A. C. 2010. Adsorption of surfactant-rich stickies onto mineral surfaces. *J. Colloid Interf. Sci.* 352, 483-490

Gribble, C. M., Matthews, G. P., Laudone, G. M., Turner, A., Ridgway, C. J., Schoelkopf, J. & Gane, P. A. C. Elucidation of Void Space Architecture of Filters by Comparison and Modelling of Porometry, Porosimetry and Microscopy. *AIChE J.*, Submitted July 2010.

Other publications in preparation

## Nomenclature

$A$  = constant simplifying Kelvin equation

$A^B$  = Lewis acid base interactions

$A_p$  = Polanyi adsorption affinity

$a$  = gradient (slope)

$B$  = structural constant

$b$  = intercept

$C_A$  = concentration of species A

$CSA$  = cross-sectional area

$CSA_{cK}$  = cross-sectional area of newly opened pores

$c$  = concentration

$c_0$  = initial fluid phase sorbate concentration

$c'$  = numerical particle concentration

$c_{BET}$  = BET constant

$c_e$  = aqueous equilibrium concentration

$c_s$  = fluid phase sorbate concentration

$D$  = density conversion factor

$D$  = empirical constant

$D_{fm}$  = free molecular diffusion coefficient

$D_{fmA}$  = free molecular diffusion of species A

$D_s$  = diffusion coefficient

$D_{tA}$  = throat diffusivity

$d$  = London dispersion forces

$d$  = differential

$d$  = diameter

$d_{avgKnew}$  = weighted average pore diameter if new pores opened

$d_{avgKold}$  = weighted average pore diameter if no new pores opened

$d_{bk}$  = breakthrough diameter

$d_{bp}$  = bubble point diameter

$d_{ext}$  = point on extended porometry asymptote at low pressure / large size equal distance from bubble point as  $d_{Fmax}$

$d_{Fmax}$  = point on porometry asymptote at high pressure / small size equal distance from bubble point as  $d_{ext}$

$dp_I$  = diameter of pores per interval

$dp_j$  = diameter of previously opened pores

$E$  = free energy of sorption per mole of the sorbate (characteristic energy for a given system)

$E_1$  = heat of adsorption for the first layer

$E_L$  = heat of adsorption for the second and subsequent layers

$F$  = fraction of pores open at both ends

$F_m$  = volumetric flow rate of the mobile phase

$F_{buoyancy}$  = buoyancy force

$F_{gravity}$  = gravitational force

$F_{total}$  = total force

$F_{wetting}$  = wetting force

$f$  = function

$f_1$  = fraction of liquid / solid interface

$g$  = gravity

$HP_{1, 2 \text{ or } 3}$  = Halsey parameter 1, 2 or 3

$I$  = interval number

$i$  = Debye dipole-induced polarisation

$J_{DA}$  = diffusive flux of species A

$j$  = previous interval

$K$  = equilibrium constant

$K_H$  = Henry constant of adsorption

$K_{sa}$  = equilibrium constant of surfactant molecules in surface aggregates of the primary layer

$k$  = number of intervals with new pores exposed

$k_B$  = Boltzmann Constant

$L^{vW}$  = Lifshitz-van der Waals interactions

$L$  = dimensionless ZLC parameter

$L_D$  = diffusion length

$l$  = length

$l_p$  = length of pores

$l_{pl}$  = length of pores per interval

$l_t$  = length of single cylindrical throat

$M_{ss}$  = bulk modulus

$m$  = constant relating length and diameter

$m_a$  = mass of adsorbent

$m_s$  = mass of adsorbed surfactants

$m_{s1}$  = mass of adsorbed surfactant in the first layer

$N$  = Avogadro's number



$n$  = number

$n_a$  = Freundlich exponent

$P$  = Keesom dipole-dipole orientation

$P$  = equilibrium pressure

$P_0$  = saturation pressure

$P^1$  = atmospheric pressure

$P_{app}$  = applied external pressure

$P_{avgK}$  = relative pressure corresponding to  $d_{avgK}$

$P_{bk}$  = breakthrough pressure

$P_{bp}$  = bubble point pressure

$P_N$  = any applied pressure

$p$  = probability

$pK_b$  = alkaline dissociation constant

$Q$  = volumetric flow rate

$q_d$  = Dubinin-Radushkevich isotherm constant

$q_e$  = adsorbed equilibrium concentration

$q_{max}$  = maximum amount adsorbed

$q_{mon}$  = monolayer adsorption capacity

$R$  = universal gas constant

$R^2$  = regression coefficient

$R_c$  = radius of curvature

$r$  = roughness ratio

$r_A$  = effective molecular radius

$r_{CI}$  = Kelvin core radius

$r_{cK}$  = Kelvin core radius of new pores exposed

$r_g$  = radius of gas droplet

$r_s$  = radius of the sorbent particle

$r_t$  = radius of single cylindrical throat

$S$  = surface area

$S$  = spreading power

$S_I$  = incremental surface area

$s$  = cross-sectional area of adsorbent gas

$s$  = constant relating length and diameter

$T$  = absolute temperature

$T_w$  = Thickness of adsorbed layer

$t$  = time

$V$  = volume of mercury

$V_a$  = volume adsorbed

$V_{\text{bulk}}^1$  = sample bulk volume at atmospheric pressure

$V_c$  = volume desorbed from newly opened pores

$V_{cI}$  = volume desorbed from newly opened pores for each interval

$V_d$  = total volume of gas desorbed from previously opened pores

$V_f$  = volume of interstitial fluid in ZLC bed

$V_I$  = volume adsorbed in liquid equivalent volume

$V_{\text{int}}$  = volume of mercury intruded into sample

$V_m$  = molar volume of adsorbed gas

$V_{\text{obs}}$  = observed volume of mercury in sample

$V_{p1,2,3}$  = volume of mercury intruded relating to pressure 1 , 2 or 3

$V_{p1}$  = incremental pore volume

$V_s$  = volume of sorbent in zero length column bed

$V_{ss}$  = volume of sample

$v$  = volume (volume of gas adsorbed)

$v_c'$  = numerical volume concentration

$v_m$  = monolayer adsorbed gas quantity

$W$  = micropore volume

$W_0$  = total micropore volume

$x$  = spatial coordinate of the diffusion system

$x_a$  = mass of the adsorbate

$x_s$  = equilibrium constant of surfactant molecules in surface aggregates in all layers above the first

$\alpha$  = cross sectional area of newly opened pores

$\beta$  = scaling factor

$\beta_n$  = ZLC dimensionless parameter

$\Gamma$  = gamma function

$\gamma$  = surface free energy (surface / interfacial tension)

$\gamma^+$  = surface tension from acidic interactions

$\gamma^-$  = surface tension from basic interactions

$\gamma_{LV}$  = interfacial tension between liquid and vapour

$\gamma_{SL}$  = interfacial tension between solid and liquid

$\gamma_{SV}$  = interfacial tension between solid and vapour

$\gamma_z$  = dimensionless ZLC parameter

$\Delta T_d$  = decrease in thickness due to desorption

$\Delta T_w$  = change in thickness

$\delta V_{\text{blank}}$  = change in the blank run volume reading

$\delta V_{\text{Hg}}$  = compression of mercury

$\delta V_{\text{pen}}$  = volume expansion of the analysis chamber of penetrometer

$\zeta$  = euler beta function intermediate argument

$\mu$  = mean

$\mu_1$  = minimum unimodal mean

$\mu_2$  = maximum unimodal mean

$\mu_{\text{max}}$  = maximum mean

$\mu_{\text{min}}$  = minimum mean

$\eta$  = kinetic viscosity of the gas

$\eta_B$  = viscosity of the medium B

$\eta_b$  = euler beta function intermediate argument

$\theta$  = contact angle

$\theta_{\text{CB}}$  = Cassie-Baxter contact angle

$\theta_e$  = equilibrium contact angle

$\theta_w$  = Wenzel contact angle

$\pi$  = pi mathematical constant (3.14159)

$\rho$  = density of the liquid

$\sigma$  = standard deviation

$\tau$  = turbidity

$\Phi^1$  = porosity of the sample at one atmosphere

$\Psi$  = euler beta function

$\Psi_{ss}$  =compressibility of the sample

# 1 Introduction

## *1.1 Structure of the thesis*

This thesis is divided into eight chapters. This introductory chapter gives insight into the rationale behind the associated research. Section 1.1 describes the structure of the thesis and explains what will be covered. Section 1.2 of the thesis details the collaborative nature of the research project. Section 1.3 includes the theory and literature review for the research project, which gives insights into the relevant but diverse scientific literature and theory that will aid the reader's understanding of the work undertaken in further chapters. Chapter 2 gives a description of existing experimental techniques and their use in this project. Chapter 2 is organised so that the techniques are introduced in the order they are encountered through the thesis.

Chapters 3 – 7 are subdivided into two research themes. Porous material and mineral characterisation is described in chapters 3 – 5. Chapters 6 and 7 cover research using minerals as a treatment for 'stickies' encountered during paper recycling. Specifically chapter 3 compares experimental techniques for determining the pore size distribution of standard filter media. The techniques involved included modelling of porometry and mercury porosimetry data to ascertain if modelling improved the information obtainable. In chapter 4 the adsorption, desorption and diffusion properties of different calcium carbonate grades were investigated, using benzene as the test solute in cyclohexane. The experimental data were obtained using a 'zero length column' adapted to improve sensitivity for liquid systems. The diffusion results are compared with a simulation of diffusion for two of the calcium carbonate grades. Chapter 5 presents experimental data explaining why different calcium carbonate grades show different degrees of hydrophilicity. In chapters 6 and 7 the experiments, methods and results

involved in removing “Stickies” from a model paper recycling system are described, with emphasis on the equilibrium constants for seven different model sticky compounds and detailed adsorption mechanisms for two of these stickies. In chapter 8, an overview of this project is presented and conclusions drawn.

At the end of chapter 3 – 7 are ‘research highlights’, given in the style of those used for the publication of chapter 7 in the Journal of Colloid and Interface Science.

## ***1.2 The collaborative basis and aim of this research project***

This research project has been developed in collaboration between Omya AG, a Swiss-based world-leading supplier of mineral pigments for paper coating, and the Environmental and Fluid Modelling Group at the University of Plymouth. The Research and Development department of Omya AG has knowledge and expertise in the study of pigmented coating layers, solid-liquid interactions, microscopy, rheology and surface chemistry. The modelling expertise of the Environmental and Fluid Modelling Group has led to the development of the Pore-Cor Research Suite, a highly sophisticated void network model. The collaboration has given rise to several prior and concurrent research projects involving the development of an inertial liquid absorption algorithm, the modelling of throats with converging-diverging geometry, the study of anisotropic structures and ink-pigment interaction, the development of a diffusion algorithm, the behaviour of natural and synthetic binder systems within paper coatings, and developing techniques for the control of pitch during virgin paper manufacture.

## ***1.3 Theory and literature review***

The following review of theory and literature highlights how the location, geometry and size of voids within porous media influence other fundamental processes such as sorption, diffusion and wettability. The second half of the review is an investigation of previous work on a major problem of paper recycling caused by “Stickies”. The

literature review also describes how modifying the treatment mineral may assist in the removal of stickies from the paper recycling process.

### **1.3.1 Porous media**

A porous medium is a solid body containing many holes or voids, and narrow and/or tortuous connecting passages. There are many characteristics that may be used to describe porous medium. The most common characteristic is porosity, the volume fraction of the media relative to the total void space.

The voids within porous media are characterised by size. Extremely small voids may be termed molecular interstices and extremely large ones caverns (Scheidegger, 1974). Laudone (Laudone, 2005) states that pores may have an intermediate size, between molecular interstices and caverns, and that they may be interconnected or isolated, as shown (Figure 1-1). Traditionally the smaller interconnecting pores have been called throats. Pores range in size from those visible with the human eye, such as holes in sponges or soil, to those which may only be visible with microscopy such as the pores in human skin or in tight rock structures (de Boer, 2003).



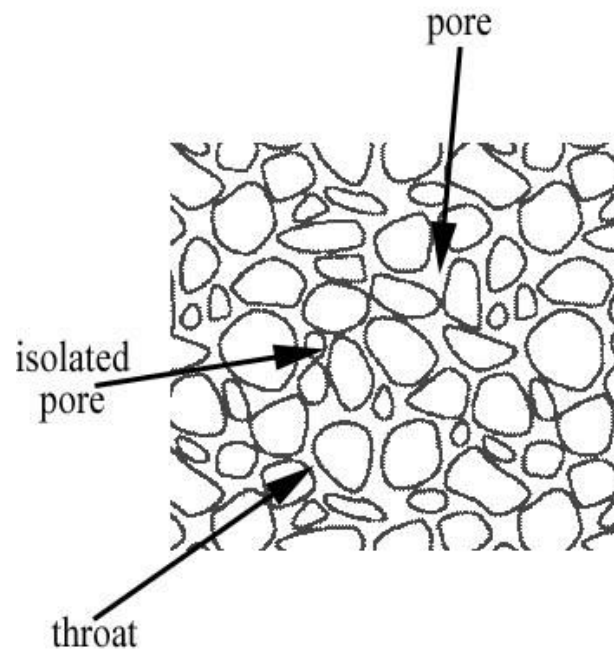


**Figure 1-1 Representation of a porous medium showing isolated pores, pores and connecting throats (Laudone, 2005)**

Porosity is a useful characterisation parameter. However, more parameters are required to allow full structural characterisation of porous media. Permeability, tortuosity, surface area, connectivity and the pore/throat size distribution are fundamental in giving a valid description of the sample in question. Figure 1-2 is reproduced from Schoelkopf (2002) and illustrates different categories of porous media using a schematic representation.

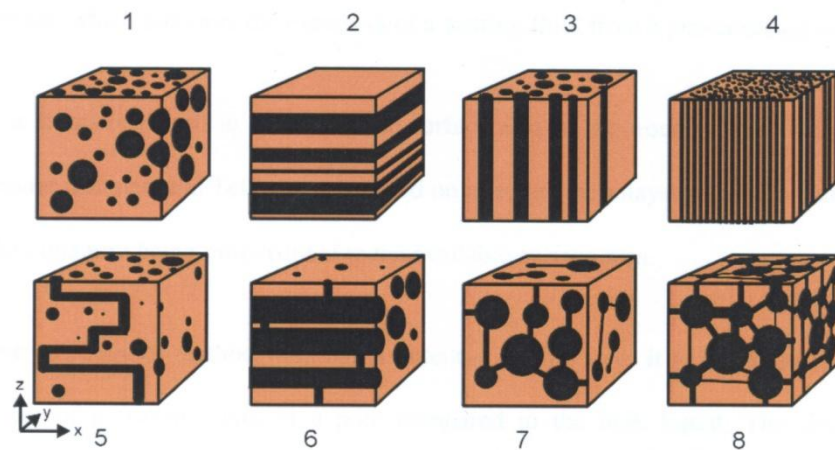


**Figure 1-2 Schematic of various porous media types (Schoelkopf, 2002)**

In the schematic (1) shows a porous medium solely containing isolated (dark) pores, while (2) shows a strongly anisotropic structure. Representations (3) and (4) show two capillary-bundle structures which contain similar porosity but differing average pore diameters. Representation (5) depicts a structure with a high tortuosity throughout the structure which contains no connectivity between pores. Structure (6) is a structure showing a small connectivity parameter with high tortuosity and isotropism. Structures (7) and (8) show pore and throat network structures with similar levels of tortuosity, but different levels of permeability. The drawbacks of this approach are discussed in detail in chapter 3.

#### ***1.3.1.1 Experimental methods to characterise porous media***

There are several techniques used to characterise porous materials. The most common is mercury intrusion porosimetry (Webb and Orr, 1997), which has been widely used in this work, and will therefore be explained in more detail in the next chapter. Another widely used method for the characterisation of porous material is the determination of surface area by measuring the amount of gas, typically nitrogen, adsorbed by the material. The surface area results are usually analysed using the BET isotherm. Alternative gases can also be used to determine the surface area such as argon, *n*-butane and carbon dioxide. This technique has been widely used in this work, and will therefore also be described in detail in the next chapter. Gas adsorption is also used to evaluate pore area and pore volume, by using an adsorption-desorption isotherm and applying the BJH algorithm (from the surnames of its originators, Barrett, Joyner and Halenda (Barrett, Joyner *et al.*, 1951)). The BJH algorithm is explained in more detail in Section 1.3.1.4. Another technique used to characterise porous media is microscopy combined with image analysis. Scanning electron microscopy combined with image analysis will be explained in more detail in the next chapter. Finally, the last technique used for characterisation of porous media, typically as a quality control instrument in

the filtration industry, is porometry, explained in more detail in Section 1.3.1.2 and in the next chapter.

### **1.3.1 Modelling of porous materials**

There are significantly different methods for modelling porous materials. Some models give specific information about the porous material, for example, the pore size distribution from gas adsorption. Other approaches using different raw data involve construction of a three-dimensional model, generating significantly more information such as pore size distribution, connectivity and tortuosity.

#### ***1.3.1.1 Mercury porosimetry and porometry modelling***

Perhaps the simplest approach is to use a continuum model, in which the porous structure is treated as a bulk, and the physical behaviour of the system is quantified by using bulk parameters, such as diffusion coefficients and permeabilities. These parameters are obtained by phenomenological equations. The assumptions and approximations required, despite being acceptable under the circumstances of each single study, limit the usefulness of such continuum models to a very narrow range of systems.

A second approach is the capillary bundle approximation, where the porous material is assumed to contain aligned, separate capillaries. A typical representation for this type of porous model is shown in Figure 1-2 (3) and (4), and enlarged in Figure 1-3.

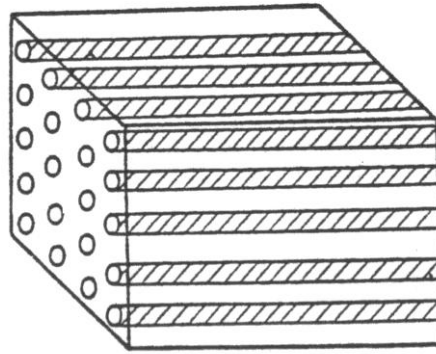


**Figure 1-3 Bundle of capillaries model for porous medium (Laudone, 2005)**

The mercury intrusion curve and porometry data can be used to obtain a capillary cross-sectional size distribution from an idealised such as that of Figure 1-3. The mercury or gas pressure is converted to a “pore” size – actually the size of the entry throat, using the Laplace-Washburn equation, as discussed in more detail in sections 2.1.2 and 2.1.3. The first derivative of the mercury intrusion curve and liquid expulsion curve is assumed to be directly related to the pore size distribution for such a model void space. The first derivative curve can be converted into pore size distribution. However, the resulting capillary sizes are unrealistically skewed to the small range of diameters. The pore voids are much larger, in reality, due to a well-known shielding effect in real porous media, (Webb and Orr, 1997), with large pores being shielded by smaller throats during the mercury intrusion and liquid expulsion processes. Figure 1-2 (5) and Figure 1-4, (Matthews, 2000), is a diagram of a capillary bundle model, with sizes derived from the first derivative of a mercury intrusion curve. In this case, the capillary tubes are tortuous, although some tortuosity cannot be obtained directly from experimental intrusion measurements. The drawbacks of this approach are discussed in detail in Chapter 3.

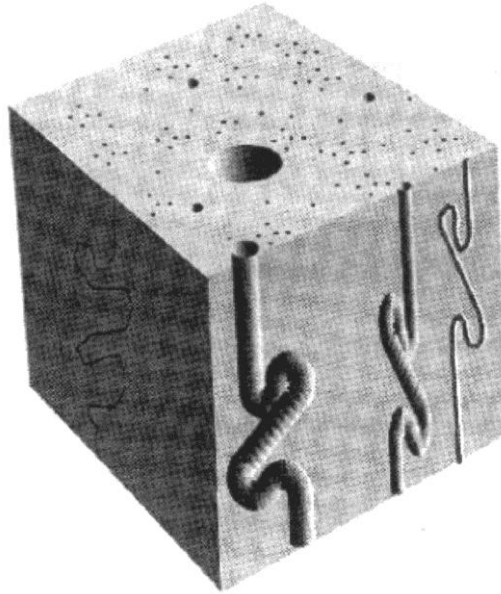


**Figure 1-4 Attempt to describe tortuosity within the one-dimensional model of a porous medium (Matthews, 2000)**

The final type of approach in the modelling of porous material is the three-dimensional network model of the porous structure. Such a model was created by Pan *et al.* (Pan, Davis *et al.*, 1995) to describe the migration of binder within the porous network of a paper coating, as shown in Figure 1-5. The model has severe limitations: the connectivity of the structure is fixed with a value of 6, which means that each cubical pore is connected to another by six throats, and the pore size distribution is completely arbitrary.

---

Figure 1-5 has been removed due to Copyright restrictions

---

**Figure 1-5 Three dimensional network model of a porous material (Pan, Davis *et al.*, 1995)**

There have also been attempts to describe the void space in a porous material by image analysis of the analysis of the modelled cross section itself (Toivakka and Nyfors, 2001). The work was illustrated using a packing model of spheres and identified pores and throats by an erosion algorithm, where each successive erosion is represented by a darker colour,

Figure 1-6.

---

Figure 1-6 has been removed due to Copyright restrictions

---

**Figure 1-6 Pore identification from a two-dimensional image and erosion of the pore space as presented in Toivakka and Nyfors (2001)**

This model also has limited use, as its application is confined to computer generated packing of spheres and this is not representative of porous materials. The analysis also neglects the effect of the connectivity in the vertical direction unless arbitrary rules are used for overlap and boundary conditions.

### ***1.3.1.2 Characterisation of pore architecture***

The non-wetting characteristic of liquid mercury on a wide range of materials is the key property in allowing mercury to be used as a probe of void architecture. The volume of mercury intruded into a porous sample is measured at increasing applied pressures of mercury, allowing time for equilibrium to be established at each pressure. Mercury porosimetry is capable of comprehensive characterisation of combined mesoporous and macroporous structures (Thommes, Skudas *et al.*, 2008). Mercury extrusion can give information about the surface texture of the macropores, which control the transport into and out of the mesopores (Rigby, Watt-Smith *et al.*, 2006; Rigby and Chigada, 2010).

By contrast to porosimetry, porometry is a non-destructive technique for the determination of pore size distribution, used for quality control purposes in the filtration industry (MiettonPeuchot, Condat *et al.*, 1997). Porometry involves the expulsion of a fully wetting fluid from a saturated porous medium by increasing the gas pressure, with higher gas pressures relating to smaller pore diameters. The flow rates at particular pressures are compared to flow rates at corresponding pressures in a ‘dry’ run, carried out after all the wetting fluid has been expelled in the initial run.

SEM can be used to image material surfaces, with its limited depth of field providing correspondingly limited information in the 3<sup>rd</sup> dimension. The technique can be coupled with 2-dimensional image analysis (Exner and Hougardy, 1988) to allow a quantitative assessment of microstructure and other characteristics such as defects in construction (Rasband, 2008).

There have been many previous multi-technique investigations of pore structure and pore architecture. A comparison of porosimetry and porometry showed that the latter is skewed towards smaller pores (Calvo, Hernandez *et al.*, 1995; Li, Frey *et al.*, 2006), as confirmed in Chapter 3. A hierarchical structural model has also been constructed for the interpretation of mercury porosimetry and nitrogen sorption, with the macroscopic ( $> 10 \mu\text{m}$ ) and microscopic ( $< 10 \mu\text{m}$ ) properties being modelled separately (Rigby, 2000).

Catalysts with multiple levels of pore size have been designed to optimise the pore network structure to maximise the surface area while maintaining optimum transport through the catalyst (Gheorghiu and Coppens, 2004). Periodically ordered mesoporous and macroporous  $\text{SiO}_2$  thin films have had their architecture characterised into either bimodal or trimodal thin films using various techniques including SEM, electrochemistry, krypton and nitrogen sorption (Sel, Sallard *et al.*, 2007).

Work has also been performed using SEM and mercury porosimetry to study the structure of rocks (Tsakiroglou, Ioannidis *et al.*, 2009) and soils (Tsakiroglou and Ioannidis, 2008), with structures comprising primary pores and throats and a secondary fractal pore system. Another study compared the deviation of void area distribution (from SEM) and pore size distribution (from mercury porosimetry), in a series of homeomorphic pigmented paper coating structures with increasing amounts of latex binder. The topological similarity provided a method for determining connectivity, i.e.

secondary structure, as a function of latex addition, by use of the Pore-Cor network model (Gane, Salo *et al.*, 2009).

A statistical model has been developed which characterises parameters such as connectivity and lattice size based on mercury porosimetry, nitrogen sorption and pulsed-gradient spin-echo nuclear magnetic resonance (PGSE NMR) (Rigby and Daut, 2002). The PGSE NMR and nitrogen sorption agree in their estimates of pore sizes, but differ from mercury porosimetry. The differences were attributed to the differing physical processes involved in probing the structure, and that the structure derived is a map of the pore space onto an abstract, random bond pore network. Characteristic properties of the pore space for mesoscopic ( $< 10\ \mu\text{m}$ ) length scales are captured by this mapping (Rigby and Daut, 2002). Other work (Rigby, Fletcher *et al.*, 2002) compares different techniques for determining pore characteristics including NMR, micro-focus x-ray (MFX) imaging, nitrogen sorption and mercury porosimetry.

### ***1.3.1.3 Gas adsorption modelling***

Porous materials that are analysed using gas adsorption to calculate the surface area, pore volume and pore area require a different treatment to model porous features, as the Laplace-Washburn equation is not applicable. Gas adsorption typically uses nitrogen for the determination of surface area. The most common surface area equation used is the BET equation shown in Equation 1-1. The BET theory is an extension of the Langmuir theory for monolayer molecular adsorption. The following hypotheses are made by BET theory: (a) gas molecules physically adsorb on a solid in layers infinitely; (b) there is no chemical interaction between each adsorption layer and (c) the Langmuir theory can be applied to each layer (Brunauer, Emmett *et al.*, 1938).



$$\frac{1}{v \left[ \left( \frac{P_0}{P} \right) - 1 \right]} = \frac{c_{\text{BET}} - 1}{v_m c_{\text{BET}}} \left( \frac{P}{P_0} \right) + \frac{1}{v_m c_{\text{BET}}}$$

**Equation 1-1**

$P$  and  $P_0$  are the equilibrium and saturation pressure of the adsorbates at the temperature of adsorption,  $c_{\text{BET}}$  is the BET constant,  $v$  is the volume of gas adsorbed and  $v_m$  is the monolayer adsorbed gas quantity. The BET constant can be expressed by Equation 1-2.

$$c_{\text{BET}} = \exp \left( \frac{E_1 - E_L}{RT} \right)$$

**Equation 1-2**

$R$  is the universal gas constant,  $T$  is the absolute temperature, and  $E_1$  and  $E_L$  are the energy of adsorption for the first layer and for the second and higher layers respectively. Equation 1-1 can be plotted as a straight line, with a linear relationship maintained in the range of  $0.05 < P/P_0 < 0.35$ . A BET plot is illustrated in Figure 1-7 with  $P/P_0$  plotted on the x-axis and  $P/(v(P_0 - P))$  plotted on the y-axis.

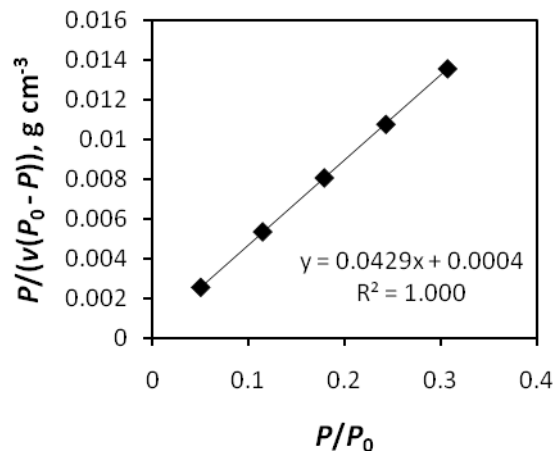


**Figure 1-7 BET plot for a modified calcium carbonate**

The slope  $a$  and the intercept  $b$  of the best fit line is used to calculate the BET constant  $c$  and the monolayer adsorbed gas quantity  $v_m$ :

$$v_m = \frac{1}{a+b}$$

Equation 1-3

$$c_{\text{BET}} = 1 + \frac{a}{b}$$

Equation 1-4

The monolayer adsorbed gas quantity is then used to calculate the surface area of porous materials as shown in Equation 1-5.

$$S = \frac{(v_m N s)}{V_m}$$

Equation 1-5

$S$  is the surface area,  $N$  is Avogadro's number,  $s$  is the cross sectional area of adsorbent gas and  $V_m$  is the molar volume of adsorbent gas. All gas adsorption experiments are carried out under isothermal conditions, so the molar volume of adsorbent gas does not change.

#### **1.3.1.4 Barrett, Joyner and Halenda (BJH) algorithm**

Gas adsorption experiments also allow the pore volume and pore area to be determined by using the desorption curve from a full adsorption-desorption isotherm. There are many different techniques for determining pore size from gas adsorption. One of the simplest techniques that can be used to generate the pore size distribution from gas adsorption is the Kelvin equation, Equation 1-6 (Rouquerol, Rouquerol *et al.*, 1999).

$$\ln\left(\frac{P}{P_0}\right) = \frac{2\gamma_{LV} V_m}{r_g RT}$$

Equation 1-6

$\gamma_{LV}$  is the surface tension (interfacial tension) of the liquid relative to its vapour,  $r_g$  is the radius of the gas droplet. The Kelvin equation can be used to calculate the core radius assuming the contact angle is  $0^\circ$ . The contact angle is the angle in which two different phases interact, and is specific for any given system. Further equations for calculating the pore size distribution are based upon the Kelvin equation. In this work a form of the BJH equation has been used (Barrett, Joyner *et al.*, 1951; Micromeritics, 2006). The BJH method can be used with the adsorption and desorption branch of the isotherm, and there are limitations with both branches of the isotherm.

Although both branches can be used for pore size calculations, from both a thermodynamic and historical point of view, the desorption branch is often favoured for pore size assessment (Neimark, Ravikovitch *et al.*, 2000). However, in the case of a broad distribution of pore sizes, pore network effects and cage-like structures, the desorption branch is in particular sensitive to the traditionally called tensile strength effect (TSE) of the adsorbed phase, leading to a forced closure of the hysteresis loop around a relative pressure of 0.45 in case of  $N_2$  at 77K (Choma, Jaroniec *et al.*, 2002). The tensile strength effect is a result of the instability of the hemispherical meniscus during desorption in pores with critical diameters approaching 4 nm. The instability is caused by an increased chemical potential of the pore walls, and an increased tensile strength in the adsorbed phase, as the pore size decreases (Gregg and Sing, 1982; Groen, Peffer *et al.*, 2003).

If interpreting the adsorption branch using the BJH algorithm, there is a fluid to crystalline-like phase transition which occurs in the relative pressure region of 0.1 – 0.2. The fluid to crystalline-like phase transition can suggest additional porosity at 2 nm. However, the pores at 2 nm are a result of a phase transition of the adsorbed  $N_2$  from a disordered “fluid” phase to a more ordered “crystalline” like phase and consequently do

not indicate real porosity (Groen, Peffer *et al.*, 2003; Groen, 2004). There are alternative methods such as non localised density functional theory that can be used to calculate pore size distribution (Ravikovitch, Haller *et al.*, 1998; Solcova, Matejova *et al.*, 2006; Thommes, Smarsly *et al.*, 2006).

### ***1.3.1.5 Calculation of pore size distribution using the BJH algorithm.***

The pore is divided into three zones as shown in Figure 1-8.

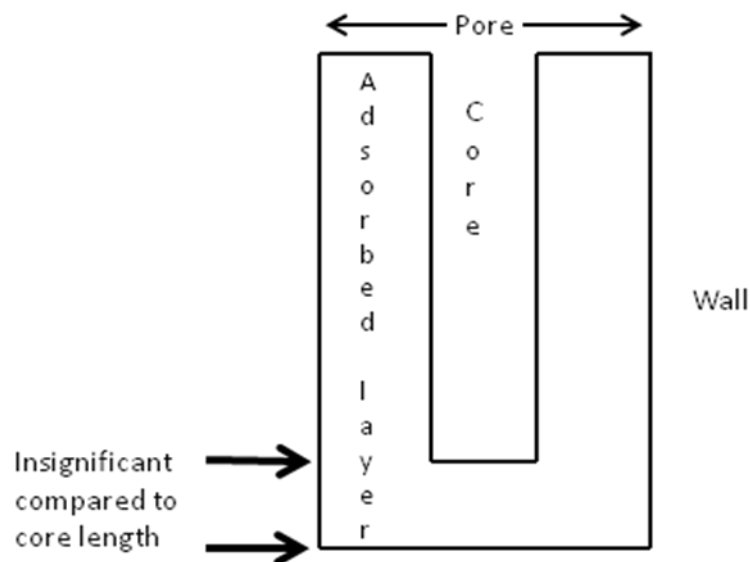


**Figure 1-8 A pore filled with condensed fluid has three distinct zones.**

Figure 1-8, shows three distinct regions of a pore that need to be considered when calculating the pore size, pore area or pore volume. The first region to consider is the core of the pore. The gas adsorbed in the core evaporates when the critical pressure is reached, and the relationship between core radius and critical pressure is defined by the Kelvin equation, Equation 1-7. The adsorbed layer is gas that has adsorbed onto the walls of the pore. With each pressure reduction step some of the adsorbed gas is removed, to an extent defined by the Halsey thickness equation, Equation 1-8. The third region of the pore shown in Figure 1-8 is the walls of the cylindrical pore, and the

diameter of the pore is required to determine the pore volume and pore area. By combining the results from the Kelvin equation and the Halsey thickness below, the pore area and pore volume is determined.

Equation 1-6 can be rearranged to calculate the Kelvin core radius ( $r_{cl}$ ), Equation 1-7 calculates the radius of the pore and was adjusted for the thickness of the adsorbed layer.

$$r_{cl} = \frac{-A}{(1 + F) \left[ \ln \frac{P}{P_0} \right]}$$

**Equation 1-7**

$F$  is the fraction of pores open at both ends. The fraction of pores open at both ends is assumed to be zero for desorption curves.  $A$  is a constant that simplifies the Kelvin equation by combining parameters from Equation 1-6. The BJH calculation uses the Kelvin equation to calculate the radius of the pore, and the Halsey thickness equation, Equation 1-8, is used to calculate the thickness of the adsorbed layer ( $T_w$ ).

The Halsey thickness equation is calculated for each pressure of the desorption or adsorption curve, where  $HP_1$ ,  $HP_2$  and  $HP_3$  are Halsey Parameters 1 – 3 respectively. The calculation assumes that all pores are filled at the highest relative pressure.

The calculation is performed in steps with Equations 1-9 to 1-22 being performed for each relative pressure interval based on the increment of volume desorbed during that interval.

$$T_{w_{I+1}} = HP_1 \left[ \frac{HP_2}{\ln \left( (P / P_0)_{I+1} \right)} \right]^{HP_3}$$

**Equation 1-8**

The variable  $I$  refers to the interval number:  $I = 1$  for the first interval from  $(P/P_0)_1$  to  $(P/P_0)_2$  and so on. For the last pressure interval from the lowest relative pressure to zero relative pressure  $T_{w_{I+1}} = 0$ . For the first pressure interval, there are no previously opened pores so the volume desorbed from walls of previously opened pores is zero. The change in thickness of the wall layer is calculated due to desorption from previously opened pores, Equation 1-9.

$$\Delta T_w = T_{w_I} - T_{w_{I+1}}$$

**Equation 1-9**

The annular cross-sectional area of the wall layer desorbed is calculated for all previously opened pores, Equation 1-10

$$CSA_j = \pi \left[ (r_{c_j} + \Delta T_w)^2 - r_{c_j}^2 \right]$$

**Equation 1-10**

$CSA$  stands for cross sectional area,  $j$  refers to each previous interval during which new pores were found. The total volume of gas desorbed ( $V_d$ ) from walls of previously opened pores is calculated, Equation 1-11 for the first pressure interval the value of  $V_d$  is zero.

$$V_{d_I} = (l_{p_j})(CSA_j)$$

**Equation 1-11**

where  $l_{p_j}$  is the length of previously opened pores. To calculate the length of previously opened pores the following calculations are performed. The volume adsorbed ( $V_a$ ) is converted into liquid equivalent volumes,  $V_l \text{ cm}^3 \text{ g}^{-1}$ , using the density conversion factor ( $D$ ), Equation 1-12.

$$V_{I_I} = (V_{a_I})D$$

**Equation 1-12**

If the volume desorbed from walls is less than the volume increment desorbed during the interval, the remaining volume must be due to new pores with core evaporation taking place. The volume desorbed from newly opened pores ( $V_{c_I}$ ) for each interval is calculated, Equation 1-13. The Kelvin radius is then calculated for the end of each interval using Equation 1-7.

$$V_{c_I} = (V_{I_I} - V_{I_{I+1}}) - V_{d_I}$$

**Equation 1-13**

All pores opened during each interval are represented by one pore having a length-weighted average pore diameter, and a corresponding length to account for the required volume of adsorbate. The weighted average pore diameter  $d_{avg_K}$  is calculated as follows, Equation 1-14.

$$d_{avg_K} = \frac{2(r_{c_K} + r_{c_{K+1}})r_{c_K}r_{c_{K+1}}}{r_{c_K}^2 + r_{c_{K+1}}^2}$$

**Equation 1-14**

$K$  is the number of intervals with new pores exposed and  $d_{avg_K}$  is the diameter of a pore which would have surface area that is the average of the areas for pores with radius  $r_{c_K}$  and  $r_{c_{K+1}}$ , if its length was the mean of the length at those radii. The relative pressure  $P_{avg_K}$  corresponding to  $d_{avg_K}$  is calculated using an adaptation of the Kelvin equation, Equation 1-15. The corresponding thickness can be calculated by using the average pressure in Equation 1-8. The thickness calculated by Equation 1-8 can then be substituted into Equation 1-9 instead of  $T_{wI}$  to calculate the decrease in thickness of the wall layer by desorption from the walls of new pores during the lower portion of the pressure interval.

$$P_{\text{avg}_K} = \ln^{-1} \left[ \frac{-2A}{(1+F)(d_{\text{avg}_K})} \right]$$

**Equation 1-15**

The steps detailed above allow the cross sectional area of newly opened pores  $\alpha$  to be calculated, Equation 1-16.

$$\alpha = \left[ \frac{d_{\text{avg}_K}}{2} + \Delta T_d \right]^2$$

**Equation 1-16**

$\Delta T_d$  is the decrease in thickness of the pore due to desorption. The length of the pores can now be calculated,

$$l_{p_K} = \frac{V_{cI}}{\alpha}$$

**Equation 1-17**

The pore diameters and pore radii previously calculated are adjusted for the change in thickness of the adsorbed wall layer. The average diameter is adjusted by the change in layer thickness during the second portion of the desorption interval as follows if new pores were opened, Equation 1-18

$$d_{\text{avg}_{K\text{new}}} = d_{\text{avg}_{K\text{old}}} + 2(\Delta T_d)$$

**Equation 1-18**

The layer thickness change during the whole interval is added to diameters of previously opened pores as follows, Equation 1-19. This does not include  $d_{\text{avg}_K}$ .

$$d_{\text{avg}_{j\text{new}}} = d_{\text{avg}_{j\text{old}}} + 2(\Delta T_w)$$

**Equation 1-19**



All of the equations from 1-9 to 1-19 are repeated for each pressure interval to calculate  $dp_j$  which corresponds to the end of the interval. Now that  $dP_{(I)}$ ,  $d_{avg(I)}$  and  $l_{p(I)}$  have been calculated the following properties of the porous material can be obtained, incremental pore volume and incremental surface area. To calculate incremental pore volume  $V_{pI}$ , Equation 1-20 is used and Equation 1-21 is used to calculate incremental surface area  $S_I$ .

$$V_{pI} = \pi(l_{pI}) \left[ \frac{d_{avgI}}{2} \right]^2$$

**Equation 1-20**

$$S_I = \pi(l_{pI})(d_{avgI})$$

**Equation 1-21**

### ***1.3.1.6 Pore-Cor Research Suite modelling***

The Environmental and Fluid Modelling Group of the University of Plymouth has developed Pore-Cor Research Suite, a network simulation software, which uses a novel approach for the modelling of the void space in a porous material. Pore-Cor stands for Pore level properties Correlator. Pore-Cor has been continuously developed throughout this study and includes features of all the model classifications described above (Section 1.3.1.1). The model represents a compromise between the highly advanced mathematical models and those of simplified nature derived from empirical data. It is a software package which allows the study of any mesoporous or macroporous solid, i.e. pore sizes greater than 2 nm (Rouquerol, Rouquerol *et al.*, 1999). The software is able to model data obtained by mercury porosimetry, porometry or soil water retention.

The model approximates the geometry of each void network as a unit cell with periodic boundary conditions containing 1000 cubic pores connected by up to 3000 cylindrical throats arranged in a regular Cartesian array Figure 1-9.

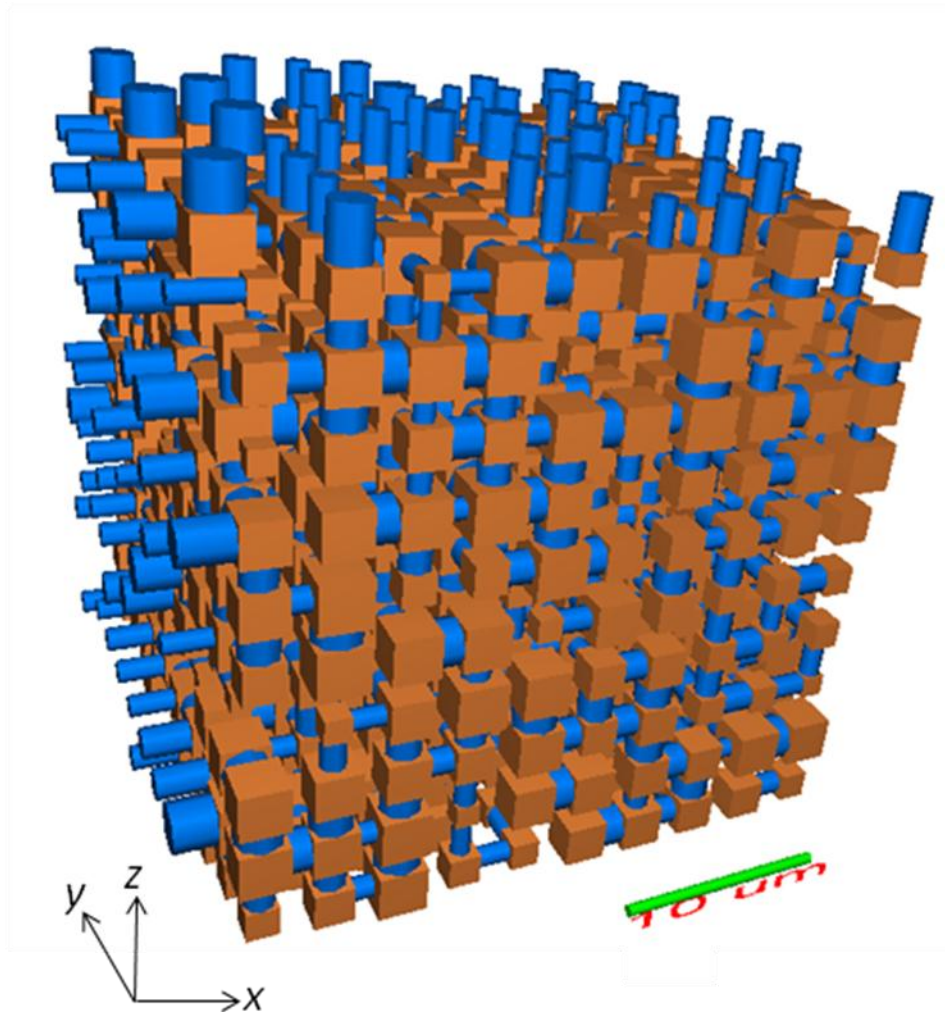


**Figure 1-9 Simulated Pore-Cor network representation showing cylindrical throat and cubic pore representation arranged in a three dimensional Cartesian array.**

Pore-Cor has been previously used to model a range of materials such as soil (Peat, Matthews *et al.*, 2000; Johnson, Roy *et al.*, 2003; Holtham, Matthews *et al.*, 2007; Laudone, Gregory *et al.*, 2009; Matthews, Laudone *et al.*, 2010), paper coating (Gane, Kettle *et al.*, 1996; Bodurtha, Matthews *et al.*, 2005; Laudone, Matthews *et al.*, 2005), sandstone (Matthews, Canonville *et al.*, 2006) calcium carbonate (Schoelkopf, Ridgway *et al.*, 2000; Laudone, Matthews *et al.*, 2007) and filters (Price, Matthews *et al.*, 2009).

The generated network structures created by the software are constructed under the criterion that they hold the same percolation characteristics as those derived from an experimental mercury porosimetry or porometry experiment. The experimental data can be interpreted using the Laplace-Washburn equation which relates applied pressure with

pore diameter. The experimental porosimetry or porometry curve is fitted using an iterative fitting of pore and throat sizes until a closest fit is found. The fitting process is undertaken using an annealed simplex algorithm, which works to find the global minimum for a five dimensional surface. Here we present an overview of the relevant aspects of the software to this work, while a detailed discussion of other algorithms used in Pore-Cor may be found in the literature e.g. (Matthews, Bodurtha *et al.*, 2004).

To simulate mercury intrusion and liquid expulsion, a computational representation of fluid is applied to the top face (maximum  $z$ ) of the unit cell only, and percolates in the  $-z$  direction, Figure 1-9. Fitting parameters which are called throat skew, throat spread, pore skew, connectivity and correlation level are adjusted by the Boltzmann-annealed amoeboid simplex (Press and Teukolsky, 1991; Johnson, Roy *et al.*, 2003) to give a close fit to the entire mercury intrusion curve or liquid expulsion curve. There are three additional Boolean constraints on the simplex: it rejects structures in which the network is fragmented, in which voids overlap, or which cannot be adjusted to give the experimental porosity.

The throat size distribution is of a flexible log/Euler-Beta form, which encompasses Gaussian like, Poisson like and bimodal distributions. The probability density function, representing the probability that the distribution lies in a small interval  $[x, x+dx]$ , is given by Equation 1-22 (Matthews, Laudone *et al.*, 2010).

$$f(x : \zeta, \eta_b) = \frac{1}{\Psi(\zeta, \eta_b)} x^{\zeta-1} (1-x)^{\eta_b-1}$$

**Equation 1-22**

where Equation 1-23 defines the ‘Beta function’.

$$\Psi(\zeta, \eta_b) = \int_0^1 x^{\zeta-1} (1-x)^{\eta_b-1} dx$$

**Equation 1-23**

The Log/Beta distribution uses two parameters, known as ‘throat spread’ and ‘throat skew’. Throat spread is a measure of the ‘fatness’ of the distribution. Throat skew is a measure of the ‘asymmetry’ of the distribution, with positive corresponding to favouring bigger sizes, negative favouring smaller sizes and 0 being symmetrical.

The parameter  $\zeta$  and  $\eta_b$  are related to the mean,  $\mu$ , Equation 1-24 and standard deviation,  $\sigma$ , Equation 1-25, of the distribution as follows.

$$\mu = \frac{\zeta}{\zeta + \eta_b}$$

**Equation 1-24**

$$\sigma^2 = \frac{\zeta \eta_b}{(\zeta + \eta_b)^2 (\zeta + \eta_b + 1)}$$

**Equation 1-25**

These expressions may be recovered by using the result that, Equation 1-26:

$$\Psi(\zeta, \eta_b) = \frac{\Gamma(\zeta) \Gamma(\eta_b)}{\Gamma(\zeta + \eta_b)}$$

**Equation 1-26**

where the ‘Gamma function’ is defined as:

$$\Gamma(x) = \int_0^{\infty} t^{x-1} e^{-t} dt$$

**Equation 1-27**

and noting that:

$$\Gamma(x) = (x-1)\Gamma(x-1).$$

**Equation 1-28**

The equations for the mean and standard deviation may be inverted:

$$\zeta = \frac{\mu^2 - \mu^3 - \mu\sigma^2}{\sigma^2}$$

**Equation 1-29**

$$\eta_b = \frac{\mu - 2\mu^2 + \mu^3 - \sigma^2 + \mu\sigma^2}{\sigma^2}$$

**Equation 1-30**

The distribution is therefore completely specified if  $\mu$  and  $\sigma$ , and therefore the quantities on the right hand side, are known.

The ‘throat spread’ is defined as twice the standard deviation  $\sigma$ . The ‘throat skew’ has a more complex definition in order to allow a balanced sampling of the simplex parameter space. It requires four quantities; the first two are the minimum  $\mu_{\min}$  and maximum  $\mu_{\max}$  possible means for a given standard deviation.

$$\mu_{\min / \max} = \frac{1}{2} \left( 1 \pm \sqrt{1 - 4\sigma^2} \right)$$

**Equation 1-31**

These can be found by substituting the following conditions, Equation 1-32 into Equation 1-29 and Equation 1-30.

$$\zeta = \eta_b = 0$$

**Equation 1-32**

If there exists a region where the distribution is unimodal for a given standard deviation then we define the minimum and maximum unimodal means as  $\mu_1$  and  $\mu_2$  respectively. The boundary case is a uniform distribution with:  $\alpha = \beta = 1$ ,  $\mu_1$  and  $\mu_2$  are obtained by solving a cubic equation, and then choosing the correct root (i.e the one nearest the median, which is always 0.5) (Press, Flannery *et al.*, 1986a):

$$\mu^3 - \mu^2 + \mu\sigma^2 + \sigma^2 = 0$$

Equation 1-33

### **1.3.1.7 Compressibility correction (Gane, Kettle *et al.*, 1996)**

When using mercury intrusion porosimetry data, due to the high pressures used during the experiment (up to 414 M Pa) and the differing compressibilities of mercury, sample and penetrometer, the experimentation is subject to various compressibility errors and these need to be corrected to obtain a true measure of the void space of a sample.

If the sample was completely incompressible, the experimentally observed mercury intruded volume,  $V_{\text{obs}}$ , would include the volume of mercury intruded into the sample,  $V_{\text{int}}$ , the volume expansion of the analysis chamber or penetrometer,  $\delta V_{\text{pen}}$ , and the compression of the mercury  $\delta V_{\text{Hg}}$  (Gane, Kettle *et al.*, 1996):

$$V_{\text{obs}} = V_{\text{int}} + \delta V_{\text{pen}} + \delta V_{\text{Hg}}$$

Equation 1-34

The term representing the expansion of the chamber can be evaluated by a blank run with no sample in the penetrometer. The term representing the compressibility of the mercury itself can be evaluated by using experimentally derived equations, which relate the volumetric compression of mercury as a function of pressure. The working equation for an incompressible sample becomes:

$$V_{\text{int}} = V_{\text{obs}} - \delta V_{\text{blank}} + \left[ 0.175(V_{\text{bulk}}^1) \log_{10} \left( 1 + \frac{P_{\text{app}}}{1820} \right) \right]$$

**Equation 1-35**

where  $\delta V_{\text{blank}}$  is the change in the blank run volume reading,  $V_{\text{bulk}}^1$  the sample bulk volume at atmospheric pressure and  $P_{\text{app}}$  the applied external pressure.

In order to obtain a correct interpretation of the mercury porosimetry intrusion curves one has to take into account this compressibility and apply another correction to the observed intruded volume. If  $\psi_{\text{ss}}$  is the compressibility of the sample and  $M_{\text{ss}}$  its bulk modulus, then

$$M_{\text{ss}} = \frac{1}{\psi_{\text{ss}}} = \frac{dP}{\left( \frac{-dV_{\text{ss}}}{V_{\text{ss}}} \right)}$$

**Equation 1-36**

The expression for the fully corrected intruded volume is shown in Equation 1-37. The raw mercury intrusion curves can be corrected for these errors using the Pore-Comp module of the Pore-Cor software.

$$V_{\text{int}} = V_{\text{obs}} - \delta V_{\text{blank}} + \left[ 0.175(V_{\text{bulk}}^1) \log_{10} \left( 1 + \frac{P_{\text{app}}}{1820} \right) \right] - V_{\text{bulk}}^1 (1 - \Phi^1) \left( 1 - \exp \left[ \frac{(P^1 - P_{\text{app}})}{M_{\text{ss}}} \right] \right)$$

**Equation 1-37**

$\Phi^1$  is the porosity of the sample at one atmosphere, and  $P^1$  is the atmospheric pressure.

Further details of the derivation of Equation 1-37 may be found in the publication by Gane, Kettle *et al.* (1996) which gives a comprehensive insight into how the correction procedure is used to provide true volumes of intrusion for a sample. It can be assumed that if intrusion and extrusion curves lie on top of each other at the highest pressures,

then in this region the increase in mercury intrusion is entirely due to compression of the solid phase of the sample, rather than percolation into its void space. Use of Equation 1-37 with this assumption allows calculation of the bulk modulus of the sample, which refers to a ratio of applied pressure to the decrease in sample volume when a uniform pressure is applied to the surface of a material. The bulk modulus is the inverse of compressibility and is given in units of pressure. So large values of bulk modulus correspond to a sample that is relatively incompressible, whereas samples with small values are highly compressible. For comparison polystyrene has a bulk modulus of around 3.5 GPa and diamond has a bulk modulus of around 440 GPa.

#### ***1.3.1.8 Diffusion algorithm (Laudone, Matthews et al., 2008)***

Pore-Cor RS modelling of diffusion applies only to diffusion occurring in two miscible fluids A and B (such as benzene and cyclohexane) driven by a concentration gradient between the porous volumes and the external fluid reservoir. The model assumes that there is no adsorption of species A or species B on the pore and throat walls, and the only phenomena occurring is the diffusion of species A. Surface diffusion is not taken into consideration, although surface diffusion can contribute significantly to the overall diffusion flux (Zalc, Reyes *et al.*, 2003; Laudone, Matthews *et al.*, 2008).

The solution of Fick's diffusion equation, Equation 1-38 (Crank, 1975) gives the profile of concentrations ( $c$ ) where  $t$  is time,  $D_{\text{fm}}$  is the free molecular diffusion coefficient and  $x$  is the spatial coordinate of the system.

$$\frac{\partial c}{\partial t} = D_{\text{fm}} \frac{\partial^2 c}{\partial x^2}$$

**Equation 1-38**

In diffusion problems, the diffusion length  $L_D$  is the characteristic length scale used to define the extent of the effective concentration:



$$L_D = \sqrt{4D_{\text{fm}}t}$$

**Equation 1-39**

The diffusion length dictates the concentration profiles. A diffusion length longer than the system causes the concentration profile within the system to be linear, whereas a shorter diffusion length causes a concentration profile which can be described by an error function. The diffusion calculation occurs in three concurrent but sequentially calculated time steps. The first step is diffusion in the  $-z$  direction, followed by the  $x$  and  $y$  directions as shown in Figure 1-9. After each time step the concentration  $C_A$  of species A, in each pore is calculated and used for each subsequent timestep (Laudone, Matthews *et al.*, 2008).

The diffusive flux of species A is given by Equation 1-40, where  $J_{\text{DA}}$  is the diffusive flux of species A,  $r_A$  is the effective molecular radius, through a single cylindrical throat of length  $l_t$ , and radius  $r_t$ . The term  $D_{\text{tA}}$  is the throat diffusivity of species A, which takes into account the restrictions to the free molecular diffusion of species A,  $D_{\text{fmA}}$ , due to steric hindrance.

$$J_{\text{DA}} = \pi r_t^2 D_{\text{tA}} \frac{\Delta C_A}{l_t}$$

**Equation 1-40**

The throat diffusivity  $D_{\text{tA}}$  may be calculated as shown in Equation 1-41 (Meyers and Liapis, 1998; Meyers and Liapis, 1999; Meyers, Crosser *et al.*, 2001; Bryntesson, 2002).

$$D_{\text{tA}} = D_{\text{fmA}} \left(1 - \frac{r_A}{r_t}\right)^2 \left[1 - 2.104 \left(\frac{r_A}{r_t}\right) + 2.09 \left(\frac{r_A}{r_t}\right)^3 - 0.95 \left(\frac{r_A}{r_t}\right)^5\right]$$

**Equation 1-41**

Using the Einstein-Stokes equation it is possible to calculate the free molecular diffusion coefficient of species A, Equation 1-42:

$$D_{\text{fmA}} = \frac{k_{\text{B}}T}{6\pi r_{\text{A}}\eta_{\text{B}}}$$

**Equation 1-42**

Here  $k_{\text{B}}$  is Boltzmann's constant,  $T$  is the temperature and  $\eta_{\text{B}}$  is the viscosity of the medium B in which species A is dissolved.

### **1.3.2 Zero length column**

The 'zero length column' (ZLC) is a device developed by Eic and Ruthven (1988) for the study of diffusion and sorption in gaseous systems. The device is particularly useful for the study of dual porous solids – i.e. particulate samples in which there is both inter- and intra-particle porosity. The ZLC allows a monolayer or 'Zero Length' of a dual porous sample to be held stationary acting as a stationary phase in a chromatography experiment, so that diffusion is controlled only by the intra-particle rather than the inter-particle porosity. The original ZLC contained a small quantity of the porous material embedded in an inert, non-porous packing material with particle size significantly larger than the particles of the sample material. The device was developed for determination of intra-particle or 'crystalline' diffusivities of strongly adsorbed species, to minimise the effect of heat transfer and inter-particle or 'bed' diffusion resistances.

For a ZLC experiment to give sufficient detail for quantitative results, the detector needs to be sensitive enough to detect small changes in concentration of mobile phase species. The ZLC technique has mainly been used for gaseous systems, with less work reported for liquid systems. The ZLC is used to study fundamental processes such as diffusion, sorption and kinetics.

There have been theoretical studies of how the molecular interactions with a ZLC are controlled. A study by Brandani considers biporous adsorbent particles, and whether the sorption rate is controlled by micropore diffusion or macropore diffusion (Brandani,

1996). A study in 2000 by Duncan and Möller (2000) considered the ‘zero length’ criteria and compared the standard continuous stirred tank reactor (CSTR) model with the plug flow model. The study concluded that the two cases can be considered identical for practical purposes. The interstitial hold-up in a well-mixed sorbent bed may be neglected if the adsorption constant of the system is large enough that  $\gamma_z < 0.1$  (Brandani and Ruthven, 1995).  $\gamma_z$  is the dimensionless parameter defined in Equation 5-3 below. When  $\gamma_z < 0.1$ , the flow pattern within the bed can be disregarded if  $L > 15$ , which implies that diffusive transport is dominant over convective transport.  $L$  is a dimensionless ZLC parameter defined by Equation 5-2 below. When  $\gamma_z < 0.1$  and  $L > 15$  the CSTR model and plug flow model provide identical results (Duncan and Möller, 2000).

Studies undertaken using a ZLC for gaseous systems have involved the study of intra-crystalline diffusion of strongly adsorbed hydrocarbons onto zeolites, and Eic and Ruthven (1988) found that this technique agreed with gravimetric data. The gravimetric technique (i.e. measuring the change in mass of the stationary phase during the adsorption or desorption step against time) was the preferred technique to investigate intra-crystalline diffusion prior to the development of the ZLC. A further paper on ZLC work with gases described the mathematical model of zero length column chromatography, using a Volterra integral technique. The model in this paper includes effects of non-linearity, extra column broadening, and sorption kinetics (Micke, Kocirik *et al.*, 1993).

A paper by Brandani, Xu *et al.* (1996) introduces the tracer ZLC technique, which uses a deuterated benzene molecule which is NMR active. The results from the tracer ZLC technique were compared with self diffusion results obtained using Pulsed Field Gradient-Nuclear Magnetic Resonance (PFG NMR). The tracer ZLC technique was

used in conjunction with a standard ZLC technique. To investigate possible external mass transfer limitations a series of experiments was performed in which the sample quantity, crystal size, sorbate partial pressure and purge gas were changed. Larger sample sizes and higher sorbate pressures, allow external effects such as external diffusion or heat transfer to become evident, and with properly controlled conditions state that desorption rates are controlled by intra-crystalline diffusion. The results obtained are consistent with earlier results obtained by ZLC (Brandani, 1996).

Liquid phase counter-diffusion in zeolite crystals has been measured using the ZLC method (Ruthven and Stapleton, 1993b). The adsorbent sample was considered to be a well mixed CSTR. It was found necessary to account for the time to purge the interstitial fluid, and that the technique was limited due to the sensitivity of detectors and the lower flow rate when compared with gas chromatography. Section 2.2.2. expands on the development of the zero length column for liquid systems. The work on liquid systems was extended by Brandani and Ruthven (1995), who improved the mathematical model for analysing the data, and found that their diffusivity measurements correspond with earlier chromatographic measurements (Awum, Narayan *et al.*, 1988). The development of ZLC theory is extended in Section 5.1.

### **1.3.3 Mineralogy**

In Chapters 4, 5, 6 and 7 the following minerals were used: sodium bentonite, two grades of talc, two grades of ground calcium carbonate and two grades of modified calcium carbonate. Their mineralogy is now described.

#### ***1.3.3.1 Bentonite***

Bentonites are composed of montmorillonites, with traces of silica, quartz and other clay minerals. The mineral arranges into stacked dioctahedral layers with a chemical formula of  $\text{Al}_2\text{Si}_4\text{O}_{10}(\text{OH})_2$ . An SEM image of bentonite is shown in Figure 1-10 and

the structure is illustrated in Figure 1-11 . The aluminium in the formula can be exchanged for different cations with a lower valency. The edges of the plates are positively charged (Asselman and Garnier, 2000), giving hydrophilic edges. There are multiple methods of adsorption onto bentonite: for positively charged species there are electrostatic interactions, and for neutral or negatively charged species hydrogen bond interactions are present (Rohl, Vonrybinski *et al.*, 1994).

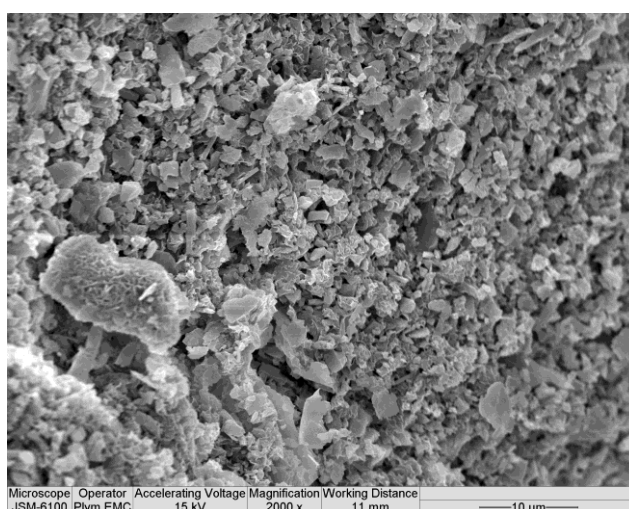


**Figure 1-10 SEM image of bentonite**

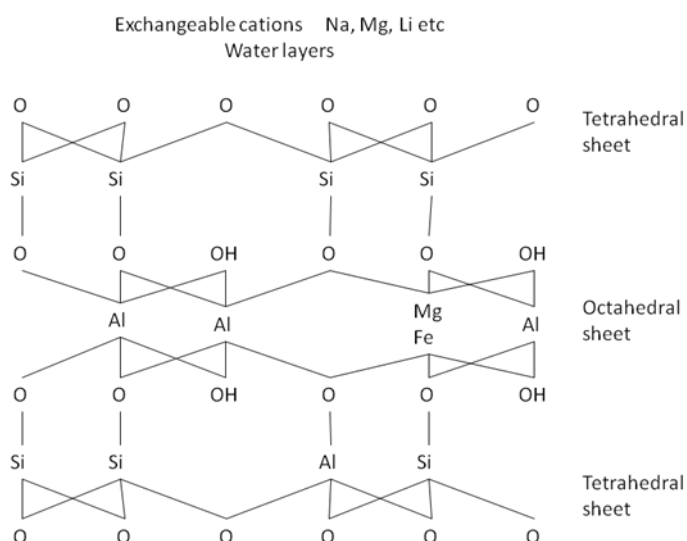


**Figure 1-11 Structure of montmorillonites, in the water layer different cations are found such as sodium, magnesium or lithium (Luckham and Rossi, 1999).**

### 1.3.3.2 Talc

Talc,  $\text{Mg}_3\text{Si}_4\text{O}_{10}(\text{OH})_2$ , is a phyllosilicate consisting of a magnesium hydroxide layer ( $\text{MgO}\cdot\text{H}_2\text{O}$ ) sandwiched by two silicate layers ( $\text{SiO}_2$ ) forming a three layer structure. Van der Waals forces hold the adjacent layers together weakly, giving talc a platy and readily delaminating morphology. The edges of the talc are predominantly hydrophilic hydroxide groups (Wallqvist, Claesson *et al.*, 2007), whereas the talc faces are largely silicate. The absence of surface charge on the silicate layers renders the surface more attractive to air than to water, and it is the retention of a suspected air layer (Sakai, Yanagisawa *et al.*, 2008) when suspended in water that allows the platelet surface to undergo hydrophobic interactions (Wallqvist, Claesson *et al.*, 2006). The chemical structure of talc, shown in Figure 1-12, illustrates the hydrophobic surfaces and hydrophilic magnesium hydroxide edges that control adsorption behaviour in aqueous suspension (Wallqvist, Claesson *et al.*, 2006; Wallqvist, Claesson *et al.*, 2007).

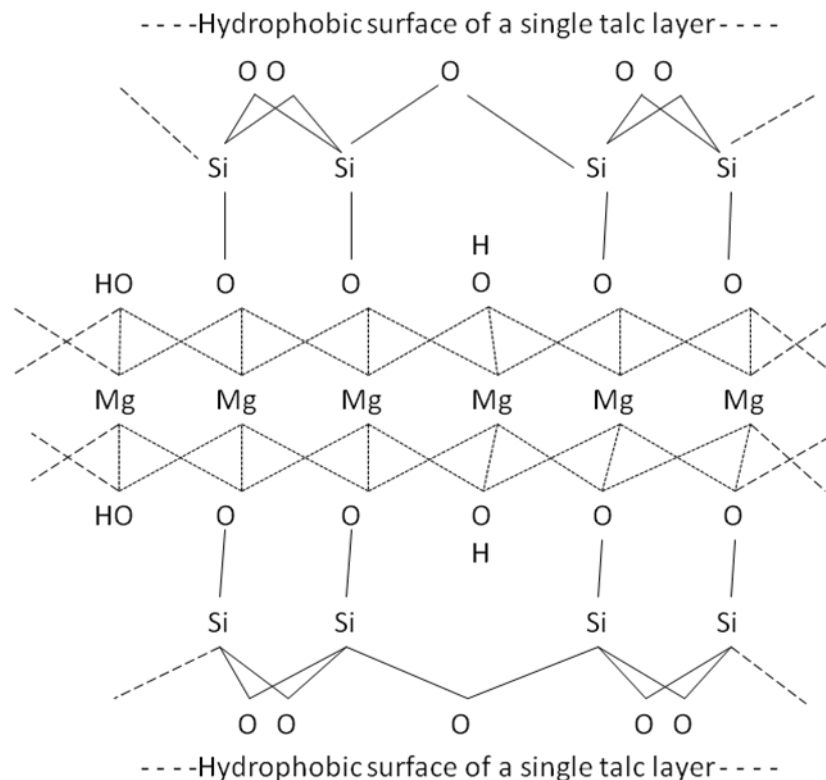


**Figure 1-12** Schematic of the chemical structure of talc. The top and bottom layers are silicates, and the middle is magnesium hydroxide.

We define ‘aspect ratio’ as the ratio of the largest dimension of the mineral particle relative to the smallest dimension. In the case of a platelet, such as found in talc, the largest axis is the diametrical dimension, related to the platelet planar surface, and the smallest that of the platelet edge thickness. The aspect ratio varies for different grades of talc, and the larger the aspect ratio, the greater the ratio of hydrophobic to hydrophilic surface area.

Talc is widely used in the paper industry, including use as a paper filler, paper coating and the treatment of pitch (Guera, Schoelkopf *et al.*, 2005) and stickies during the manufacturing process from raw materials and recycled paper respectfully. A SEM image of talc platelets is shown in Figure 1-13, and it is possible to see the different layers which make talc easily to delaminate.

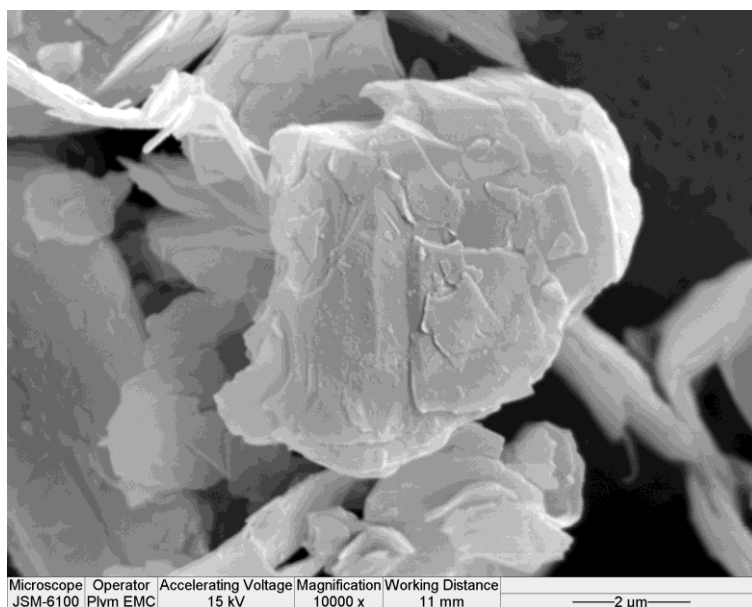


Figure 1-13 Scanning Electron Micrograph of talc, note the layers of platelets which allow for delamination.

### ***1.3.3.3 Calcium carbonate***

In this investigation ground calcium carbonate and modified calcium carbonates were used. To make modified calcium carbonate a ground calcium carbonate is modified using either citric acid, phosphoric acid or a combination of both acids.

#### ***1.3.3.4 Ground calcium carbonate***

Calcium carbonate ( $\text{CaCO}_3$ ) naturally occurs as calcite (Figure 1-14) in various rock forms, namely chalk, limestone and marble.



**Figure 1-14 Calcite** (from <http://www.ggl.ulaval.ca>)

Calcium carbonate is almost always ground using a ‘wet’ process, and the resulting ground calcium carbonate delivered as a slurry. There are several advantages to using a ‘wet’ process: energy is saved, the slurry can be pumped, it is free of dust and is ready for water based formulations. There are different grinding methodologies and these result in different particle size distributions, with typically 40 w/w% to 98 w/w% of the particles having a diameter  $< 2 \mu\text{m}$ . The slurry is usually stabilised by adding 0.1 – 1 w/w % active component of anionic dispersing agents (such as sodium poly-phosphate or sodium poly-acrylate) to avoid flocculation, aggregation or settling of the calcium carbonate, and to maximise transportation and applications solid content. An SEM image of ground calcium carbonate is shown below, Figure 1-15.



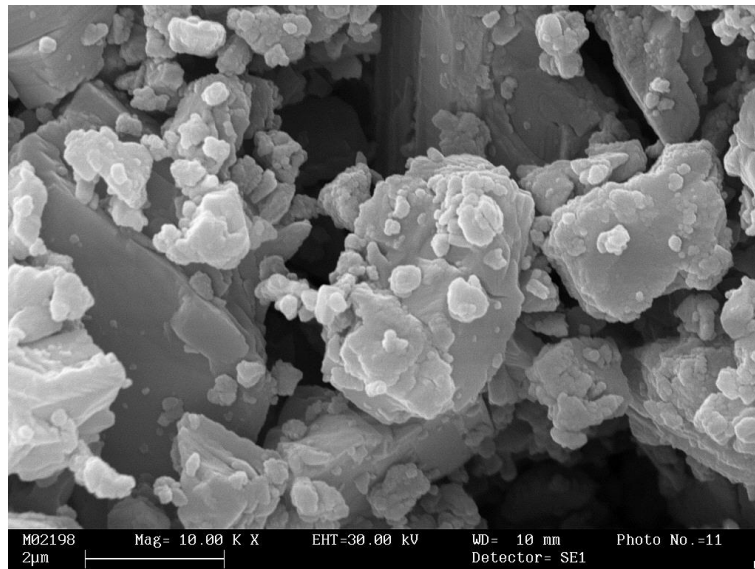
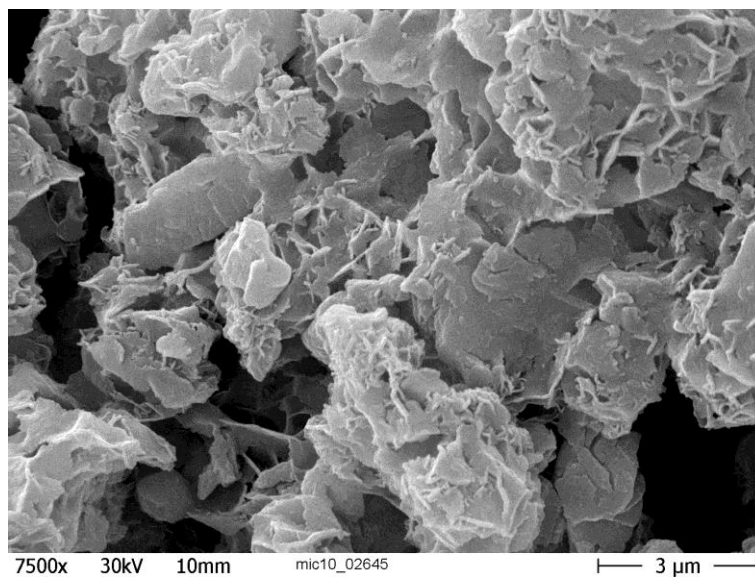


Figure 1-15 SEM image of a ground calcium carbonate with no identifiable internal porosity as seen with modified calcium carbonate.

### ***1.3.3.5 Modified calcium carbonate (Ridgway, Gane et al., 2004)***

Modified calcium carbonates are based on natural ground calcium carbonate, with the modification process changing the surface and porous properties of the ground calcium carbonate. The modified calcium carbonates have been modified by using citric acid, phosphoric acid or a combination of the two acids in a reactor to modify the porous structure and surface chemistry of the ground calcium carbonate. The modification to the calcium carbonate also increases the surface area of the calcium carbonate relative to the source calcium carbonate. Modified calcium carbonate can be produced with three distinct morphologies, “Roses”, Figure 1-16, “Eggs”, Figure 1-17 and “Golf balls”, Figure 1-18. The three different structure types have different aspect ratios and structures and are summarised in the figure captions (Ridgway, Gane *et al.*, 2004).



**Figure 1-16 SEM image of a “Roses” structure modified calcium carbonate, which is nano-dimensional surface edge-like structures of high aspect ratio formed on micro-particles.**

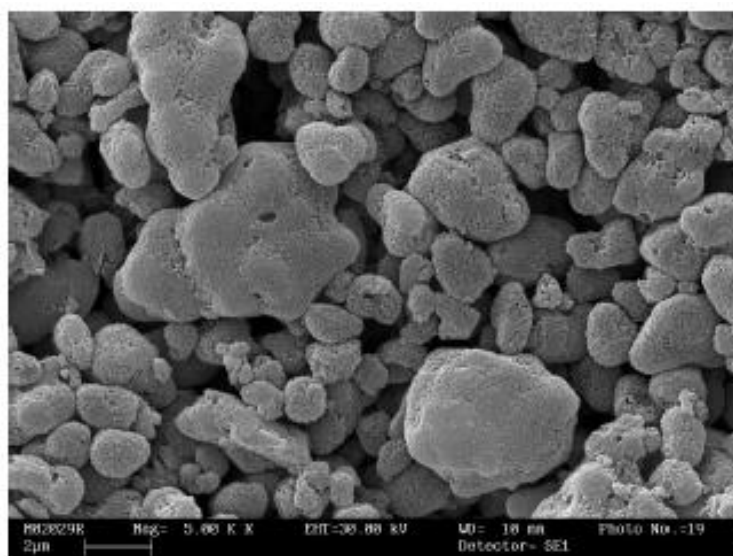


**Figure 1-17 SEM image of a “Eggs” structure modified calcium carbonate, which is an internally nano-porous calcium carbonate.**

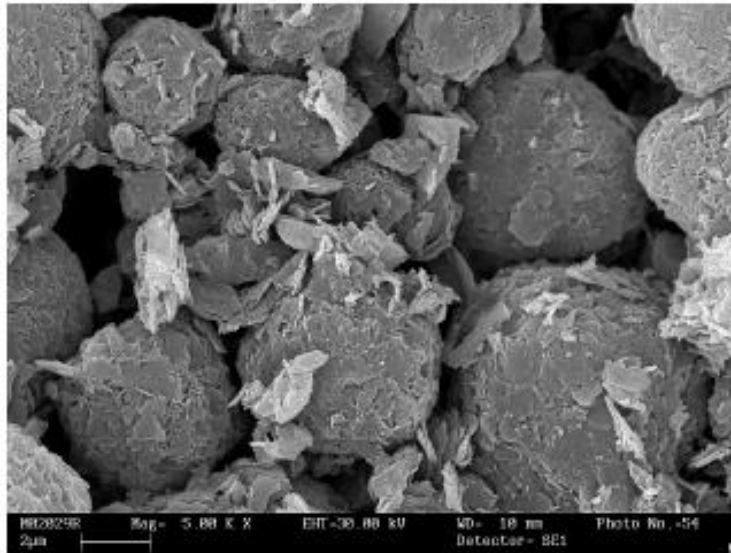


**Figure 1-18 SEM image of “Golf balls” modified calcium carbonate structure, which is a description of sub micrometre pores contained within a micro-particle cake.**

The structure modifications to the modified calcium carbonates allow the different structure types to form discrete networks, one associated with internal pores (intraparticle) and another associated with external voids (interparticle). The discrete networks allow their permeability and absorption driving force to be considered separately (Ridgway, Gane *et al.*, 2004).

### **1.3.4 Wettability**

Wetting is a property associated with the interface properties between a liquid and a surface. The surface may be another liquid, in the case of two immiscible liquids, or, more usually, a solid surface, as in the case of a porous material. The degree of wetting is dependent on various factors. The relative surface energy difference between the liquid and the porous structure material surface defines whether a liquid will wet the surface (Feng and Jiang, 2006). The rate of wetting is additionally dependent on further geometrical factors, including internal and surface structure.

### ***1.3.4.1 Wetting fluid properties***

Liquids and gases form the family of materials known as fluids, which in turn can be divided into potentially non-wetting and wetting fluids depending on the surface in contact with the fluid. For example, mercury is a non-wetting fluid in respect to most surfaces, such as when in contact with a steel sinter. However, if in contact with an aluminium sinter mercury becomes a wetting fluid.

The contact angle is defined as the three phase confluence angle subtended by a liquid front in equilibrium with its vapour in contact with a continuous uniform planar surface. The term is used to define whether the liquid is wetting or non-wetting, with angles less than  $90^\circ$  classified as wetting and greater than  $90^\circ$  classified as non-wetting (Bico, Thiele *et al.*, 2002).

At the surface of a liquid with its vapour, molecules of the liquid have fewer neighbours than those in the bulk. The resulting difference in interaction energy manifests itself as a surface tension at the interface between the liquid (L) and its vapour (V),  $\gamma_{LV}$ . Surface tension is a force that acts to reduce the surface area of a free liquid. For example, to minimise the surface free energy when a volume of liquid can freely adjust its shape, the liquid tends to form a sphere, as a sphere has the smallest surface area (Shirtcliffe, McHale *et al.*, 2010). Surface tension can be regarded as a force per unit length acting in the surface interface layer, and has units of  $\text{N m}^{-1}$  or as energy per unit area  $\text{J m}^{-2}$  (Adamson and Gast, 1997). The interaction between solid and liquid is controlled by surface tension in combination with any other externally acting force that may be present, for example gravity dependent on the scale of the features and mass of liquid. Surface tension scales as a function of length, namely the radius of curvature,  $R_c$ , whereas gravity scales with the mass, which, for a liquid droplet, is related to volume, i.e.  $R_c^3$ , and the density of the liquid,  $\rho$ . The ratio of gravitational to surface tension

forces for a droplet scales as  $\rho g R_c^3 / \gamma_{LV} R_c \sim R_c^2$ , (where  $g = 9.81 \text{ m s}^{-2}$  is the acceleration due to gravity), and so is large when the length scale is large, but vanishes as the length scale becomes small. Therefore, the dominant force crosses over from gravity to surface tension as the size reduces (Shirtcliffe, McHale *et al.*, 2010).

Since it is the balance of forces between liquid and the solid surface which defines the wettability of that surface for the given liquid, the surface energies of all interfacial components must be considered.  $\gamma_{LV}$  is the surface tension at the interface between the liquid and vapour phase,  $\gamma_{SL}$  that between the solid and the contacting liquid and  $\gamma_{SV}$  the solid-vapour interface energy. These are considered at the three phase intersection between liquid, solid and vapour at the meniscus contact point. The spreading power  $S$  is dependent on the action between these potentials so as to minimise the free energy of the system, and can be represented by Equation 1-43 (Shirtcliffe, McHale *et al.*, 2010).

$$S = \gamma_{SL} + \gamma_{LV} - \gamma_{SV}$$

**Equation 1-43**

The contact angle is independent of droplet size and is described by the Young equation, Equation 1-44 (Adamson and Gast, 1997), where  $\theta_e$  is the equilibrium contact angle at the edge of a stationary droplet. The concept of a single equilibrium contact angle is a simplified view and does not take into account contact angle hysteresis related to how the droplet arrived at its resting state through advancing or receding on the surface. The lowest possible contact angle is  $0^\circ$ , which indicates a perfectly wetting surface. A super-wetting surface is where a liquid apparently moves even faster than the Wilhelmy wetting force, described by the contact angle relationship, would predict, i.e. faster than perfect wetting on a plane. The derivation of Young's equation is made under the assumptions of spreading of a non-reactive liquid on an ideal planar solid

(physically and chemically inert, smooth, homogeneous and rigid), a condition that is rarely met in practical situations (Kumar and Prabhu, 2007).

$$\cos \theta_e = \frac{(\gamma_{SV} - \gamma_{SL})}{\gamma_{LV}}$$

**Equation 1-44**

Surface tension  $\gamma$  is generally considered to consist of two components, the Lifshitz-van der Waals (dispersive) and the Lewis acid-base interactions (polar), respectively. The surface tension component (STC) theory developed by van Oss and co-workers (Van Oss, Good *et al.*, 1986; Van Oss, Good *et al.*, 1988; Van Oss, Ju *et al.*, 1989) explains the split between the two components (Schoelkopf, 2002).

Lifshitz-van der Waals (LvW) interactions (formerly called dispersive interactions) result from an uneven charge (electron density) distribution in (net) uncharged molecules and are relatively weak compared to other interactions, but they are ubiquitous, i.e. they act between all kinds of molecules and particles. LvW interactions are composed of London dispersion forces, (<sup>d</sup>), caused by a fluctuating electron distribution, Debye dipole-induced dipole polarisation, (<sup>i</sup>), and Keesom dipole-dipole orientation (<sup>P</sup>), as denoted in Equation 1-45.

$$\gamma^{LvW} = \gamma^d + \gamma^i + \gamma^P$$

**Equation 1-45**

Lewis acid base (<sup>AB</sup>) interactions occur mainly through specific donor-acceptor interaction sites between uncharged surfaces and molecules, and mainly through the formation of hydrogen bonds (forming a strong contribution to polarity), themselves a special case of the hydrogen (or proton) donor-acceptor interaction, Equation 1-46.  $\gamma^+$  arises from an acid and  $\gamma^-$  arises from a base (Kwok, 1999).

$$\gamma^{AB} = 2(\gamma^+ \gamma^-)^{\frac{1}{2}}$$

Equation 1-46

In addition, electrostatic Coulombic forces act between charged surfaces and ions. The way these forces interact, and the resultant impact on contact angle, is shown in Figure 1-19, (Van Oss, Good *et al.*, 1986).

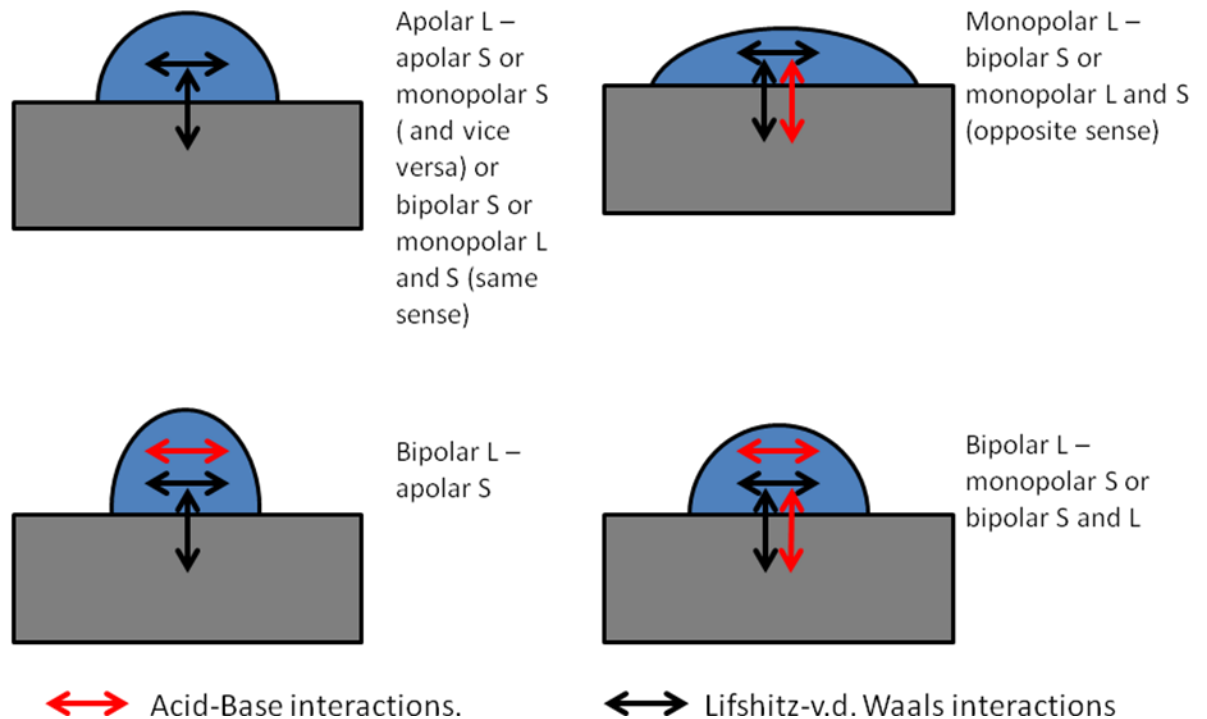


Figure 1-19 Influence of different phase interactions (L = liquid, S = solid) and their effect on contact angle.

The polarity of the wetting liquid also influences the wetting behaviour, in that a polar liquid will generally preferentially wet a polar surface. This has important applications, for example in ink-jet printing where the degree of absorption is important (Ridgway, Gane *et al.*, 2004).

### 1.3.4.2 Wenzel wetting equation

The Wenzel wetting equation refers to a homogeneous wetting regime, and is defined by Equation 1-47, to account for the apparent contact angle on a rough surface. The roughness ratio,  $r$ , is a measure of how surface roughness affects a homogeneous

surface, and is defined as the ratio of the true area of the solid surface to the apparent area:

$$\cos \theta_w = r \cos \theta_e$$

Equation 1-47

where  $\theta_w$  is the Wenzel contact angle. The roughness ratio acts as an amplification of the effect of the term  $\cos \theta_e$  (equilibrium contact angle) determined by surface chemistry. Small changes in the surface chemistry result in larger changes for the Wenzel contact angle  $\theta_w$  (Shirtcliffe, McHale *et al.*, 2010). The Wenzel roughness emphasizes the tendency of a surface to be either completely wetting or completely non-wetting (McHale, Shirtcliffe *et al.*, 2004). For heterogeneous surfaces, the Wenzel equation may not be applicable because of the change in apparent contact angle for heterogeneous surfaces. A schematic indicating the differences between the different wetting mechanisms is shown in Figure 1-20.

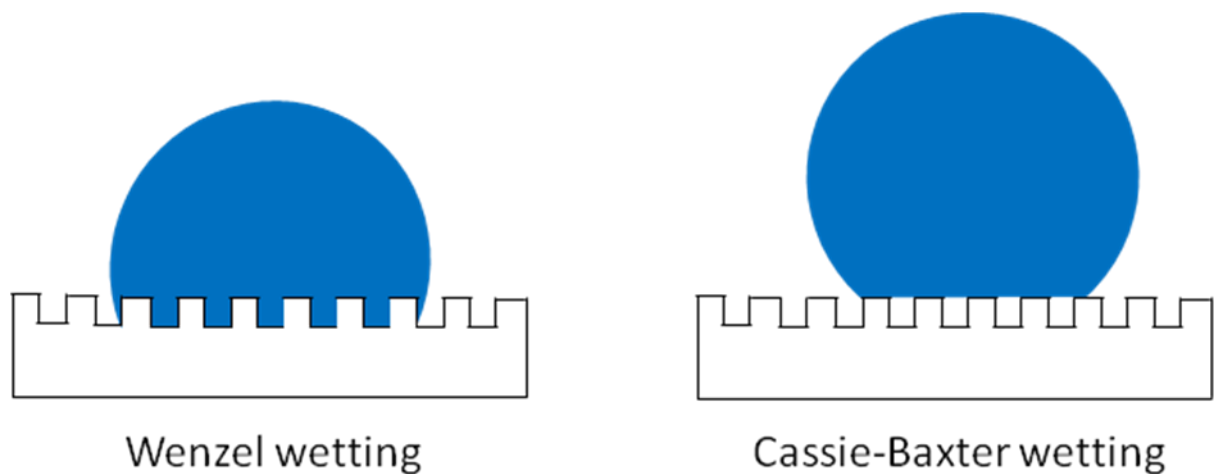


Figure 1-20 Diagram showing the differences between Wenzel wetting and Cassie-Baxter wetting. The diagram shows the Wenzel wetting filling the surface features and Cassie-Baxter wetting sitting on top of the features.

#### 1.3.4.3 Cassie-Baxter equation

The Cassie-Baxter equation describes the effective contact angle for a liquid on a composite surface and explains how roughening the surface increases the apparent



contact angle. In this model, by increasing the roughness, the liquid may not maintain complete contact with the surface as in the Wenzel case. So the liquid in this situation contacts the top of the surface with air trapped between the rough protrusions of the surface. Therefore, the liquid contacts both the rough asperities and the air in between the protrusions, and the contact angle is given by Equation 1-48 (Wang, Ying *et al.*, 2006). A schematic of Cassie-Baxter wetting is shown in Figure 1-20.

$$\cos \theta_{CB} = -1 + f_1 (\cos \theta_e + 1)$$

**Equation 1-48**

Here  $\theta_{CB}$  is the apparent contact angle determined using the Cassie-Baxter equation and  $f_1$  is the fraction of the liquid/solid interface.

With natural materials, such as calcium carbonate, the surfaces are more complex than the models of simple flat topped protrusions. In these cases, it is often difficult to measure the roughness factor  $r$  and/or the solid surface fraction  $f_1$  that a droplet experiences. Therefore, it is possible that neither a pure Wenzel nor pure Cassie-Baxter state will occur. It is also possible to have a Cassie-Baxter to Wenzel transition (Shirtcliffe, McHale *et al.*, 2010). It is envisaged that the calcium carbonate systems studied will have some hybrid form of wetting, which depends on the surface roughness.

Neither Wenzel nor Cassie-Baxter wetting matches a porous material undergoing absorption, and it is impossible practically to measure the contact angle for porous media. The differences in pore architecture formed in compacted beds of fine carbonate particles will be significant in determining the wetting rate. Additionally, the surface chemistry of the particulate carbonate product plays a crucially important role. The products tested here are, or are derived from, wet ground calcium carbonates, GCC, which are stabilised in suspension by anionic polyacrylic dispersants. These dispersants

are strongly polar, are swelling in contact with water and are hygroscopic. Thus, the polar interaction component is the dominant factor for polar liquids.

### **1.3.5 Stickies**

There continues to be considerable environmental pressure to increase the use of recycled paper, but its use is not without complications. Some of the most difficult problems result from the presence of adhesives, arising from hot melt glues, binders and other thermoplastic materials, for example from book-backs and adhesive tape or from silicone based defoamers. They tend to be pliable organic materials, such as styrene-butadiene and styrene acrylic latex binders, rubber, vinyl acrylates, polyisoprene, polybutadiene and hot melts (Doshi, 1991; Douek, Guo *et al.*, 1997; Doshi and Dyer, 1998; Jones and Fitzhenry, 2003). Under certain conditions, these compounds can become tacky and deposit as ‘stickies’ in the paper machine. Stickies have multiple deleterious effects on paper quality including sheet indentations, sheet structural defects, web breaks, and discolouration such as black spots (Olson and Letscher, 1992; Hutten, Diaz *et al.*, 1997; Nguyen, 1998). The correction of these faults increases production costs.

Once stickies are released by the pulping process, they can accumulate in the white water system of the recycled fibre section of a paper recycling mill. Similarly, fibre stock containing recycled fibre can suffer from a build-up of stickies on the paper making machine. As paper mills are continuing to reduce their fresh water usage to minimise costs, white water recycling is becoming more prevalent, increasing the concentration of stickies and thus making them even more problematic.

Studies of stickies that have been reported in the literature are mainly concerned with how the effects of these compounds may be reduced in paper mills (Nguyen, 1998; Onusseit, 2006), or the development of alternative paper additives that have less of a

detrimental effect during paper recycling (Onusseit, 2006; Delagoutte, 2008). Some studies focus on the removal of stickies and pitch from the recycled fibre system by, for example, screening (Spiess and Renner, 2004; Delagoutte, 2005; Benecke, Gantenbein *et al.*, 2009), flotation (Kemper, 1999; Heise, Kemper *et al.*, 2000; Delagoutte, 2005) and adsorption (Douek and Allen, 1991; Allen and Douek, 1993; Rogan, 1994), or from the white water in the paper mill (Holmbom and Sundberg, 2003; Vähäsalo and Holmbom, 2006). Stickies are classified by size and how they are introduced into the system, as defined in Table 1-1 (Doshi, 2003).

**Table 1-1 Classification of stickies.**

Sticky formation method	Microstickies	Macrostickies
Introduced by pulping chemically or mechanically at start of recycling process.	Primary microstickies smaller than 100 or 150 $\mu\text{m}$ , not removed by screening through 100 or 150 $\mu\text{m}$ screen.	Primary macrostickies, larger than 100 or 150 $\mu\text{m}$ , removed by screening during recycling.
Introduced by changing physical or chemical conditions during recycling process.	Secondary microstickies smaller than 100 or 150 $\mu\text{m}$ , formed by aggregation of colloidal particles, or breakup of larger particles.	Secondary macrostickies, formed by aggregation of microstickies. Sometimes removed by screening, dependent on paper recycling stage when formed.

### **1.3.5.1 Equilibrium**

Stickies typically establish colloidal suspensions in aqueous solution, usually in the presence of surfactants. One method of removing the stickies is by adsorption of sticky onto mineral. The sticky and mineral mixture in suspension establishes an equilibrium, which is the starting point for this investigation described in Chapter 6.

### **1.3.5.2 Adsorption**

Adsorption occurs whenever a solid surface is exposed to a gas or liquid: it is defined as the enrichment of material or increase in the density of the fluid near an interface. Adsorption is of great technological importance. Thus, some adsorbents are used on a

large scale as desiccants, catalysts or catalyst supports; others are used for the separation of gases, the purification of liquids, or for pollution control. Adsorption phenomena also play a vital role in many solid-state reactions and biological mechanisms (Rouquerol, Rouquerol *et al.*, 1999).

Adsorption can be broken down into two distinct adsorption types, chemisorption where molecules adsorb onto the surface by the process of chemical bonding. The other adsorption mechanism is physisorption, which occurs when van der Waals interactions are involved. Adsorption is a key process in the study of surface science and the studies of adsorption initially undertaken involve the adsorption of gases onto the surface.

### ***1.3.5.3 Adsorption isotherms***

There are many different adsorption isotherms that could be used for studying the removal of stickies by adsorption onto a mineral surface; the isotherms discussed below were considered for the modelling of the removal of stickies.

### ***1.3.5.4 Freundlich equation***

Freundlich proposed a general mathematical relationship, which took into account the role of the solid surface in adsorption of solutes, now referred to as the Freundlich adsorption equation (Freundlich, 1926). The Freundlich equation, (Equation 1-49) can be used for the study of gases and liquids adsorbing onto the surface.

$$x_a / m_a = Kc_e^{1/n_a}$$

**Equation 1-49**

Here  $x_a$  is the mass of adsorbate,  $m_a$  is the mass of adsorbent;  $K$  is the (Freundlich) equilibrium constant,  $c_e$  is the aqueous concentration and  $n_a$  is the Freundlich exponent and if  $n = 1$  the equation reduces to a linear form.

### **1.3.5.5 Langmuir equation**

The Langmuir isotherm was initially proposed for the study of adsorption of gases and was later modified for adsorption from solution. Langmuir isotherms assume single layer, localised adsorption with identical interaction energies for each adsorbed molecule (Langmuir, 1918).

A linear form of the Langmuir adsorption isotherm for adsorption from solution is shown in Equation 1-50. Here  $c_e$  is the aqueous concentration,  $q_e$  is the adsorbed concentration,  $K$  is the equilibrium constant and  $q_{\max}$  is the maximum amount adsorbed.

$$\frac{c_e}{q_e} = \frac{c_e}{q_{\max}} + \frac{1}{Kq_{\max}}$$

Equation 1-50

### **1.3.5.6 Dubinin-Radushkevich equation (Rouquerol, Rouquerol et al., 1999)**

The Dubinin-Radushkevich equation relates to physisorption by microporous solids and filling of micropores by expanding the potential theory of Polanyi, in which the physisorption isotherm data were expressed in the form of a temperature-invariant ‘characteristic curve’.

The Dubinin-Radushkevich equation was proposed in 1947 for the characteristic curve in terms of fractional filling,  $W/W_0$ , of the micropore volume,  $W_0$ , and is expressed in the following form,

$$W/W_0 = \exp\left[-(A/E)^2\right]$$

Equation 1-51

where  $A$  is the Polanyi adsorption affinity and  $E$  is a characteristic energy for the given system. In turn,  $A$  is given by:

$$A = -RT \ln(c/c_0)$$

**Equation 1-52**

where  $c$  is the concentration and  $c_0$  is the initial concentration. By combining Equation 1-51 and Equation 1-52 and introducing a scaling factor  $\beta$ , the isotherm equation is obtained, Equation 1-53:

$$W/W_0 = \exp\left\{-\left[RT \ln(c_0/c)\right]^2 / (\beta E)^2\right\}$$

**Equation 1-53**

Another parameter, the structural constant,  $B$  is defined as:

$$B = 5.304(R/E)^2$$

**Equation 1-54**

Rearrangement of Equation 1-53 gives the Dubinin-Radushkevich equation in its usual form, Equation 1-55:

$$\log_{10}\left[\frac{W}{W_0}\right] = -D \log_{10}^2\left(\frac{c_0}{c}\right)$$

**Equation 1-55**

where  $D$  an empirical constant is given by Equation 1-56:

$$D = 0.434B(T/\beta)^2$$

**Equation 1-56**

The characteristic energy calculated during the Dubinin-Radushkevich isotherm can be used to determine the chemical character of adsorption. When the adsorption energy is less than  $5 \text{ kJ mol}^{-1}$  the method of adsorption is defined as physisorption and for

adsorption energies greater than  $10 \text{ kJ mol}^{-1}$  the adsorption mechanism is chemisorption.

## **2 Techniques**

All experimental techniques used during the PhD project are summarized in this chapter, with some background information. Each research theme is covered separately, with the techniques used for each put in the context of the project aims.

### ***2.1 Characterisation of porous materials***

The void structure of porous materials is important in regulating the various physical and chemical processes that occur within the material or on the surfaces of the material, both external and internal to the pore network. Experimental characterisation of porous materials is of interest in itself to establish knowledge of the structures involved, and also allows models to be constructed, based on the experimental data, to simulate pore-fluid phenomena.

#### **2.1.1. Scanning electron microscopy (SEM) and image analysis**

In a scanning electron microscope, electrons are emitted from a cathode filament and drawn towards an anode. The electron beam is focused by successive magnetic lenses into a very fine spot (from 0.5 – 5 nm in diameter). As electrons strike the surface of a material they are scattered by atoms in the sample. Through these scattering events, the beam spreads and fills a teardrop-shaped volume extending about 1  $\mu\text{m}$  into the surface. The sample density, atomic number and electron energy affect the scattering event. Interactions in this region lead to the subsequent emission of electrons and x-rays, which are then detected. There are different types of collection of the electrons generated used to generate images; secondary electrons and backscattered electrons capture are two commonly used types.

Secondary electrons are electrons generated by the process of ionization; they are called secondary electrons as they are generated from the interaction with the primary electron



beam. Secondary electrons are low energy electrons and can be detected using an Everhart-Thornley scintillator photomultiplier detector positioned to the side of the sample (Goldstein, Newbury *et al.*, 1981). The secondary electron collection is primarily used for detailed imaging of the surface of materials.

Backscattered electrons are primary electrons, i.e. originating from the incident beam, which have been reflected or backscattered from the material being analysed. The contrast in backscatter electron images is dependent on the atomic number of the element. The higher the atomic number of the element the more the backscattered electrons will be scattered, and the more the electrons have been scattered, the brighter is the image. So, heavier elements appear brighter in backscatter images than lighter elements. Unlike the side mounted scintillator used for generating the secondary electron image. Backscatter electrons are detected from a position above the sample in the form of a doughnut shaped detector array. The primary use of backscatter electrons is to generate atomic number mapping, and provide information about the topography of the sample.

The X-rays that are generated emerge from within the teardrop volume and can be used to characterise the elemental content of the material. They provide a spatial mapping, depending on resolution in respect to the teardrop dimensions and subsequent X-ray absorption of the various elemental/chemical constituents. The X-ray emission is usually limited to inorganic materials containing elements of higher atomic number than C, H and O in the periodic table, unless specialist equipment is used to identify such “light” elements.

SEM is very useful in obtaining visual images and qualitative information on the surface pore level structure of materials. By applying image analysis procedures, quantitative information can be obtained (Toivakka and Nyfors). The analysis of the

image involves the manipulation of the image by thresholding, or a similar process, to gather information about the structure, such as the circumference of features, and the ‘feret’ diameter of porous features, where the feret is the longest distance between any two points along the boundary.

Image analysis as a technique is limited by the quality of the images obtained. To ensure a fair comparison between different samples, the images need to be acquired using the same technique, under identical conditions preferably with the same equipment. The images acquired then need to be analysed using equivalent parameters in the image analysis software. To consider the image analysis data quantitatively, the number of images analysed needs to be representative of the entire structure (1988; Rasband, 2008).

### **2.1.2. Mercury intrusion porosimetry (MIP)**

Mercury intrusion porosimetry is a technique that renders the sample non-reusable. The technique is dependent on the behaviour of non-wetting mercury as it inundates (intrudes) a porous object under the action of external pressure, and was first described by E.W. Washburn (Webb and Orr, 1997). The Laplace equation 2-1, is derived from the Young-Laplace equation for the pressure across a curved liquid boundary held in tension, and governs the behaviour of non wetting liquids in a capillary:

$$d = \frac{-4\gamma_{LV} \cos \theta}{P}$$

**Equation 2-1**

where  $d$  is the pore equivalent capillary diameter,  $\gamma_{LV}$  is the interfacial tension between mercury and air,  $P$  is the applied pressure and  $\theta$  is the contact angle.

Porosimetry measurements are nearly always carried out using mercury, since it is the only liquid that is sufficiently inert and non-wetting for general applications. Equation 2-1 is widely applicable, and the non-wetting nature of mercury means that it is necessary to apply pressure in inverse proportion to pore diameter, such that a record of the pressure provides the analysis of pore diameter.

After intrusion, the reverse procedure, with pressure reduction, allows the drainage or extrusion curve to be obtained, as the mercury emerges from the regions of the sample where it is possible to do so. The commonly used values for  $\gamma_{LV}$  and  $\theta$ , for mercury entering an evacuated sample, are  $0.485 \text{ N m}^{-1}$  and  $140^\circ$ , respectively. There are, however, uncertainties and variations in these values, the consequences of which have been reviewed (van Brakel, Modry *et al.*, 1981; Webb and Orr, 1997).

The void size distribution, obtained by the first derivative of the cumulative volume-pressure intrusion curve, subsequently applying the Laplace equation, is representative of a one-dimensional model of a porous solid, consisting of parallel equivalent capillaries, as described in Section 1.3.1.1. However, this “bundle of capillaries” model of a porous material cannot fully explain some of the typically encountered geometrical features of pore networks which result in important subtleties in the data obtained from mercury intrusion porosimetry. For example, the intrusion and extrusion curves typically differ. The ‘shielding’ of larger void spaces, or pores, by narrower void spaces, or throats leading to them, causes this hysteresis effect. The shielding requires a higher than expected pressure for many of the features to fill. Similarly, rapid extrusion of mercury can lead to detachment, known as “snap off”, within the mercury column as the strictures imposed by throats prevent the flow of mercury needed to replenish that being extruded. Modelling of mercury porosimetry results for determination of pore architecture is described in Section 1.3.1.1 and 1.3.1.2 Such problems in the

interpretation of the mercury intrusion measurements can be partially overcome by using a void space network model, such as Pore-Cor, which is described in Section 1.3.1.6. these limitations are also discussed, and compared with those of porometry in Section 3.1.1.

The results of this technique have to be carefully interpreted and a number of correction factors have to be applied in order to obtain a true measure of the void space of the sample. These procedures are explained in more detail in Section 1.3.1.7.

The porosimetric analysis of the samples in this project has been carried out using either a Micromeritics Autopore III 9420 mercury porosimeter (Figure 2-1) or a Micromeritics Autopore IV 9520 mercury porosimeter (Micromeritics Instrument Corp. USA). Both are able to apply a maximum pressure of mercury of 414 MPa, corresponding to a diameter of 4 nm via the Laplace equation (Equation 2-1).



**Figure 2-1 Photograph of a Micromeritics AutoPore III 9420 mercury porosimeter, showing the twin ports for mounting the penetrometer containing the sample for analysis over progressive pressure ranges.**

### 2.1.3. Porometry

Porometry is used within the filtration industry as a quality control tool to ensure consistency of filter media between production batches, and to characterise filters. Porometry is a technique also utilised for the determination of pore-size distribution of a porous material. Porometry is a non-destructive technique, in the sense that the same sample can be repeatedly measured. The method utilises a liquid expulsion technique, where a sample that has been fully wetted and saturated by a liquid is expelled by increasing the gas pressure above the menisci. The wetting liquid (Porofil) is specifically chosen to have the properties of low surface tension, low vapour pressure and low reactivity. To ensure complete saturation by wetting, some samples may require wetting under vacuum (Calvo, Hernandez *et al.*, 1995). The sample has to be saturated, not just wetted. Wetting alone can mean that just the inner surface of the pores is wetted by a film of liquid. It is necessary to establish a meniscus bridging the whole pore diameter if a measure of pore size is to be obtained.

Once the sample has been wetted a continually increasing gas pressure is applied across one external sample face. The gas phase progressively replaces the wetting fluid in ever finer pores as the gas pressure is increased. Eventually, the liquid is expelled as the gas phase pressure exceeds the capillary wetting pressure. Throughout the analysis, the surface tension of the wetting fluid acts to retain the wetting phase within the pore structure. Therefore, when removing the wetting fluid from the pore structure, by gas overpressure, the surface tension needs to be overcome. The pressure required is therefore assumed to be equal equivalent to the capillary pressure (Amey, Stott *et al.*, 2008), but this assumption ignores any dynamic effects caused by the flow of gas through the sample, described in Section 3.1.1.



**Figure 2-2** Photograph of a Porvair Porometer 4 (Amey, Stott *et al.*, 2008), showing the sample holder in the central unit of the apparatus, with the pressure application pipe and reservoir leading from it.

The sizes of pore features are related to flow rate versus gas pressure by the Laplace equation (Equation 2-1). The Laplace parameters are changed for porometry performed using Porofil when compared with mercury porosimetry, in that the contact angle  $\theta$  is  $0^\circ$ , thus changing the negative sign into a positive sign in respect to the cosine function, and interfacial tension  $\gamma_{LV}$  is  $0.016 \text{ N m}^{-1}$ . The instrument is connected to a gas supply with a maximum pressure of 13 bar and a maximum flow rate of  $100 \text{ dm}^3$  per minute.

The limits of validity for porometry have not been rigorously determined in the literature. The instruction manual for the instrument, written with the help of the EFMG research group at Plymouth, states the pore size range for the instrument is  $0.07 - 300 \mu\text{m}$ . Modelling of porometry results for determination of pore architecture is described in Section 1.3.1.1 and 1.3.1.2.

#### **2.1.4. Particle size distribution**

The size of a particle can be defined as the effective interaction size with whatever is being used to measure it. This can be loosely described as the envelope size of the

particle. There are more detailed definitions of particle size, each depending on measurement method, but they are not considered here as the aim is to provide a consistent size measurement from a single technique. Static light scattering was the technique used to determine the particle size in this investigation. The instrumentation used to analyse the particle size distribution was a Mastersizer 2000 (Malvern Instruments Ltd, U.K.). Figure 2-3 shows a schematic of the Mastersizer 2000 reproduced from the product brochure (Malvern Instruments, 2005).

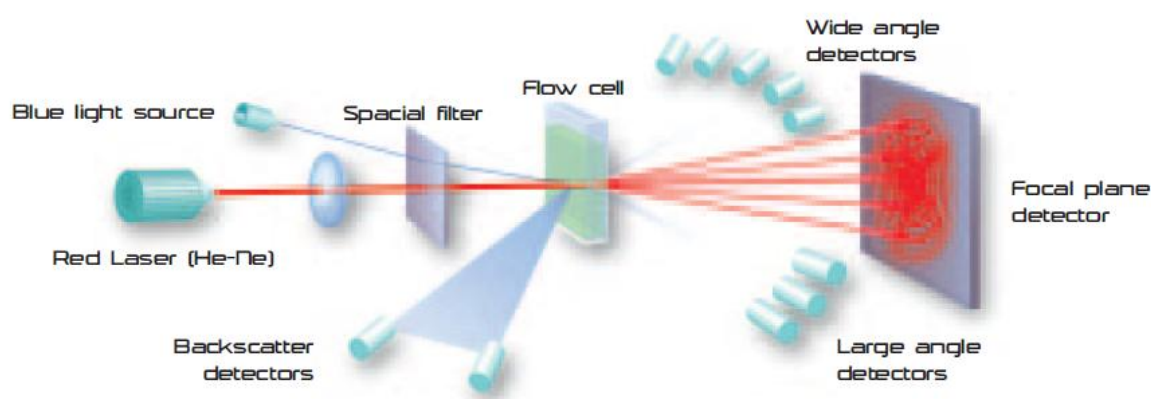


**Figure 2-3 Schematic of a static light scattering system for measuring particle size distribution.**

The measurement of particle size distribution by static light scattering involves dispersing the particles in suspension. The suspending liquid typically used is water, and all measurements reported in this investigation were obtained using water as the dispersing medium. The suspension of particles in water flows through a measurement cell. The light is scattered elastically by the particles within the cell, dependent on the size of the particle. In this case, the envelope size is defined via its scattering cross-section. The smaller particles scatter the incident light to larger angles than the larger particles. The intensity of light as a function of scattering angle is determined by the array of detectors in the plane of scatter, which compares the intensity to that of the blank system containing only water. The intensity distribution obtained by this method

is then interpreted using mathematical models of the light scattering, such as provided by Mie theory (Mie, 1908).

## ***2.2. Physicochemical process differences due to void structure***

In order to investigate how different void structures affect the sorption and diffusion characteristics within packed particulate beds of various calcium carbonate grades, including some with internal particle porosity, high performance liquid chromatography was used in conjunction with a ‘zero length column’.

### **2.2.1. High performance liquid chromatography (HPLC)**

HPLC is one of the most widely used separation techniques. The reasons for the popularity of the method are its sensitivity, its adaptability for accurate quantitative determination, its ease of automation, its suitability for separating species with widely varying properties and its wide ranging applicability to substances important to industry, scientific fields and the public.

There are different analytical methods that can be used with HPLC; the appropriate method is chosen depending on solubility, molecular mass and polarity of the chemical mixture. Figure 2-4 summarises common HPLC procedures, and the applicability of the procedures relevant to polarity, solubility and molecular mass.



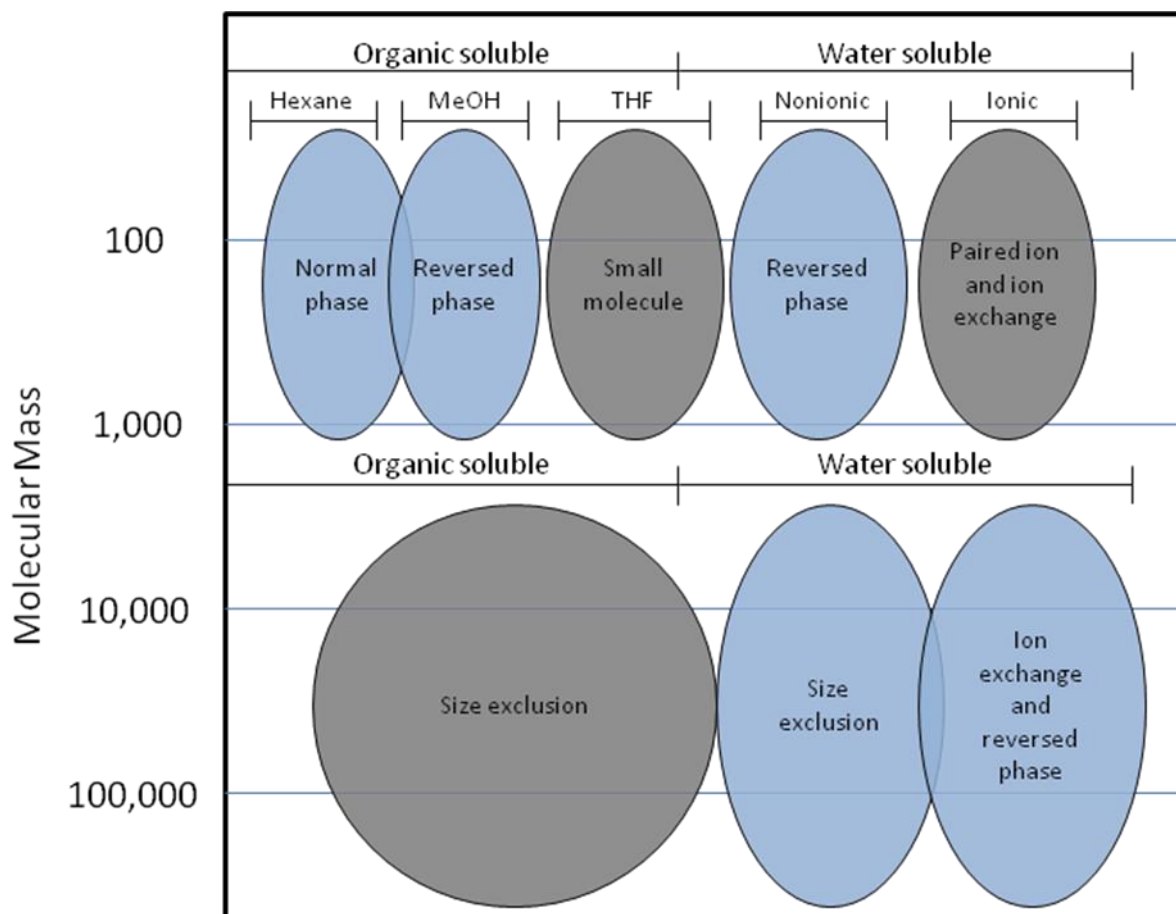


Figure 2-4 Selection of HPLC procedures (Skoog, Holler *et al.*, 2006)

Figure 2-4 shows that HPLC has a wide applicability to the separation and quantification of mixtures of chemicals. HPLC can be configured with many different mobile and stationary phases, which gives a wide range of applications for the technique. There are many different detectors that can be used with HPLC, including UV/VIS, mass spectrometry, refractive index and electrochemical detectors. It is also possible to use more than one detector during an HPLC experiment.

The solutes being analysed by HPLC are separated in a chromatographic column, housing the stationary phase. The stationary phase is typically a solid matrix, with which the solute interacts in either a physical or chemical way. The degree of interaction slows the movement of the solute through the column. The more the solute interacts with the stationary phase, the longer the retention time for the solute. There are different types of chromatographic columns that can be used with HPLC depending on the methodology being used, Figure 2-4. A typical chromatographic column is 10 – 30

cm in length, with a stationary phase particle size of 3 – 5  $\mu\text{m}$ . A basic schematic of an HPLC system is shown in Figure 2-5.

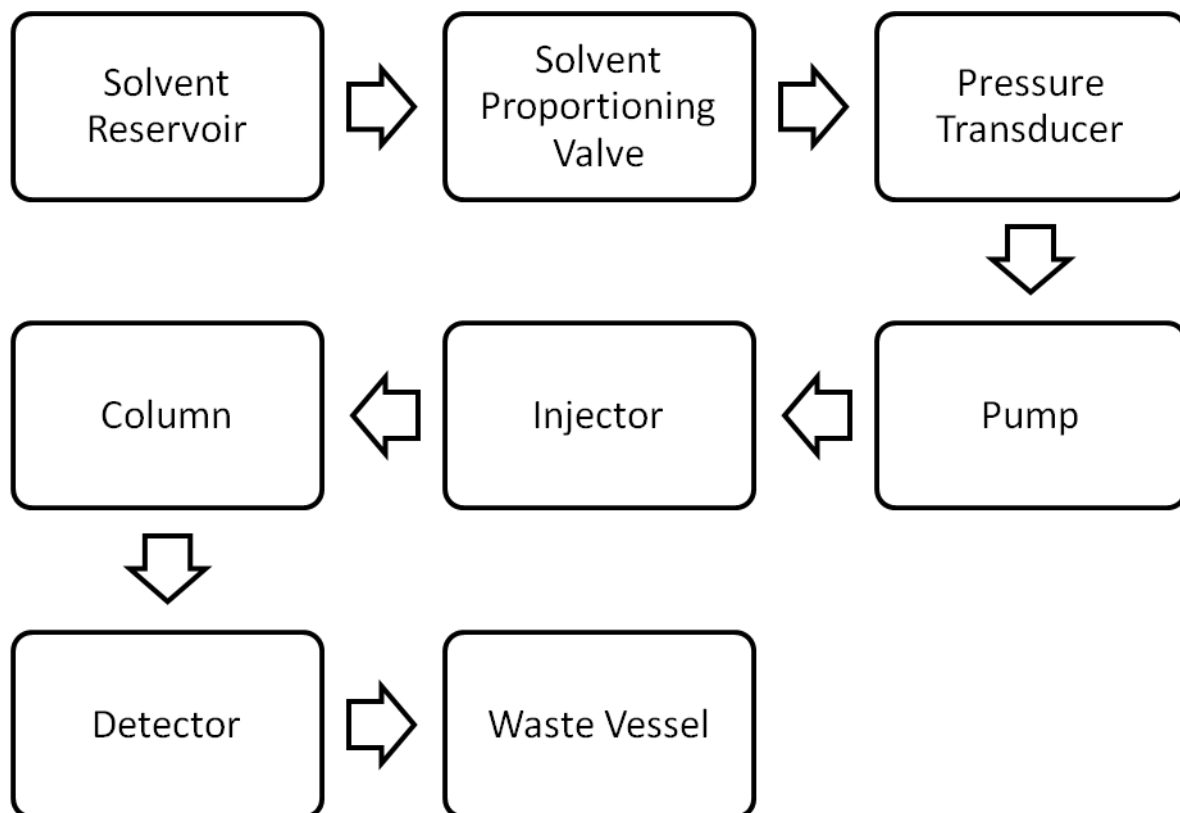


Figure 2-5 Basic schematic indicating flow of mobile phase through an HPLC system (Skoog, Holler *et al.*, 2006).

HPLC was used in this project not because of these many capabilities, but because it works at high pressures. High liquid pressures were required to obtain a useful flow rate through the fine sinters needed to confine the sample in the zero length column.

### 2.2.2. Zero length column (ZLC)

The zero length column is a specialised chromatographic column that can be used with gas chromatography or liquid chromatography systems, for the study of sorption, diffusion and the associated kinetics. The theory of the zero length column is explained in more detail in Section 1.3.3.

The zero length column was developed for use with gas chromatography systems, to study intracrystalline diffusivities of strongly adsorbed species in zeolites (Eic and

Ruthven, 1988), exploiting the sensitivity of the flame ionisation detector. It is, therefore, ideally suited to study the transport properties within particulates having internal pores, to separate the action of intraparticle pore structure from that of the collective action of both the intra- and interparticle pores present in a typical chromatographic column of such particles. The zero length limit of a column represents a single particle thickness at most versus that of an infinite packed bed. The design of the gas chromatography zero length column used by Eic and Ruthven featured a very thin layer of zeolite crystals placed between two sinter discs in a vertical position relative to a 1/8 " stainless steel tube, inside a gas chromatography oven. The experiment measured desorption of a sorbate from a saturated zeolite sample. The technique has been adapted since the gas chromatography experiment to allow an HPLC instrument to be used. A schematic of a zero length column for a liquid system, as used by Ruthven and Stapleton (1993a), is shown in Figure 2-6. The design of this zero length column uses two sinters to hold the sample in place during experiments, but the design also uses a packing material, so interaction between the packing material and mobile phase also has to be determined by performing a blank analysis.

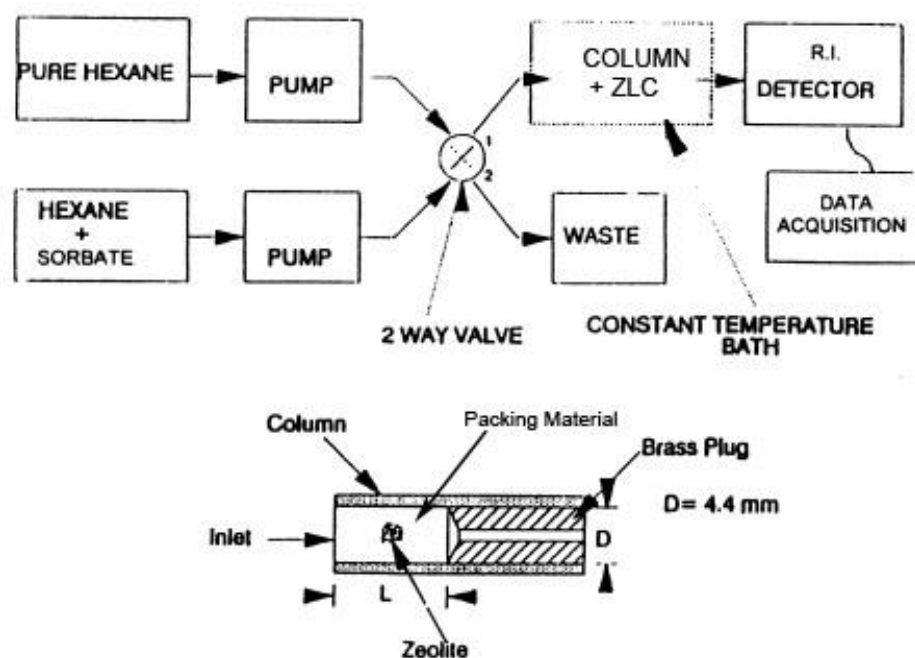


Figure 2-6 Schematic of zero length column and how it is integrated into an HPLC system (Ruthven and Stapleton, 1993a).

The design of the zero length column detailed in Figure 2-6 is the basis for subsequent developments supporting investigations with liquid systems. These developments have refined the design of the zero length column, and our design is a development of the one described by Zabka and Rodrigues (2007), Figure 2-7.

The initial step of the experimental procedure is to saturate the stationary phase, containing the sorbent that is being studied, with the relevant sorbate. The second step is then to switch the mobile phase to a pure solvent for the sorbate to allow desorption and diffusion to be studied. Once the sorbate has been completely removed, it is possible to reverse the process by gradually switching the mobile phase once again to allow known adsorbate concentrations to flow, until saturation of the stationary phase surface with sorbate is once again achieved. The re-saturation with sorbate then allows the study of adsorption to be performed.

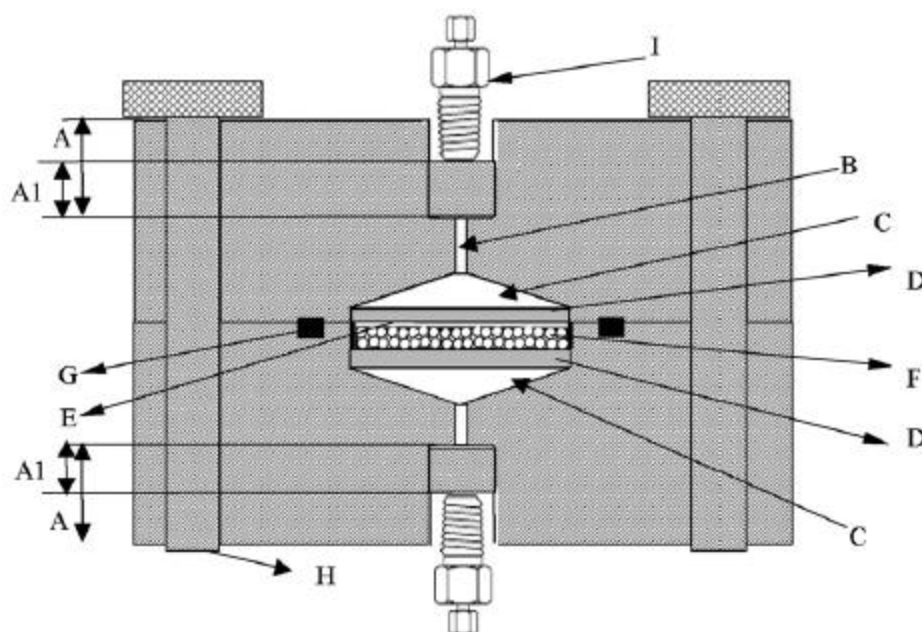


Figure 2-7 Schematic design of ZLC cell in detail. (A) Threaded inlet for male connector (1.06 cm x 0.75 cm i.d.); (B) orifice between threaded inlet and truncated cone (0.5 cm x 0.23 cm i.d.); (C) truncated cone ( $h = 0.1$  cm;  $d_B = 2.3$  cm;  $d_T = 0.23$  cm); (D) replaceable frit (micrometre size 10  $\mu\text{m}$ ); (E) filter; (F) space for shallow bed (0.1 cm x 2.5 cm i.d.); (G) O-ring; (H) bolt; (I) male connector. (Zabka and Rodrigues, 2007)

In this investigation, the zero length column design for the liquid system has been refined and the refinement is described in detail in Section 5.2.

### 2.3. Effect of surface rugosity on wetting

Calcium carbonate is able to be modified to give internal structure and surface rugosity. The surface rugosity affects the wettability of the material, and to determine the effect it is necessary to study the structure of porous features on the surface, such as nanopores. The nanopores were investigated using nitrogen adsorption and *n*-butane adsorption. The choice of the different molecular sizes enables a definition of the meso-level structure properties. The wetting study was performed in Switzerland by Dr Cathy Ridgway from Omya Development AG.

#### 2.3.1. Gas adsorption

The adsorption of gases onto the surface of materials has been used for the determination of surface area, calculated by using the BET equation described in Section 1.3.2.2. The BET equation can also be adapted to be used with alternative gases

such as argon, carbon dioxide, krypton, methane and *n*-butane. In this investigation nitrogen has been used to obtain the specific surface area of the minerals used in the investigation. Nitrogen and *n*-butane have also been used to obtain full adsorption / desorption isotherms for different grades of modified calcium carbonates, to see how the hysteresis effect between adsorption and desorption differs between the two gases (Banaresmunoz and Escibano, 1991). The hysteresis encountered allows the use of the BJH algorithm, described in Section 1.3.1.4, to calculate the pore size, pore volume and pore area of the modified calcium carbonates. The information gained by comparing the two gases allows the surface rugosity of the modified calcium carbonates to be studied and to infer why some modified calcium carbonates are super wetting, i.e. wet faster than their intrusion measured pore size, and, hence, capillarity, would suggest, whilst other modified calcium carbonates follow the expected capillarity dynamic alone. The wetting experiment is described in Section 2.3.2.

The gas adsorption experiments were performed on a Gemini 2360 surface area analyser (Micromeritics Instrument Corp. USA). A photograph of the Gemini 2360 is shown in Figure 2-8. The instrument uses a static volumetric technique in which the analysis gas flows into a tube containing the sample (right hand tube) and a balance tube (left hand tube), at the same time. The internal volume and the temperature are maintained at identical conditions, the only difference being the presence of the sample in the sample tube. The difference in volume between the two tubes was determined by using helium prior to the adsorption experiment.



**Figure 2-8** Photograph of the Gemini 2360 surface area analyser and FlowPrep 060. The vessel for sample exposure to the adsorbing gas is shown in the left-hand unit of the apparatus.

The sample and reference-balance tubes are both immersed in a liquid nitrogen bath in the case of nitrogen adsorption, and in a static ice-water bath for the case of *n*-butane adsorption. By maintaining both tubes simultaneously under isothermal conditions, the condensation properties can be equalised. The analysis gas is delivered to the sample tube by a servo valve mechanism, and the delivery rate of analysis gas into the balance tube is controlled by a second parallel servo valve mechanism. Using independent pressure transducers for each delivery system, the differential pressure recorded between the sample and balance tubes provides a measure of the adsorption of the analysis gas onto the sample. A schematic of how the Gemini 2360 works is shown in Figure 2-9 (Micromeritics, 2006).

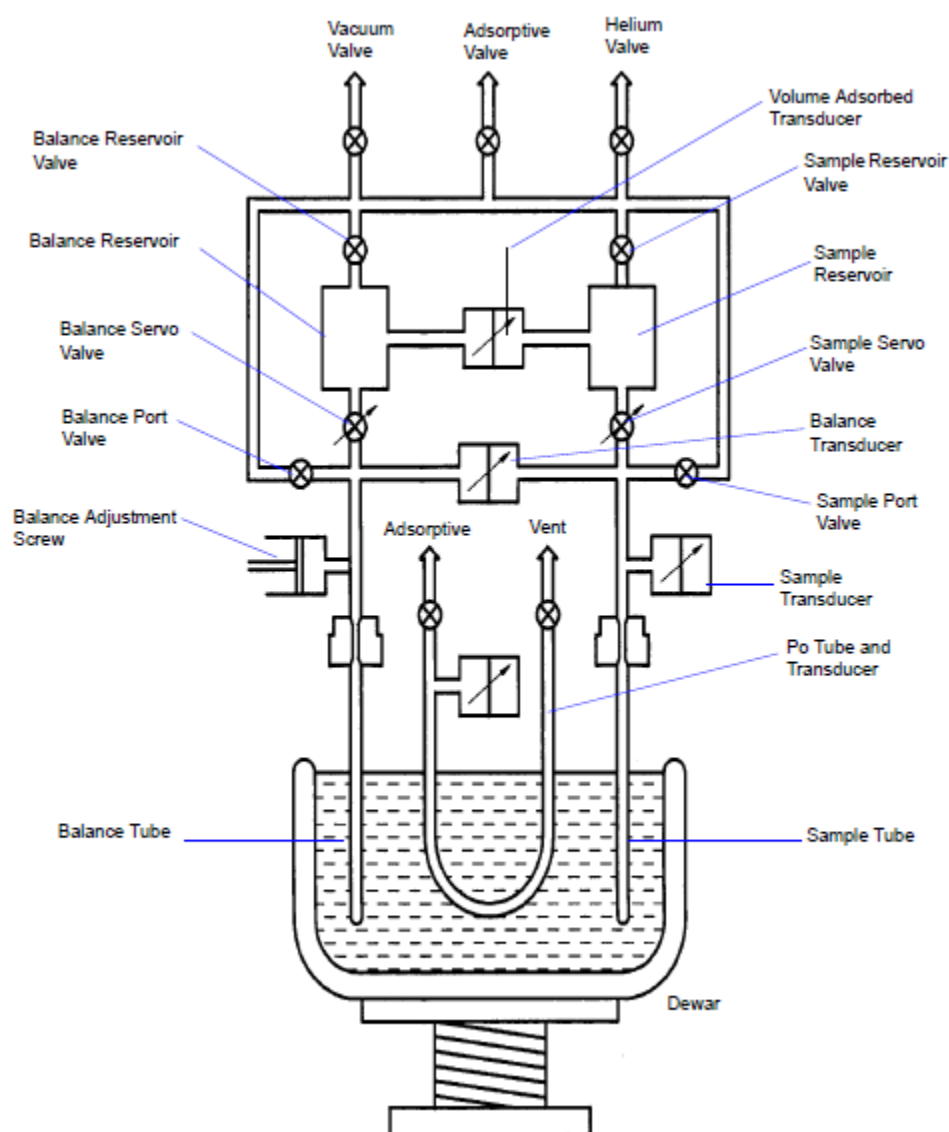


Figure 2-9 Schematic showing the layout of the Gemini series of surface area analysers (Micromeritics, 2006).

### 2.3.2. Wetting experiment

To determine the wettability of calcium carbonate samples, tablets of different calcium carbonate grades were produced, and the wettability of the samples was tested by measuring the short term and long term absorption rates of *n*-hexadecane. A schematic of the equipment used to produce the tablets from a dispersed suspension / slurry is shown in Figure 2-10. The tablets are formed by applying a constant pressure to the suspension / slurry for several hours such that water is released by filtration through a fine 0.025  $\mu\text{m}$  filter membrane, resulting in a compacted tablet of the pigment. The



tablets are removed from the apparatus and are then dried in an oven at 80 °C for 24 hours (Ridgway, Gane *et al.*, 2004).

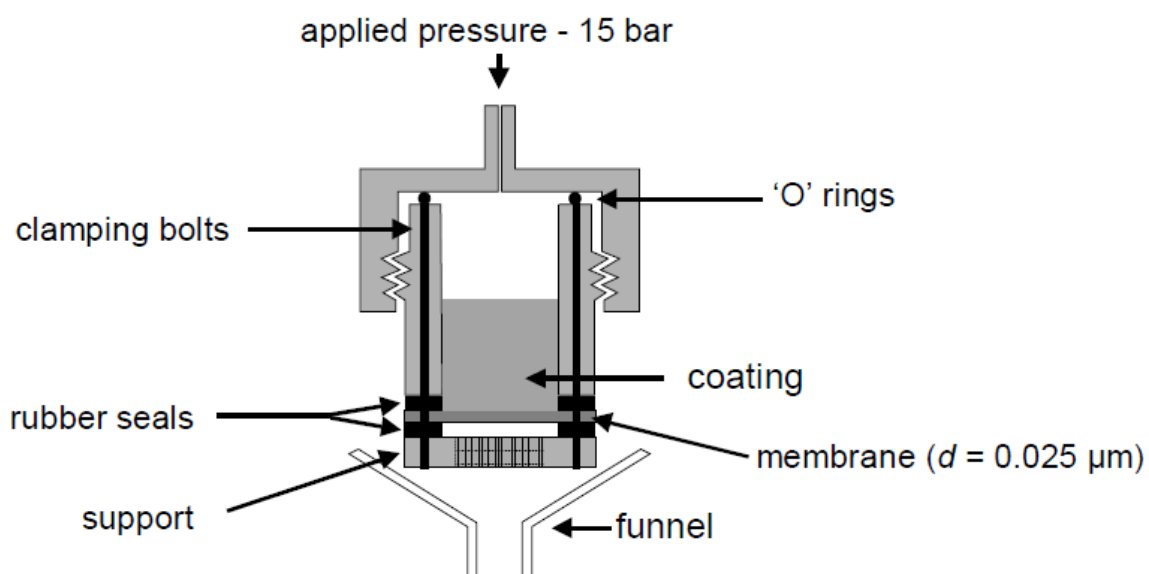


**Figure 2-10** Schematic of the equipment used to create tablets from mineral suspensions / slurries (Ridgway, Gane *et al.*, 2004)

The tablets are cut and ground to form regular 12 x 12 mm<sup>2</sup> cross-sectional blocks using a rotary disc grinder and a specially constructed, precisely adjustable jig.

The wetting experiments were performed with 99 % purity hexadecane sourced from Sigma-Aldrich. The rate of liquid uptake was measured using an automated microbalance, namely a PC-linked Mettler Toledo AX504 Delta Range (Mettler Toledo (Schweiz) GmbH), with a precision of 0.1 mg, capable of 2.7 measurements per second. To provide a sufficiently slow and precise approach of the sample down to the liquid surface, a special sample holder was constructed, Figure 2-11. The chamber around the sample allowed the sample to be shielded from external air movement. Troughs full of the wetting liquid were mounted in the chamber to saturate the atmosphere and minimise evaporative weight loss from the main liquid reservoir.

The imbibitions experiments were performed following the procedure detailed in (Schoelkopf, Ridgway *et al.*, 2000), but a summary of the technique is included below.

Prior to the experiment each tablet sample was allowed to equilibrate for 48 h in a chamber being flushed through with dry nitrogen at a rate of 1 litre min<sup>-1</sup>. The experiment was performed in the apparatus shown in Figure 2-11 flushed with a steady stream of nitrogen at 1 litre min<sup>-1</sup> to reduce changes in the weight of the tablet. The tablet sample is gradually lowered toward the wetting liquid, with the flat sample surface parallel to that of the liquid. In practice it is impossible to make the liquid and rough surface perfectly parallel to each other. Therefore, at some moment of the approach, the fluid touches some point on the solid surface. When this point touches the liquid surface, fluid wets it and then the whole surface. A contact meniscus rapidly forms which connects the entire surface of the liquid to that of the solid in a time  $t_1$ . To minimise the liquid creeping up the side of the tablet a ring of wax is used (Schoelkopf, Ridgway *et al.*, 2000).

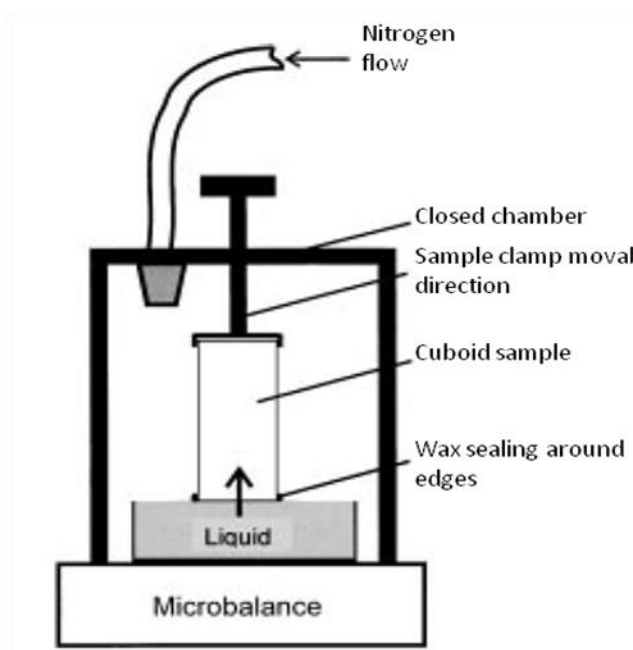


**Figure 2-11** Schematic of the equipment used to measure absorption into the mineral samples (Schoelkopf, Ridgway *et al.*, 2000).

To interpret the data, when the sample comes into contact with the liquid the weight of liquid decreases. The system also has inertia, which causes a lag and then an overshoot

in the recorded weight, assumed to be completed in a time  $t_2$ , which is greater than  $t_1$ . The total force  $F_{\text{total}}$  acting on the solid-liquid interface during the permeation of  $n$ -hexadecane into the calcium carbonate blocks is the sum of wetting, gravity and buoyancy forces, which are all functions of time  $t$ :

$$F_{\text{total}}(t) = F_{\text{wetting}}(t) + F_{\text{gravity}}(t) + F_{\text{buoyancy}}(t)$$

**Equation 2-2**

The buoyancy term can be neglected, because the absorbing surface is always above the free liquid surface, gravity has a very negligible effect and  $F_{\text{gravity}} = 0$  to a very good approximation. The wetting force is therefore assumed to be entirely responsible for the observed wetting of the calcium carbonate tablets.

## ***2.4. Adsorption characteristics of mineral particles in paper recycling***

Minerals can be added at a paper recycling plant to control a problem caused by “stickies”, which was explained in more detail in Chapter 1. There are different methods that can be used to determine the efficiency of a mineral for stickies collection. Most of the techniques do not measure the sticky concentration directly, but instead provide a proxy method using a behavioural property of the sticky to determine the concentration in aqueous suspension.

### **2.4.1. Turbidity**

The turbidities of the sticky suspensions, mineral suspensions, and sticky and mineral suspensions, were measured either on a Hach DR/890 Colorimeter (Hach Company, USA) or a Novasina 155 Model NTM-S. Turbidity is a measure of light scattering by particles in suspension, assessed by the drop in light transmission through a given sample length. The Novasine 155 Model NTM-S instrument transmits light in the near

infrared spectrum through an optical fibre probe where the emerging beam is scattered by small particles in suspension. Light scattered back at 180° to the incident beam is collected by parallel optical fibres in the probe and focused onto a photo-diode. The resulting signal is amplified and displayed directly in Nephelometric Turbidity Units (NTU), defined as the intensity of light at a specified wavelength scattered, attenuated or absorbed by suspended particles at a method-specified angle from the path of the incident light, compared to a synthetic chemically prepared standard. Interference from ambient light is eliminated by using a modulated transmitting signal, removing the need for light-tight sample handling systems.

The particle size distribution and concentration of the scattering particles are key factors in altering the turbidity of the suspension (Lawler, 1995). The turbidity,  $\tau$ , is proportionally related to the volume occupied by each individual scattering particle,  $v$ , and the numerical volume concentration,  $vc'$ , where  $c'$  is the numerical particle concentration, Equation 2-3.

$$\tau \propto v^2 c' = (vc') v$$

**Equation 2-3**

If species aggregate, the volume  $v$  of the individual aggregates will increase while the number concentration of the aggregates will decrease proportionally. Therefore, the term  $vc'$  remains constant, and the turbidity  $\tau$  is directly proportional to the volume of the aggregates.

In this investigation the turbidity is used as a proxy for the sticky concentration, Chapter 6, and also used to see if aggregation affects the results obtained in Chapter 7, when calculating proxy adsorption isotherms.

### **2.4.2. Chemical oxygen demand (COD)**

The COD is a property commonly used as an indirect measure of the amount of organic compounds in water. The COD indicates the amount of oxygen required to oxidise organic compounds completely into carbon dioxide. It is a useful measure of water quality. The organic compounds are fully oxidised into carbon dioxide using potassium dichromate. On oxidising the organic compounds, the chromium ion is reduced from  $\text{Cr}_2\text{O}_7$  to  $\text{Cr}^{3+}$ . The  $\text{Cr}^{3+}$  concentration is then determined spectrophotometrically. The concentration of  $\text{Cr}^{3+}$  indicates the COD of the sample.

In this investigation, the COD is used as a proxy for the concentration of stickies, by comparing the starting and ending COD concentration, Chapter 6.

### **2.4.3. Gravimetric analysis**

Gravimetric analysis is a basic analytical technique that has a wide applicability to various chemical systems, and is one of the most precise and accurate methods of macro-quantitative analysis. Gravimetric analysis involves converting the analyte to an insoluble form, and the separated precipitate is then dried and accurately weighed. From the weight of the precipitate, and knowledge of the chemical composition, one can calculate the weight of analyte in the desired form (Christian, 2004).

Gravimetry is used in this investigation as a direct method to determine the non-volatile sticky concentration, Chapter 6.

### **2.4.4. Dissolved organic carbon (DOC)**

Dissolved organic carbon analysis is a technique that obtains the concentration of dissolved organic carbon present in a solution. The instrumentation used for the analysis was a Shimadzu TOC-5000A coupled to an ASI-5000A autosampler (Shimadzu Corp. Japan). The instrumentation induces high temperature combustion (680 °C) to convert

all dissolved organic carbon to CO<sub>2</sub>, which is quantified by infrared gas detection (Watanabe, Badr *et al.*, 2007). A photograph of the instrumentation is shown in Figure 2-12.



**Figure 2-12 Photograph of the Shimadzu TOC-5000A coupled to the autosampler ASI-5000A**

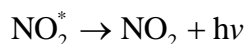
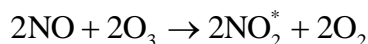
The dissolved organic carbon results were used as a proxy for sticky concentration, Chapters 6 and 7. The dissolved organic carbon results were also used to calculate equilibrium constants, Chapter 6, and adsorption isotherms, Chapter 7, for removal of stickies.

#### **2.4.4.1. Total dissolved nitrogen (TDN)**

The instrumentation used in this investigation to determine total dissolved nitrogen was coupled to the dissolved organic carbon method instrumentation described above. The instrument is a Siemens NCD 255 detector controlled by LabView software.

The total dissolved nitrogen instrumentation uses the same gases after having passed through the infrared detector of the dissolved organic carbon instrumentation. Any remaining water vapour not removed by the dissolved organic carbon dehumidifier is

removed by a gas dehumidifier before the total dissolved nitrogen instrumentation. The NO in the gas stream is reacted with O<sub>3</sub> in the NCD 255 to give the radical species NO<sub>2</sub>\* that chemiluminesces upon decay to its ground state:



The emitted light, of frequency  $\nu$ , and thus energy  $h\nu$  (where  $h$  is Planck's constant), is recorded by a photomultiplier tube and the resulting signal is recorded. The signals recorded are proportional to the amount of total dissolved nitrogen (Badr, Achterberg *et al.*, 2003; Pan, Sanders *et al.*, 2005; Watanabe, Badr *et al.*, 2007).

The total dissolved nitrogen results were used as a proxy for sticky concentration in applicable samples, Chapter 6.

#### **2.4.5. Elemental analysis**

The elemental analysis was performed on a Carlo Erba EA-1110 CHNS elemental analyser (Thermo Fisher Scientific, USA). Elemental analysis is a technique that combusts solid samples to quantify the percentage of carbon, hydrogen and nitrogen present in the sample, and is commonly used in helping to determine the molecular or empirical formula of organic compounds. The experimental procedure oxidises the carbon and hydrogen into carbon dioxide and water, and reduces nitrogen compounds into nitrogen. The burnt samples pass through two reaction columns. The first reaction column is known as the oxidation column and is at 1 000 °C. The oxidation column is loaded with chromium trioxide followed by silvered cobaltic /cobaltous oxides to oxidise the carbon completely into carbon dioxide. The gases then pass into a reduction column containing copper oxide followed by pure copper wires at 750 °C, which removes some contaminants, and processes the nitrogen compounds, reducing them to

nitrogen. A photograph of the Carlo Erba EA-1110 CHNS elemental analyser is shown in Figure 2-13.



**Figure 2-13** Photograph of the Carlo-Erba EA-1110 CHNS elemental analyser, with the sample mount seen on top of the analytical instrumentation.

#### **2.4.6. Zeta potential**

There are two regions of charge surrounding particles in suspension because of the electrical charge on the surface of particles. The electrical charge on the surface of the particles forms an ionic atmosphere, because ions of opposite charge tend to cluster nearby. First there is a fairly immobile layer of ions that adhere tightly to the surface of the colloidal particle, and may include water if this is the support medium. The radius of the sphere that just includes this rigid layer is called the radius of shear and is the major factor in determining the mobility of the particles (Derjaguin and Landau, 1941; Verwey and Overbeek, 1948). The zeta potential, also known as the electrokinetic potential, is the electric potential at the radius of shear relative to its value in the distant, bulk medium. Second, the charged unit attracts an oppositely charged atmosphere of



mobile ions. The inner shell of charge and the outer ionic atmosphere is called the electrical double layer (Atkins and de Paula, 2002).

The zeta potential of the sticky suspensions was measured on a Zetasizer Nano (Malvern Instruments Ltd, UK.) before the mineral was added, and after the mineral with adsorbate was removed. The zeta potential gave a measure of the coulombic stability of the colloidal suspensions, and how the stability of the remaining suspension changed because of the adsorption of sticky onto mineral surfaces. A change in magnitude of the zeta potential was also useful in determining if cationic or anionic species were adsorbed preferentially (Hunter, 1981).

### **3 Elucidation of void space architecture of filters by comparison and modelling of porometry, porosimetry and microscopy (Gribble, Matthews *et al.*, 2010b)**

#### ***3.1 Introduction***

This work is an investigation of the extent to which various ‘orders’ of architecture of the void space of porous media can be deduced from a combination of standard experimental techniques when aided by a void network model. The experimental samples are metal, cellulose and glass-fibre macro- and meso-porous filters of various types. The network model, ‘Pore-Cor’, has been described in previous publications (Price, Matthews *et al.*, 2009; Matthews, Laudone *et al.*, 2010). In this work, we apply it for the first time to porometry, which necessitates an extrapolation of the experimental data from the instrument. Pore-Cor has been previously used to model a range of materials such as soil, sandstone, catalysts and paper coatings (Ridgway and Gane, 2002; Bodurtha, Matthews *et al.*, 2005; Laudone, Matthews *et al.*, 2005; Matthews, Laudone *et al.*, 2010). The network model has also been used as a predictive tool for the study of absorption, diffusion and filtration (Ridgway and Gane, 2002; Laudone, Matthews *et al.*, 2008; Price, Matthews *et al.*, 2009).

Various orders of void space architecture can be postulated, analogous to the orders of molecular structures in proteins. The primary structure of a porous material is taken to be the distribution of void and throat sizes, the secondary structure the connectivity of these voids, the tertiary structure the relationship between the sizes of voids and the sizes of their immediate connecting neighbours, and the quaternary structure the size auto-correlations and gradations over the sample as a whole. All these different levels of structure contribute to important properties of the sample, such as its filtration

efficiency and capacity (Price, Matthews *et al.*, 2009), absorption and wetting characteristics (Ridgway, Schoelkopf *et al.*, 2001; Hicyilmaz, Ulusoy *et al.*, 2004; Bodurtha, Matthews *et al.*, 2005; Wallqvist, Claesson *et al.*, 2009), and the adsorption and diffusion of fluids in the pores (Meyers, Crosser *et al.*, 2001; Laudone, Matthews *et al.*, 2008). Specifically, the quaternary structure determines the anisotropy of these characteristics relative to the direction of application or flow of fluids as discussed further below.

In this work, we use mercury porosimetry (Calvo, Hernandez *et al.*, 1995; Matthews, 2000), porometry (Calvo, Hernandez *et al.*, 1995; MiettonPeuchot, Condat *et al.*, 1997; Li, Frey *et al.*, 2006), and scanning electron microscopy (SEM) coupled with image analysis (Hernández, Calvo *et al.*, 1997; She, Tung *et al.*, 2008; Ziel, Haus *et al.*, 2008). Each technique has advantages and disadvantages in the determination of the pore size distribution. We also show how shielded mercury porosimetry, in which the coarser or more porous faces of the samples are shielded by the application of resin, can mimic porometry and complement standard porosimetry. We also demonstrate the extent to which the void structure model Pore-Cor, with its simplified void shapes arranged along Cartesian axes, can assist in elucidating the various orders of architecture. Other techniques are available but not used in this work, including NMR (Rigby, Fletcher *et al.*, 2002; Gane, Ridgway *et al.*, 2004; Matthews, Canonville *et al.*, 2006), and gas adsorption, which is more appropriate for nanoporous materials (Ravikovitch, Odomhnaill *et al.*, 1995; Ravikovitch, Haller *et al.*, 1998; Ravikovitch and Neimark, 2002).

### 3.1.1 Theoretical considerations regarding porosimetry and porometry

As already described in Section 2.1.2 and 2.1.3 it is possible to calculate the size of a cylindrical pore-throat ('throat') intruded by a non-wetting fluid applied at a pressure  $P$  relative to the evacuated void space within a sample, by means of the Laplace equation:

$$d = \frac{-4\gamma_{LV} \cos \theta}{P}$$

Equation 3-1

Mercury intrusion measures the volume  $v$  of mercury intruded at a pressure  $P$ , corresponding to a throat diameter  $d$ . Mercury typically has a mercury / solid / vacuum contact angle  $\theta$  of between  $130 - 140^\circ$  and interfacial tension of mercury relative to its vapour  $\gamma_{LV}$  of  $0.485 \text{ N m}^{-1}$  (van Brakel, Modry *et al.*, 1981).

A common, usually implicit, approximation is to assume that the void space comprises a bundle of aligned capillary tubes, as described in Section 1.3.1.1. Suppose for purposes of illustration that there are  $n_1$  such tubes of diameter  $d_1$  and length  $l_1$ ,  $n_2$  of diameter  $d_2$  and length  $l_2$ , and  $n_3$  of diameter  $d_3$  and length  $l_3$ , where  $d_1 > d_2 > d_3$ . We assume that  $d_1$ ,  $d_2$  and  $d_3$  are logarithmically distributed, i.e. that  $d_1/d_2 = d_2/d_3$ , as typically found for natural samples. Suppose that there is a constant relationship between the diameters  $d$  of each feature and their lengths  $l$ , such that  $l = s d^m$ , where  $s$  and  $m$  are empirical constants for all features. Suppose mercury at a pressure  $P_2$  is applied, where

$$-\frac{4\gamma_{LV} \cos \theta}{d_3} > P_2 > -\frac{4\gamma_{LV} \cos \theta}{d_2}$$

. Then a volume  $V_{P_2}$  of mercury will intrude all the tubes of diameter  $d_1$  and  $d_2$ , where by simple geometry:

$$V_{P_2} = \frac{n_1 \pi d_1^2 l_1}{4} + \frac{n_2 \pi d_2^2 l_2}{4} = \frac{s\pi}{4} (n_1 d_1^{2+m} + n_2 d_2^{2+m})$$

**Equation 3-2**

Analogously, if there is an increase to a pressure  $P_3 > -\frac{4\gamma_{LV} \cos \theta}{d_3}$ , such that features of size  $d_3$  are intruded, then

$$V_{P_3} = \frac{n_1 \pi d_1^2 l_1}{4} + \frac{n_2 \pi d_2^2 l_2}{4} + \frac{n_3 \pi d_3^2 l_3}{4} = \frac{s\pi}{4} (n_1 d_1^{2+m} + n_2 d_2^{2+m} + n_3 d_3^{2+m})$$

**Equation 3-3**

such that for any applied pressure,  $P_N$ ,

$$V_{P_N} = \frac{s\pi}{4} \sum_{i=1}^N n_i d_i^{2+m}$$

**Equation 3-4**

Almost universally in the literature, the first derivative of the intrusion curve  $dV/d(\log_{10} d)$  is calculated, as shown schematically in Figure 3-1, which we will refer to simply as the gradient. However, remembering that  $d_i$  is logarithmically distributed, combining Equation 3-3 and 3-4 shows that

$$dV_{P_N} / d(\log_{10} d) = \frac{(2+m)s\pi}{4} \sum_{i=1}^N n_i d_i^{1+m} \propto n d^{1+m}$$

**Equation 3-5**

i.e. not that  $dV_{P_N} / d(\log_{10} d) = \propto n$  only, as is almost universally assumed in the literature. The persistence of the wrong assumption is based on the partial, but unquantified, cancellation of two implicit approximations – namely, this assumption of number rather than volume, which over-estimates the numbers of voids of larger sizes, and the ignoring of shielded pore space, which under-estimates voids of larger sizes.

Shielded pore space is that for which the only access is via a throat of smaller diameter, Figure 3-2 a) and 3-2 b).

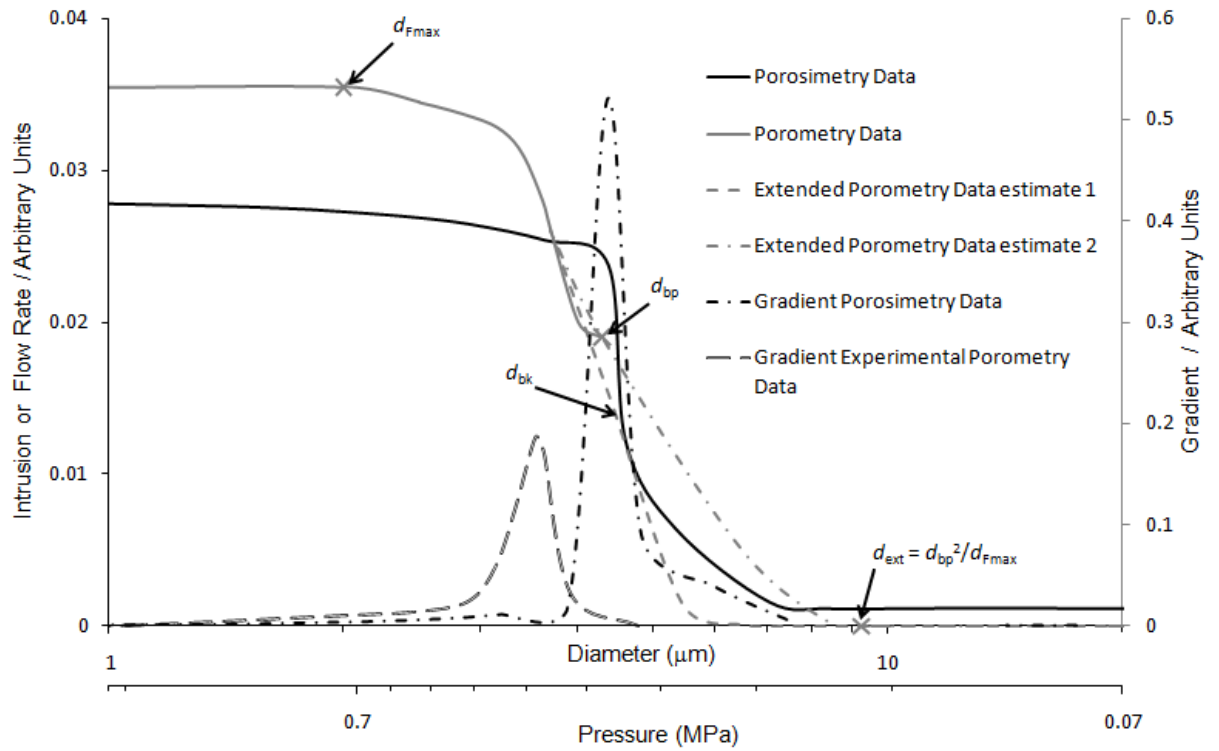
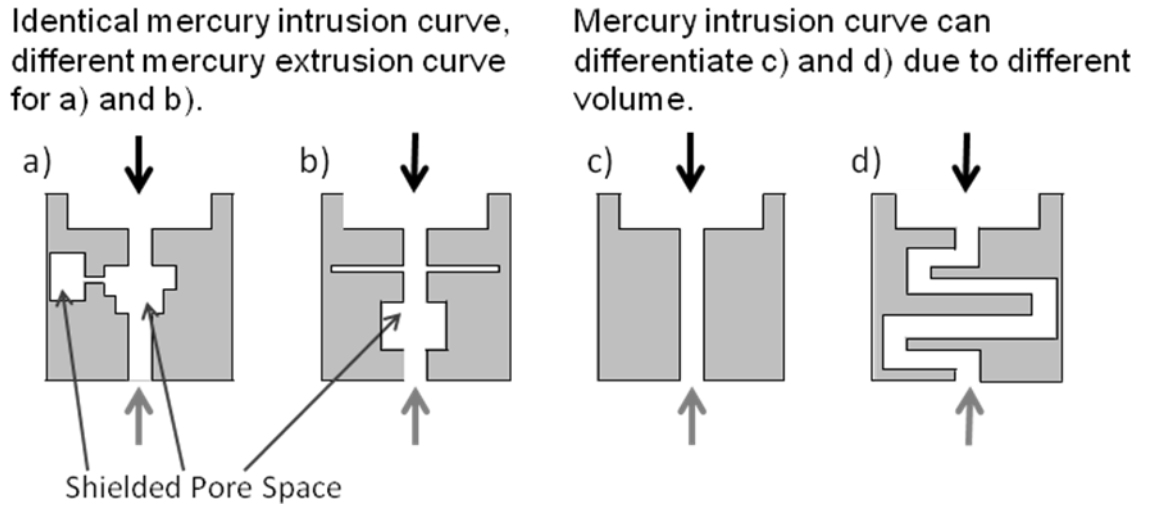


Figure 3-1. Schematic graph showing how extrapolated porometry data should compare with mercury intrusion data, and how mercury porosimetry and porometry data are interpreted using the capillary bundle model.

When carrying out mercury porosimetry, the breakthrough of mercury from one side of the sample to the other occurs close to the point of inflection of the mercury intrusion curve at a breakthrough pressure  $P_{bk}$ , equivalent to a breakthrough diameter  $d_{bk}$  via Equation 3-1. As illustrated in Figure 3-1, the volume intruded at  $P_{bk}$  (diameter  $d_{bk}$ ) is generally around 50 % of the total intrusion volume.



**Figure 3-2.** Comparison of how mercury porosimetry and porometry probe the pore architecture of schematic structures with simple quaternary level pore architecture. Mercury for standard porosimetry is applied in the direction of the black and grey arrows, and for shielded mercury porosimetry in the direction of the grey arrows only. Air, for porometry, is applied in the direction of the black arrows. Porometry would not be able to differentiate between the four different structures.

Porometry also uses Equation 3-1 with a contact angle for air of  $180^\circ$  against a wetting liquid, and the assumption that the gradient, as defined above, gives the relative number of features of a certain size  $d$ . However, in the case of porometry, measurement does not start until the bubble point pressure, corresponding to a size  $d_{bp}$  via Equation 3-1, at which gas first breaks through the sample. At this point, gas has already displaced fluid from all features larger and upstream of those controlling the breakthrough flow path through the sample. The porometry bubble point ( $P_{bp}$ ,  $d_{bp}$ ) therefore corresponds to the breakthrough point ( $P_{bk}$ ,  $d_{bk}$ ) in mercury intrusion. Consequently, the characteristic porometry curve covers only void sizes smaller than  $d_{bp}$ , and its traditional interpretation exaggerates the number of smaller void sizes relative to porosimetry. Once the bubble point has been reached, air flows through the sample in a totally different way than mercury. Assuming that the flow is laminar, it will obey Poiseuille's equation, such that the volumetric flow rate  $Q$  of the gas is

$$Q = \frac{\Delta P \pi d^4}{128 \eta l}$$

**Equation 3-6**

where  $\Delta P$  is the pressure differential across the sample, equated to  $P$  in Equation 3-1, and  $\eta$  is the kinetic viscosity of the gas. By analogy with equations 3-2 to 3-4:

$$Q_{\Delta P_N} = \frac{\Delta P_N \pi}{128 \eta} \sum_{i=1}^N \frac{n_i d_i^4}{l_i} = \frac{\Delta P_N \pi}{128 \eta s} \sum_{i=1}^N n_i d_i^{4-m} \propto n d^{4-m}$$

**Equation 3-7**

In porometry, the absolute flow  $Q$  at a particular differential pressure  $\Delta P$  is almost universally assumed to be proportional to the number of features, rather than using the 1<sup>st</sup> differential of the intrusion curve for this assumption as in porosimetry. For porometry, it can be seen from Equation 3-7 that in fact the flow rate is proportional to  $(n d^{4-m})$ . Therefore, equating the proportionalities in Equation 3-5 and Equation 3-7,  $m = 3/2$  is the one condition whereby porosimetry and porometry deliver the same proportional distribution. The likelihood of this single criterion being met in a real system is very small, so the traditional data analysis for porometry grossly underestimates the number of smaller features. The flowing gas can also cause venturi suction effects for other adjoining features, or blow into them, so the results for individual size ranges are liable to be affected by those for other sizes.

Shielded pore space is largely ignored by porometry, Figure 3-2. For filtration purposes, this shielded pore space will add to the holding capacity but not greatly affect the filtration size characteristics. The exaggeration and underestimation of smaller voids, as described earlier, partially compensate for each other, and so fortuitously the assumptions implicit in the porometry interpretation for filters are useful and appropriate.



Two other assumptions need to be borne in mind, however. Firstly, there are other special aspects of the fluid dynamics in porometry. A flowing gas is likely to leave a wetting film, coating all the feature surfaces, if the surfaces are rough, however high the applied pressure. Also, the results at different increasing pressures may not be truly independent of each other, due to the kinetic effects of gas flow causing changes in void sizes other than those predicted by the Laplace Equation 3-1. Furthermore, the ‘dry’ run, against which the ‘wet’ or displacing run is compared, is not actually dry – it corresponds to the sample with residual un-displaceable wetting fluid. Therefore, it would be sensible to carry out an actual dry run, and compare the results with the nominal dry run to ascertain whether wetting fluid remains on the sample at high gas flow rates, which is an indicator of nano-porosity or low-access micro-porosity. There are two experimentally based caveats concerning porometry. The first is that the sample is not evacuated or dessicated before analysis, so that material hygroscopy could affect the results. The second is that pouring wetting liquid onto a sample can cause air pockets to form due to the advanced wetting fronts of the liquid ‘over-taking’ the bulk wetting front (Schoelkopf, Ridgway *et al.*, 2000), which will interfere with the flow characteristics.

To compare porometry with porosimetry, we assume that the porometry curve commences at exactly 50 % of the intruded volume by analogy with the mercury porosimetry curve, as shown in Figure 3-1. We also specify one point  $d_{\text{ext}}$  on the extended porometry asymptote at low pressure / large size, the same distance above the bubble point  $d_{\text{bp}}$  on the logarithmic axis as the high pressure / low size asymptote  $d_{\text{Fmax}}$  is below it, as shown in Figure 3-1, so that :

$$d_{\text{ext}} = d_{\text{bp}}^2 / d_{\text{Fmax}}$$

**Equation 3-8**

When modelled using the network model Pore-Cor, there is the possibility of wide variations in the extended porometry curves between different stochastic realisations of the model, illustrated as estimates 1 and 2 in Figure 3-1, because there are no experimental points in that region. This is a genuine reflection that porometry omits much of the larger detail of the pore structure, as further illustrated below. The stochastic variation could be reduced by comparing the simulated permeability of different stochastic realisations with the permeability measured by the porometer during its nominal (and also, ideally, actual) dry runs, although variations in permeability are more sensitive to void sizes below the breakthrough diameter than they are above it.

Closer inspection of Figure 3-2 highlights the difference between porosimetry and porometry measurements, and the role of shielded porosimetry. Figures 3-2 a) and 3-2 b) show cross-sections of structures with different pore geometries, but with the same initial mercury intrusion (percolation or drainage) characteristics because there is initially an identical size / volume progression from large to smaller void features within the void network. However, mercury extrusion (equivalent to imbibition in the opposite direction of a wetting fluid into accessible mercury-exchangable volume) would detect the difference between the networks if the single entry ('ink bottle') pore to the left of Figure 3-2 a) is much larger (typically more than five times larger) than its entry throat so that snap-off occurs (Dawe and Egbogah, 1978). Structures c) and d) have the same diameter throat with different volumes and tortuosities. In theory, mercury porosimetry should be able to detect the difference between these structures, because for structure d) there would be greater volume of piston flow down the throat once the required pressure was reached according to Equation 3-1. In real samples, however, differences of this type are more subtle and difficult to detect.

The application of porometry to the samples in Figure 3-2 would involve initial application of a proprietary wetting fluid in the direction of either the black or grey arrows, which is then held in the structures by capillarity. Air, also applied in the direction of either the black or grey arrows would break through all the structures at the same pressure, so would be unable to differentiate between them. The flow rates through the dry structures, largely controlled by the smallest throats, would also be identical. So, porometry would suggest the presence of smaller voids than porosimetry, as found for real samples (Calvo, Hernandez *et al.*, 1995; Li, Frey *et al.*, 2006).

Shielded porosimetry, for which the top and sides of the sample are resin embedded, would involve intrusion of mercury in the direction of the grey arrows only, Figure 3-2. So it would mimic porometry and be unable to differentiate between the four structures. However, the fact that the results of standard porosimetry, and those of porometry or shielded porosimetry, were different, would identify that the structures had a quaternary level of pore architecture – in this case that they had one face with large pores, and one with small.

### **3.1.2 The network model**

Application of the Pore-Cor model to porometry has the advantage of estimating all the void space of a porous sample, and hence its holding capacity. Absolute numbers of features per unit volume of sample may be calculated or absolute volumes of features at each size, thus making it ideally suitable for describing both porosimetry and porometry results. Finally, a direct simulation of the filtration capacity of the modelled structure can be calculated, which calculates the gradual increase of differential pressure, decrease in holding capacity and increase in filtration capability as the filter captures increasing numbers of particles (Price, Matthews *et al.*, 2009).

## ***3.2 Materials***

The materials used in this investigation are materials with known pore sizes or nominal pore sizes provided by the respective manufacturers. Due to the size and nature of the samples, not all the materials could be tested with all the techniques. All of the manufacturers' filtration ratings where available (i.e. minimum sizes of particles that are filtered), and the void sizes in the next paragraph are also those supplied by the manufacturers.

Two filters prepared by Porvair Filtration Group were studied. One was a stainless steel mesh filter '3AL3' that had a filtration rating of 3  $\mu\text{m}$ . The second was specially constructed with two layers of stainless steel sinter. The bottom sinter was coarse with porous features greater than 20  $\mu\text{m}$ , and the top layer a fine sinter with a pore size distribution of approximately 0.5 – 1.5  $\mu\text{m}$ . A stainless steel sinter with a pore size of 2 – 5  $\mu\text{m}$  from Aegis Advanced Materials Ltd, U.K, was also used. A Fisherbrand GF300 Glass Fibre Filter with a filtration rating of 0.7  $\mu\text{m}$  was additionally studied. Finally, the following filters from Whatman were investigated; a grade 1 filter paper with a filtration rating of 11  $\mu\text{m}$  (catalogue number 1001 042), a Whatman cellulose nitrate filter with a filtration rating of 0.45  $\mu\text{m}$  (reference number 7184-004 lot number FN0056-1) and a Whatman Nucleopore track etch membrane, with a filtration rating of 1.0  $\mu\text{m}$  (lot number 5102005).

## ***3.3 Experimental and modelling methods***

### ***3.3.1 Mercury porosimetry***

Mercury porosimetry was performed on a Micromeritics AutoPore III 9420 or Autopore IV 9520 mercury porosimeter (Micromeritics Corporation, USA) with a pressure table from 0.01 MPa to 400 MPa. The equilibrium time for each pressure point was 30

seconds. The pressure values were converted into pore diameters by using the Laplace equation, Equation 3-1. The pore diameter was subsequently plotted against the gradient of the intrusion curve (as defined above) to give a volumetric distribution of pore size.

### 3.3.2 Porometry

Porometry was performed on a Porvair Porometer 4 (Porvair Filtration Group, UK), with control software written by Laudone<sup>1</sup> to control the instrument and carry out the extrapolation described earlier. The sample chamber had a diameter of 25 mm. The samples were first wetted by soaking the samples in the proprietary wetting fluid, Porofil from Beckman Coulter. Porofil has a low vapour pressure 0.4 kPa, a low reactivity and a low interfacial tension of  $0.016 \text{ Nm}^{-1}$ , so it is assumed that the liquid does not exhibit rapid evaporation, is inert with respect to the material of the samples and that the samples are fully wetted (Calvo, Hernandez *et al.*, 1995; MiettonPeuchot, Condat *et al.*, 1997; Li, Frey *et al.*, 2006; Solcova, Matejova *et al.*, 2006). The samples were placed in the sample chamber, additional Porofil was added to ensure the samples were saturated, and then the sample chamber was sealed. A pore size range was chosen initially arbitrarily by the user, and then refined to the discovered range of the particular sample. Treatment and analysis of the results were as described above.

---

<sup>1</sup> Environmental and Fluid Modelling Group, University of Plymouth.

### **3.3.3 Scanning electron microscopy and image analysis**

Scanning electron microscopy was performed on a Jeol JSM-5600 LV or Jeol JSM-6100 SEM (Jeol Ltd, Japan) under high vacuum conditions in secondary electron mode. The non-conductive samples were coated with gold before imaging. The SEM images were analysed using ImageJ (Rasband, 2008) to obtain the feret diameter of the porous features, where the feret diameter is the longest distance between any two points along the boundary of the void feature.

Size calibration was based on the SEM image scale-bars. The images were thresholded using ImageJ to distinguish between void space and material. The thresholding also removed imperfections such as scratches on the surface. Feret diameters were converted to histograms to combine the pore size number distribution obtained from multiple images.

### **3.3.4 Pore-Cor Research Suite modelling**

The mercury porosimetry samples were corrected for the blank chamber run and compressibility of the sample using Pore-Comp (Gane, Kettle *et al.*, 1996). No allowance was made for any distortion of the sample by the intruding mercury, which would be likely in the case of both the glass-fibre and paper filters. In the case of porometry, both compression and distortion of the samples under the maximum pressure applied during porometry (6 bar) was assumed to be insignificant.

Porosimetry and porometry sample data were modelled using Pore-Cor Research Suite v6.31 to generate a stochastic series of five void structures, all of which closely matched the experimental data. The most representative stochastic realisation of the five (i.e. with all the parameters closest to the mean of the set of five) was chosen for comparison

with the experimental results. The fitting parameters for the five stochastic generations for every sample can be found in Appendix A.

### ***3.4 Results***

Table 3-1 summarises all of the results for all filters with all of the experimental and modelling techniques used. The table also includes basic conclusions about the experimental and modelling results.

**Table 3-1. Ranges of void size distributions, and summary of conclusions**

Sample Name	Visual inspection of SEM	Image analysis of SEM	Direct Analysis of porometry	Direct analysis of mercury porosimetry	Void size range derived from modelled porometry	Void size range derived from modelled mercury porosimetry	Comparison of data	Conclusions
Stainless Steel Mesh	0.5 – 10 µm > 15 µm Figure 3-3	Fibrous material	3 – 5 µm Figure 3-4	3 – 8 µm 15 – 40 µm Figure 3-4	3 – 6 µm Figure 3-4	6 – 10 µm 30 – 55 µm Figure 3-4	Good agreement between all techniques. Porometer does not indicate structure.	SEM and mercury porosimetry indicate quaternary structure.
Stainless Steel Sinter (Porvair)	0.5 – 5.0 µm > 40 µm Figure 3-5	0.6 – 4.0 µm 20 – 80 µm Figure 3-6	1 – 6 µm Figure 3-6	0.5 – 10 µm 30 – 60 µm Figure 3-6	1 – 9 µm Figure 3-6	0.5 – 1 µm 20 – 75 µm Figure 3-6	Good agreement between techniques and model.	SEM and mercury porosimetry indicate quaternary structure.
Stainless Steel Sinter (Aegis)	0.5 – 5 µm Figure 3-7a	0.5 – 4.0 µm Figure 3-8	Sample too small for instrument	3 – 9 µm Figure 3-8	No experimental data to model	0.1 – 14 µm Figure 3-8	Mercury porosimetry data and model data agree.	All applicable techniques confirm uniform structure.
Glass fibre	1 – 7 µm > 10 µm Figure 3-7b	Fibrous material	1.0 – 1.6 µm Figure 3-9	0.5 – 6 µm 6 – 60 µm Figure 3-9	0.8 – 2.1 µm Figure 3-9	1 – 7 µm 10 – 60 µm Figure 3-9	SEM and mercury porosimetry agree, porometry indicates filtration capability.	SEM and mercury porosimetry indicate quaternary structure.
Grade 1 Paper	5 – 30 µm Figure 3-10a	Fibrous material	2 – 10 µm Figure 3-11	2 – 6 µm 6 – 25 µm Figure 3-11	4 – 8 µm Figure 3-11	4 – 8 µm 8 – 25 µm Figure 3-11	Good agreement between all techniques	SEM and mercury porosimetry indicate quaternary structure.
Cellulose nitrate membrane	0.5 – 3.0 µm Figure 3-10b	3 dimensional image analysis required.	0.4 – 0.9 µm Figure 3-12	0.3 – 1.2 µm Figure 3-12	0.4 – 0.9 µm Figure 3-12	0.3 – 2.0 µm Figure 3-12	Good agreement between all techniques.	Thin (quasi 2-dimensional) so no higher levels of structure.
Track etch membrane	1 - 4 µm Figure 3-13	0.5 – 2.5 µm Figure 3-14	1.1 – 1.4 µm Figure 3-14	0.5 – 1.5 µm Figure 3-14	1 – 2 µm Figure 3-14	0.3 – 3.0 µm Figure 3-14	Good agreement between techniques. Void structure model able to deduce that capillaries can overlap as seen in SEM.	Thin (quasi 2-dimensional) so no higher levels of structure.



The SEM images of the stainless steel mesh filter, Figures 3-3a and 3-3b, show why image analysis was impossible on this sample due to the 3-dimensional fibrous structure of the filter, which could not be analysed using two dimensional image analysis. Pores in the range 30 to 50  $\mu\text{m}$  are visible in the surface view shown in Figure 3-3a, while the cross-section in Figure 3-3b shows that there are also pores in the range 5 to 10  $\mu\text{m}$ , with a high degree of anisotropy relative to Figure 3-3a. Although anisotropy can be modelled (Bodurtha, Matthews *et al.*, 2005), all the experimental approaches in this work, and hence also the modelling, assumed isotropic voids. Under this approximation, the voids appear as a bimodal distribution of isotropic voids, rather than a unimodal or bimodal distribution of anisotropic voids.

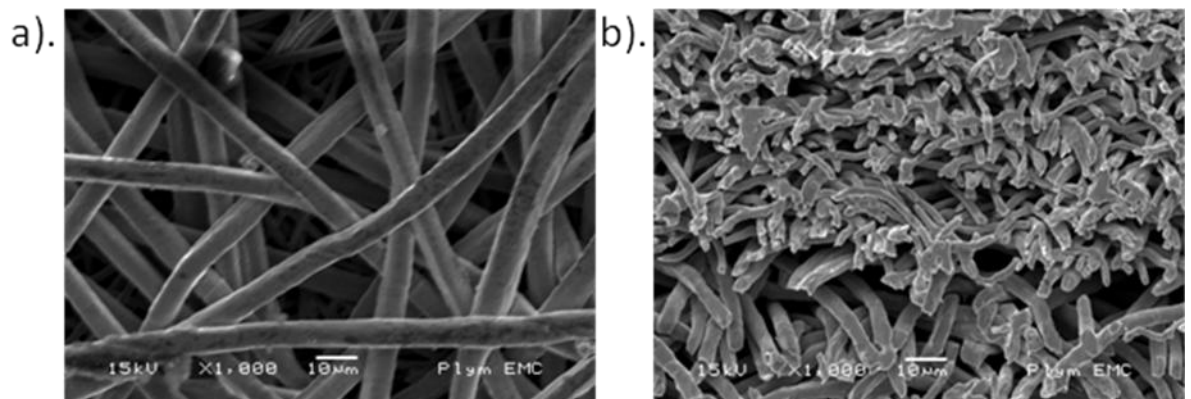


**Figure 3-3.** a) SEM image of surface of stainless steel filter 3AL3 and b) SEM cross-section of stainless steel filter 3AL3: both with 10  $\mu\text{m}$  scale bars.

The gradient of the mercury intrusion curve of the stainless steel filter sample indicated a bimodal distribution, as expected from the anisotropy, with features from 3 – 8  $\mu\text{m}$  and from 15 – 40  $\mu\text{m}$ , Figure 3-4. The network modelling of the mercury porosimetry results for the stainless steel mesh filter also gave a bimodal pore size distribution, with larger void sizes, as explained earlier, concentrated in the ranges 6 – 10  $\mu\text{m}$  and 30 – 55  $\mu\text{m}$ . Porometry gave a pore size distribution ranging from 3 – 5  $\mu\text{m}$ , Figure 3-4, without the larger pores visible in the SEM image, Figure 3-3a. The modelling of the porometry results gave a pore size distribution of 3 - 8  $\mu\text{m}$  in diameter. Although the

modelling of the porometry data moved the pore size distribution closer to the modelled porosimetry distribution, neither the porometry nor the modelling of the extended porometry curve revealed the large void sizes apparent in Figure 3-3a. To allow a comparison of results from the different techniques, the results needed to be normalised. The modelling, image analysis and porometry results were all normalised by the total number of features, while the mercury porosimetry results were normalised by total volume of features.

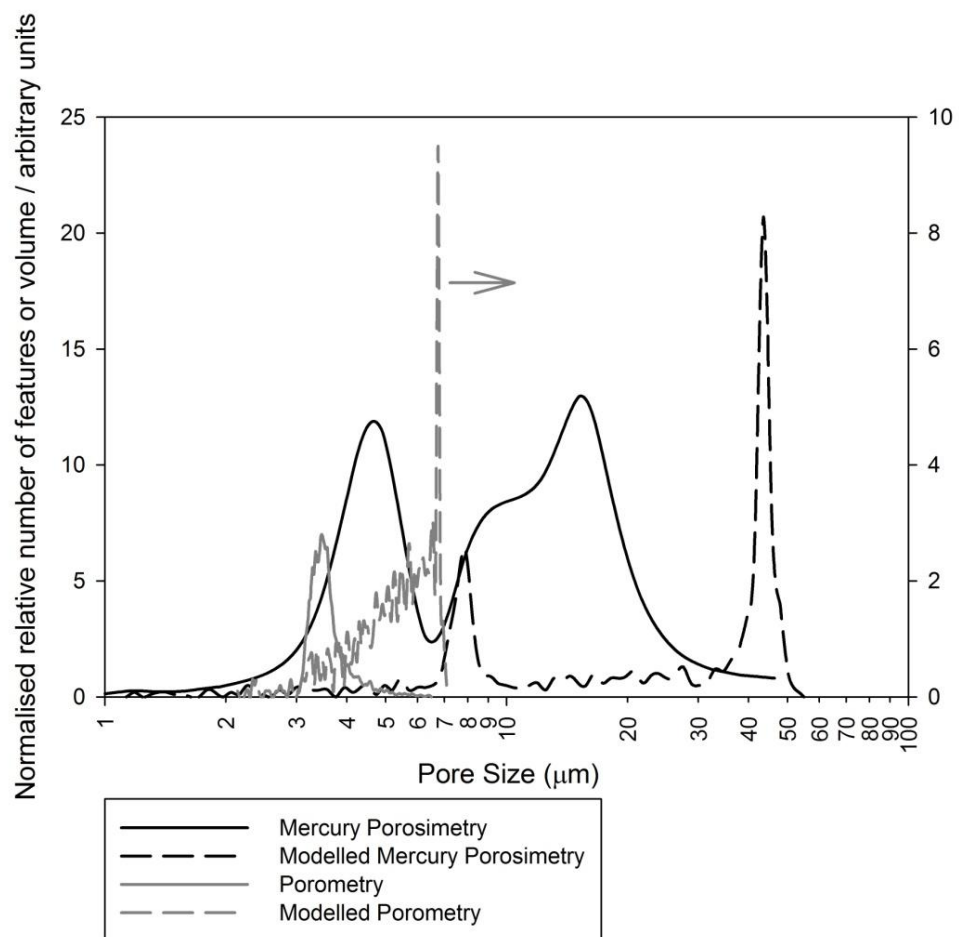


**Figure 3-4.** Pore size distribution of stainless steel mesh filter 3AL3 determined by mercury porosimetry, porometry and pore size distribution modelled by Pore-Cor. The same units are used on the primary and secondary y-axes on all graphs, the differences in scale being chosen to illustrate the features more clearly.

Next, the Porvair stainless steel sinter was tested using mercury porosimetry and SEM coupled with image analysis. Porometry was impossible as the sinter diameter was smaller than the sample chamber. The SEM images of the fine and coarse sides of the Porvair sinter, Figure 3-5, shows two different pore distributions. Figure 3-5a reveals

numerous pores smaller than 5  $\mu\text{m}$ , whereas Figure 3-5b shows pores with different diameters, above 40  $\mu\text{m}$ .

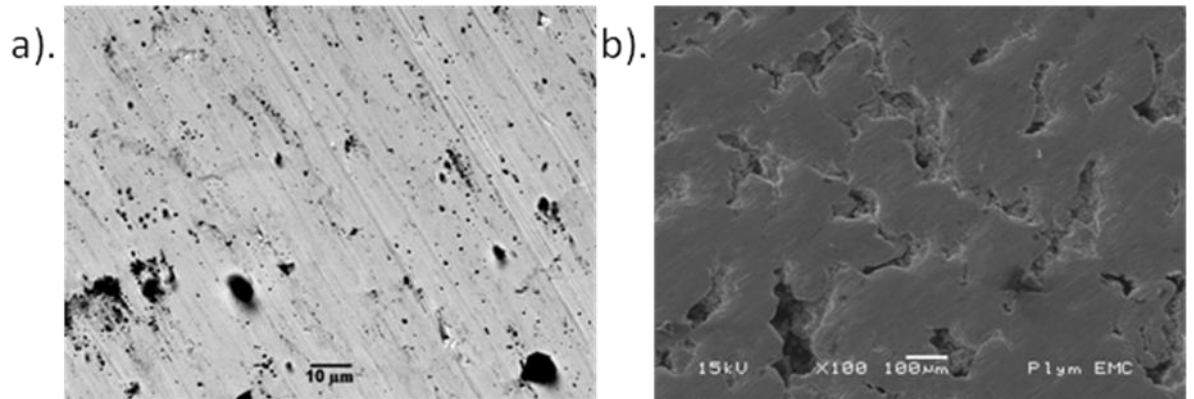


**Figure 3-5. SEM images of fine and coarse surfaces of Porvair stainless steel sinter: a) fine features, with 10  $\mu\text{m}$  scale bar, and b) coarse features, with 100  $\mu\text{m}$  scale bar.**

The SEM images of the fine features in Figure 3-5 were analysed using image analysis and give a void feature distribution with a modal size of 0.9  $\mu\text{m}$  within a range of 0.6 – 4.0  $\mu\text{m}$ , Figure 3-6. The large features covered a range from 20 – 80  $\mu\text{m}$ .

The gradient of the mercury intrusion gave a pore size volumetric distribution for the coarse features between 30 – 60  $\mu\text{m}$ , Figure 3-6, which corresponds to SEM and image analysis for the large features. The Pore-Cor modelling of the mercury porosimetry results gives a bimodal distribution for the Porvair stainless steel sinter, Figure 3-6, with pore sizes of 0.5 – 1.0  $\mu\text{m}$  and 20 – 75  $\mu\text{m}$ , much more in agreement with the image analysis than results based only on the intrusion volume gradient. The shielded porosimetry results gave a pore size range of 1 – 6  $\mu\text{m}$ , close to the 3  $\mu\text{m}$  filtration rating size, and the modelling of these data extended the range to include 1 – 9  $\mu\text{m}$ .

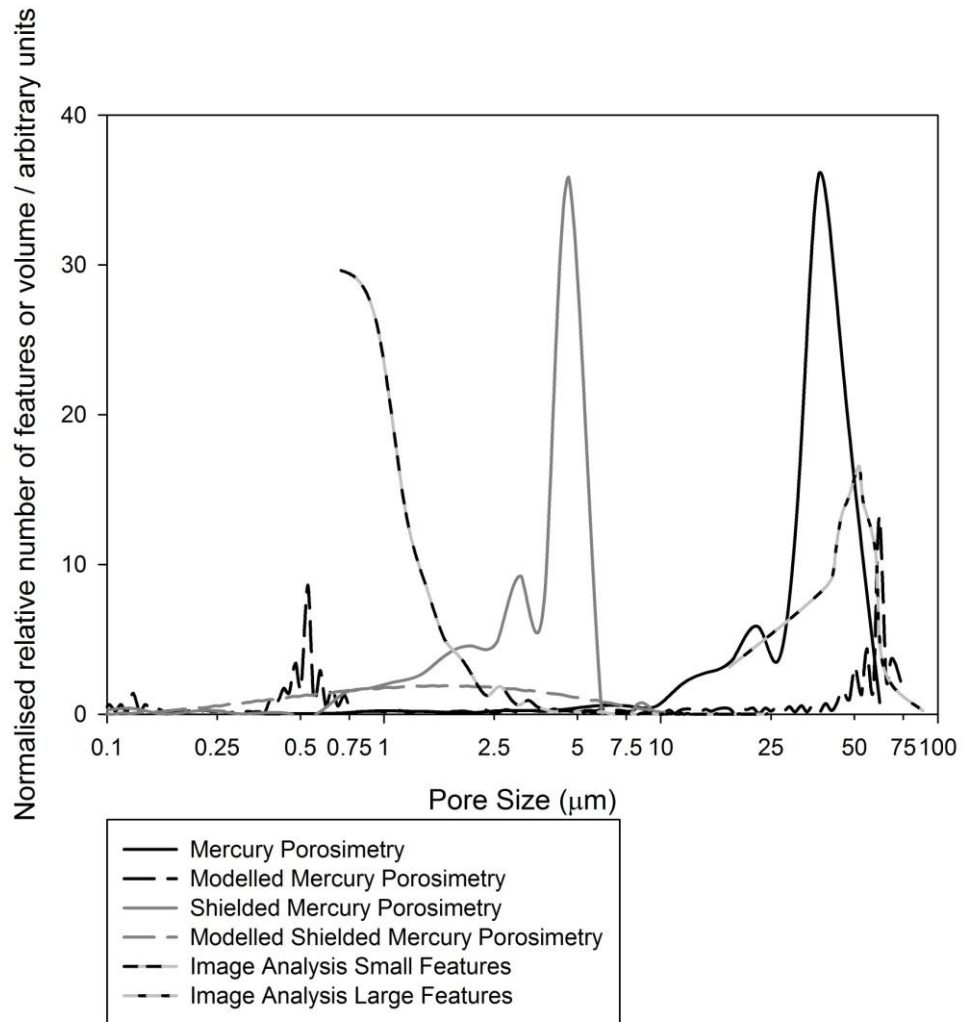


**Figure 3-6. Pore size distributions of a 3 µm rated Porvair stainless steel sinter using mercury porosimetry, shielded mercury porosimetry, and SEM and image analysis.**

The structure of the Aegis stainless steel sinter was investigated by mercury porosimetry and SEM only. The porometer was not used for this investigation as the diameter of the sinter was too small for the sample chamber. One example of the SEM images of the Aegis sinter is shown in Figure 3-7a.

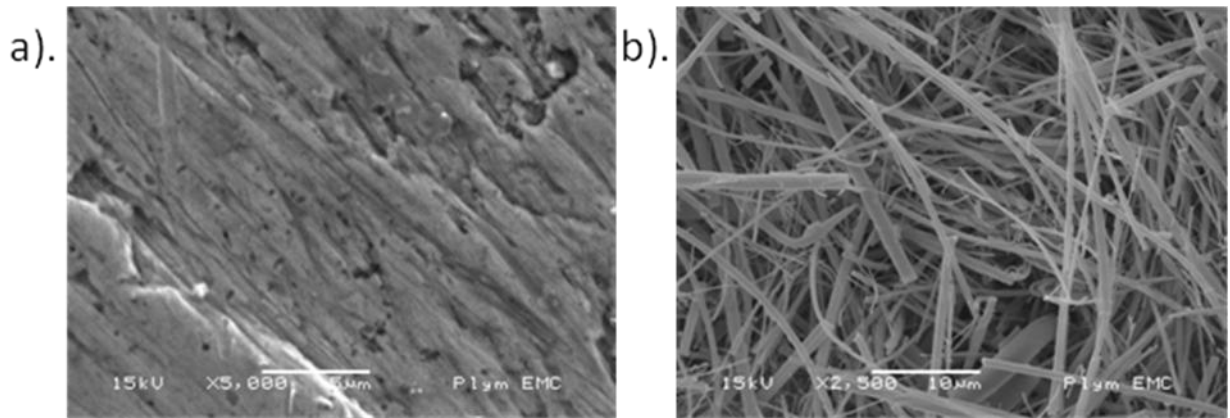
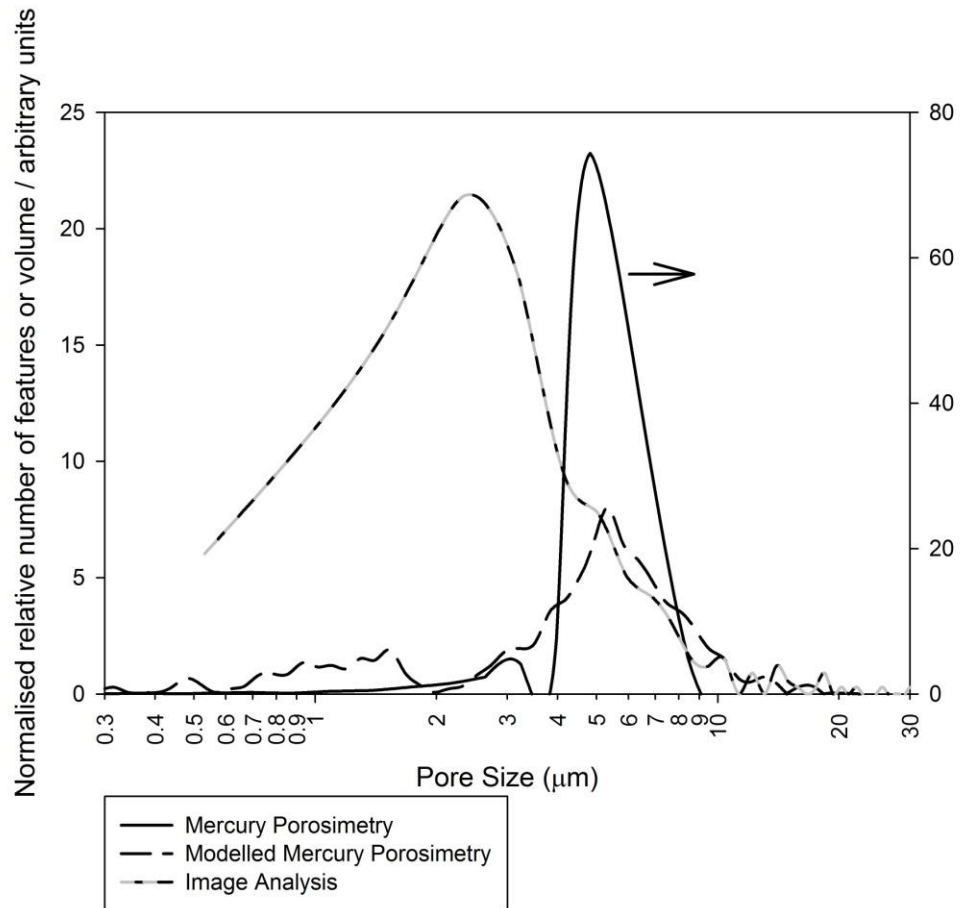


Figure 3-7. a) SEM image of Aegis stainless steel sinter, with 5  $\mu\text{m}$  scale bar, b) SEM image of glass fibre filter, with 10  $\mu\text{m}$  scale bar.

The image analysis of the Aegis sinter SEM images give a unimodal pore size distribution ranging 0.5 – 20.0  $\mu\text{m}$ , with a mode near 2.5  $\mu\text{m}$ , Figure 3-8. The mercury porosimetry results for the Aegis sinter give a modal pore size of 5  $\mu\text{m}$  with a pore size volumetric distribution of 3 – 9  $\mu\text{m}$ , Figure 3-8. The modelling of the mercury porosimetry data for the Aegis stainless steel sinter gives a range of pore sizes of 0.1 – 14  $\mu\text{m}$ . This modelled distribution is closer to the range of sizes found by image analysis of cross-sections, but continues to show a peak at around 5  $\mu\text{m}$ , which is higher than revealed by image analysis. Figure 3-7a shows surface striations, which were eliminated by the image analysis thresholding, and it is likely that some larger pores contained within these striations were lost to the image analysis, hence explaining the discrepancy.



**Figure 3-8. Pore size distribution of Aegis stainless steel sinter determined using mercury porosimetry, image analysis and a pore size distribution calculated using Pore-Cor.**

The glass fibre filter, rating 0.7  $\mu\text{m}$ , was tested using mercury porosimetry, porometry, and SEM, Figure 3-7b, but with no image analysis because of the fibrous nature of the filter. Visual inspection of the SEM image, Figure 3-7b, suggests a distribution of pores mainly in the range of 1 – 7  $\mu\text{m}$ , but extending up to sizes of the order of 20  $\mu\text{m}$ . The pore size distributions are shown in Figure 3-9. The mercury porosimetry results give a bimodal distribution ranging 0.5 – 6.0  $\mu\text{m}$  and 6 – 60  $\mu\text{m}$ , and the modelling of these data moves the distributions to larger sizes. Although the lower part of the bimodal distribution agrees with visual inspection, the sizes above 20  $\mu\text{m}$  are likely to be caused by distortion of the filter during mercury porosimetry, or the large pores between the folds of the filter paper fitted into the sample chamber (penetrometer). The larger pores could also be caused by mercury occlusion (Ridgway and Gane, 2003), due to the surface ragged nature of the fibrous material. In this investigation it is not taken into

consideration, mercury occlusion would indicate the presence of larger pores, which would also affect the modelling results. Porometry suggests a void size distribution between 0.9 and 2  $\mu\text{m}$ . Modelling of the data spreads the distribution over 0.8 – 2.1  $\mu\text{m}$ , with a lower bound closer to the manufacturer's filtration rating of 0.7  $\mu\text{m}$ .

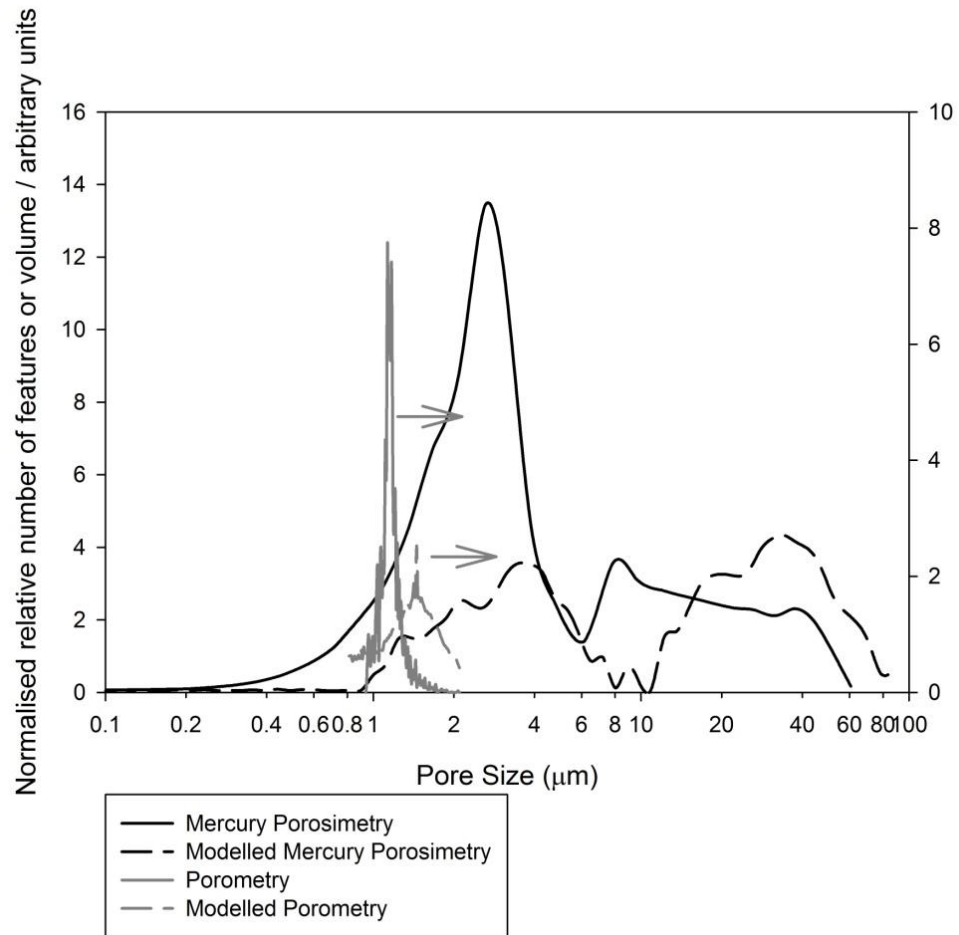


**Figure 3-9. Pore size distribution of a 0.7  $\mu\text{m}$  filtration-rated Fisherbrand glass fibre filter determined experimentally using mercury porosimetry and porometry, and by modelling the experimental data.**

The Whatman grade 1 filter paper was tested using SEM, porometry and mercury porosimetry. As for the glass fibre sample above, the SEM results were not able to be analysed using image analysis due to the fibrous structure of the filter paper, Figure 3-10a. The SEM figure shows a variety of pore sizes with a range of 5 – 30  $\mu\text{m}$  being common throughout the different levels of the filter paper.

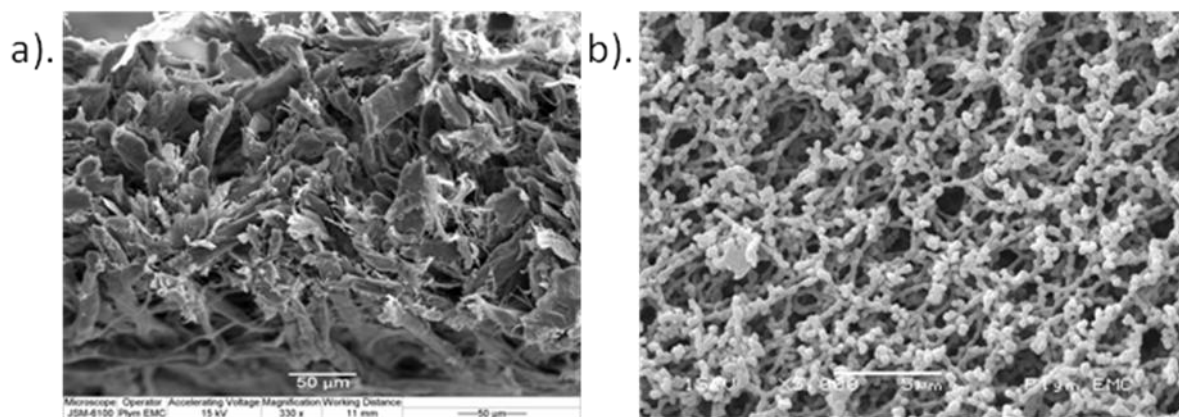


**Figure 3-10** a) SEM image of grade 1 filter paper, with 50μm scale bar, b) SEM image of cellulose nitrate membrane, with 5 μm scale bar.

Porometry of the filter paper yielded a pore size distribution range of 2.0 – 10.0 μm, with most of the pores less than 5 μm in size, Figure 3-11. However, it is possible to see in Figure 3-10a that there are pores larger than 10 μm in size, which are undetected by the porometer. The mercury porosimetry gradients show two distinct ranges of pore size, 2 – 6 μm and 6 – 25 μm, respectively, Figure 3-11. Modelling of the porosimetry and porometry moves the void size distributions to larger sizes, which are in accord with those observable in Figure 3-10 a).



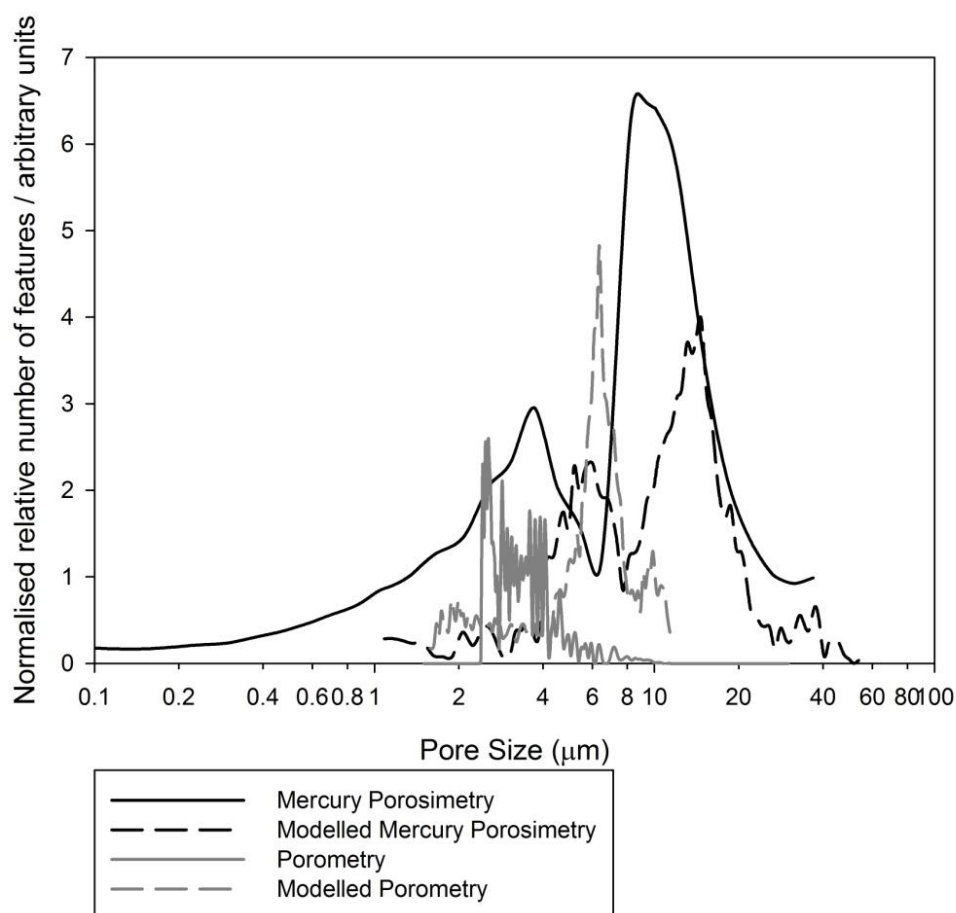


**Figure 3-11.** Pore size distribution of grade 1 filter paper determined by mercury porosimetry and porometry, together with Pore-Cor modelling of mercury porosimetry and porometry.

The Whatman cellulose nitrate membrane, with filtration rating  $0.45\ \mu\text{m}$ , was also studied with SEM, porometry and mercury porosimetry. The SEM image, Figure 3-10 b), shows pores ranging from  $0.5 - 3.0\ \mu\text{m}$ , but image analysis was impossible due to the deep 3-dimensional morphology of the pores. Porometry only showed features from  $0.4 - 0.9\ \mu\text{m}$ , Figure 3-12, corresponding to the filtration characteristic. The mercury porosimetry gradient gave a unimodal distribution of pore size from  $0.3 - 1.2\ \mu\text{m}$ , which expanded to  $0.3 - 2.0\ \mu\text{m}$  after modelling, which is more in agreement with the directly observed size distribution.

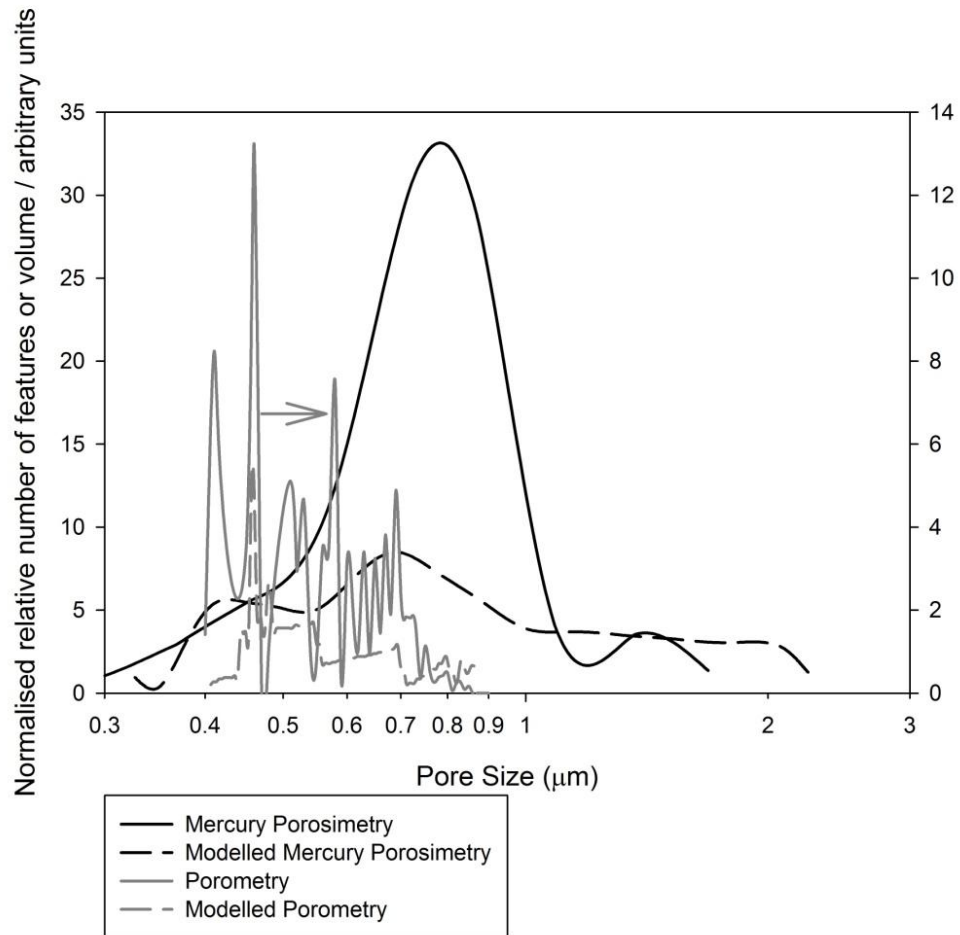


**Figure 3-12. Pore size distribution of a Whatman cellulose nitrate membrane filter determined by mercury porosimetry and porometry, together with the pore size distribution determined by modelling the porometry and mercury porosimetry data with Pore-Cor.**

Figure 3-13 is an SEM image of the final sample, a Whatman 1  $\mu\text{m}$ -rated track etch membrane. Image analysis gave a modal feature size of 0.8  $\mu\text{m}$  with a distribution of 0.5 – 2.5  $\mu\text{m}$ , Figure 3-14. The porosimetry and porometry distributions cover a narrow size range around 0.7 and 1.2  $\mu\text{m}$ , respectively, Figure 3-14. Modelling spreads the distributions, in the case of mercury porosimetry nearly to 3  $\mu\text{m}$ . Inspection of Figure 3-13 shows that these large sizes, revealed only by the modelling, arise from overlapping pore tracks. Individual overlaps may not extend through the entire thickness of the sample, so may not alter the filtration characteristic.

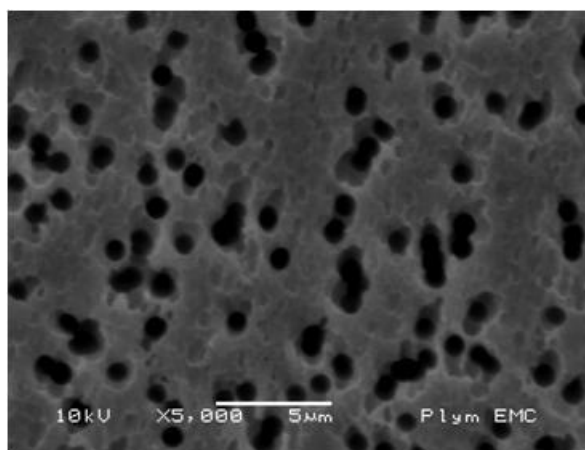


Figure 3-13 SEM image of 1  $\mu\text{m}$ -rated track etch membrane, with 5  $\mu\text{m}$  scale bar.

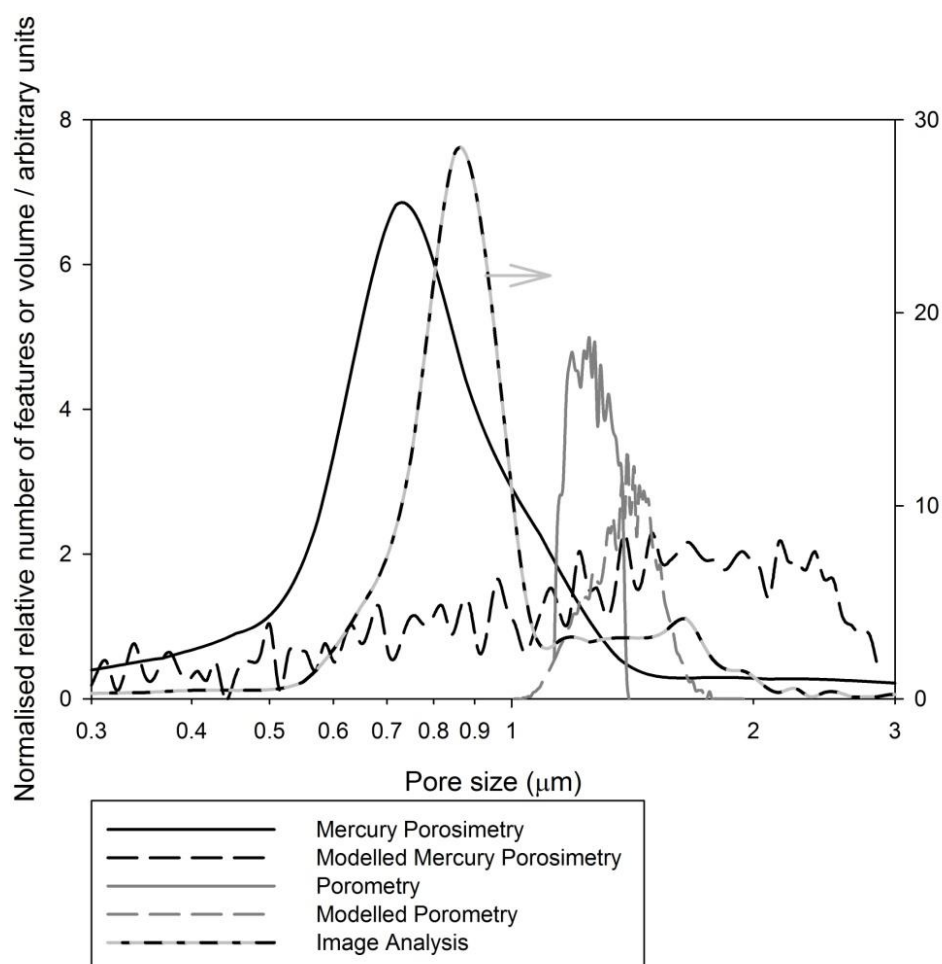


Figure 3-14. Pore size distribution for a Whatman track etch membrane determined using image analysis, mercury porosimetry and porometry with a pore size distribution calculated by the Pore-Cor model for porometry and mercury porosimetry.

### 3.5 Discussion and conclusion

Various themes emerge from the study of the seven different filters above. Firstly, modelling of the porosimetry results can reveal small voids ignored by the traditional

false assumption that the number of voids is equal to the relative volume of voids, e.g. in the case of the stainless steel sinters, Figures 3-6 and 3-8. Modelling of porometry can reveal larger voids, normally ignored because fluid is already displaced from them before the breakthrough occurs at the bubble point, for example in the stainless steel mesh filter, Figure 3-4, and grade 1 filter paper, Figure 3-11. Additionally, network modelling gives structures revealing all orders of void architecture that occur over lengths smaller than the unit cell size – normally, the primary, secondary and tertiary structuring. Porometry is shown to be an entirely satisfactory method of measuring the filtration characteristics in the case of filters with narrow size distributions, such as track etch membranes, Figure 3-14, and cellulose membranes, Figure 3-12. For filters with highly anisotropic structures with quaternary level structuring, such as the stainless steel filter, Figures 3-3 and 3-4, and glass fibre filter, Figures 3-7b and 3-9, porometry reveals the filtration characteristics but gives no indication of holding capacity, nor the quaternary structure, nor, hence, the anisotropy of the holding characteristic to flow. It must also be remembered that the holding capacity affects the ageing of the filter under flow conditions – for example, whether particles challenging the filter from the fine direction form a filter cake, or challenging the filter from the coarse direction get trapped within the coarse body of the filter just prior to challenging, from the inside, the fine face of the filter.

Overall, the series of approximations within the traditional analysis of porosimetry and porometry happen fortuitously to hold good, mainly because they tend partially to cancel each other, or happen to be appropriate for the experimental conditions applying. However, since the cancellation of the approximations is normally ignored and unquantified, the approach can fall apart for filters and other porous samples with complex quaternary structuring or wide void size ranges.

There is a simple means of gaining additional information from porometry for samples which have a suspected or actual significant quantity of nano- or micro-porosity in line with and fully accessible to the flowing gas. That is, to carry out a completely dry run before application of the proprietary wetting fluid, and to compare this result with the nominal dry run carried out after the wet run. Discrepancies between the actual and nominal dry run would reveal significant nano-porosity or micro-porosity.

### **3.5.1 Highlights**

- Primary, secondary, tertiary and quaternary levels of pore architecture have been defined.
- Porometry is very useful in providing filtration ratings.
- Porometry, mercury porosimetry and SEM, individually can only characterize primary pore architecture.
- A combination of experimental and modelling techniques allows a full characterisation of pore architecture from primary to quaternary levels.

## **4 Wetting and absorption properties of calcium carbonate**

The void structure of porous materials is important in regulating the various physical and chemical processes that occur within the material or on the surfaces of the material, both external and internal to the pore network. Experimental characterisation of porous materials is, therefore, of interest to establish knowledge of the structures involved. The surface chemistry and void network structure regulate the wetting and subsequent absorption behaviour of porous materials. The wetting behaviour of solid surfaces by a liquid is an important aspect of surface chemistry, which can have a variety of practical applications, such as switchable surfaces also known as ‘smart surfaces’ (Liu, Mu *et al.*, 2005). A switchable surface is a surface that can respond to an environmental stimuli (Russell, 2002), such as photoillumination and potential effects (Prins, 2001).

### ***4.1 Introduction***

Wetting is a property associated with the interface properties between a liquid and a surface. The surface may be another liquid, in the case of two immiscible liquids, or, more usually, a solid surface, as in the case of a porous material. The degree of wetting is dependent on various factors, which were described in Section 1.3.4 and its subsections.

In this investigation, calcium carbonate grades with defined particle size distribution and pore structure are investigated to see why some surface-modified calcium carbonate (MCC) grades apparently wet faster than their measured pore structures and assumed surface chemistry would suggest. To investigate the internal pore surface features in more detail, adsorption-desorption isotherms for nitrogen and *n*-butane were measured. The mesopore size distribution was determined using the Barrett-Joyner and Halenda

(BJH) algorithm (Barrett, Joyner *et al.*, 1951) in conjunction with the Halsey adsorbed thickness equation for the desorption isotherms of both gases (Halsey, 1948), sections 1.3.1.4 and 1.3.1.5.

## ***4.2 Experimental***

This investigation used different experimental techniques to investigate the porous features of calcium carbonate, to see how surface modification processes affect the wetting properties. The investigation techniques were mercury porosimetry, gas adsorption and wetting/absorption with hexadecane.

### **4.2.1 Minerals**

There are three different grades of calcium carbonate investigated in this experiment; all provided by Omya Development AG. The three grades of calcium carbonate include one ground calcium carbonate (GCC), which is used as the source material to produce modified calcium carbonate (MCC). The remaining two grades are MCCs produced from the GCC by treating the GCC with phosphoric and/or citric acid. The first MCC grade is a discretely bimodal (dual) porous modified calcium carbonate (DP MCC), which contains macro (inter particle) and micro (intra particle) porosity. The modification creates the intra particle porous structure and modifies the surface chemistry of the calcium carbonate. The second MCC grade is a high surface area modified calcium carbonate (HSA MCC) with macro porosity but minimal intraparticle microporosity. It is believed that the HSA MCC has nano features that create surface rugosity/roughness. The surface rugosity is in turn believed to improve the wetting of the mineral to a similar degree as the additional microporosity encountered in the DP MCC. The absorption rate is defined by the decoupling of permeability and capillarity, with the absorption rate for GCC and DP MCC obeying the model described by Gane and Ridgway (Gane, 2006; Ridgway, Gane *et al.*, 2006), when absorption is controlled

by the intraparticle pore capillarity and interparticle permeability, with different short and long term absorption rates differently proportional to time<sup>0.5</sup>. The HSA MCC wets unexpectedly fast, does not show a transition between short term and long term absorption, and the absorption is not proportional to  $t^{0.5}$ . Therefore, a study of the minerals is important to understand the differences in wetting behaviour between the calcium carbonate grades. SEM images of the three different grades of calcium carbonate are shown below.

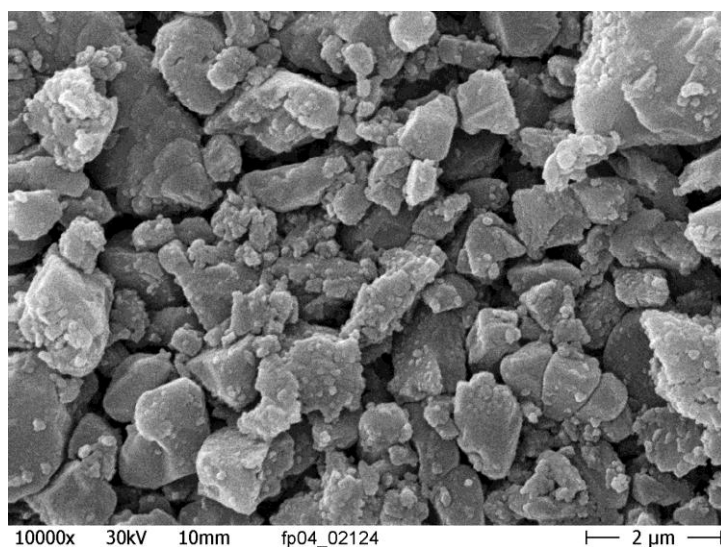


**Figure 4-1** Scanning electron micrograph of GCC.

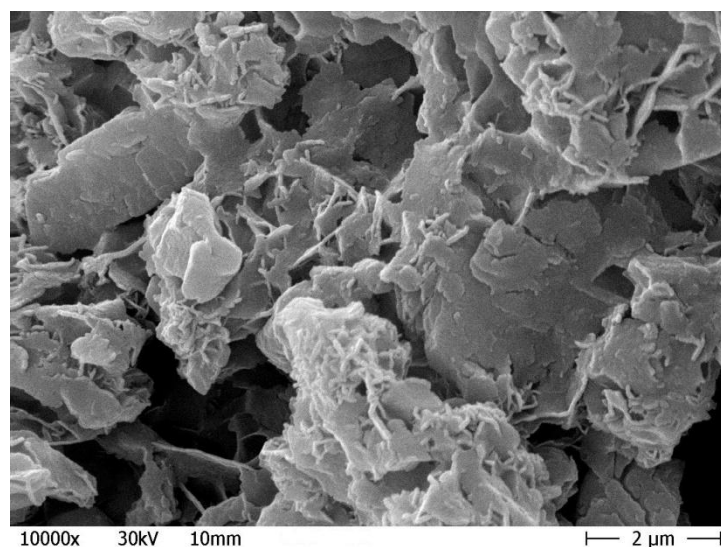


**Figure 4-2** Scanning electron micrograph of DP MCC.



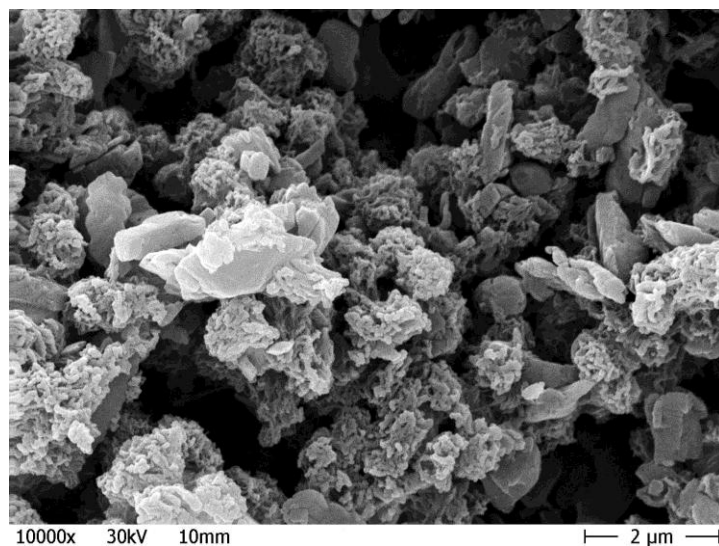


**Figure 4-3** Scanning electron micrograph of HSA MCC.

In Figure 4-2, the SEM image of the DP MCC, it is possible to see internal pore structure, which explains why it absorbs very well. In Figure 4-1, there is no visible internal porosity, which explains the low absorption rate for the GCC. In Figure 4-3, it is possible to see internal porosity but there is a problem in explaining why its wetting rate is not proportional to  $t^{0.5}$ .

### **4.2.2 Materials**

The wetting experiments were performed using 99 % purity hexadecane sourced from Sigma-Aldrich. The 99.99 % purity mercury for the mercury porosimetry experiment was also sourced from Sigma-Aldrich. The adsorption-desorption isotherms were made using gases supplied by BOC gases Ltd, with instrument grade *n*-butane being used, and high purity nitrogen was used for degassing the minerals prior to analysis.

### **4.2.3 Hexadecane wetting experiment**

The absorption experiment was performed using the method detailed by Schoelkopf *et al.* (Schoelkopf, Ridgway *et al.*, 2000). The balance used for the experiment was an AX504 Delta Range (Mettler Toledo (Schweiz) GmbH). The hexadecane wetting experiment is described in detail in Section 2.3.2.

#### 4.2.4 Mercury porosimetry

Mercury porosimetry of the MCC samples was performed using Micromeritics mercury porosimeters, Autopore III 9420 and/or Autopore IV 9520 (Micromeritics Instrument Corporation, USA). All samples were analysed using identical pressure steps ranging from 0.013 MPa to 414 MPa (equivalent to a pore size of 4 nm), and each pressure point was allowed to equilibrate for 30 seconds. The mercury porosimetry results were corrected for compressibility and blank sample run according to the procedure documented in Gane, Kettle *et al.* (1996). More details about the experimental technique were given in Section 2.1.2.

#### 4.2.5 Gas adsorption desorption isotherms

The adsorption and desorption isotherms of the calcium carbonate samples were performed on a Micromeritics Gemini 2360, using a 10 second equilibrium time for each partial pressure. The partial pressures of nitrogen and *n*-butane (instrument grade > 99.5 %) spanned the range of 0.00 – 0.97 P/P<sub>0</sub>.

Prior to analysis, all samples were degassed by blowing helium at 250 °C for 30 minutes and then evacuated for 10 minutes to ensure any residual moisture was removed. The nitrogen adsorption isotherms were performed at 77 K, the temperature of liquid nitrogen, whereas the *n*-butane adsorption isotherms were performed at 273 K using an ice-water bath. More details about the experimental procedure can be found in Section 2.3.1.

The following parameters were used to calculate the specific surface area from the nitrogen and *n*-butane isotherm data using the BET equation explained in Section 1.3.2.2. Molecular cross sectional area of N<sub>2</sub>: 0.162 nm<sup>2</sup>. Density conversion factor: 0.0015468. (The density conversion factor is used to convert the density from the adsorbate gas to the adsorbate liquid.) Molecular cross sectional area of *n*-butane: 0.430

nm<sup>2</sup>. Density conversion factor 0.0043151. The gas desorption data were analysed using the BJH algorithm to determine the pore size distribution of meso structures / nanopores present in the sample (Barrett, Joyner *et al.*, 1951; Micromeritics, 2006). The BJH algorithm was explained in detail in sections 1.3.1.4 and 1.3.1.5, which explained the differences between using the adsorption and desorption branch, and comparison of the surface area results with the BET equation.

### ***4.3 Results and discussion***

The intraparticle void space was characterised using mercury porosimetry, with the data processed using the Laplace equation, Equation 2-1.

The characterisation of the MCCs with mercury porosimetry is shown in Figure 4-4. Figure 4-4 is the first derivative of the intrusion curve, so must be viewed with the caveats discussed in Section 3.1.1. It shows the macropore size distribution of the MCC to be bimodal for the DP MCC with the modal points at 0.09 and 0.5  $\mu\text{m}$ . The HSA MCC has a unimodal distribution with the mode at 0.5  $\mu\text{m}$ . Mercury porosimetry at the highest measured pressures should have identified the presence of nanopores, unless they are restricted in respect to entrance geometry. So within those approximations we can initially assume that if there are surface feature differences, then these differences are related to surface rugosity and not intrudable nanopores.

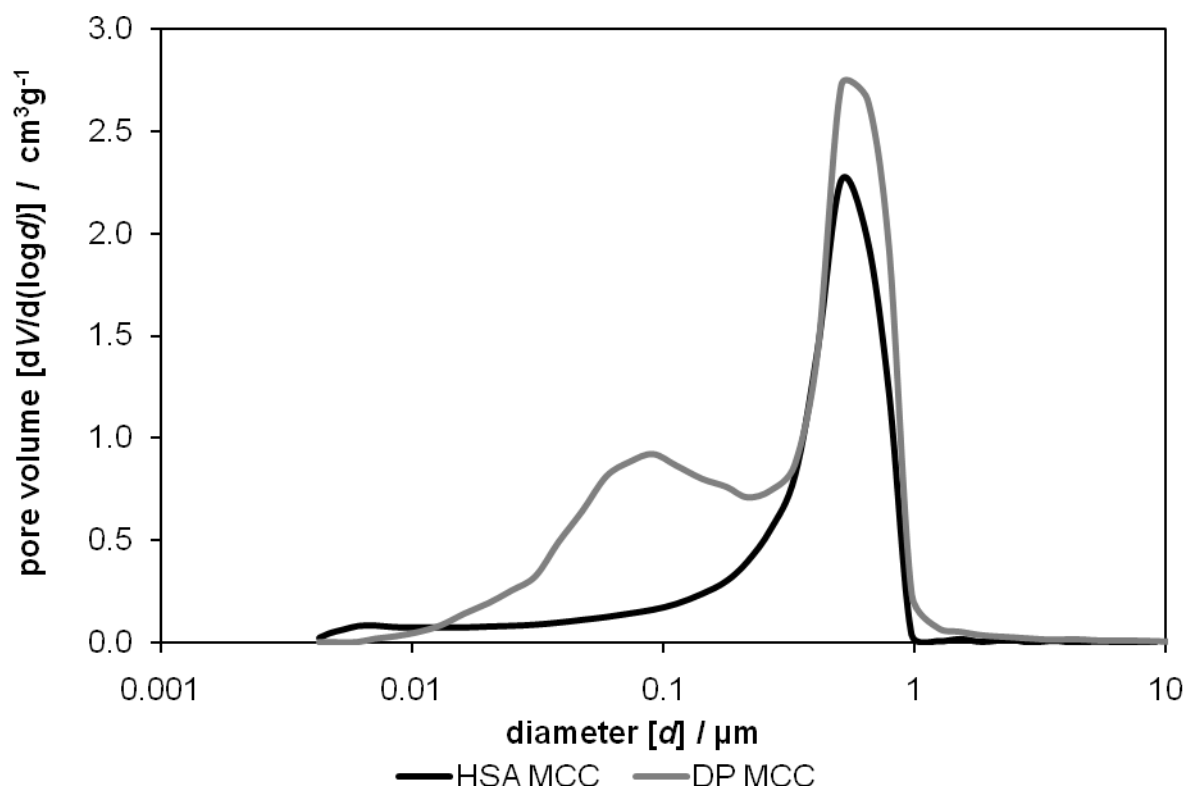


**Figure 4-4.** Graph comparing pore volume against diameter for MCC calculated from mercury porosimetry results using the Laplace equation.

The average nitrogen adsorption-desorption isotherms for the GCC, DP MCC and HSA MCC are shown in Figure 4-5. There is an increased degree of hysteresis in the order  $\text{GCC} < \text{DP MCC} < \text{HSA MCC}$ . The increase in hysteresis implies an increased quantity of nanopores/rugosity available for capillary condensation. The results show minimal hysteresis for the GCC which implies there are no nanorugose surfaces available. The hysteresis curve for DP MCC and HSA MCC both end at a relative pressure of 0.4, which shows there are similar sizes of nanopores in the materials but a greater amount present in the HSA MCC. Once again, since in the HSA MCC case no mercury intrusion of nanopores was recorded, we initially assume that the sorption hysteresis associated with this sample is related to surface rugose structures (wrinkles, roughness, period structures etc.) or hidden, entrance restricted, porosity.

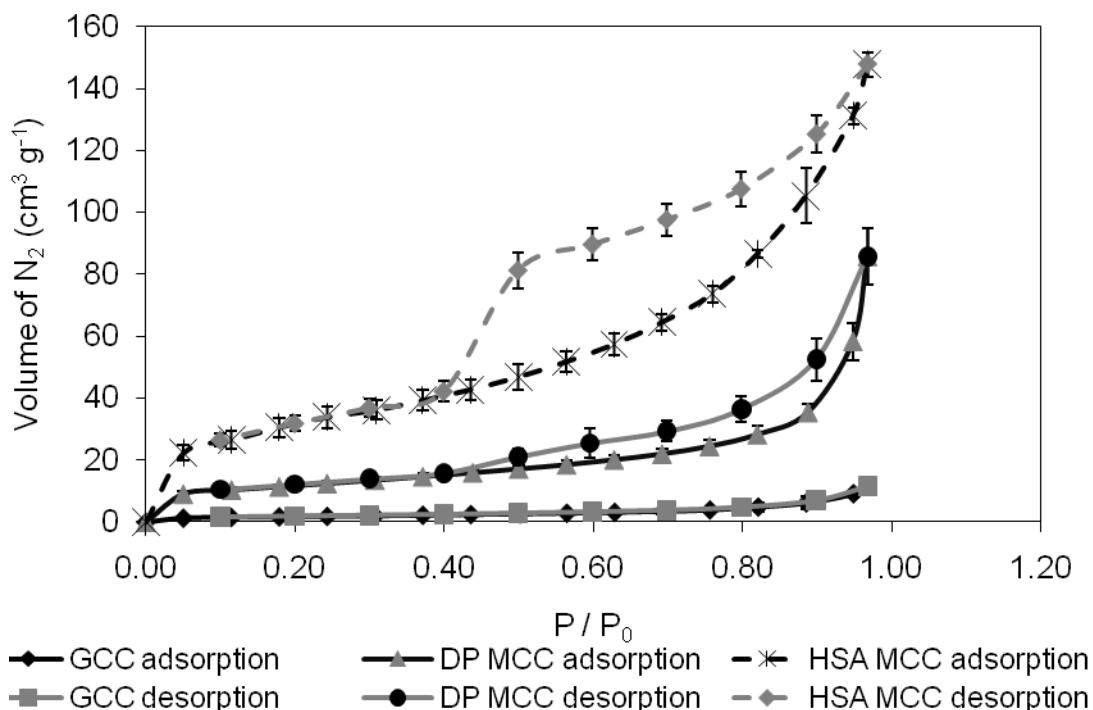


**Figure 4-5. Adsorption-desorption average isotherms with nitrogen for calcium carbonate systems. The error bars represent two times the standard deviation from six replicates.**

To distinguish between the surface features seen by nitrogen adsorption (nanopores and nanorugosity), we then investigated the response of adsorption for *n*-butane, a larger molecule which allows us to probe the size scale of these surface features. The adsorption footprints nitrogen and *n*-butane molecules cover 0.162 nm<sup>2</sup> and 0.43 nm<sup>2</sup> respectively. The respective adsorption-desorption isotherms for *n*-butane are shown in Figure 4-6. The *n*-butane isotherms confirm the result that there is no hysteresis for the GCC. The hysteresis curve for the HSA MCC and DP MCC do not start and finish at identical relative pressures, as was the case seen for nitrogen in Figure 4-5. Therefore, the *n*-butane has detected differences in the nanopore structures between DP MCC and HSA MCC which are not detectable by nitrogen adsorption alone. Thus, there are more and larger rugose structures on the surface of the HSA MCC.

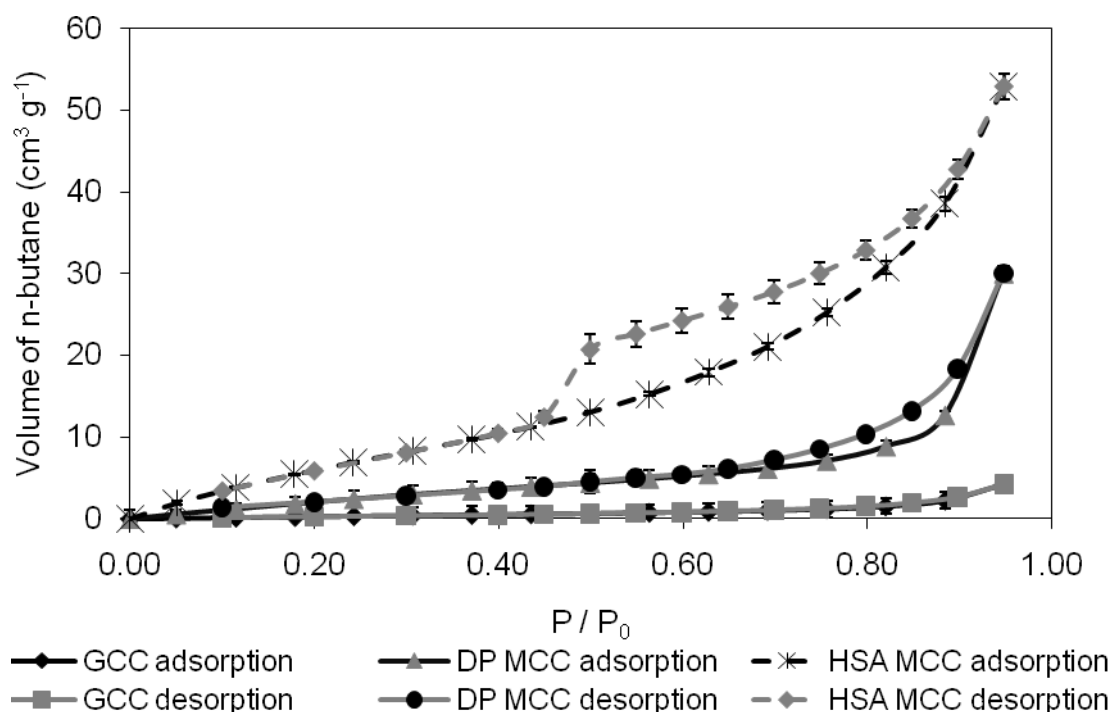


**Figure 4-6.** Adsorption-desorption average isotherms with *n*-butane for calcium carbonate systems. The error bars represent two times the standard deviation from four replicates.

The surface areas of the sample powder were calculated using the BET equation to find how the apparent surface area changes depending on the gas used. The results are shown in Table 4-1, with the surface area of the GCC being almost identical, as identified by the two gases. This result confirms the lack of rugosity at the two size scales studied. The nitrogen surface areas are larger for the MCCs than the surface area determined by *n*-butane. This signifies that some of the surface area is not detectable using *n*-butane, which suggests the presence of nano features smaller than the molecular area of *n*-butane ( $0.43 \text{ nm}^2$ ) but larger than the molecular area of nitrogen ( $0.162 \text{ nm}^2$ ).

**Table 4-1** Surface area of minerals determined using BET equation with a relative pressure range up to  $0.03 P / P_0$ .

Mineral	Specific surface area nitrogen ( $\text{m}^2 \text{ g}^{-1}$ )	Specific surface area <i>n</i> -butane ( $\text{m}^2 \text{ g}^{-1}$ )
GCC	$6.25 \pm 0.81$	$6.53 \pm 1.61$
DP MCC	$41.39 \pm 1.37$	$38.64 \pm 1.26$
HSA MCC	$113.15 \pm 4.18$	$95.28 \pm 6.25$

By comparing the pore size distributions calculated using the BJH algorithm for both MCCs it is possible to determine whether the nanopores are surface based, or whether they are hidden additional pore volume with, for example, restricted entry geometry.

The pore size distribution of the DP MCC, calculated using BJH analysis of the desorption branch of the nitrogen and *n*-butane isotherms, is shown in Figure 4-7.

Similarly, Figure 4-8 shows the pore size distribution for HSA MCC.

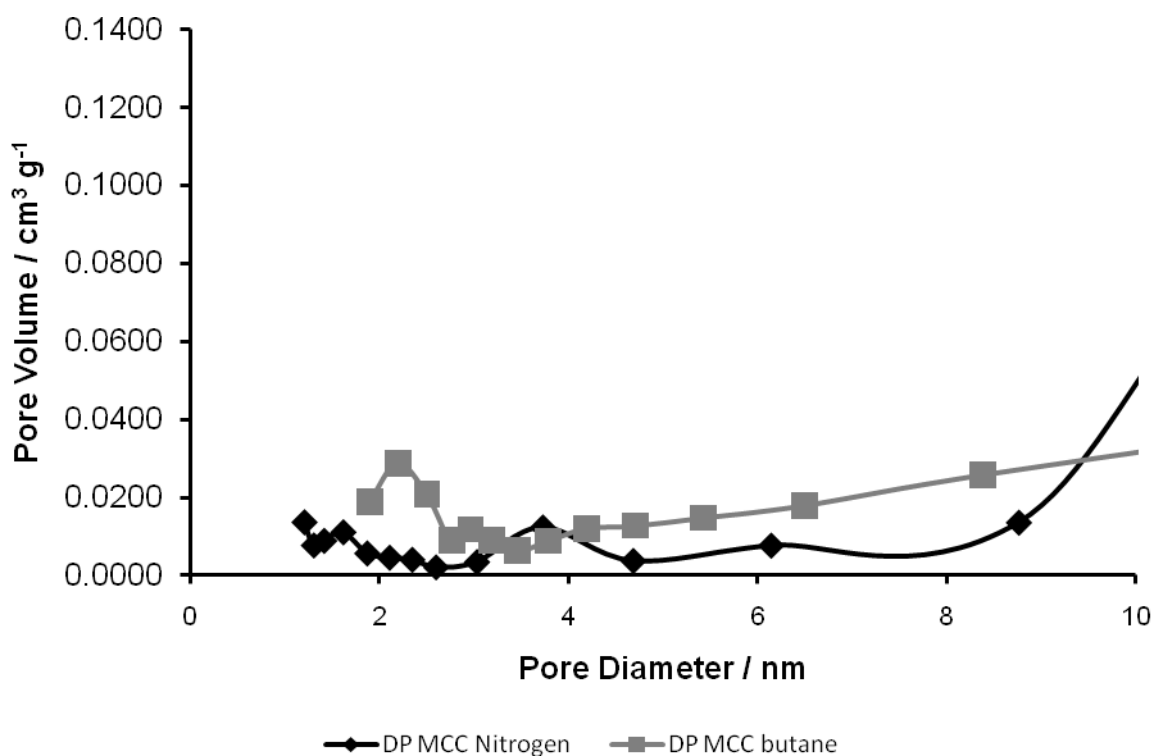


**Figure 4-7** Pore size distribution of DP MCC, determined using the BJH algorithm to analyse the average desorption curve for both adsorbates.

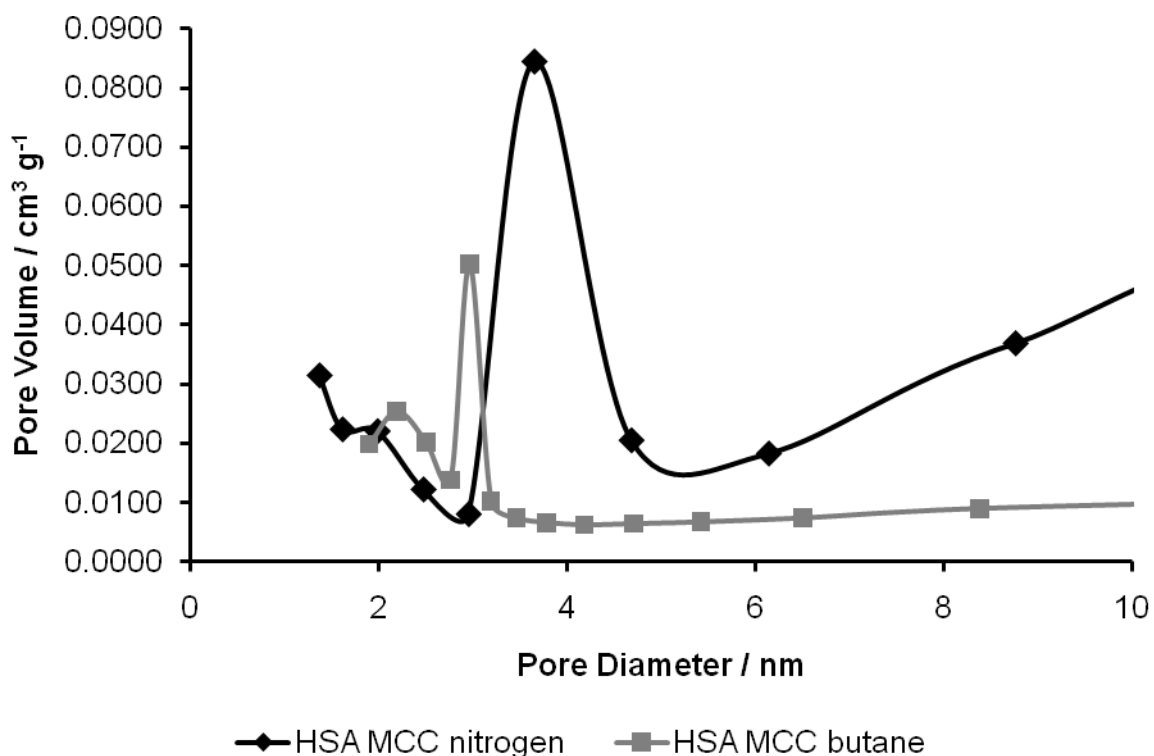


**Figure 4-8** Pore size distribution of HSA MCC, determined using the BJH algorithm to analyse the average desorption curve for both adsorbates.

By comparing Figures 4-7 and 4-8, we can see an increase in available apparent pore volume for the HSA MCC when compared with DP MCC. The total area under the curve is ten times greater for the HSA MCC when compared with DP MCC. The results imply the presence of nanopores for both systems, but in a significantly greater number for the HSA MCC.

The HSA MCC results show a definite peak of pore volume at 3.7 nm for the nitrogen system and 2.9 nm for the *n*-butane system. The peak at 3.7 nm for the nitrogen system could be attributed to a tensile strength effect which forces the hysteresis loop closed (Groen, Peffer *et al.*, 2003). To double check whether it was a tensile strength effect the pore size distribution was calculated using the adsorption branch and a pore size of 2.7 nm was calculated for the HSA MCC, which correlates with the *n*-butane desorption calculation.



The pore areas calculated for the MCCs for every pore size are shown in Figure 4-9 using the desorption branch of the gas adsorption experiment. The results show a significantly increased pore area for the HSA MCC when compared with the DP MCC. The sum of surface areas calculated by the BJH algorithm for the individual pore sizes when compared with the BET surface area can indicate the presence of ink bottle pores, specifically when the BJH total surface area is greater than the BET surface area. The presence of ink bottle pores significantly increases the surface rugosity of the material (Lowell, Shields *et al.*, 2004).

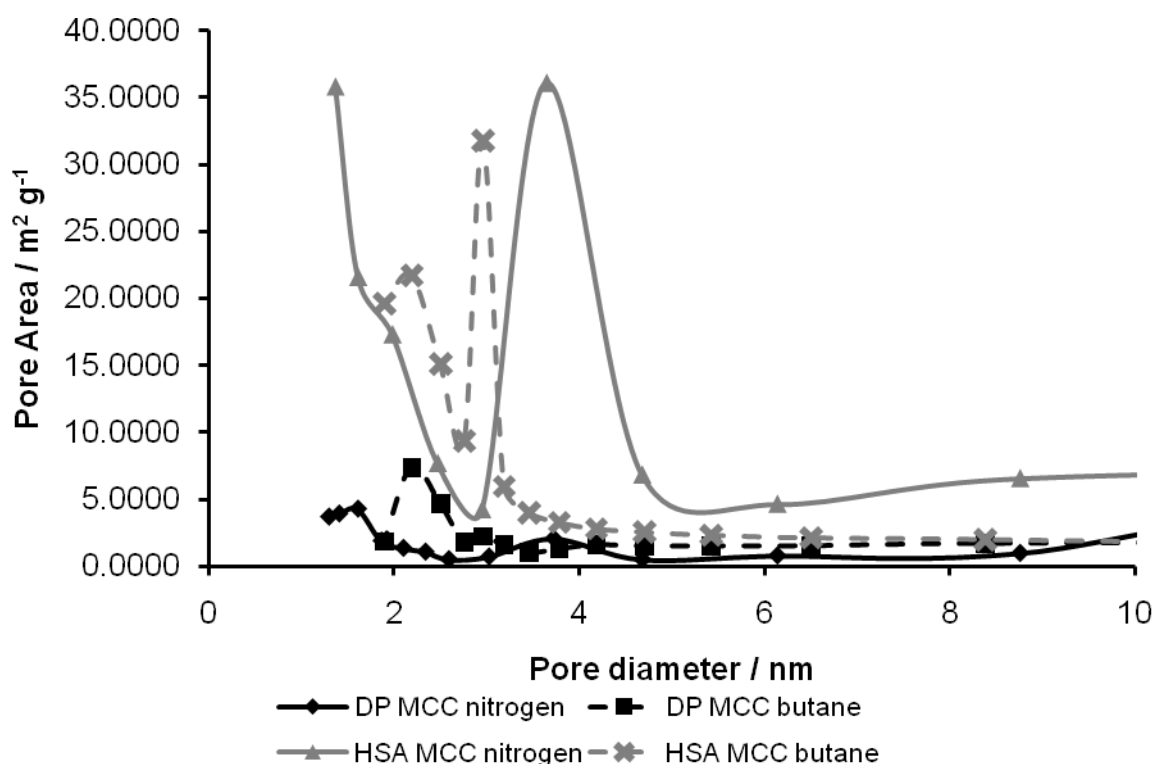


Figure 4-9 Pore area of MCCs determined using the BJH algorithm, with the sum of the individual pore areas being similar to the BET specific surface area.

### 4.3.1 Wetting

The hexadecane wetting and absorption experiment, for the three calcium carbonate samples, shows faster wetting rates for the two MCCs in comparison to the GCC, Figure 4-10. The chart shows the volume of liquid absorbed per unit area of sample,

equivalent to the apparent distance travelled by the wetting front in a single equivalent capillary of unit cross-sectional area, against the square root of time.

Figure 4-10 also shows that the wetting and absorption of the GCC and DP MCC tablets have two distinct phases, a short term absorption rate and a long term absorption rate. GCC and DP MCC calcium carbonate systems show linear trends with respect to the square root of time for the long term absorption rate. The HSA MCC, however, does not show this behaviour but a continuous change of gradient with root time. The calculated long term and short term absorption rates are stated in Table 4-2.

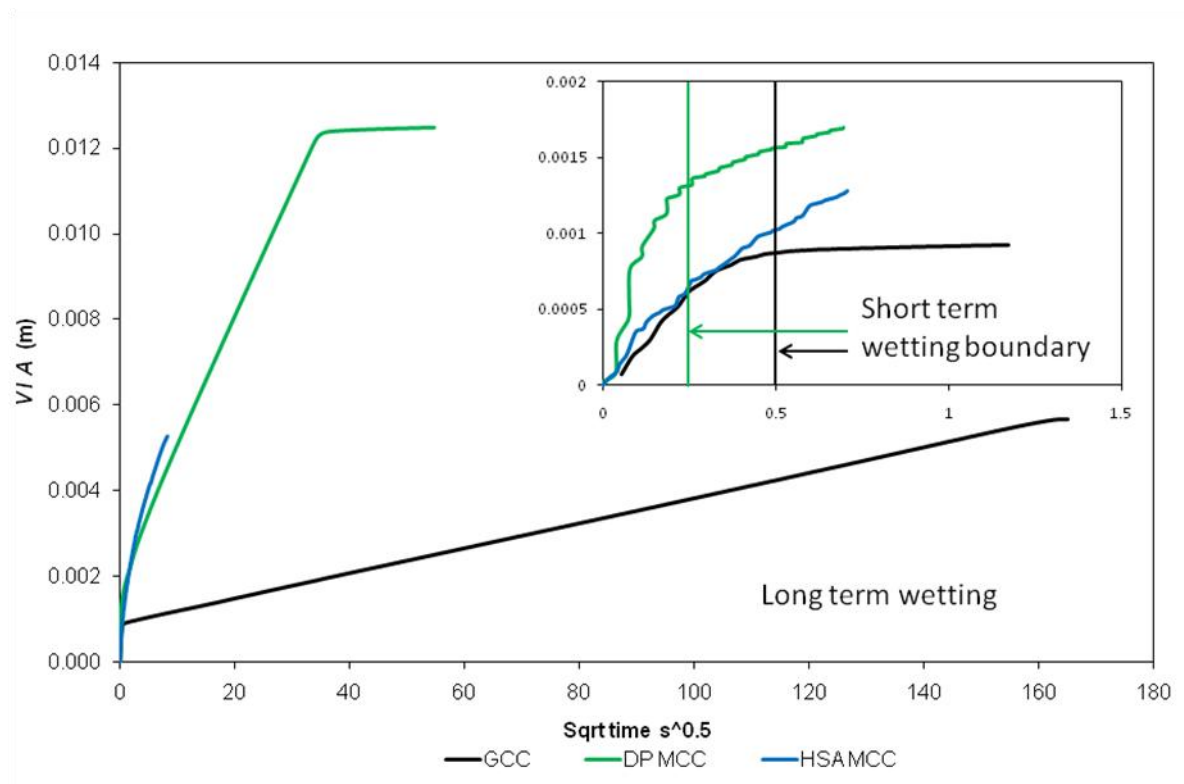


**Figure 4-10. Chart showing differences in absorption behaviour of three calcium carbonate systems.**

Figure 4-10 shows a significant difference between the two absorption phases for the DP MCC and GCC mineral tablets. This reflects the difference between the dual porous nature of the DP MCC and the monomodal pore size distribution of the GCC. Nonetheless, the wetting mechanism in each case is similar in that the separate phases are distinguishable. The wetting of DP MCC is much faster, as expected according to the decoupling theory of the two discrete pore size structures, where absorption is

driven by the intraparticle pore capillarity and resisted by the interparticle permeability (Gane, 2006; Ridgway, Gane *et al.*, 2006). The short term absorption rate is defined by the absorption into the surface accessible finest pore space (intra particle void space), before the larger inter particle void features of the modified calcium carbonates will fill. Such absorption is highly dependent on the inertia of the fluid (Bosanquet, 1923; Schoelkopf, Ridgway *et al.*, 2000; Schoelkopf, Gane *et al.*, 2001). The long term absorption rate is influenced by the balance between the wetting force and the permeable resistance of the structure.

**Table 4-2 Hexadecane absorption rates for the ground calcium carbonate and dual porous modified calcium carbonate. The high surface area modified calcium carbonate is not listed as the curve for the high surface area modified calcium carbonate is not linear with  $t^{0.5}$ , so no continuous gradient can be defined.**

Hexadecane absorption rate $d(V/A)/d(t^{0.5}) / \text{m s}^{-0.5}$	GCC	DP MCC
Short term absorption rate	$2.50 \times 10^{-3}$	$5.53 \times 10^{-3}$
Long term absorption rate	$2.94 \times 10^{-5}$	$3.00 \times 10^{-4}$

In contrast to the other two samples, the HSA MCC shows no clear transition between the absorption phases. This leads to the postulate that the difference in the surface morphology of the HSA MCC makes it behave like a super-wetting material, i.e. wetting at a rate unexpectedly fast compared to the theoretical planar surface meniscus wetting, and faster than would be expected from the absence of internal nanopores as measured by mercury intrusion.

The results from the models propose a surface rugosity present in the pores of the HSA MCC, whereas the DP MCC surface, though not a planar, is only slightly roughened. The postulated differences in surface and void structure of the three minerals are shown schematically in Figure 4-11.

The results of the BET experiment show nanopores which account for an additional  $18 \text{ m}^2 \text{ g}^{-1}$  of specific surface area for the HSA MCC between the size of the nitrogen

molecule and the *n*-butane molecule. A comparison of the BJH surface area with the BET surface area indicates the presence of ink-bottle nanopores for the HSA MCC, i.e. pores with only one connection. Another way of interpreting this information is in terms of surface roughness or rugosity at the nanometre scale.

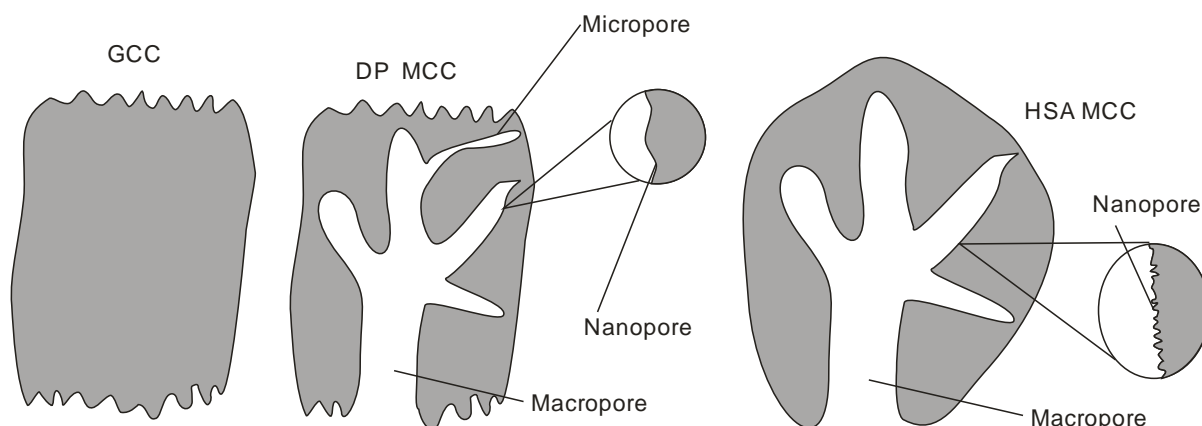


**Figure 4-11** Schematic representation of the differences between the calcium carbonate systems. The GCC has no internal porosity, where both MCC minerals have macropores present. The DP MCC additionally has significant quantities of micropores and the HSA MCC has nanopores and nanorugosity on the surface of its pores.

## 4.4 Conclusion

A super-wetting surface has been identified and proposed as consisting of pore surface nano rugose features, unidentifiable by mercury intrusion, acting to accelerate wetting of a porous packed bed consisting of fine calcium carbonate particles of various surface morphologies. The surface features have been identified and placed within a characterisable size range using two adsorption gases of differing molecular size: nitrogen and *n*-butane, respectively. The mechanism of surface super-wetting is proposed by comparison with a dual porosity structure, where all the pores are identifiable by mercury intrusion porosimetry.

The results show that the long term absorption rate is influenced significantly by the presence of nano features on the surface of the micro and macro pores making up the inter particle pore structure in the HSA MCC. The effect of this is to increase the

surface rugosity, which influences the effective contact angle for wetting, and makes the HSA MCC wet better than expected when compared with another MCC that does not have this additional surface rugosity.

#### **4.4.1 Highlights**

- The differences between two grades of MCC have been explained by using a combination of experimental techniques.
- A super wetting MCC surface has been identified.
- The nano-rugosity of the MCC removes the distinction between the short term and long term wetting rates.

## **5 Use of a zero length column to investigate diffusion and desorption in calcium carbonates.**

This chapter summarises the work undertaken using a ‘zero length’ column (Eic and Ruthven, 1988) to study the diffusion of benzene in cyclohexane inside a porous mineral. The zero length column and experimental methodology were refined to maximise the efficiency of the technique. The zero length column study can be broken down into three distinct stages. The first was the development of the zero length column to prevent the high pressure mobile phase from leaking out during an experiment. The second tested different concentrations of benzene and cyclohexane mixtures to determine the optimum mobile phase concentration for the study of diffusion and desorption of benzene. The second also created a calibration series for converting the detector signal into benzene concentration. The third measured desorption and diffusion coefficients of different grades of calcium carbonate, to determine how they change because of changes in porous and surface structure as discussed in Chapter 4.

There are two main diffusion processes that can occur during a liquid zero length column experiment: bulk diffusion and surface diffusion. Diffusion is the process by which matter is transported from one part of a system to another as a result of random molecular motions down a concentration gradient (Crank, 1975). Bulk diffusion refers to diffusion in the mobile phase only and concentration differences caused by factors which include steric hindrances. Surface diffusion is migration of the species being investigated along the surface of the stationary phase, by jumping between adjacent adsorption sites (Zalc, Reyes *et al.*, 2003). Surface diffusion has a specific activation energy for each system, and is thermally activated. When the surface diffusion activation energy is higher than the activation energy for desorption, desorption will take place preferentially (Atkins and de Paula, 2002; Zalc, Reyes *et al.*, 2003).

## 5.1 Theory

In this study, diffusion and sorption properties of benzene in cyclohexane were investigated with different grades of dual porous calcium carbonate, relative to a ground calcium carbonate with only inter-particle porosity. During the experiment it was possible for benzene to undertake three different processes: intra-particle diffusion, adsorption and desorption. Adsorption and desorption could occur on and from all exposed surfaces of the sample, both on the exterior of a particle, and, in the case of dual porous samples, at the intra-particulate surfaces. Discrimination between the exterior and intra-particle adsorption and desorption would require a technique such as NMR (Preston, Bird *et al.*, 2001), although the discriminative ability can be lost by the necessity of calibration. A full quantitative discrimination is beyond the scope of the present experiment, but can be performed semi-quantitatively by comparing dual porous and particulate samples of the same material, as in the present study. During the experiment both sorption and diffusion processes occur on and within the dual-porous (DP) and high surface area (HSA) modified calcium carbonate (MCC) grades, whereas the ground calcium carbonate (GCC), with no intra-particle porosity, will only have sorption processes occurring.

The development of zero length column theory assumes that the adsorber is well mixed (a continuous stirred-tank reactor), i.e. mathematically (if not physically) identical to a differential plug flow reactor, and leads to the following relation (Brandani and Ruthven, 1995; Duncan and Möller, 2000):

$$\frac{c_s}{c_0} = 2L \sum_{n=1}^{\infty} \frac{\exp\left(-\beta_n^2 \left(D_s / r_s^2\right) t\right)}{\beta_n^2 + \left(1 - L + \gamma_z \beta_n^2\right)^2 + L - 1 + \gamma_z \beta_n^2}$$

Equation 5-1

Here  $c_s$  is the fluid phase sorbate concentration,  $c_0$  is the initial value of the fluid phase sorbate concentration,  $L$  is a dimensionless zero length column parameter defined by Equation 5-2,  $\beta_n$  is the dimensionless root of Equation 5-4,  $D_s$  is the diffusion coefficient,  $r_s$  is the radius of the sorbent particle,  $t$  is the time and  $\gamma_z$  is the dimensionless parameter defined by Equation 5-3.

$$L = \frac{F_m r_s^2}{3 V_s K_H d_s}$$

**Equation 5-2**

Here  $F_m$  is the volumetric flow rate of the mobile phase,  $V_s$  is the volume of sorbent in the zero length column bed,  $K_H$  is the Henry constant of adsorption, and  $V_f$  is the volume of interstitial fluid in bed.

$$\gamma_z = \frac{V_f}{3 V_s K_H}$$

**Equation 5-3**

$\beta_n$  in Equation 5-1 is given by the roots of

$$\beta_n \cot \beta_n + L - 1 - \gamma_z \beta_n^2 = 0$$

**Equation 5-4**

Negligible fluid hold up ( $\gamma_z = 0$ ) leads to the following standard relation for the desorption curve:

$$\frac{c_s}{c_0} = 2L \sum_{n=1}^{\infty} \frac{\exp\left(-\beta_n^2 \left(D_s/r_s^2\right)t\right)}{\beta_n^2 + (L(L-1))}$$

**Equation 5-5**

with  $\beta_n$  now given by



$$\beta_n \cot \beta_n + L - 1 = 0$$

Equation 5-6

A semilogarithmic plot of normalised concentration versus time allows the parameters  $(D_s/r_s^2)$  and  $L$  to be obtained from the gradient and intercept respectively from the linear desorption region (Duncan and Möller, 2000).  $L$  may be interpreted as the ratio of a characteristic diffusion time  $(r_s^2/D_s)$  to a convection/adsorption time  $(V_s K_H / F_m)$  (Ruthven and Brandani, 1997).

### 5.1.1 Pore-Cor Research Suite modelling

The mercury porosimetry results were corrected for compressibility and blank porosimetry run, according to the method proposed by Gane et al. (Gane, Kettle *et al.*, 1996) and explained in Section 1.3.1.7. These results were modelled using Pore-Cor RS using an annealed simplex (Press, Flannery *et al.*, 1986b; Johnson, Roy *et al.*, 2003). The annealed simplex fits a Euler-Beta function of void sizes to the mercury porosimetry results, explained in detail in Section 1.3.1.6. Pore-Cor RS generates a 3D representation (unit cell) of DP MCC's internal structure. The unit cell can be used for simulations of diffusion, as was explained in Section 1.3.1.8.

Diffusion out of the unit cell for the dual porous modified calcium carbonate (DP MCC) and high surface area modified calcium carbonate (HSA MCC) was simulated using the built in diffusion algorithm, with the free molecular diffusion coefficient, calculated using the Einstein-Stokes equation, Equation 1-42 (Laudone, Matthews *et al.*, 2008). The Einstein-Stokes equation is an approximation which is frequently adopted. Pore-Cor RS only simulates bulk diffusion of the benzene out of the unit cell, and does not consider any sorption processes or surface diffusion.

## ***5.2 Methodology***

The zero length column technique involves sandwiching a thin layer or ‘zero length’ of stationary phase between two stainless steel sinters. Then a mobile phase is pumped through the sinter and stationary phase to determine the interaction between stationary and mobile phase. Benzene in cyclohexane was selected as the sorbate-solvent system because the aromatic nature of benzene yields a high sensitivity with a UV detector.

### **5.2.1 Refinement of the zero length column design**

The first experiment involved testing the zero length column to ensure it did not leak and that the mobile phase flowed through the sinter. Figure 5-1 is a photograph of the first zero length column tested with a HPLC system. The stainless steel sinter in this design is resin-embedded within an empty chromatography column tube. The design was changed because the mobile phase flowed around the edges of the sinter, and did not provide a laminar flow. To correct the lack of flow of mobile phase through the sinter, the shape of the sinter was changed to a cylindrical shape that was silver-soldered into the chromatography column tube. The sinter properties were changed from a sinter with a uniform pore size to a bimodal sinter, to reduce the pressure required to pump the mobile phase through the zero length column. The characterisation of pore size distribution of the two sinters was described in Chapter 3. To ensure a good seal of the two halves of the zero length column, an O-ring was added.



**Figure 5-1 Photograph of the initial design of the zero length column used in this investigation.**

Figure 5-2 shows a cross-sectional schematic of the zero length cell. Figure 5-3 shows how the mobile phase interacts with the stationary phase and how it flows through the zero length column. In this investigation, the design of the zero length column has been optimised for liquid systems by shaping the entry and exit channels to minimise dead space. The redesigned zero length column allows an effective monolayer of material to be sandwiched between two fine stainless steel sinters (approximately 1  $\mu\text{m}$  pore size). We assume the flow is laminar through the zero length column. The volume of the zero length column through which the mobile phase flows is 1.3  $\text{cm}^3$ .

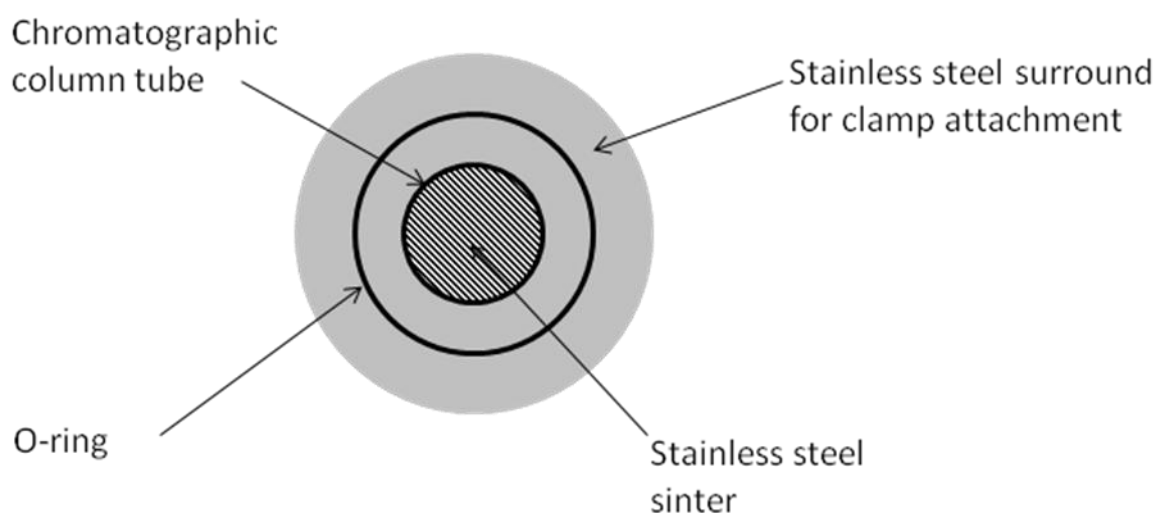


**Figure 5-2** Cross sectional schematic of zero length column. Not to Scale

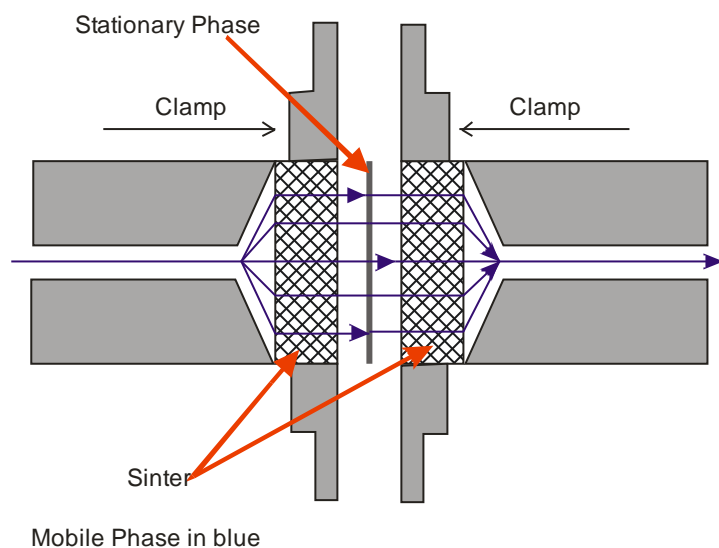


**Figure 5-3** An exploded schematic of the zero length column, showing how the sample (stationary phase) interacts with the mobile phase. Not to scale

The design of the zero length column allows one to assume that the concentration at the surface of each particle is the same as in the bulk mobile phase (Brandani and Ruthven, 1995).

A photo of the assembled zero length column is shown in Figure 5-4.

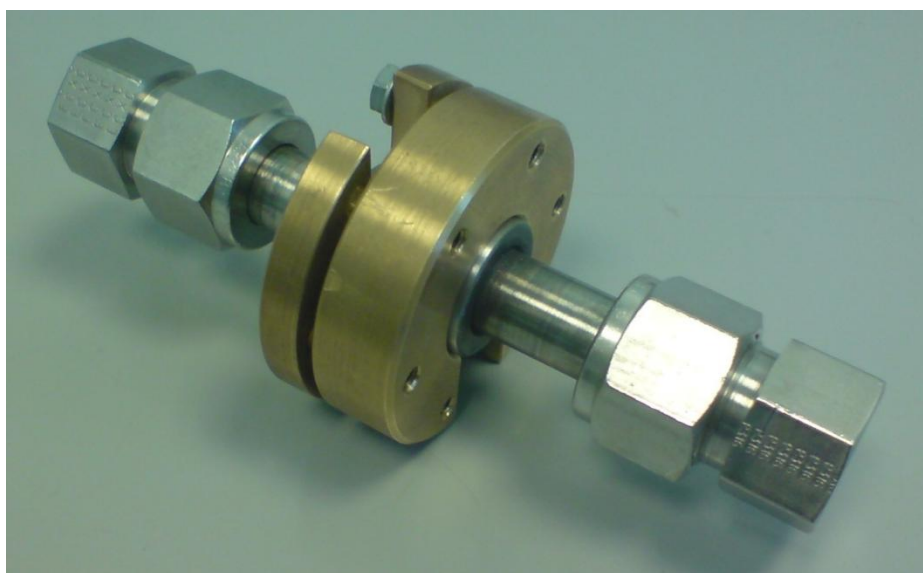


**Figure 5-4** Photograph of final constructed zero length column. The internal diameter of the entry and exit tubes is 0.12mm.

## 5.2.2 Materials

The investigation tested three different calcium carbonate grades to see how desorption and diffusion differ for the different grades. The modified calcium carbonate slurries were freeze dried to form a powder that was used for testing with the zero length column. The calcium carbonates were all supplied by Omya Development AG. The first calcium carbonate was a ground calcium carbonate, with no internal porosity. The second sample was a modified calcium carbonate with macro and micro porosity, as determined by mercury porosimetry. The third sample was another modified calcium carbonate with macro, meso and nano porosity as determined by mercury porosimetry and gas sorption. The mineral properties are summarised in

Table 5-1. The techniques used for characterisation of the minerals were explained in Section 2.1.4 and Section 2.3.1. The characterisation of the modified calcium carbonates using mercury porosimetry and gas sorption was covered in Chapter 4.

**Table 5-1 Properties of minerals used during investigation.**

Name	Specific surface area ( $\text{m}^2 \text{g}^{-1}$ )	Particle Size-Weight Distribution* ( $\mu\text{m}$ )		
		$d_{10}$	$d_{50}$	$d_{90}$
Ground calcium carbonate (GCC)	1.53	1.51	7.70	20.3
Dual porous modified calcium carbonate (DP MCC)	36.1	2.55	5.49	9.85
High surface area modified calcium carbonate (HSA MCC)	113	1.82	4.26	9.37

\*  $d_N$  represents the particle diameter for which  $N$  % of the sample mass has particles finer than  $d$ .

## 5.2.3 Instrumentation

An HP 1050 HPLC system, with quaternary pump and UV detector using a wavelength of 230 nm, was used for all the experiments. A flow rate of  $0.5 \text{ cm}^3 \text{ min}^{-1}$  was the flow rate used for all investigations. It was the highest flow rate that could be used while

being certain that the pump would not cut out because of exceeding the maximum pressure.

#### **5.2.4 Fluids**

The benzene and cyclohexane were both HPLC grade, sourced from Sigma-Aldrich and Thermo-Fisher scientific respectively. All mobile phase solutions were degassed prior to use for a minimum of 15 minutes.

#### **5.2.5 Detector calibration**

The zero length column was loaded with 4 – 5 mg of the ground calcium carbonate. A Hewlett Packard 1050 HPLC (Agilent Technologies USA) system was used to measure the concentration of benzene flowing through a UV/VIS detector at 230 nm, with a 2.5 s integration time. Then the liquid mixture was pumped through a blank ZLC, at concentrations of benzene in cyclohexane from 0 to 100 g dm<sup>-3</sup>. The response from the detector was monitored to find its range of response, which was found to be up to 20 g dm<sup>-3</sup>. Experiments over this range were used to construct a calibration graph. Each experiment was run in triplicate. The calibration graph is shown in Figure 5-5, with linear correlation  $R^2 = 0.996$ .

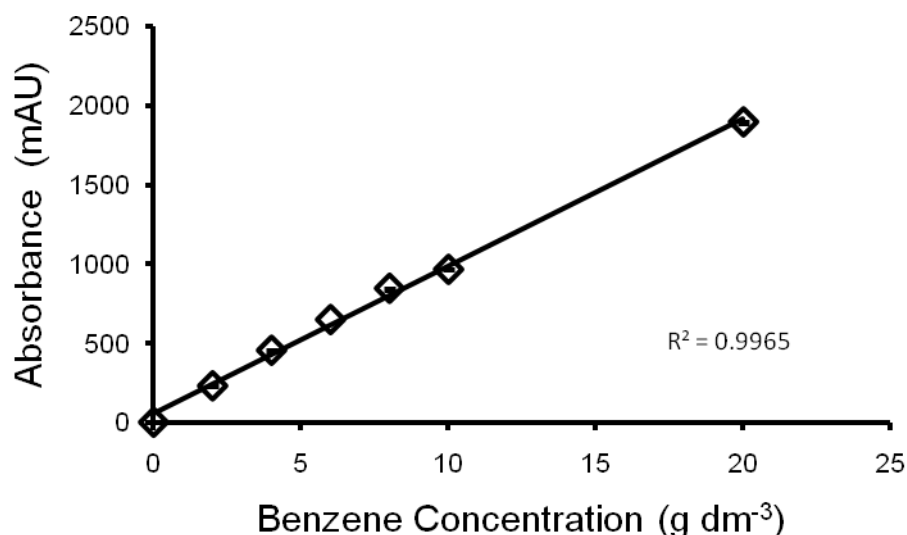


Figure 5-5 Zero length column calibration curve for benzene concentration. The error bars represent two times the standard deviation from three replicates.

### 5.3 Method for diffusion and sorption studies

The experiment started with the zero length column mobile and stationary phase equilibrating at 20 g of benzene per dm<sup>3</sup> of cyclohexane (2.27% v/v) for 30 min. Then the concentration of benzene ( $c_s$ ) was changed to 0 g per dm<sup>3</sup> over a period of 6 s. The benzene in cyclohexane concentration remained at 0 g dm<sup>-3</sup> for a total of 60 min, and then the concentration of benzene in cyclohexane was increased to 20 g dm<sup>-3</sup> over a 6 s period. The experiment continued for a further 30 minute period. This experiment was replicated twice for both the blank and mineral experiments.

Every data set for the systems was partially smoothed to remove undetermined signal noise, using the exponential centre-weighted moving-average formula given in Equation 5-7. as illustrated in Figure 5-6.

$$y_{i\_smooth} = \frac{(y_{i-2}) + 2(y_{i-1}) + 4y_i + 2(y_{i+1}) + (y_{i+2})}{10}$$

Equation 5-7

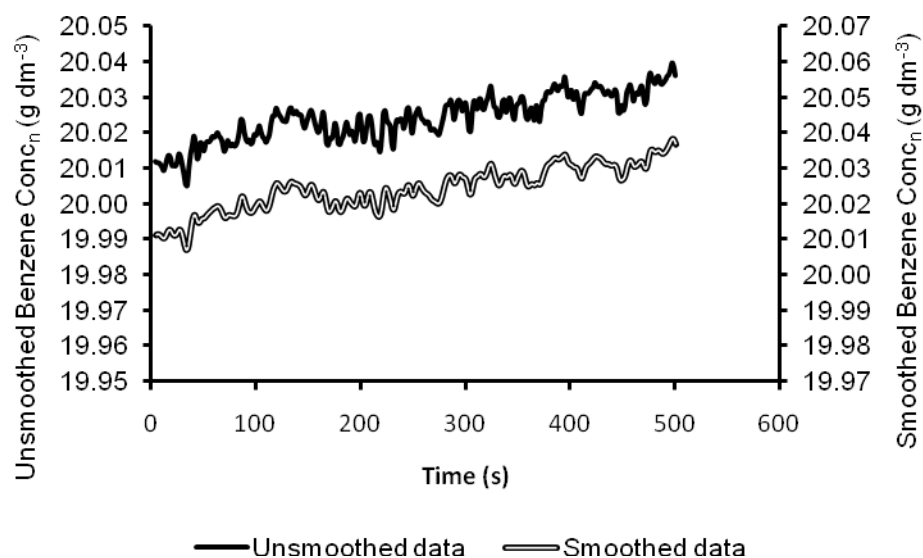


Figure 5-6 Graph showing the justification for using a centrally weighted moving average function on a section of raw concentration data. For clarity, the smoothed data has been displaced downwards, as shown by the secondary axis.

The partially smoothed data were then averaged across the three replicates. To obtain a meaningful average, the nominal start times were displaced so that the data superimposed on each other with respect to the actual experiment start time as described in Section 5.5.2 below. The data was then used to ascertain parameters relating to the desorption and diffusion of benzene for the calcium carbonate systems.

### ***5.4 Computer modelling of diffusion***

A computer simulation of diffusion was performed for both modified calcium carbonate samples. The simulation was described in Section 1.3.1.8. The simulation started with a benzene in cyclohexane concentration of  $20 \text{ g dm}^{-3}$  and was diffused out of the unit cell for 10 000 s. The free molecular diffusion coefficient calculated using the Einstein-Stokes equation was  $1.74 \times 10^{-9} \text{ m}^2 \text{ s}^{-1}$ .



## ***5.5 Results and discussion***

### **5.5.1 Qualitative results**

The desorption and diffusion experiment results from the zero length column for all the systems are shown in Figure 5-7. The results for the blank show how the zero length column concentration changes against time and shows the greatest change in benzene concentration. The GCC shows a change in benzene concentration from 20.3 to 1.03 g dm<sup>-3</sup> compared with 20.5 to 1.62 g dm<sup>-3</sup> for HSA MCC and 20.3 to 1.50 g dm<sup>-3</sup> for the DP MCC. The differences between the blank and calcium carbonate systems can be explained by the interactions between benzene and the calcium carbonate systems which do not occur with the stainless steel sinter.

The GCC was non-porous. Therefore there was no intraparticle porosity for diffusion, and the only interaction seen between the GCC and benzene was desorption of the benzene. The GCC results are able to provide quantitative and qualitative information about desorption of benzene from the surface of calcium carbonate. The results imply that desorption of benzene is quicker than diffusion from the intra particle porosity, because the gradient of the desorption curve is steeper for the GCC than either of the MCC grades, whereas if desorption was the rate limiting step the gradients would be identical.

The MCC grades were both porous, as explained earlier, with both grades having macro pores of a similar magnitude and volume according to mercury porosimetry, Figure 4-6. The DP MCC also had a significant volume of micro pores which the HSA MCC did not have. Therefore, we assume the benzene will diffuse slowly in the DP MCC because of the micro porosity. The HSA MCC also has nano-rugosity and nano-porosity, and we do not know how this will affect the diffusion and desorption of benzene relative to the DP MCC. Figure 5-7 shows that the HSA MCC diffuses more slowly than the DP

MCC, which implies diffusion of benzene from the HSA MCC is affected by its macro porosity and nano features as discussed in Chapter 4.

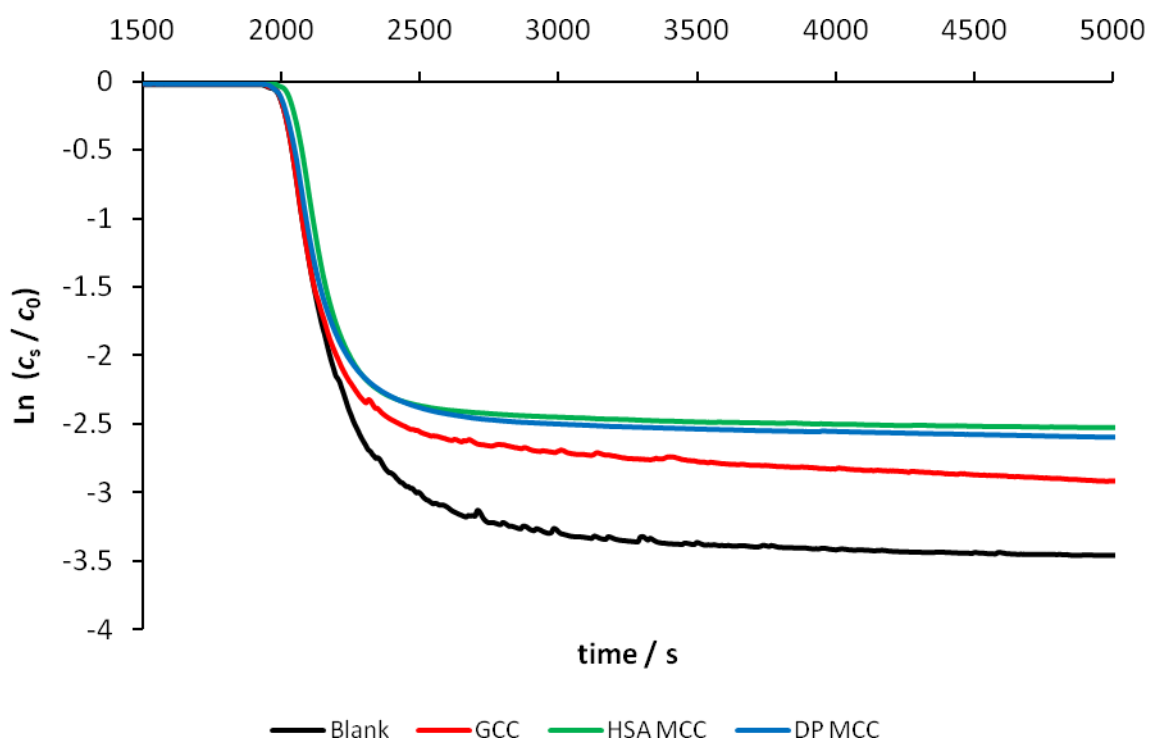


Figure 5-7 Graph of the zero length column results of time versus the natural log of the benzene concentration divided by the initial benzene concentration. The data presented is average data obtained from a minimum of three replicates.

### 5.5.2 Quantitative analysis of results.

By adjusting the x-axis so the switchover point from  $20 \text{ g dm}^{-3}$  to  $0 \text{ g dm}^{-3}$  of benzene in cyclohexane becomes the origin, the gradients and intercepts of the linear region of the desorption curve provides values for  $(D_s/r_s^2)$  and  $L$  respectively, Equation 5-1 and Equation 5-2. All the linear regions have an  $R^2$  greater than 0.96. The diffusion and desorption coefficient calculated are shown in Table 5-2 and can be compared with the Fickian diffusion coefficient  $1.74 \times 10^{-9} \text{ m}^2 \text{ s}^{-1}$  used in the simulation.

**Table 5-2 Table of gradient and intercept values calculated using the linear region of the desorption curve.**

	<b>Blank</b>	<b>GCC</b>	<b>DP MCC</b>	<b>HSA MCC</b>
<b>Gradient</b> ( $D_s / r_s^2$ )	9.90 x 10 <sup>-1</sup>	9.90 x 10 <sup>-1</sup>	9.90 x 10 <sup>-1</sup>	9.91 x 10 <sup>-1</sup>
<b>Intercept</b> ( $L$ )	4.85	6.17	5.65	6.70
<b>Desorption and diffusion coefficient</b> / m <sup>2</sup> s <sup>-1</sup>	n/a	1.47 x 10 <sup>-11</sup>	7.46 x 10 <sup>-12</sup>	4.49 x 10 <sup>-12</sup>

The desorption and diffusion coefficients calculated for the calcium carbonate systems show that as the void structure complexity increases, the diffusion rate decreases. Therefore, the differences detected by the zero length column can be attributed to the rugosity and porosity of the MCCs.

The dimensionless zero length column parameter ( $L$ ) calculated from our data is shown in Table 5-2 for all systems. The value of  $L$  provides information about the operating parameters of the zero length column (Zabka and Rodrigues, 2007). When the value of  $L > 1$  as in our experiments, it informs us that the flow rate of mobile phase is large enough to ensure transport rather than equilibrium control (Brandani, Xu *et al.*, 1996). Equilibrium control occurs when the mobile phase flow rate is too low and subsequently the diffusion of the species being investigated is slowed significantly, because the concentration gradient is not maximised at all times.

### 5.5.3 Pore-Cor RS diffusion simulation

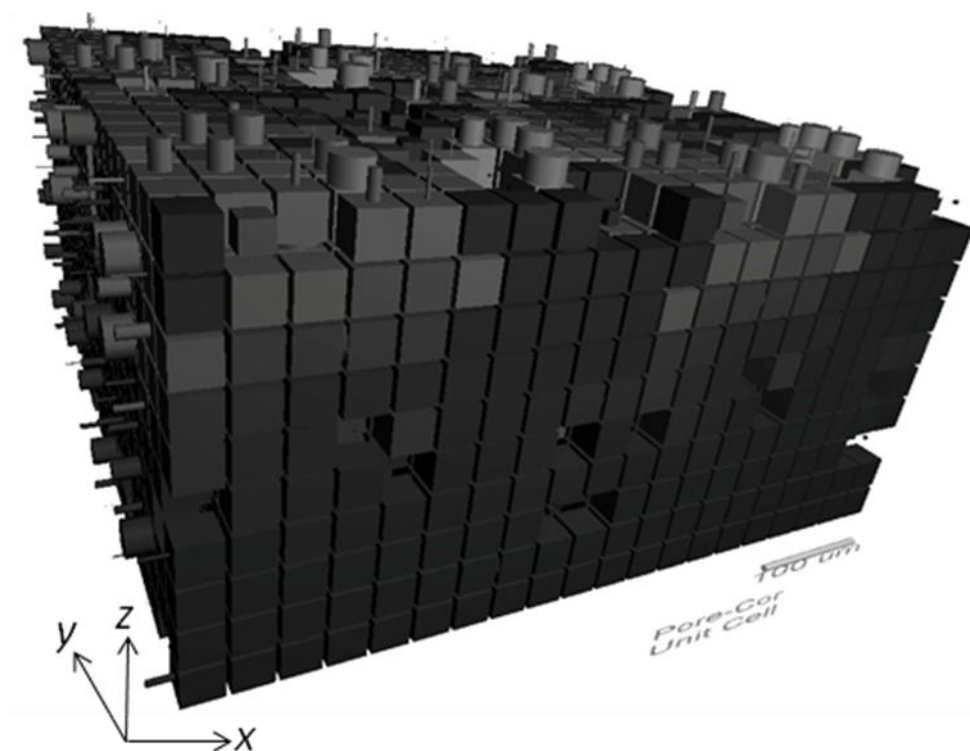


**Figure 5-8** Three dimensional representation of DP MCC after 100 seconds of diffusion has taken place. The cubes represent pores in the sample and the cylinders represent throats connecting the pores. With the  $x$ ,  $y$  and  $z$  axes identified.

The modelling of the experimental mercury porosimetry data for DP-MCC by Pore-Cor RS generated a unit cell, Figure 5-8, with the same percolation characteristics as determined experimentally. The model can be used to provide characteristics of the unit cell. One of the key characteristics is pore row spacing, i.e. the distance between each row of pore features in the unit cell. The parameter is used to calculate the exposed surface area of the unit cell, so that the diffusion simulation results can be scaled to match the experimental envelope surface area of DP MCC and HSA MCC. The experimental stationary phase has a specific envelope surface area, i.e. the total surface area of the particles ignoring the intraparticle features. The simulation and experimental envelope surface areas need to correspond to allow a direct comparison of results. Figure 5-8 also shows the extent of diffusion from the unit cell. In Figure 5-8 the dark grey features in the unit cell are saturated with benzene. The features are shown

progressively lighter as benzene diffuses from them, as seen on the surface of the DP MCC in Figure 5-8. The model can also model diffusion into the unit cell, although in this investigation it is not considered.

The diffusion simulation results are shown in Figure 5-9 for the DP MCC and HSA MCC. The simulations show that it is easier for benzene to diffuse from the HSA MCC than the DP MCC during the experimental timescale. The DP MCC has over 10 times the benzene concentration at the end of the simulation when compared with the HSA MCC. The DP MCC has macro and micro porosity, whereas the HSA MCC has macro porosity with minimal micro porosity. Consequently, the diffusion in the DP MCC is slowed by the micro porous void features (pores and throats), because the diffusion is proportional to the diameter of the throats, and the smaller features provide greater steric hindrance. The simulation overestimates the diffusion from the system with respect to the experiment. The simulation only considers bulk diffusion, and the rate of diffusion is increased by surface diffusion and decreased by adsorption and desorption of benzene onto the surface (Laudone, Matthews *et al.*, 2008).

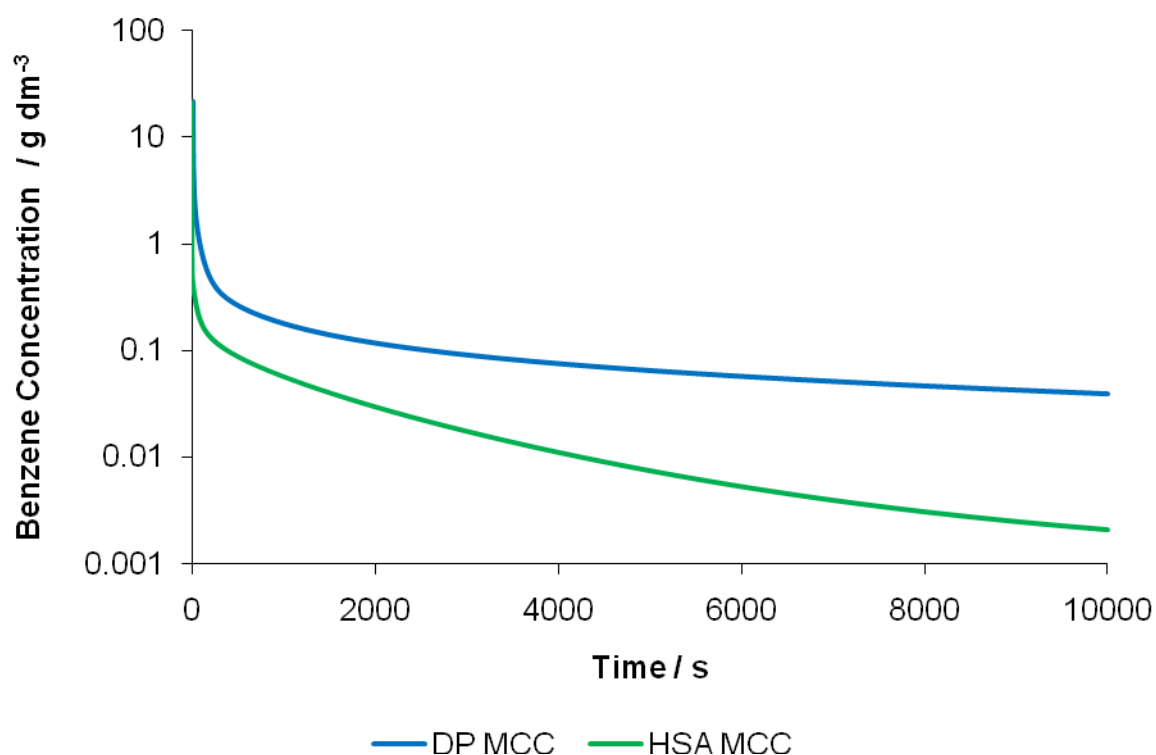


**Figure 5-9** Graph showing the differences in bulk diffusion rate for the two different modified calcium carbonate grades, simulated using the diffusion algorithm of Pore-Cor RS.

The simulation is very useful in determining a theoretical diffusion curve which does not consider any surface diffusion or sorption processes interacting with the stationary phase. The simulation results for the DP MCC after one hour provide a benzene concentration of  $0.08 \text{ g dm}^{-3}$ , whereas the minimum experimental concentration was  $1.49 \text{ g dm}^{-3}$ . A weakness of the model is the simplicity of the unit cell when compared with a real system and the effect this will have on the rate of diffusion.

The comparison between the simulation and experiment highlights the need to consider surface diffusion, adsorption and desorption behaviour of benzene with the stationary phase when simulating diffusion. It also shows the need for a model to have pore features that correspond to the entire pore size distribution by combining techniques to allow full characterisation of the surface and internal structure. The simulation is not able to take account of any differences in surface chemistry which will affect the diffusion rate. The zero length column experiment used a non-polar adsorbate (benzene)

interacting with a polar stationary phase (calcium carbonate). The different phases reduce the strength of the interaction between adsorbate and stationary phase, which makes surface diffusion less favourable but does not completely eliminate it. Surface diffusion is also influenced by the total surface area (i.e. not envelope surface area which excludes intraparticle surface area). An increased surface area allows more surface diffusion and sorption processes to occur, which the simplified model cannot represent. The model produces smooth internal surfaces, which we know from Chapter 4 is not a realistic method of representing the internal structure.

## ***5.6 Conclusions***

In conclusion the zero length column is a sensitive technique that can be used to investigate diffusion and desorption of systems. The zero length column technique provided possible supporting evidence for the surface rugosity of the HSA MCC, because of the disagreement with the simulation differences in the intraparticle micro- and nano-porosity that influence the diffusion rate of benzene with HSA MCC. The results also highlight the effect adsorption and desorption of benzene on the surface of the calcium carbonate has on the rate of diffusion compared with a simulation that only considers bulk diffusion. The results provide evidence on how the diffusion simulation can be improved by considering additional types of diffusion that can take place, and the need to include surface rugosity in the model.

### **5.6.1 Highlights**

- Development of a working zero length column for liquid systems.
- Comparison of experimental results with a simulation of diffusion.
- Development of the model is required to include surface effects within the model of diffusion.
- Zero length column results supported the presence of nano rugosity on the surface of HSA MCC.



## **6 Equilibrium coefficients for the adsorption of colloidal stickies onto mineral suspensions to improve paper recycling**

### ***6.1 Introduction***

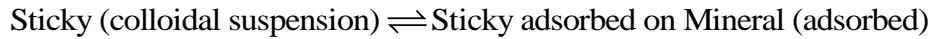
The work in this chapter is divided into two distinct parts with significant overlap between the two in respect to methodology. The first set of results compares different experimental techniques for measuring the concentration of stickies indirectly, and provides the means for an assessment of whether any of these techniques could generate equilibrium adsorption constants in an industrial setting. The second part is the measurement and interpretation of the equilibrium constants of different sticky compounds adsorbed onto different minerals. The interpretation of the equilibrium constants requires a consideration of the molecular structure of the sticky and surface chemistry of the mineral particle.

We have measured the equilibrium constant for the adsorption of model stickies onto selected minerals – namely talc, modified calcium carbonate, and bentonite – in the special case where the adsorbent mineral is maintained in excess in relation to the model sticky adsorbed on the surface and/or in suspension. The determination of equilibrium for the different mixtures of mineral and sticky provides information on whether the sticky remains in colloidal suspension or adsorbs onto the surface of the mineral, and is therefore a means of describing the efficacy of a chosen mineral for stickies control. The measurements of these equilibria are complicated by the fact that the species are colloidal both before and possibly after, adsorption. We assess the accuracy and applicability of a range of experimental techniques, namely dissolved oxygen concentration (DOC), turbidity, chemical oxygen demand (COD), gravimetric, total

dissolved nitrogen (TDN) and elemental analysis. Similar methods were employed by Gantenbein *et al.* for the assessment of wood pitch adsorption on talc (Gantenbein, Schoelkopf *et al.*, 2009). Wood pitch is the tacky product derived from wood resin. Stickies, however, are less easily defined and characterised than wood pitch, as they can have partially retained surfactant and charge stabilisation arising from their original product form, as delivered in water suspension. This current work is an extension of that reported by Benecke *et al.*, who used turbidity, chemical oxygen demand and gravimetric techniques for the measurement of adsorption of stickies (Benecke, Gantenbein *et al.*, 2009).

### 6.1.1 Background theory

The adsorption equilibrium is defined by the balance between concentrations of sticky in suspension and concentrations of sticky on the particle surface:

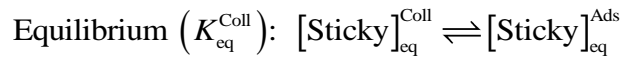


which we write, in abbreviated form, as

$$[\text{Sticky}]^{\text{Coll}} \rightleftharpoons [\text{Sticky}]^{\text{Ads}}.$$

**Equation 6-1**

At the start, the concentrations are  $[\text{Sticky}]_0^{\text{Coll}} + [\text{Mineral}]^{\text{Susp}}$  where  $[\text{Sticky}]_0^{\text{Coll}}$  is determined by the amount of sticky added at the beginning of the experiment and  $[\text{Mineral}]^{\text{Susp}}$  is determined by the mineral concentration during the experiment. The extent of movement toward equilibrium is initially zero, such that  $[\text{Sticky}]_0^{\text{Ads}}$  is zero. On mixing the sticky and mineral suspension, an equilibrium is set up:



**Equation 6-2**

The equilibrium constant for the adsorption, is:

$$K_{\text{eq}}^{\text{Coll}} = \frac{[\text{Sticky}]_{\text{eq}}^{\text{Ads}}}{[\text{Sticky}]_{\text{eq}}^{\text{Coll}}}$$

**Equation 6-3**

This equilibrium constant does not involve  $[\text{Mineral}]^{\text{Susp}}$ , which was in excess. The exclusion of this term was justified experimentally as described below in Section 6.3.

Figure 6-1 shows schematically how adsorption might change if  $[\text{Mineral}]^{\text{Susp}}$  is changed even further. In Figure 6-1a and 6-1b the mineral is in excess and the adsorption behaviour is controlled by the sticky concentration in colloidal suspension and that adsorbed onto the surface. The adsorption behaviour for Figure 6-1b may not equal Figure 6-1a, because of adsorbate-adsorbate interactions, shown as  $\leftrightarrow$  in Figure 6-1b. Figure 6-1c illustrates alteration of the equilibrium by chemical or physical perturbation. Figure 6-1d shows the adsorption behaviour when the sticky is in excess, with sorption entirely controlled by the mineral concentration. In this investigation, all sticky and mineral suspensions have the mineral in excess, as in Figure 6-1a.

## Schematic of the effects influencing the observed $K_{eq}$

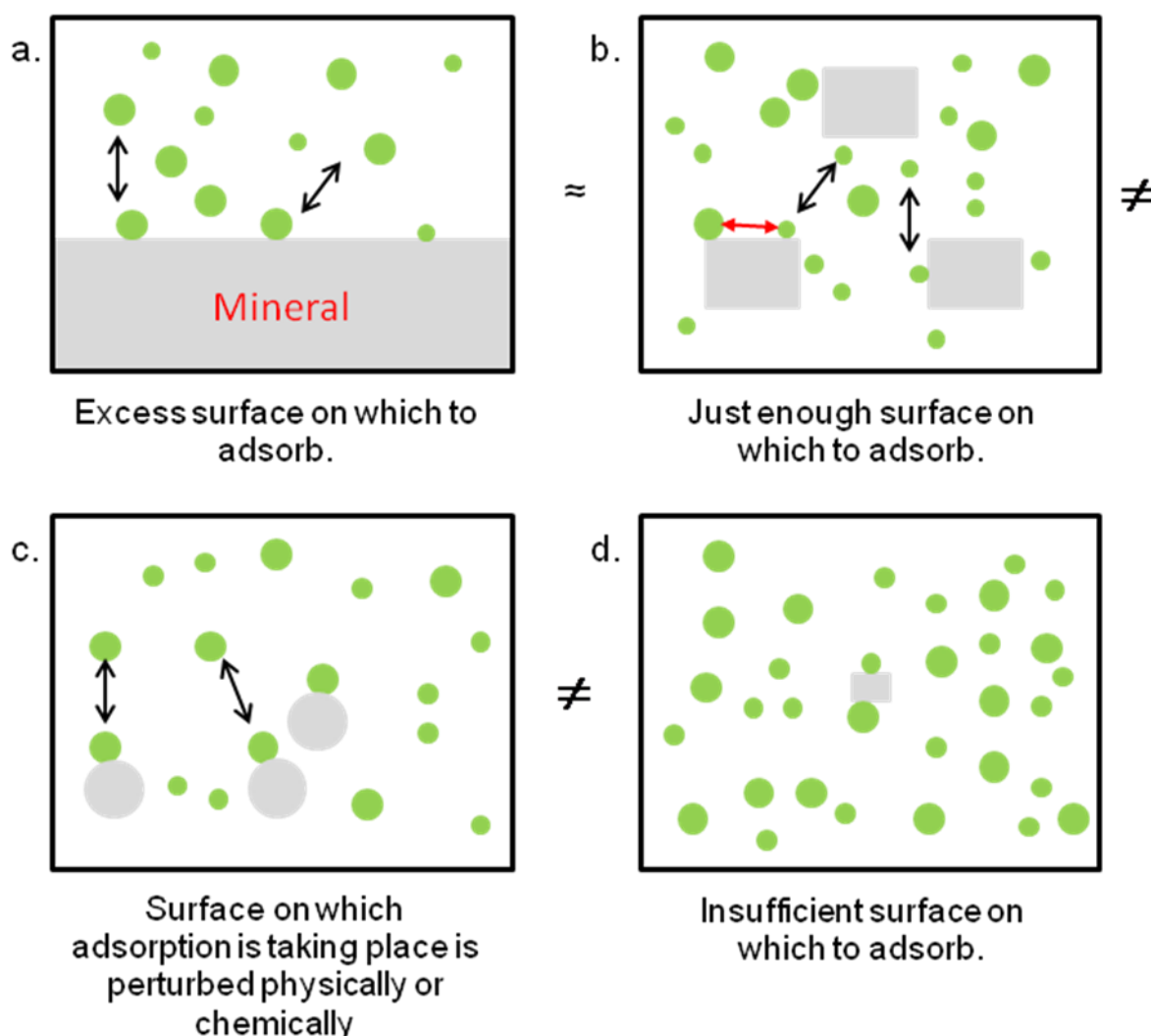


Figure 6-1 Schematic highlighting how the equilibrium adsorption behaviour is modified by mineral concentration.

The experimental methods employed either measure the aqueous concentration or adsorbed concentration of sticky. When measuring the aqueous concentration, mass balance can be used to determine the adsorbed concentration. Mass balance cannot be used to determine the aqueous concentration from the adsorbed concentration because a calibration series cannot be constructed using the adsorbed concentration.

The aqueous concentration can be determined by using a calibration series of reference sticky concentrations for the experimental techniques to convert back to sticky concentration. When determining the aqueous concentration, we assume the mineral and

sticky adsorbed onto mineral is completely removed by centrifugation. We also assume the mineral particle size does not affect the adsorption behaviour as the mineral is in excess.

The adsorbed concentration is determined by measuring the carbon content of the mineral before and after adsorption, having adopted a suitable separation technique for the mineral from the host suspension. The measurements assume uniform adsorption behaviour onto the mineral, i.e. Figure 6-1a rather than Figure 6-1b. The measurements are corrected for the initial carbon content of the mineral, so the additional carbon content is associated only with the sticky concentration on the surface.

## 6.2 Experimental

### 6.2.1 Materials and minerals

The artificial stickies used are commercially available analogues of typical products found to contribute to stickies found in a paper mill, and are listed in Table 6-1. For those components obtained as a suspension, the solids contents reported have been measured experimentally, by evaporating the suspension at 130 °C and measuring the weight change.

**Table 6-1 Stickies used in investigation**

<b>Illustrative Sticky</b>	<b>Product name</b>	<b>Supplier</b>	<b>Solids Content (%)</b>
Acrylic acid ester copolymer	Acronal V 212	BASF	68.29 %
Alkyldiphenyloxide disulphonate	Dowfax 2A1	DOW Corning	45.00 %
Colophonium resin	Colophonium	Resina AG	Not applicable
Fatty acid ester defoamer	Afranil RS	BASF	30.31 %
Mineral oil / silicone defoamer	Agitan 700	Münzing Chemie	83.61 %
Polyvinyl acetate	Vinnapas B 17	Wacker	Not applicable
Styrene-butadiene latex	Styronal D 809	BASF	53.21 %

The minerals used in this investigation, as described previously in Chapter 1, are talc, MCC and bentonite. All of the minerals used in the investigation have been used in paper manufacture either as a paper coating pigment or filler, and all are commercially available.

The talc was obtained as undispersed talc from Mondo Minerals, Finland<sup>2</sup> (Finntalc PO5). The Finntalc was further processed by delaminating and grinding in the laboratories of Omya Development AG to give two different surface area and particle size grades. These materials are also reported in the work of Gantenbein, Schoelkopf *et al.* (2009). The surface area data for these experimental products, with respect to the BET technique (Brunauer, Emmett *et al.*, 1938), are reported in Table 6-2. These are then referred to as low surface area (LSA) and high surface area (HSA) talc, respectively. The LSA talc has less exposed facial surface, and, thus, relatively more edges which are dominated by hydrophilic interactions. By contrast the HSA talc is dominated by the hydrophobic interaction on the relatively greater area of exposed talc faces. The particle size distributions of the minerals were obtained using dynamic light scattering measured by a Malvern Mastersizer 2000<sup>3</sup>. The light scattering results were processed applying Mie theory (Mie, 1908) to obtain the particle size distribution. The median particle diameter,  $d_{50}$ , defined by mass distribution within the defined size range, for each material is reported in Table 6-2.

The MCC was obtained from Omya Development AG<sup>4</sup> and the sodium bentonite was obtained from Morocco<sup>5</sup>.

---

<sup>2</sup> Mondo Minerals B.V. Kasarmikatu 22, Helsinki, Finland

<sup>3</sup> Malvern Instruments Ltd, Enigma Business Park, Grovewood Rd, Malvern, U.K.

<sup>4</sup> Omya Development AG, Baslerstrasse 42, CH-4665, Oftringen, Switzerland

<sup>5</sup> S&B Industrial. Minerals. Morocco S.A.R.L

**Table 6-2 Summary of mineral properties.**

Mineral Name	Specific Surface Area (m <sup>2</sup> g <sup>-1</sup> )	Particle Size-Weight Distribution* (μm)		
		<i>d</i> <sub>10</sub>	<i>d</i> <sub>50</sub>	<i>d</i> <sub>90</sub>
LSA talc	7.13	2.24	4.50	10.1
HSA talc	45.30	1.56	5.02	21.0
MCC	36.13	2.55	5.49	9.85
Sodium bentonite	100.13	0.11	1.84	19.72

\* *d*<sub>N</sub> represents the particle diameter for which *N* % of the sample mass has particles finer than *d*.

### 6.2.2 Methods

The mineral and sticky suspensions were mixed for 30 minutes at 150 revolutions per minute on an orbital shaker. The minerals with adsorbed sticky were removed by centrifuging at 2 000 g for 15 minutes for talc and MCC, whereas the bentonite samples were centrifuged for 20 minutes. The supernatant was stored in clean glass bottles. The mineral precipitate with adsorbed sticky was kept in the centrifuge tubes for freeze drying before elemental analysis.

There are two methods for determining the sticky concentration. The first method involves measuring the removal of stickies from suspension, using a technique that can measure a property of the sticky in aqueous suspension; turbidity, chemical oxygen demand, gravimetric analysis, dissolved organic carbon and total dissolved nitrogen analysis. The second method involves measuring an increase of stickies on the mineral. To measure the increase of adsorbed sticky we used elemental analysis; it is also possible to use thermo gravimetric analysis (TGA).

### 6.2.3 Artificial sticky preparation

All the stickies were prepared to form colloidally stable suspensions with an initial concentration of 0.5 g dm<sup>-3</sup> with pH between 7 and 7.5 and conductivity in the range of 1 000 to 1 500 μS cm<sup>-1</sup>. They were adjusted to these ranges where necessary using dilute analytical grade hydrochloric acid, analytical grade sodium hydroxide and laboratory grade sodium chloride. Most of the artificial stickies were available as

colloidal suspensions. However, for the colophonium resin and polyvinyl acetate, which were not in suspension, the following procedures were followed and then adjusted to the correct pH and conductivity range.

Colophonium: 5 g of colophonium was saponified in 10 000 g deionised water by the addition of 5 g sodium hydroxide. The pH was afterwards adjusted back to 7.5 by the addition of hydrochloric acid with a resulting turbidity of 130 NTU and a COD of 813 mg O<sub>2</sub> per dm<sup>3</sup>.

Polyvinyl acetate: 5 g polyvinyl acetate was dissolved in 100 cm<sup>3</sup> acetone (propanone). The solution was added under vigorous stirring to a solution of 5 g polyvinyl alcohol and 10 000 g distilled water. The acetone was evaporated at 60 °C overnight to give a colloidal stable suspension with a turbidity of 64 NTU and a COD of 1280 mg O<sub>2</sub> per dm<sup>3</sup>.

All sticky suspensions were then diluted to 0.1, 0.05, 0.01 and 0.005 g dm<sup>-3</sup>, and reference samples of each concentration were taken to construct a calibration series. The sticky suspensions then had mineral suspension added to give a mineral concentration of 2 g dm<sup>-3</sup>. All the experimental techniques were used for all concentrations of the sticky suspensions after the mineral had been removed.

#### **6.2.4 Turbidity**

A sample was taken to analyse for turbidity before and after adsorption using a Novasina 155 Model NTM-S, Section 2.4.1.

#### **6.2.5 Chemical oxygen demand**

Before and after the adsorption experiment, a 2 cm<sup>3</sup> sample was taken for chemical oxygen demand analysis to obtain a value for the change in total organic content.

More details about the experimental procedure can be found in Section 2.4.2.



### **6.2.6 Gravimetric analysis**

After the adsorption experiment was performed and the minerals removed by centrifuging, 50 cm<sup>3</sup> of supernatant was transferred by pipette into a pre-weighed aluminium tray. The supernatant was then evaporated at 95 °C in a fan assisted oven. Once the supernatant was evaporated, the aluminium trays contained the non-volatile sticky residues, which were weighed to determine total non-volatile stickies left in the sticky suspension. More details about the experimental procedure were given in Section 2.4.3.

### **6.2.7 Dissolved organic carbon and total dissolved nitrogen analysis**

The dissolved organic carbon analysis was run on a Shimadzu TOC-5000A total organic carbon analyser coupled to a Shimadzu ASI-5000A auto sampler and also coupled to a Siemens NCD 255 analyser, which analyses for total dissolved nitrogen. Details of the experimental procedure were given in Sections 2.4.4 and 2.4.4.1.

### **6.2.8 Elemental analysis**

Elemental analysis was performed on a Carlo Erba EA-1110 CHNS elemental analyser. Section 2.4.5 details the experimental procedure. The results were cross checked against a certified reference material with a certified carbon concentration of  $3.69 \pm 0.11$  % with a 95 % confidence limit, which compares well with  $3.58 \pm 0.15$  % with a 95 % confidence limit for our measurements.

## ***6.3 Results and discussion***

To confirm the excess concentration and to justify the exclusion of [Mineral]<sup>Susp</sup> from the equilibrium, an experiment was carried out in which the mineral concentration was changed from 0.5 – 20 g dm<sup>-3</sup> and the sticky concentration kept constant. The

equilibrium constant calculated incorporating the mineral concentration in the calculation stayed constant at  $0.001377 \pm 0.000077$ .

### **6.3.1 Aqueous phase – turbidity**

The results obtained from the turbidity meter are very quick to obtain and simple to perform, though they can be affected by the efficiency of the centrifuge in removing the minerals. This technique can be used for sticky concentrations generally higher than  $0.05 \text{ g dm}^{-3}$ . At lower concentrations, because the initial turbidity is lower, the technique becomes less sensitive to changes in turbidity, especially if mineral remains in suspension after centrifuging. The results obtained for the high sticky concentrations are shown in Table 6-3 for all stickies except alkylidiphenyloxide disulphonate as this suspension has a negligible turbidity at high concentration.

Bentonite is very difficult to remove from the suspension by centrifuging, even after twenty minutes at 2 000 g. Indeed, in some bentonite adsorption experiments, centrifugation actually increased the turbidity instead of clarifying the suspension. (Table 6-3). Some of the results obtained, however, indicate that bentonite does reduce the turbidity if it can be centrifuged out, when the bentonite is sufficiently coagulated with the sticky to render centrifuging more effective.

**Table 6-3** Turbidities expressed as percentage change on adding 2 g dm<sup>-3</sup> of respective mineral to the stickies shown bold for three concentrations of sticky. Cells highlighted in yellow indicate an increase in turbidity. The error range indicates two times the standard deviation from three replicates.

<b>Sticky / Mineral</b>	<b>0.5 g dm<sup>-3</sup></b>	<b>0.1 g dm<sup>-3</sup></b>	<b>0.05 g dm<sup>-3</sup></b>
<b>Fatty acid ester defoamer</b>			
LSA talc	-57.3 ± 0.3	-26.3 ± 0.4	44.4 ± 3.8
HSA talc	-76.9 ± 0.2	-66.7 ± 0.8	-33.3 ± 0.6
MCC	-17.8 ± 0.7	-29.4 ± 0.9	-50.0 ± 0.2
Bentonite	33.7 ± 0.9	533 ± 5.2	1110 ± 15
<b>Acrylic acid ester copolymer</b>			
LSA talc	-32.1 ± 0.4	-84.5 ± 0.9	233 ± 7.9
HSA talc	-96.2 ± 0.7	-43.3 ± 1.3	243 ± 6.8
MCC	-51.0 ± 0.9	-80.6 ± 0.6	-98.0 ± 1.7
Bentonite	-52.6 ± 1.4	20.6 ± 2.8	175 ± 10
<b>Mineral oil / Silicone defoamer</b>			
LSA talc	25.0 ± 2.6	414 ± 9.9	2 500 ± 44
HSA talc	50.0 ± 1.1	325 ± 5.4	1 300 ± 26
MCC	-95.3 ± 0.1	-100 ± 0.0	-100 ± 0.0
Bentonite	339.0 ± 6.7	1450 ± 20	12 300 ± 147
<b>Polyvinyl acetate</b>			
LSA talc	-21.8 ± 0.4	-9.38 ± 0.6	14.3 ± 0.5
HSA talc	-36.8 ± 0.4	-9.09 ± 0.6	26.7 ± 0.7
MCC	-30.3 ± 0.3	-43.8 ± 0.3	-64.3 ± 0.4
Bentonite	-70.3 ± 0.2	-100 ± 0.0	-100 ± 0.0
<b>Styrene – butadiene latex</b>			
LSA talc	-6.19 ± 0.19	-14.4 ± 0.2	-20.2 ± 0.3
HSA talc	-5.27 ± 0.14	-16.6 ± 0.2	-8.94 ± 0.72
MCC	-45.2 ± 0.1	-99.5 ± 0.2	-100 ± 0.0
Bentonite	-1.42 ± 0.11	12.4 ± 0.5	37.8 ± 1.1
<b>Colophonium resin</b>			
LSA talc	-37.2 ± 1.2	-64.9 ± 0.3	-57.9 ± 0.5
HSA talc	-52.5 ± 0.7	-70.2 ± 0.8	-35.5 ± 0.4
MCC	-93.9 ± 0.5	-99.4 ± 0.2	-100 ± 0.0
Bentonite	-43.4 ± 0.4	-48.5 ± 0.3	63.5 ± 0.6

The talc turbidity results show that for most stickies the HSA talc is better than the LSA talc at reducing the turbidity. At lower concentrations of sticky with the HSA talc, it is more likely to affect the turbidity measured as HSA talc is more difficult than LSA talc to remove by centrifuging. The sticky compound itself can also affect how well the mineral is removed, as the sticky can cause the mineral to aggregate making its removal easier.

The MCC showed a trend in that the relative efficiency of reducing the turbidity increased as the concentration of stickies decreased as expected. The MCC was also easily removed from suspension, so there were no effects due to the calcium carbonate

remaining in suspension. The MCC was the outstanding performer in reducing the turbidity of colophonium resin and styrene-butadiene latex, Table 6-3.

The lowest two concentrations of sticky concentration are not presented because of the low starting turbidity.

### 6.3.2 Aqueous phase – chemical oxygen demand

The chemical oxygen demand results are shown in Table 6-4. The table shows how much the chemical oxygen demand was reduced relative to the starting chemical oxygen demand for each sticky concentration.

**Table 6-4 Chemical oxygen demand expressed as percentage change on adding 2 g dm<sup>-3</sup> of the respective mineral to the stickies shown bold for three concentrations of sticky. Cells highlighted in yellow indicate an increase in chemical oxygen demand. The error range indicates two times the standard deviation from three replicates.**

<b>Sticky / Mineral</b>	<b>0.50 g dm<sup>-3</sup></b>	<b>0.10 g dm<sup>-3</sup></b>	<b>0.05 g dm<sup>-3</sup></b>
<b>Fatty acid ester defoamer</b>			
LSA talc	-57.1 ± 0.4	-59.6 ± 1.2	>-89.6
HSA talc	-75.8 ± 0.5	-84.1 ± 1.5	>-88.9
MCC	-41.4 ± 0.5	-13.6 ± 1.0	-77.2 ± 2.4
Bentonite	-73.3 ± 0.8	-73.6 ± 1.1	-51.1 ± 2.2
<b>Acrylic acid ester copolymer</b>			
LSA talc	-14.3 ± 1.9	-25.2 ± 1.3	>-84.1
HSA talc	-71.6 ± 2.7	-30.5 ± 3.8	-65.5 ± 2.2
MCC	-57.7 ± 2.2	-41.1 ± 2.7	>-80.6
Bentonite	-61.1 ± 3.4	-38.4 ± 1.9	-68.0 ± 2.0
<b>Mineral oil / Silicone defoamer</b>			
LSA talc	-20.9 ± 0.5	-45.7 ± 3.7	-72.1 ± 1.9
HSA talc	-16.0 ± 0.3	-61.3 ± 5.6	>-96.4
MCC	-51.2 ± 0.2	-54.5 ± 2.1	-55.1 ± 1.8
Bentonite	-48.9 ± 0.6	-62.1 ± 1.3	-59.9 ± 1.8
<b>Polyvinyl acetate</b>			
LSA talc	-2.06 ± 0.48	-10.9 ± 1.4	-4.65 ± 1.62
HSA talc	-4.00 ± 0.33	-15.9 ± 2.0	-15.9 ± 1.5
MCC	-14.5 ± 0.5	-9.62 ± 1.03	-26.2 ± 1.0
Bentonite	-36.0 ± 0.2	-19.6 ± 2.2	-29.9 ± 0.4
<b>Styrene – butadiene latex</b>			
LSA talc	-6.67 ± 0.37	-15.5 ± 0.9	-18.1 ± 0.7
HSA talc	-6.18 ± 0.29	-21.4 ± 1.4	-31.9 ± 0.5
MCC	-50.6 ± 0.8	-60.9 ± 3.6	>-89.6
Bentonite	-4.71 ± 0.88	-2.21 ± 1.4	-9.72 ± 0.81
<b>Colophonium resin</b>			
LSA talc	-16.8 ± 2.0	-9.91 ± 1.34	-33.0 ± 0.3
HSA talc	-29.0 ± 1.9	-18.5 ± 2.4	-20.3 ± 0.8
MCC	-37.1 ± 2.1	10.8 ± 3.6	-3.54 ± 0.6
Bentonite	-25.3 ± 1.9	-17.2 ± 2.6	-14.9 ± 0.9

The chemical oxygen demand measurements are suitable for high sticky concentrations. A chemical oxygen demand experiment takes more time than a straightforward turbidity measurement, but is more reliable as the efficiency of removing the mineral has a negligible effect.

For talc, the HSA talc performed better than the LSA talc, which is to be expected as the specific surface area is 6 times larger. Both of the talc grades performed well on the fatty acid ester defoamer and on the acrylic acid ester copolymer, in agreement with the behaviour shown by the turbidity results. The tests with lower concentration stickies were sometimes below the limit of detection, so it is uncertain exactly how much the chemical oxygen demand was lowered under these conditions. These results are shown in Table 6-4 as > specific percentages.

The MCC was a consistent performer for all the stickies analysed, and performed particularly well with the acrylic acid ester copolymer and styrene butadiene latex. For bentonite, the results indicated a 2 – 74 % reduction in chemical oxygen demand. The talc grades and MCC, however, generally outperformed the bentonite for all of the stickies tested.

### **6.3.3 Aqueous phase – gravimetric analysis**

The results from the gravimetric analysis show that non-volatile sticky residue was left in suspension after the mineral treatment, and that the analytical (weighing) balance used was not accurate enough to quantify the sticky concentrations when at low sticky concentrations. The technique worked well, however, at high initial sticky concentrations. The analysis was also compromised by mineral removal efficiency earlier in the procedure; if any mineral was remaining it increased the residual sticky weight. The gravimetric results for the top three concentrations are shown in Table 6-5.

**Table 6-5 Non volatile organic residue expressed as percentage change on adding 2 g dm<sup>-3</sup> of the respective mineral to the stickies shown bold for three concentrations of sticky. Cells highlighted in yellow indicate an increase in non volatile organic residue. The error range indicates two times the standard deviation from three replicates, and highlights the lack of precision.**

<b>Sticky / Mineral</b>	<b>0.5 g dm<sup>-3</sup></b>	<b>0.1 g dm<sup>-3</sup></b>	<b>0.05 g dm<sup>-3</sup></b>
<b>Fatty acid ester defoamer</b>			
LSA talc	-35.3 ± 1.8	-23.6 ± 3.6	-17.4 ± 3.9
HSA talc	-24.6 ± 2.6	-7.74 ± 3.46	-3.93 ± 4.67
MCC	-16.3 ± 0.9	-18.7 ± 1.8	-7.66 ± 2.34
Bentonite	44.5 ± 4.6	65.5 ± 7.9	65.8 ± 8.0
<b>Acrylic acid ester copolymer</b>			
LSA talc	-10.8 ± 3.2	-11.1 ± 4.2	-47.9 ± 4.6
HSA talc	-38.7 ± 3.6	34.1 ± 3.2	55.2 ± 9.8
MCC	-24.8 ± 1.2	9.44 ± 4.56	117 ± 14
Bentonite	28.2 ± 10.2	87.4 ± 17	322 ± 29
<b>Mineral oil / Silicone defoamer</b>			
LSA talc	-9.09 ± 0.98	13.9 ± 2.4	5.37 ± 2.09
HSA talc	7.66 ± 1.6	22.4 ± 1.8	12.8 ± 3.7
MCC	-10.8 ± 1.9	11.2 ± 2.0	6.27 ± 2.48
Bentonite	63.4 ± 6.7	122 ± 5	102 ± 4
<b>Polyvinyl acetate</b>			
LSA talc	-4.90 ± 2.43	-4.85 ± 2.39	-2.86 ± 0.79
HSA talc	-8.98 ± 1.79	-7.16 ± 2.04	-0.26 ± 0.18
MCC	-2.72 ± 2.04	-2.77 ± 1.89	-0.26 ± 0.13
Bentonite	-4.08 ± 3.01	-13.6 ± 2.5	-2.34 ± 1.06
<b>Styrene – butadiene latex</b>			
LSA talc	-3.04 ± 1.06	-5.85 ± 1.57	-3.27 ± 2.08
HSA talc	4.38 ± 2.78	9.16 ± 0.99	8.99 ± 4.26
MCC	-22.1 ± 1.1	13.2 ± 1.0	-9.26 ± 4.34
Bentonite	43.5 ± 3.2	64.4 ± 4.1	76.8 ± 4.7
<b>Colophonium resin</b>			
LSA talc	-11.1 ± 0.9	-0.94 ± 0.38	3.23 ± 2.16
HSA talc	-8.60 ± 1.1	7.26 ± 1.5	23.1 ± 3.9
MCC	-15.0 ± 0.97	-0.47 ± 0.91	1.99 ± 3.04
Bentonite	22.6 ± 4.3	55.0 ± 3.9	104 ± 8

The results obtained for the gravimetric analysis become easily distorted by the presence of mineral in the suspension. At high sticky concentration it is possible to see that non-volatile sticky residues have decreased for the majority of stickies with all the minerals except bentonite. The gravimetric results do not give any useful data when testing with bentonite due to the difficulty in removal.

To improve the gravimetric analysis, an analytical balance with higher precision than 0.1mg would be required.

### **6.3.4 Aqueous phase – dissolved organic carbon analysis**

#### **(DOC) and total dissolved nitrogen analysis (TDN)**

The dissolved organic carbon analysis results, showed that the technique could be used over a range of sticky concentrations from  $0.005$  to  $0.5 \text{ g dm}^{-3}$ , to determine the suspended organic carbon. Additionally, the analysis required more preparation steps, which also make it harder to apply as an analysis in a paper mill. The results obtained from this analysis had the advantage of being directly quantitative, and determinable over the complete sticky range, albeit with secondary dilution, so they are able to deliver the most information about how the sticky concentration changed during the experiment. The results from this technique had only small errors between replicates as shown in Appendix C.

The total dissolved nitrogen analysis was carried out with identical experimental conditions as the dissolved organic carbon analysis. However, the method was only usable in this study series with styrene butadiene latex, as it was the only sticky with definable nitrogen concentration present. For this species, it confirmed that the sticky had been removed from the aqueous phase as discussed below (Figure 6-6).

The DOC and TDN methods were additionally checked using certified reference materials. The reference material used was a deep sea water from the Sargasso, collected at 2 600 m with a certified dissolved organic carbon content of  $44 - 45 \text{ } \mu\text{M C}$  within a 95 % confidence limit. The total dissolved nitrogen value is quoted as  $21.3 \text{ } \mu\text{M N}$  for the reference material. Our results agreed with these reference values: our DOC value was  $44.4 \pm 4.2 \text{ } \mu\text{M C}$  and the TDN value was  $22.8 \pm 4.2 \text{ } \mu\text{M N}$  within the 95 % confidence limit from 30 analyses.

In Figures 6-4 – 6-9, the dissolved organic carbon results are compared against the turbidity, chemical oxygen demand and gravimetric analyses. The total dissolved

nitrogen results are also compared, where applicable. All of the data are converted back into concentration by constructing calibration curves using the reference sample results. If the results obtained using these calibration curves were obviously erroneous in that they exceeded the initial concentration or were negative, they have been omitted from the comparison graphs.

Figure 6-2 shows a comparison of the techniques in the case of the fatty acid ester defoamer. The results for dissolved organic carbon analysis correspond well with the turbidity and chemical oxygen demand results for the initial concentration range 0.05 – 0.5 g dm<sup>-3</sup>. The chemical oxygen demand is a better fit with an  $R^2$  value of 0.925 compared with the turbidity  $R^2$  value of 0.844. The gravimetric results did not generate enough data to draw any conclusions. The total dissolved nitrogen technique is not applicable for this sticky.



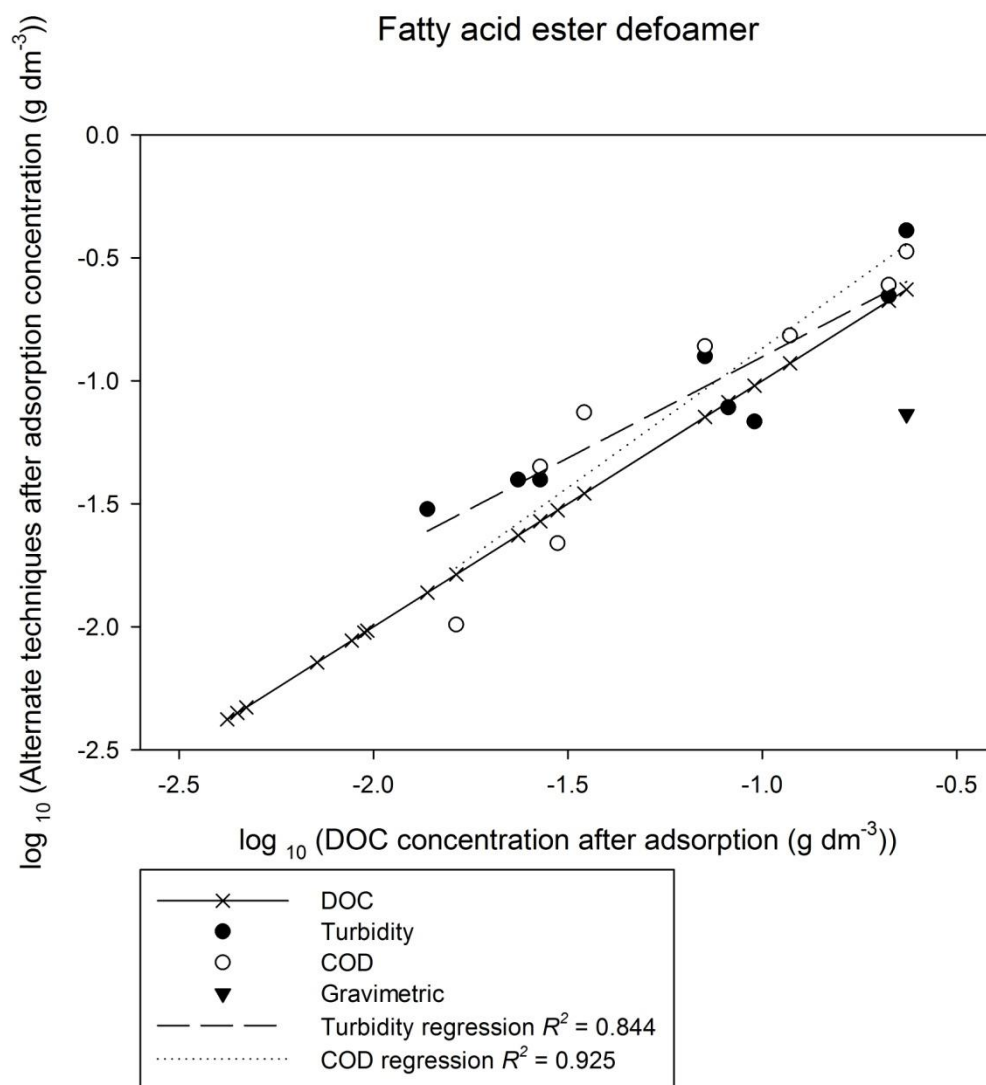


**Figure 6-2** Graph showing how the different techniques of measuring fatty acid ester defoamer concentration varied when compared with the dissolved organic carbon analysis. The turbidity and chemical oxygen demand show a good correlation over a smaller concentration range from  $0.05 - 0.5 \text{ g dm}^{-3}$ . The gravimetric results for this sample did not have enough data to generate a comparison best fit line. The total dissolved nitrogen analysis is not applicable to this sticky as nitrogen is not present.

The acrylic acid ester copolymer dissolved organic carbon results are compared with the turbidity and chemical oxygen demand results in Figure 6-3. The turbidity  $R^2$  value of 0.882 arises from a good linear correlation along the dissolved organic carbon results for a limited concentration range, but the low concentration result is significantly different, which strongly affects the  $R^2$  value. The chemical oxygen demand  $R^2$  value of 0.688 generally also represents the good correlation with respect to the dissolved organic carbon results but there is some occasionally strong deviation, which lowers the  $R^2$  value. The gravimetric data mainly cluster at high concentration, so cannot be used to construct a best fit line.

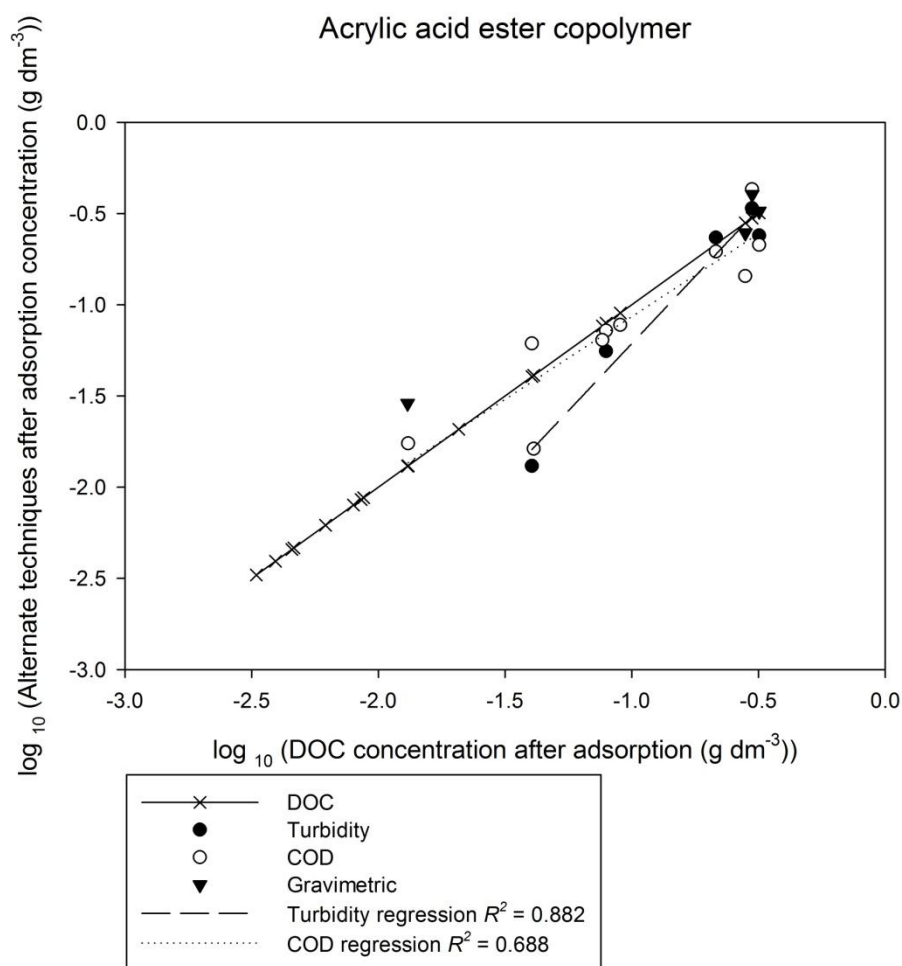


**Figure 6-3** Graph showing how the different techniques of measuring acrylic acid ester copolymer concentration varied when compared with dissolved organic carbon analysis. The total dissolved nitrogen data are not relevant as the results obtained are very inconsistent. The turbidity and chemical oxygen demand results show a correlation with the dissolved organic carbon analysis over a limited concentration range.

The mineral oil / silicone defoamer results are compared with turbidity and chemical oxygen demand results in Figure 6-4. The turbidity results indicate lower values than the dissolved organic carbon results for all of the test series. This is traceable back to the low starting turbidity; any mineral left in the supernatant will increase the turbidity, falsely implying that less sticky is removed. The low  $R^2$  value for turbidity of 0.082 reflects this discrepancy. The chemical oxygen demand  $R^2$  value of 0.831 shows good agreement.

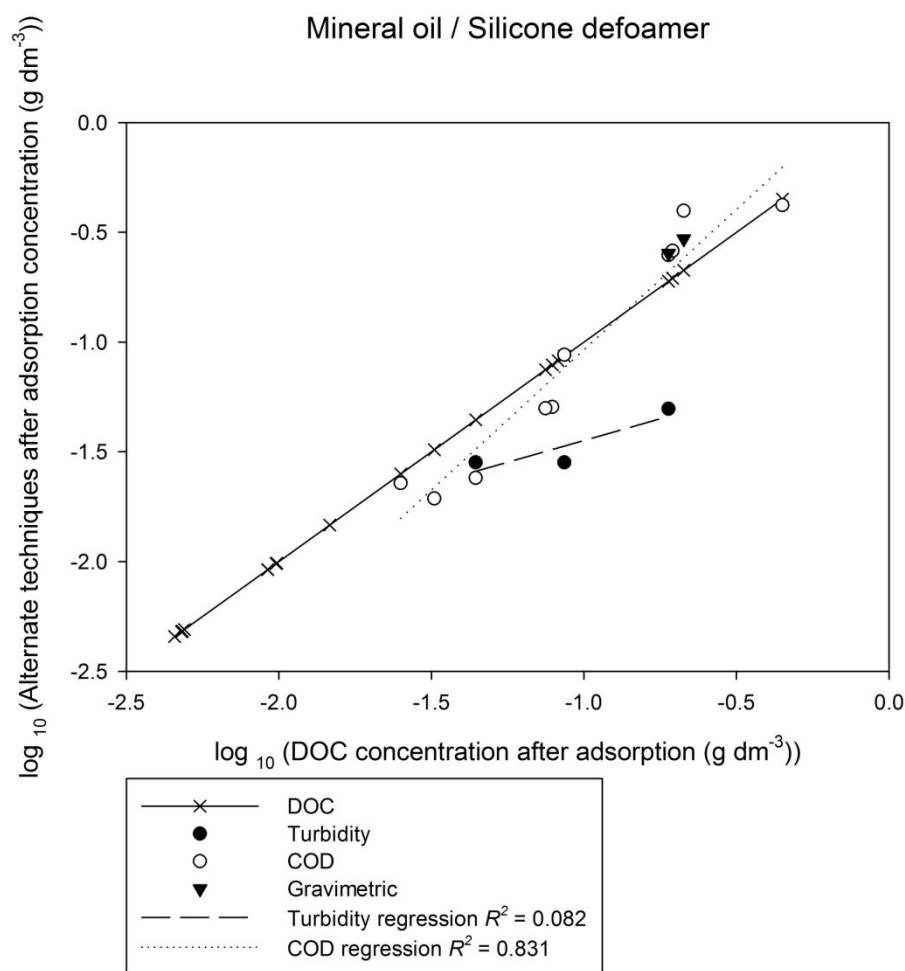


**Figure 6-4 Comparison of dissolved organic carbon analysis with turbidity and chemical oxygen demand. The results for the turbidity did not agree with the dissolved organic carbon or chemical oxygen demand analysis, due to incomplete removal of mineral, which affects the less turbid mixtures proportionally more.**

The polyvinyl acetate results are compared with turbidity, chemical oxygen demand and gravimetric data in Figure 6-5. The total dissolved nitrogen results are also shown for polyvinyl acetate, but as the sticky does not have nitrogen present the results have no significance. The turbidity shows good correlation around the dissolved organic carbon results but is affected by possible outliers; the  $R^2$  value is 0.901. The chemical oxygen demand has very good correlation around the dissolved organic carbon results at high concentration, but as the concentration decreases the results become more scattered; the  $R^2$  value is 0.965. The gravimetric results are seen to be slightly higher than the dissolved organic carbon data, but this is expected as there is probably residual mineral influencing the results. They have an  $R^2$  value of 0.850.

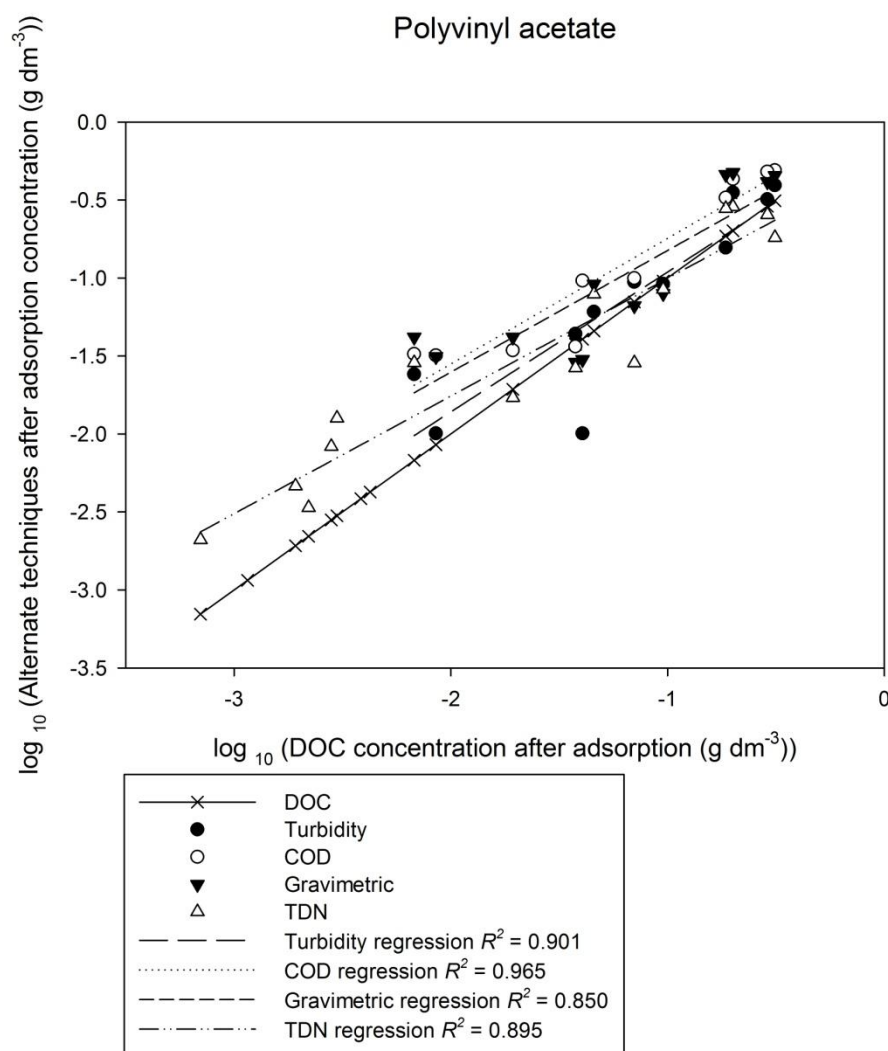


**Figure 6-5 Comparison of all aqueous techniques with the dissolved organic carbon results. The reporting of values by total dissolved nitrogen analysis is unexpected as polyvinyl acetate *per se* does not have nitrogen, which explains the lower  $R^2$  value obtained, but not that some reporting of nitrogen appears to be present.**

The dissolved organic carbon results for styrene butadiene latex are compared with all of the aqueous phase techniques and shown in Figure 6-6. All of the techniques for this sticky performed well. The turbidity is slightly higher than the dissolved organic carbon results throughout, but the results still show good correlation with an  $R^2$  of 0.964. The chemical oxygen demand is slightly high at low and high concentration when compared with the dissolved organic carbon data, but generally agrees, with an  $R^2$  of 0.970. The gravimetric results have a good agreement, with an  $R^2$  of 0.993. These three techniques are only applicable for the sticky concentration range  $0.05 - 0.5 \text{ g dm}^{-3}$ , as concentrations lower than  $0.05 \text{ g dm}^{-3}$  are below the limit of detection. The total dissolved nitrogen versus dissolved organic carbon has an  $R^2$  correlation of 0.994, and

there is a very good agreement for the complete concentration range despite some small scatter.

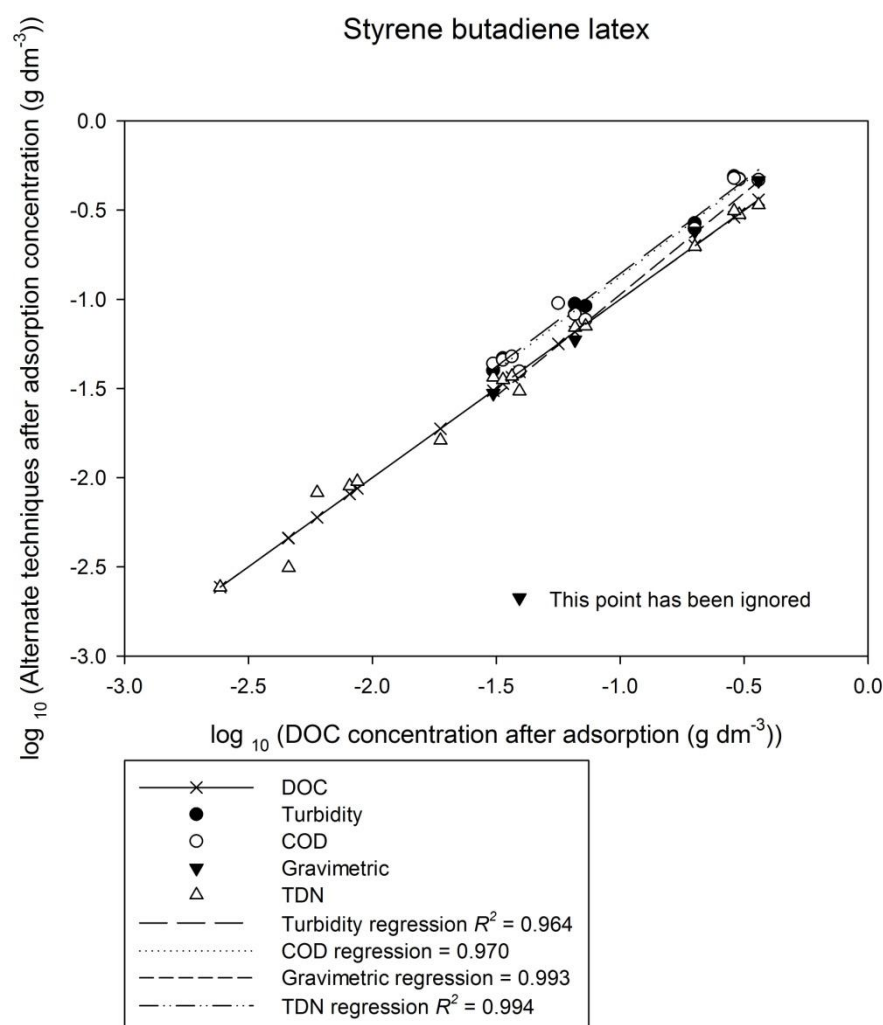


**Figure 6-6** Comparison of how the styrene butadiene latex concentration determined using all investigated techniques has a very good correlation with the dissolved organic carbon results. The turbidity, chemical oxygen demand and gravimetric results have a smaller concentration range than the dissolved organic carbon, but they overlap well. The total dissolved nitrogen results have a very good correlation with the dissolved organic carbon analysis of about 99.5 %, which indicates that the technique can be used successfully when nitrogen is present in the sticky even at low concentrations, as it is in this case.

The dissolved organic carbon results for colophonium resin are compared with turbidity, chemical oxygen demand and gravimetric results in Figure 6-7. The turbidity results for this technique are lower than the dissolved organic carbon results, due to the lack of sensitivity of the technique when dealing with less turbid suspensions. The  $R^2$  value reflects this at 0.347. The chemical oxygen demand results show good agreement over a limited concentration range with an  $R^2$  of 0.826. The gravimetric results show

good agreement generally but are influenced by possible outliers due to incomplete removal of the mineral, which is most common for bentonite and HSA talc. The  $R^2$  value is 0.649.

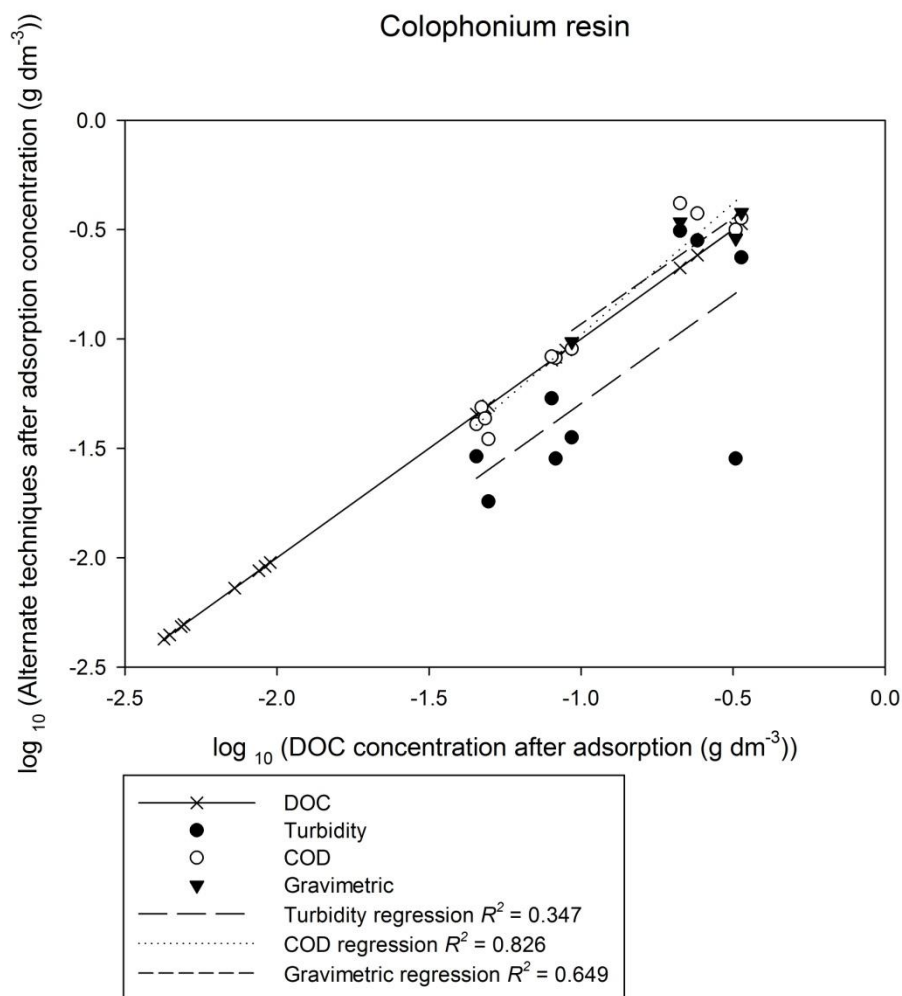


**Figure 6-7 Comparison of techniques for the colophonium. The turbidity results were affected by the low starting turbidity for colophonium resin alone. The chemical oxygen demand and gravimetric analyses have a good correlation with the dissolved organic carbon analysis at high initial concentrations.**

In conclusion, we see that the comparison of the techniques shows that the dissolved organic carbon analysis agrees fairly well with the respective alternate techniques at the higher concentration range.

### 6.3.5 Technique comparison

A comparison of the techniques used in this investigation is summarised in Table 6-6.

Table 6-6 Advantages and disadvantages of the studied techniques to evaluate sticky removal.

Method	Applicable Concentration Range	Advantages and Disadvantages
<b>Turbidity</b>	$> 0.05 \text{ g dm}^{-3}$	Universal technique for supernatant analysis (following mineral removal after adsorption) Very simple and fast analysis Can be used in laboratory or paper mill Cheap technique to use Needs complete removal of mineral for quantitative data Not suitable for very low concentrations or when suspension of sticky is not turbid. Can use data to construct calibration curve, assuming complete removal of mineral
<b>Chemical oxygen demand</b>	$> 0.05 \text{ g dm}^{-3}$	Universal technique for supernatant analysis (following mineral removal after adsorption) Cheap and simple analysis Not affected by incomplete removal of mineral Not suitable at low concentrations due to limit of detection for the technique Can use data to construct calibration curve
<b>Gravimetric analysis</b> <sup>6</sup>	$> 0.5 \text{ g dm}^{-3}$	Universal technique for analysis of supernatant (following mineral removal after adsorption) Cheap and simple to perform. Can be used for laboratory or paper mill studies assuming suitable reference can be found. Needs complete removal of mineral for quantitative data Can use data to construct calibration curve, as long as complete removal of mineral occurs
<b>Total dissolved nitrogen</b> <sup>7</sup>	$> 0.005 \text{ g dm}^{-3}$	Sensitive technique, needs nitrogen present in sticky so not universally applicable Time consuming preparation steps mean only suitable for laboratory studies Dilution of samples may be required due to limited linear calibration range. Cost per sample is high Can use data to construct calibration curve

<sup>6</sup> Depends on the sample size: evaporated larger samples will increase sensitivity and applicable concentration range.

<sup>7</sup> May be able to determine lower concentration samples - not investigated further here

<b>Dissolved organic carbon</b> <sup>6</sup>	$> 0.005 \text{ g dm}^{-3}$	Universal technique for analysis of supernatant. Sensitive technique Time consuming preparation steps mean only suitable for laboratory studies Cost per sample is high Can use data to construct calibration curve
<b>Elemental Analysis</b> <sup>6</sup>	$> 0.005 \text{ g dm}^{-3}$	Universal technique for analysis of minerals. Sensitive Need baseline mineral information Preparation steps are time consuming meaning technique really only suitable for detailed laboratory analysis. Technique could be simplified to study paper mill minerals, but would only give trends, not quantitative data Cost per sample is high

---

An overall conclusion is that by combining techniques, weaknesses of individual techniques can be overcome.

### 6.3.6 Equilibrium constants

The equilibrium constants for all the sticky and mineral systems were calculated using the dissolved organic carbon data and elemental analysis carbon data. The results are shown in Figure 6-8. Equation 6-3 was used for calculating the equilibrium constants and standard deviation. The error bars in Figure 6-8 represent two standard deviations for each of the equilibrium constants, i.e. 95 % of the assumed statistical distribution of the calculated equilibrium constants at each different concentration are within the error bars.

The use of Equation 6-3 has limitations depending on different factors, including the particle size of both the mineral and sticky, the location of adsorption sites on the surface, and, hence, whether the adsorption isotherm is linear for the concentration range investigated.



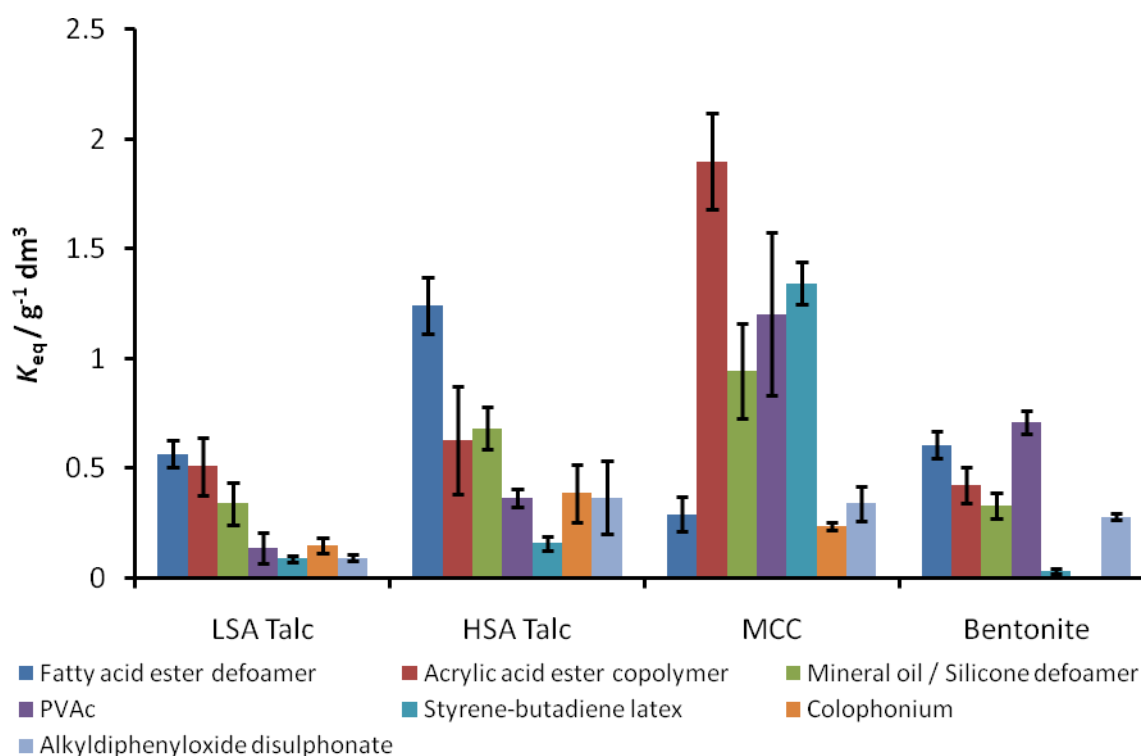


**Figure 6-8 Average equilibrium constants for all experimental systems investigated, calculated from the dissolved organic carbon and elemental analysis carbon data. The error bars represent double the standard deviation determined from a minimum of three replicates of elemental analysis and dissolved organic carbon analysis.**

Figure 6-8 shows that the equilibrium constants are higher for HSA talc than LSA talc by a factor of between 1.10 and 3.88 for the talc grades. The ratio between the equilibrium constants provides information about the adsorption mechanism and whether the sticky prefers to adsorb on hydrophobic or hydrophilic species, as discussed in more detail in Chapter 7. This ratio for the acrylic acid ester copolymer is 1.10, which implies hydrophilic adsorption, since the increased hydrophobic surface relative to hydrophilic surface makes little difference. The ratio for alkyldiphenyloxide disulphonate is 3.88, which implies that adsorption onto hydrophobic surfaces is preferred relative to hydrophilic surfaces. For the fatty acid ester defoamer and colophonium, the ratios of 2.18 and 2.61 respectively suggest HSA talc is better at adsorbing stickies from colloidal suspension, implying the adsorption is dominated by hydrophobic forces. However it must be borne in mind that the adsorption may also be assisted by surfactants present in the suspension.

The MCC used in this investigation had the highest equilibrium constants for the adsorption of acrylic acid ester copolymer, mineral oil / silicone defoamer, polyvinyl acetate and styrene-butadiene latex. MCC is a charged species, so the dominant adsorption mechanism is likely charge related (Ridgway, Gane *et al.*, 2004). Adsorption onto bentonite is also charge related (Asselman and Garnier, 2000). However, the particle size of the bentonite is smaller than the MCC in this investigation. The results imply that for the alkyldiphenyloxide disulphonate system one should preferably use HSA talc, MCC or bentonite to remove the sticky, and that the sticky is able to be removed using either hydrophobic or charge interaction sites for adsorption.

### **6.3.7 Limitations on adsorption and the assumption of linearity**

#### **( $K_{eq}$ )**

Three different mechanisms for possible adsorption of stickies are shown schematically in Figure 6-9. The particle size of the mineral and the arrangement of sorption sites affect the arrangement of sticky and mineral. When the mineral is much larger than the sticky, a sandwich of sticky particles can be formed between mineral particles, bottom right of Figure 6-9.

The mechanism represented in the top left schematic occurs when the sticky molecule is larger than the diameter of the mineral particle. The agglomeration mechanism is most probable for polyvinyl acetate and colophonium resin as the median particle diameters are 125.5 and 128.7  $\mu\text{m}$ , respectively (Benecke, Gantenbein *et al.*, 2009) in relation to mineral particle sizes ranging from 1.84 to 5.02  $\mu\text{m}$ . This mechanism requires more mineral particles adsorbed onto the surface before the sticky is detackified.

The schematic in the bottom left of Figure 6-9 represents a hybrid adsorption mechanism between that of the sandwich system and the agglomeration system, described above, and is likely to occur when the diameter of the sticky particle is of a

similar size to the mineral particle. Both previous adsorption mechanisms can happen simultaneously, such that sandwiches can be formed at the same time as agglomerates of sticky and mineral. The hybrid mechanism is likely to occur with the fatty acid ester defoamer and mineral oil / silicone defoamer as the median particle diameters are 3.9 and 3.1  $\mu\text{m}$ , respectively (Benecke, Gantenbein *et al.*, 2009). The sandwich adsorption mechanism is most likely for the acrylic acid ester copolymer and styrene butadiene latex because of their smaller median particle diameter of 0.77 and 0.19  $\mu\text{m}$ .

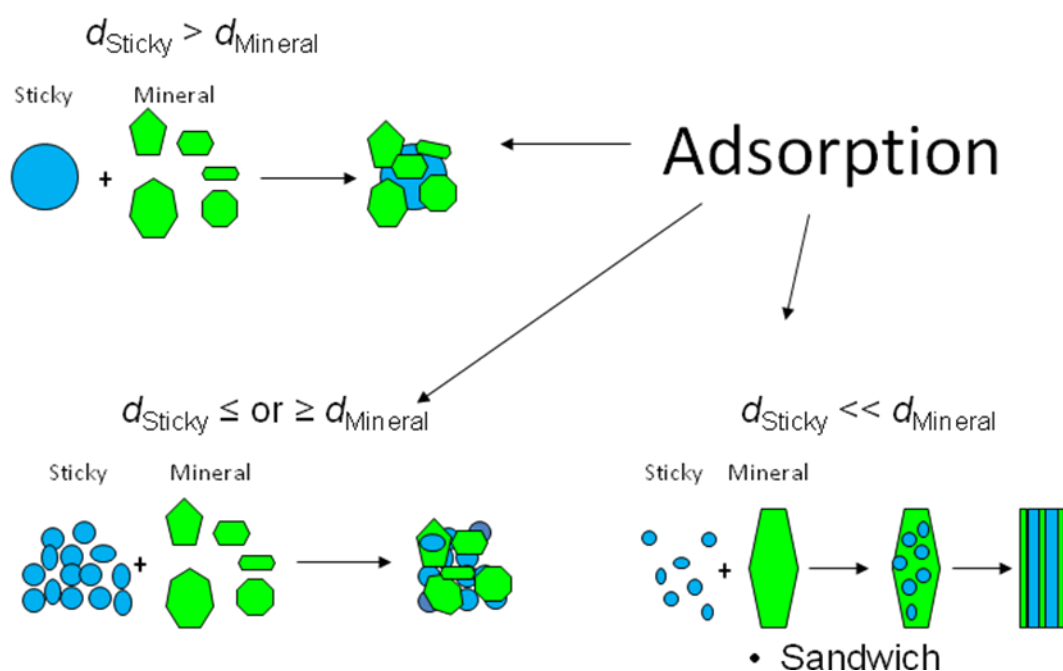


**Figure 6-9** Schematic representation of how adsorption can vary dependent on the diameter of the mineral particle or sticky species. The concentration of mineral is always in excess, Figure 6-1a.

The particle size of the sorbate is different for each sticky and each sticky will have a preferred adsorption site on the sorbent. The sorbent may not be completely covered at all available active adsorption sites for all the stickies. Sometimes the adsorption sites will be located close together on the sorbent. Neighbouring sorbate particles will compete with each other spatially, and this will affect the adsorption equilibrium constant. Therefore, at higher concentrations of stickies as the sticky concentration approaches the mineral concentration, as in Figure 6-1b, the equilibrium constant may deviate from being linear. The raw (i.e. unaveraged) equilibrium constants confirm this

deviation from linearity for the most concentrated system ( $0.5 \text{ g dm}^{-3}$ ), Appendix B. All systems highlighted in yellow in Table 6-7 have a linear range of  $0.1 - 0.005 \text{ g dm}^{-3}$ . All other systems have a linear equilibrium range of  $0.5 - 0.005 \text{ g dm}^{-3}$ . The  $R^2$  values of the aqueous and adsorbed concentrations against the original sticky concentration are shown in Table 6-7.

**Table 6-7** Table of  $R^2$  values to indicate that the results used to generate the equilibrium constants are within the linear range. The top line value indicates the adsorbed  $R^2$  value and the bottom line value indicates the aqueous  $R^2$ .

Sticky	LSA Talc	HSA Talc	MCC	Bentonite
<b>Fatty acid ester defoamer</b>	0.966 0.951	0.979 0.981	0.961 0.968	0.996 0.995
<b>Acrylic acid ester copolymer</b>	0.833 0.876	0.851 0.861	0.967 0.927	0.998 0.996
<b>Mineral oil / silicone defoamer</b>	0.949 0.980	0.972 0.955	0.966 0.964	0.996 0.995
<b>Polyvinyl acetate</b>	0.936 0.941	0.953 0.972	0.938 0.929	0.999 0.998
<b>Styrene butadiene latex</b>	0.980 0.986	0.998 0.997	0.999 0.998	1.000 0.999
<b>Colophonium</b>	0.999 0.998	0.963 0.951	0.993 0.991	0.999 0.999
<b>Alkyldiphenyloxide disulphonate</b>	0.989 0.998	0.983 0.959	0.996 0.999	0.994 0.991

The linear ranges can be explained by the adsorption mechanism and particle sizes for the systems as follows.

- The fatty acid ester defoamer prefers adsorbing onto hydrophobic species, so is limited by the particle size of the mineral, and because they are of a similar size more than one mineral particle may be required to detackify the sticky. Consequently, at higher concentrations of sticky there will be competition for adsorption sites and neighbour-neighbour interaction can perturb the adsorption process.
- The acrylic acid ester copolymer has a high equilibrium constant. Thus the sticky prefers adsorbing onto the hydrophilic regions of the MCC, and talc

grades, and saturates the surface, so the equilibrium constant is reduced. The turbidity data also confirms the saturation of the surface for the LSA talc and MCC.

- The mineral oil / silicone defoamer has a similar particle size to the HSA talc and MCC. Therefore, the sticky may require more than one mineral particle adsorbed onto the surface to completely detackify the sticky, so the system shifts to Figure 6-1b, where competitive adsorption occurs because of a reduced mineral surface area available.
- The polyvinyl acetate is much larger than the mineral size, so at high concentrations of sticky, the mineral is not in sufficient excess and the equilibrium is shifted to the colloidal sticky particles.
- The styrene-butadiene latex has a significantly smaller particle size than the mineral, so at a high sticky concentration there are bound to be interactions between adsorbed stickies, which will affect the equilibrium. The styrene-butadiene latex adsorbs onto the MCC. However the MCC does not have hydrophobic sites, which should offer the preferential method of adsorption. So the surfactants present must alter the chemistry of either the sticky or mineral to allow adsorption.

The results shown in Figure 6-8 do not take account of adsorption kinetics; certain minerals may adsorb the stickies more quickly than others. The results suggest that using a synergy derived from a mixture of minerals may be the best approach for treating a mixture of stickies if encountered in a paper mill. Furthermore, the results are only for adsorption phenomena onto the mineral surface; in a paper mill with fluctuating sticky concentrations, the stickies could also desorb from the surface of the mineral to re-establish equilibrium conditions.

## **6.4 Conclusions**

The techniques used in this investigation which measured aqueous properties of the colloidal suspension before and after exposure to mineral, can generate quantitative data for the individual properties measured. These in turn can be converted to sticky concentrations by using a series of known material concentrations to construct a calibration series. The different techniques studied here generated data which correlated well over their respectively applicable concentration ranges, and which was used to construct effective adsorption equilibrium constants.

The concentration of adsorbed carbon was measured by elemental analysis. However, because of the likely presence of unknown surfactants it was not possible to convert the concentration back to actual sticky concentration.

The resulting equilibrium constants provide fundamental information about the interaction of these model stickies with different minerals. Comparison of the two talc grades shows whether hydrophilic or hydrophobic adsorption is preferred. The MCC and bentonite primarily use electrostatic adsorption, via charge and/or Lewis acid sites in the case of bentonite. The major difference between the two minerals is the relative particle size, the bentonite being much finer. The difference in particle size changes the agglomerate size and composition ratio in respect to the sticky-mineral adsorbed structure and geometry, determining whether sticky is adsorbed to mineral (mineral size >> sticky size) or mineral is adsorbed to sticky (sticky size >> mineral size).

### **6.4.1 Highlights**

- ‘Stickies’ (tacky species) cause problems in paper recycling.
- Stickies can be adsorbed onto the minerals within the recycled paper.
- A proxy method can be used to calculate equilibrium constants for adsorption.
- These equilibrium constants show whether hydrophilic or hydrophobic adsorption is preferred.
- The adsorption method varies dependent on the size of sticky and mineral.

## **7 Adsorption of surfactant-rich stickies onto mineral surfaces (Gribble, Matthews *et al.*, 2010a)**

### ***7.1 Introduction***

To remove stickies from the white water system, it is possible to adsorb them onto a mineral surface, and then incorporate the mineral and adsorbate into the paper structure, thus transporting the stickies out of the machine within the final product. The aim of this investigation was to define the extent and nature of adsorption of stickies onto various contrasting mineral surfaces. Because of the colloidal nature of the adsorbent and inexact knowledge of the commercially-supplied model stickies and surfactants, the isotherms and other measurements all refer to operationally defined conditions. However, the general approach and interpretation is applicable to other systems in which species in aqueous colloidal suspension adsorb onto suspended solid particles.

The adsorption measurements presented here involve colloidal species with hydrophilic and hydrophobic regions adsorbing onto hydrophilic and hydrophobic mineral surfaces. The model stickies constituting these colloidal species are stabilised in aqueous solution, most probably by unknown quantities of surfactant and/or surface charge moieties. The adsorption conditions of the experiment allow more than one adsorption mechanism to exist. In order to understand the processes that are occurring, it was decided to fit the experimental data with simple Langmuir gas-adsorption isotherms in an attempt to generate relations between the operationally-defined colloidal conditions. Langmuir isotherms assume single layer, localised adsorption with identical interaction energies for each adsorbed molecule (Langmuir, 1918). The adsorption interactions studied in this work are much more complicated, nevertheless, fitting of the Langmuir



isotherm to individual adsorption stages provides a convenient method of smoothing and quantifying the measurements, and of calculating surface saturation asymptotes.

The adsorption of a typical surfactant onto a solid/liquid surface can be divided into four stages (Paria and Khilar, 2004). The first stage, in which individual isolated species adsorb by electrostatic interaction, obeys the Gouy-Chapman equation (Zhang and Somasundaran, 2006) or Henry's Law (Samiey and Golestan, 2010) with adsorption increasing linearly with concentration (Paria and Khilar, 2004). At the onset of the second stage, surfactant species start to associate with lateral electrostatic interactions to form hemimicelles etc. This lateral interaction causes a sharp increase in adsorption density, which can be studied using an isotherm appropriate for monolayer formation. The third adsorption stage can be analysed using a bilayer isotherm (Samiey and Golestan, 2010). The fourth stage is the desorption of surfactants (El Shafei and Moussa, 2001).

We have fitted the monolayer formation stages (I and II) to a form of the Dubinin-Radushkevich (D-R) equation adapted for adsorption in aqueous systems (Horsfall and Spiff, 2004; Igwe and Abia, 2006):

$$q_e = q_d \exp \left( - \left( \frac{1}{2E^2} \right) \left[ R T \ln \left( 1 + \frac{1}{c_e} \right) \right]^2 \right) .$$

**Equation 7-1**

Here  $q_e$  is the adsorbed concentration at equilibrium on the surface of the mineral,  $R$  is the universal gas constant,  $T$  is the absolute temperature,  $E$  the free energy of sorption per mole of the sorbate,  $c_e$  the aqueous equilibrium concentration, and  $q_d$  the D-R isotherm constant. A plot of  $\ln q_e$  against  $RT \ln(1+1/c_e)$  yields  $E$  and  $q_d$ . An adsorption energy  $E$  of less than 5 kJ mol<sup>-1</sup> implies physisorption, whereas a value greater than 10 kJ mol<sup>-1</sup> implies chemisorption (Motoyuki, 1990).

For adsorption of surfactants, a finite number of layers of surfactant may form on the surface (Samiey and Golestan, 2010), whereas BET theory allows formation of an unlimited number of layers (Brunauer, Emmett *et al.*, 1938; Atkins and de Paula, 2002). A new ‘ARIAN’ (adsorption isotherms regional analysis) equation was derived by Samiey to study bilayer isotherms, Equation 7-2. There are alternate forms of this equation also derived by Samiey for low bilayer coverage, Equation 7-2, and for monolayers, which converge as expected to a Langmuir-type equation, Equation 7-3, (Samiey and Golestan, 2010).

$$q_e = c_e \left( \frac{q_{\text{mon}} K_{\text{sa}} + 2q_{\text{mon}} x_s c_e K_{\text{sa}}}{1 + c_e K_{\text{sa}} + x_s c_e^2 K_{\text{sa}}} \right)$$

**Equation 7-2**

Here,  $q_{\text{mon}}$  is the monolayer adsorption capacity,  $K_{\text{sa}}$  is an equilibrium constant of surfactant molecules in surface aggregates of the primary layer, and  $x_s$  is an equilibrium constant of surfactant molecules in surface aggregates in all layers above the first.

If surfactant molecules adsorb mostly on the first layer,  $m_s \cong m_{s1}$ , where  $m_s$  is the mass of adsorbed surfactants and  $m_{s1}$  is the mass of adsorbed surfactant in the first layer, and Equation 7-2 can be written as:

$$q_e = c_e \left( \frac{q_{\text{mon}} K_{\text{sa}}}{1} + \frac{q_{\text{mon}}}{c_e} + \frac{q_{\text{mon}}}{x_s c_e^2} \right)$$

**Equation 7-3**

If adsorption only forms a monolayer, Equation 7-2 can be reduced to Equation 7-4, which is a Langmuir-type equation.

$$q_e = c_e \left( \frac{q_{\text{mon}} K_{\text{sa}}}{1} + \frac{q_{\text{mon}}}{c_e} \right)$$

**Equation 7-4**

Non-ionic surfactants are also able to form surface aggregates, e.g. when adsorbing onto silica-gel, and the adsorption of non-ionic surfactants is normally reversible with little hysteresis. The surfactants are unable to adsorb onto some mineral surfaces such as alumina because the surfactant is unable to disrupt the rigid water layer surrounding the substrate. Surfactants use hydrogen bonding to adsorb onto the surface, which is relatively weak in comparison with electrostatic and chemical bonds (Somasundaran and Krishnakumar, 1997; Zhang and Somasundaran, 2006).

## **7.2 Materials**

### **7.2.1 Minerals**

The minerals used in this investigation were talc and modified calcium carbonate, in forms that have been used in paper manufacture either as a paper coating or filler, and which are commercially available. Details about the chemical structure of talc and modified calcium carbonate can be found in Section 1.3.3.2 and 1.3.3.5 respectively.

In this investigation, two grades of modified natural calcium carbonate were used; LSA (lower surface area) MCC and HSA (higher surface area) MCC. Scanning electron microscope (SEM) images of freeze-dried LSA MCC, Figure 7-1, and HSA MCC, Figure 7-2, are displayed below. MCCs have hydrophilic surfaces, and each material exhibits both calcium phosphate and carbonate crystal structure as determined by X-ray powder diffraction. Mercury porosimetry of the MCC samples revealed that both have a peak in pore size at 510 nm, but that the LSA MCC is bimodal with a second peak at 91 nm.

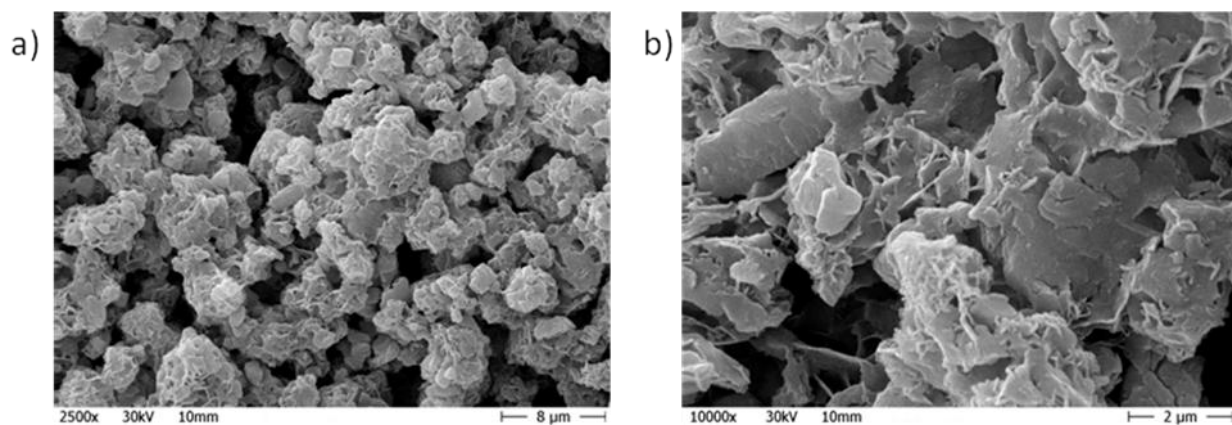


**Figure 7-1** a) SEM image of LSA MCC with 8  $\mu\text{m}$  scale bar shown. b) SEM image of LSA MCC with 2  $\mu\text{m}$  scale bar shown.

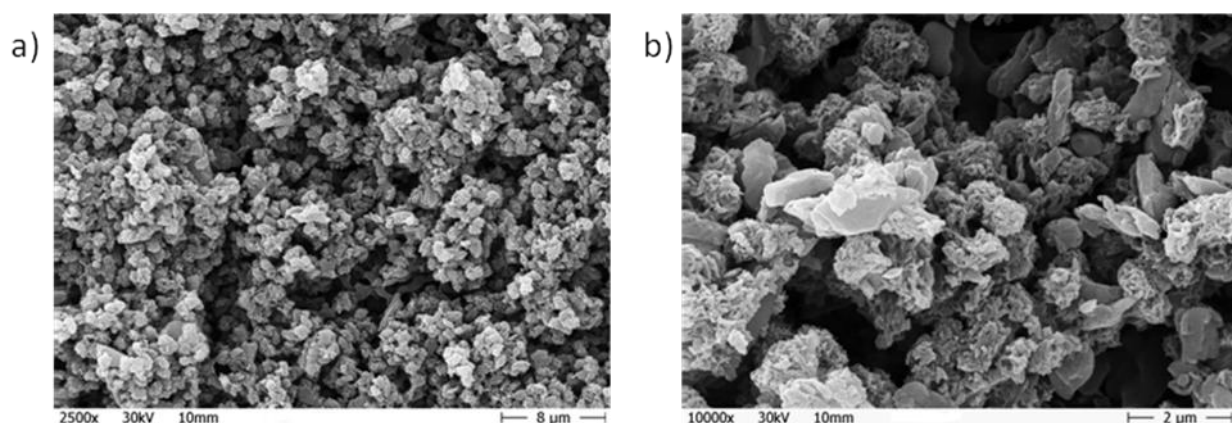


**Figure 7-2** a) SEM image of HSA MCC with 8  $\mu\text{m}$  scale bar shown. b) SEM image of HSA MCC with 2  $\mu\text{m}$  scale bar shown.

The talc used in this investigation is described in Section 6.2.1. Mondo Minerals Oy, Finland, supplied undispersed talc (Finntalc PO5), i.e. as a powder without surfactant. The feedstock for Finntalc PO5 was then processed by delaminating and grinding to give an additional talc grade, with different surface areas measured by nitrogen adsorption on a Micromeritics Gemini 2360 (Micromeritics Instrument Corp. USA) (Brunauer *et al.* 1938). The unprocessed talc is referred to as low surface area (LSA) talc and the processed talc is referred to as high surface area (HSA) talc. The method of preparation gave talcs of different aspect ratios. We recall from Section 1.3.3.2 that the aspect ratio is defined as the ratio of the largest dimension of the mineral particle relative to the smallest dimension. The particle size distribution was obtained in aqueous suspension using static light scattering measured by a Malvern Mastersizer 2000 (Malvern Instruments Ltd, UK.). The talc (refractive index (RI): 1.59, absorption

value: 0.01) was dispersed into suspension for the size measurement using polyacrylate and a wetting agent (sodium dodecyl sulphate). The results were then interpreted with Mie theory (Mie 1908) to obtain the weight-averaged particle size distribution. The mineral samples were dispersed using either water (RI: 1.33) or polyacrylate (RI: 1.49).

The MCC grades (RI: 1.59, absorption value: 0.1), LSA MCC and HSA MCC, were obtained from Omya Development AG, Switzerland. HSA MCC is a natural calcium carbonate marble treated with 20 % phosphoric acid and 5 % citric acid, which creates a surface rugosity with no significant internal pore volume. It is supplied as a dispersed product, where the dispersant once again is polyacrylate, rendering the surface on average anionic. The LSA MCC is a natural calcium carbonate chalk treated with phosphoric acid to give micro- and macro-porosity coupled with some surface rugosity. When dry, the substance acts as a porous system, with fine intra-particle and coarser inter-particle porosity. However, when in suspension, as in this study, the effect of the inter-particle porosity disappears and the substance acts as a system of porous suspended particles. The LSA MCC is supplied as an undispersed product. Table 7-1 summarises the surface area and particle size distribution of the minerals used.

**Table 7-1 Details of minerals used in this investigation.**

Name	Specific surface area ( $\text{m}^2 \text{g}^{-1}$ )	Particle Size-Weight Distribution ( $\mu\text{m}$ )		
		$d_{10}$	$d_{50}$	$d_{90}$
Low surface area talc (LSA talc)	7.13	2.24	4.50	10.1
High surface area talc (HSA talc)	45.3	1.56	5.02	21.0
Low surface area modified calcium carbonate (LSA MCC)	36.1	2.55	5.49	9.85
High surface area modified calcium carbonate (HSA MCC)	113.0	1.82	4.26	9.37

$d_N$  refers to the particle size for which N % by weight of the sample is finer.

### 7.2.2 Stickies

The two stickies selected for the present study were supplied by BASF<sup>8</sup> and are commercially available analogues of typical stickies found in a paper mill. The first is an acrylic acid ester copolymer (AAEC), product name Acronal V 212, and the second a fatty acid ester defoamer (FAED), named Afranil RS. Their solid contents of 68.3 % and 30.3 %, respectively, were measured by evaporating a known weight of sticky suspension at 130 °C until constant weight was achieved. It was assumed that no volatile organic compounds were lost in the measurement of solid content, since these materials are used in an environment where VOCs are generally minimised, and where thermal energy is frequently applied in the processes of papermaking. Both stickies investigated have hydrophilic and hydrophobic regions of the molecule, with the ester group being hydrophilic (Binks, Fletcher *et al.*, 1992) and the alkyl chain being hydrophobic (Wang, Yan *et al.*, 2007).

## 7.3 Experimental methods

Data were derived using two analytical techniques for initial concentrations of model stickies, covering the range 0.005 – 0.5 g dm<sup>-3</sup>; namely dissolved organic carbon analysis and elemental analysis.

### 7.3.1 Sticky preparation

All experiments were undertaken at room temperature (20.5 ± 1.5 °C). Both stickies were prepared to form colloidally stable suspensions in Millipore Milli-Q water with an initial dry weight concentration of 0.5 g dm<sup>-3</sup>. The initial pH was between 7 and 7.5 and initial conductivity was in the range of 1 000 to 1 500 µS cm<sup>-1</sup>. They were adjusted to

---

<sup>8</sup> BASF plc P.O. Box 4, Earl Road, Cheadle Hulme, Cheadle, Cheshire, U.K.

these ranges where necessary using dilute analytical grade hydrochloric acid, analytical grade sodium hydroxide and laboratory grade sodium chloride (all supplied by Thermo Fisher Scientific UK).

These sticky suspensions were then diluted in Milli-Q water to 0.1, 0.05, 0.01 and 0.005 g dm<sup>-3</sup>. Minerals were added to the sticky suspensions as slurries (solid contents 8 – 10 %) to give a concentration of 1.93 – 2.22 g dm<sup>-3</sup>. The pH and conductivity were not controlled during the experiments.

Resulting suspensions were agitated for 30 min at 150 min<sup>-1</sup> on an orbital shaker before minerals with adsorbed stickies were removed by centrifuging at 2 000 g for 15 min. The mineral with adsorbed sticky collected after centrifuging was freeze-dried for two days, then transferred to air-tight bags for storage (under desiccation) prior to analysis.

### **7.3.2 Dissolved organic carbon analysis**

Dissolved organic carbon analysis was performed using standard operating procedures (Badr, Achterberg *et al.*, 2003; Pan, Sanders *et al.*, 2005), as detailed in the Section 2.4.4. Dissolved organic carbon (DOC) analysis was performed with a Shimadzu TOC-5000A total organic carbon analyser coupled to a Shimadzu ASI-5000 autosampler (Shimadzu Corp. Japan).

### **7.3.3 Elemental analysis**

The elemental analysis was performed on a Carlo Erba EA-1110 CHNS elemental analyser, (Thermo Fisher Scientific, USA), using standard operating procedures, as described in Section 2.4.5.

### **7.3.4 Turbidity**

The turbidity of the sticky suspensions, mineral suspensions and sticky and mineral suspensions were measured on a Hach DR/890 Colorimeter (Hach Company, USA). More details about the technique can be found in Section 2.4.1.

### **7.3.5 Zeta potential**

The zeta potential of the  $0.5 \text{ g dm}^{-3}$  sticky suspensions was measured on a Zetasizer Nano (Malvern Instruments Ltd, UK.) before the mineral was added, and after the mineral with adsorbate was removed by centrifugation. The zeta potential gives a measure of the coulombic stability of the colloidal suspensions, and how the stability of the remaining suspension changed because of the adsorption of sticky onto mineral surfaces. A change in magnitude of the zeta potential was also useful in determining if cationic or anionic species were adsorbed preferentially (Hunter, 1981). More details about the technique can be found in Section 2.4.6.

### **7.3.6 Data presentation and analysis**

Dissolved organic carbon analysis gives the carbon content remaining in solution after adsorption of the sticky occurs and the mineral has been removed by centrifuging. The equilibrium carbon concentration on the surface of the mineral is determined by elemental analysis. The elemental analysis results are normalised to allow for the change in mass encountered because of adsorption of the respective sticky, i.e. the fatty acid ester defoamer and acrylic acid ester copolymer. The elemental analysis results are also corrected for the carbon content found in the minerals themselves.



The values for the dissolved carbon and elemental analysis, representing proxies for the adsorbed sticky, represent two techniques which are independent of each other. It is also possible to convert the carbon values into absolute values of sticky concentration using a calibration series of dissolved organic carbon measurements, and then using mass balance calculations for the concentrations of the species adsorbed onto the surfaces. However, once presented in this way, the variables are no longer independent of each other, so we have not used this method of data analysis in this work.

## ***7.4 Results and discussion***

Each of the individual samples was analysed in triplicate, and the resulting data used to generate error bars showing two standard deviations either side of the mean. As can be seen in the Figures 7-3, 7-4, 7-5, 7-8, 7-9 and 7-10 the error bars are typically small for the techniques employed, indicating consistent and reproducible results. The three-stage fitting of adsorption isotherms is discussed below.

Although it might be considered that the most appropriate model for fitting the results is the ARIAN bilayer model, since the authors of the ARIAN model fitted it only to stage III of their data, it is unlikely that the model can describe a complete range of adsorption. Fits to the whole range of our data did not, in general, properly represent the stages we observed; the fits are available in Appendix D. The first two stages of adsorption can however, be acceptably modelled using the D-R equation. This allows us to derive suitable values for the energy of adsorption and subsequent characterisation of the adsorption into physisorption or chemisorptions. Therefore, as explained above, we used the Langmuir isotherm (Langmuir, 1918) (Equation 7-5) as a means of providing a smooth trend to our data, and of calculating asymptotes. Aqueous concentrations ( $c_e$ ) were plotted against the aqueous phase concentrations divided by adsorbed

concentration ( $q_e$ ). From the line of best fit it was then possible to calculate the maximum amount adsorbed ( $q_{\max}$ ) and the equilibrium constant ( $K$ ), Table 7-2.

$$\frac{c_e}{q_e} = \frac{c_e}{q_{\max}} + \frac{1}{Kq_{\max}}$$

Equation 7-5

**Table 7-2 Comparison of regression coefficient  $R^2$  and significance  $p$  values of the gradient for fatty acid ester defoamer (FAED) and acrylic acid ester copolymer (AAEC) isotherms.**

Mineral	Adsorbate	Single isotherm		Stage I		Stage II		Stage III	
		$R^2$	$p$	$R^2$	$p$	$R^2$	$p$	$R^2$	$p$
LSA Talc	FAED	0.221	0.0119	0.795	<0.0001	0.686	0.0260	0.618	0.0015
HSA Talc	FAED	0.300	0.0033	0.710	0.0009	0.892	0.0029	0.896	<0.0001
LSA MCC	FAED	0.698	<0.0001						
HSA MCC	FAED	0.527	<0.0001	0.988	<0.0001	0.661	0.0047		
LSA Talc	AAEC	0.854	<0.0001	0.970	<0.0001	0.993	0.0001		
HSA Talc	AAEC	0.324	0.0022	0.818	<0.0001	0.985	<0.0001	0.695	0.024
LSA MCC	AAEC	0.663	<0.0001						
HSA MCC	AAEC	0.681	<0.0001	0.584	0.0001	0.809	0.0093		

The statistical justification for the multi-stage fits is shown in Table 7-2. It can be seen that the regression coefficient  $R^2$  (corrected for the number of data points) increases considerably when multiple stages are fitted. The confidence level of the fit is always better than 95 % (i.e.  $p < 0.05$ ) and in most cases better than 99 %. The first stage is arbitrarily defined as linear when three stages are fitted, as there are insufficient low concentration data to fit a Langmuir isotherm with confidence, and stages II and III are both Langmuir.

Due to the presence of both hydrophilic and hydrophobic mineral surfaces, and the colloidal nature of the adsorbate, it was expected that a single Langmuir isotherm would be inadequate for describing the adsorption process. Visual inspection of Figure 7-3, Figure 7-4, Figure 7-8 and Figure 7-9, confirms that there are distinct adsorption stages.

The D-R adsorption energies calculated using Equation 7-1 are much lower than  $200 \text{ J mol}^{-1}$ , Table 7-3 implying that physisorption (Motoyuki, 1990) is the adsorption mechanism for forming a sticky monolayer.

**Table 7-3 Table of Dubinin-Radushkevich characteristic energies.**

	Fatty acid ester defoamer J mol <sup>-1</sup>	Acrylic acid ester copolymer J mol <sup>-1</sup>
LSA Talc	36.1	162
HSA Talc	32.4	64.8
LSA MCC	71.6	50.8
HSA MCC	71.2	46.2

#### **7.4.1 Adsorption of fatty acid ester defoamer on mineral surfaces**

The carbon concentrations, as a proxy for the concentrations of the fatty acid ester defoamer, adsorbed onto LSA and HSA talc are shown on a mass basis and as a function of ester defoamer remaining in solution in Figure 7-3, and on a surface area basis in Figure 7-4. The figures show that HSA talc adsorbed more efficiently than LSA talc per unit mass, Figure 7-3, but less efficiently per unit surface area, Figure 7-4. It is likely that the geometrical size ratio plays a role, i.e. the finer HSA talc is probably adsorbing onto larger destabilised stickies, whereas the coarser LSA talc is likely able to remain as single particles with sticky adsorbed.

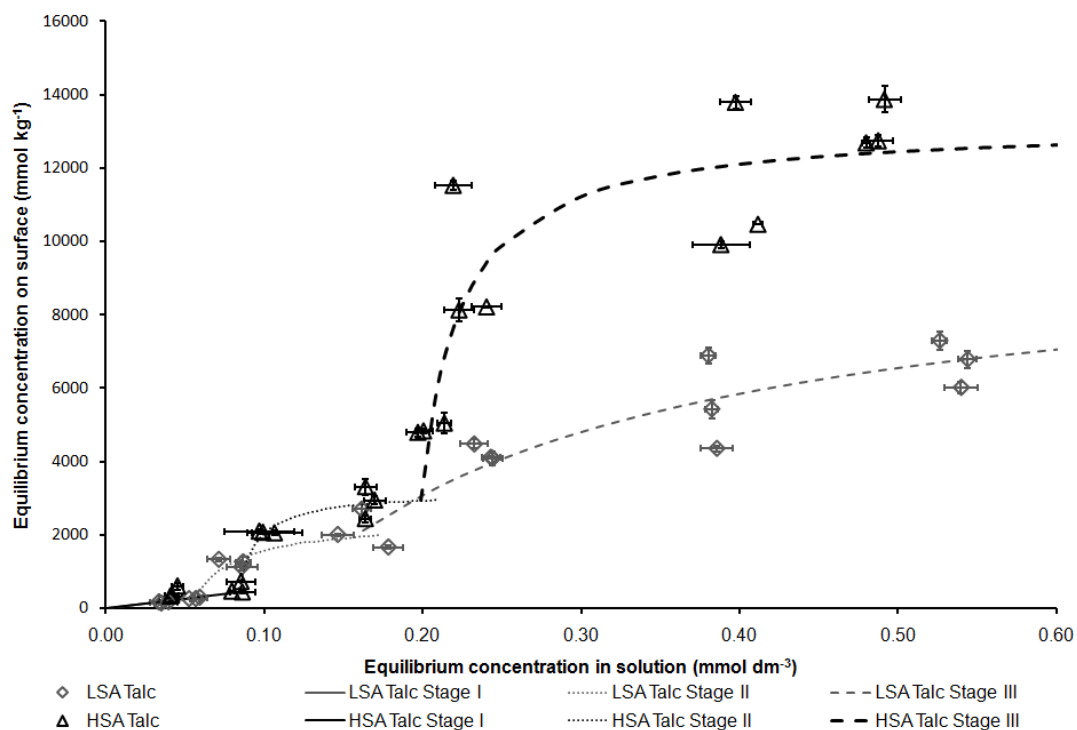


Figure 7-3 Adsorption of the fatty acid ester defoamer onto LSA and HSA talc.

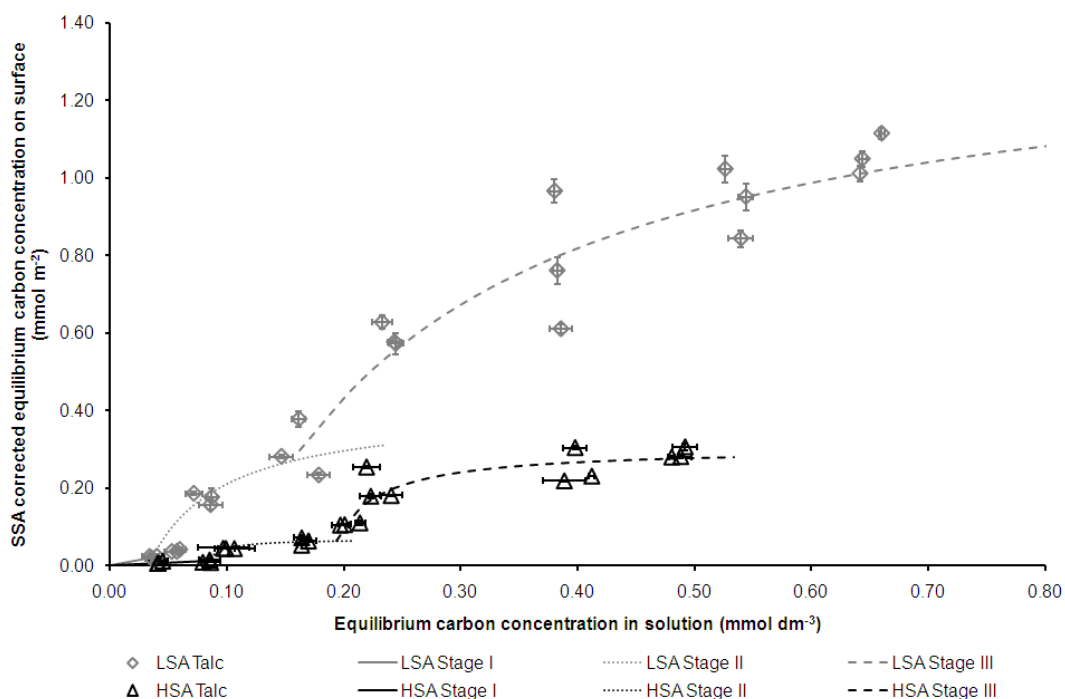
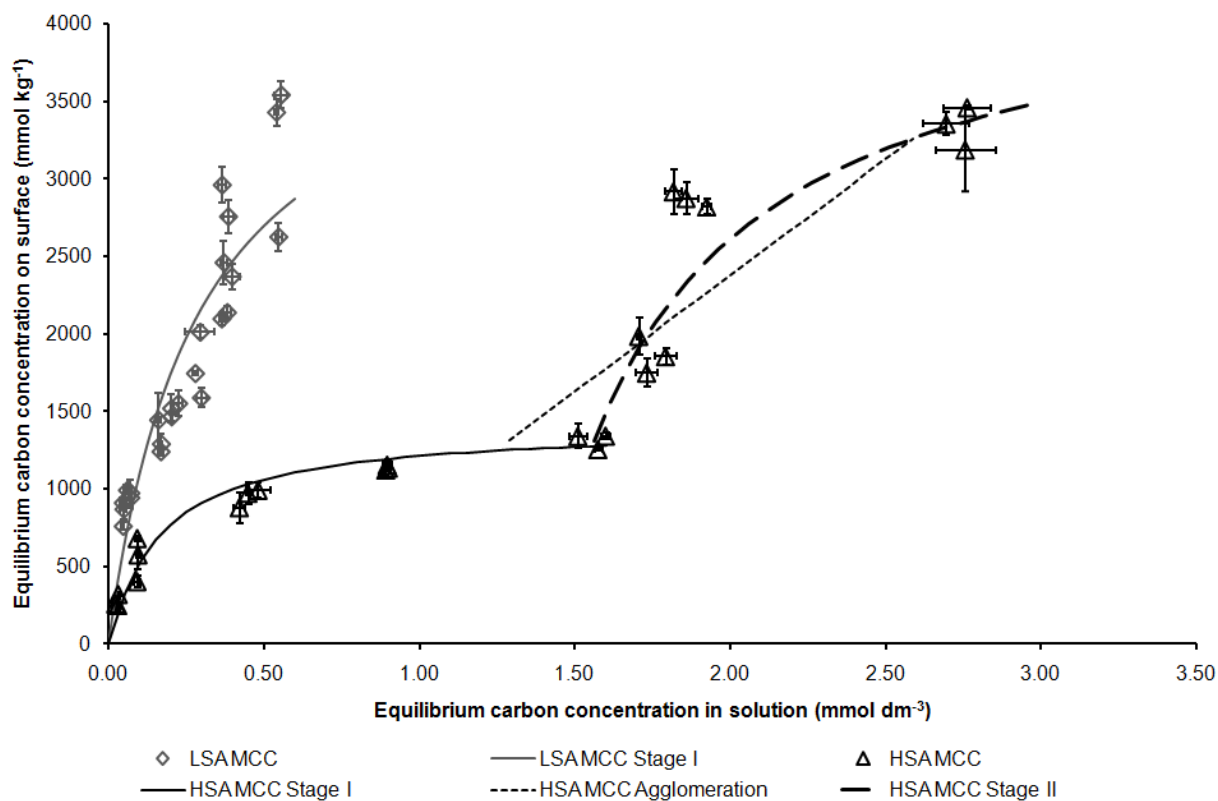


Figure 7-4 Adsorption of the fatty acid ester defoamer onto LSA and HSA talc, after correction for specific surface area.

Figure 7-5 shows the extent of adsorption of fatty acid ester defoamer onto the two types of MCC. The results show that the HSA MCC does not adsorb the sticky as well, per unit mass, as the LSA MCC. The LSA MCC range could not be extended in respect

to adsorbate, due to visible deposits forming on glassware at concentrations greater than  $0.5 \text{ g dm}^{-3}$ .



**Figure 7-5 Adsorption of fatty acid ester defoamer onto LSA MCC and HSA MCC.**

An explanation for the adsorption stages encountered for talc and the MCC can be suggested using knowledge of the structure of a fatty acid ester molecule, which we suggest forms a dimer when present in water to increase the stability of the molecule (Silva, Sobral *et al.*, 2007; Paturej and El Fray, 2009)

In Figure 7-3 and Figure 7-4 the adsorption of the fatty acid ester species onto talc has been divided into three distinct stages; each of the stages has a different adsorption mechanism proposed due to the heterogeneity of talc and fatty acid ester defoamer. Before adsorption can occur, we suggest that hydroxide groups may leave the edges of the talc and enter solution. Magnesium hydroxide has an alkaline dissociation constant ( $pK_b$ ) of 2.60 at 25 °C (Lide (eds), 2004). However, it is also possible for the magnesium hydroxide to be protonated by a hydronium ion forming  $\text{OH}_2^+$ , which is

more likely in acidic conditions (Guyard, Daneault *et al.*, 2006) similar to how a silica gel would adsorb (Parida and Mishra, 1998). For both mechanisms a positively charged species is available for adsorption, either  $Mg^{2+}$  or  $OH_2^+$ , so the mechanism will not change. The first adsorption stage occurs over a limited aqueous concentration range with no significant adsorption for either talc grade. We suggest the initial adsorption stage uses a dimeric form of the fatty acid ester defoamer adsorbing on the hydrophilic edges of the talc, Figure 7-6.

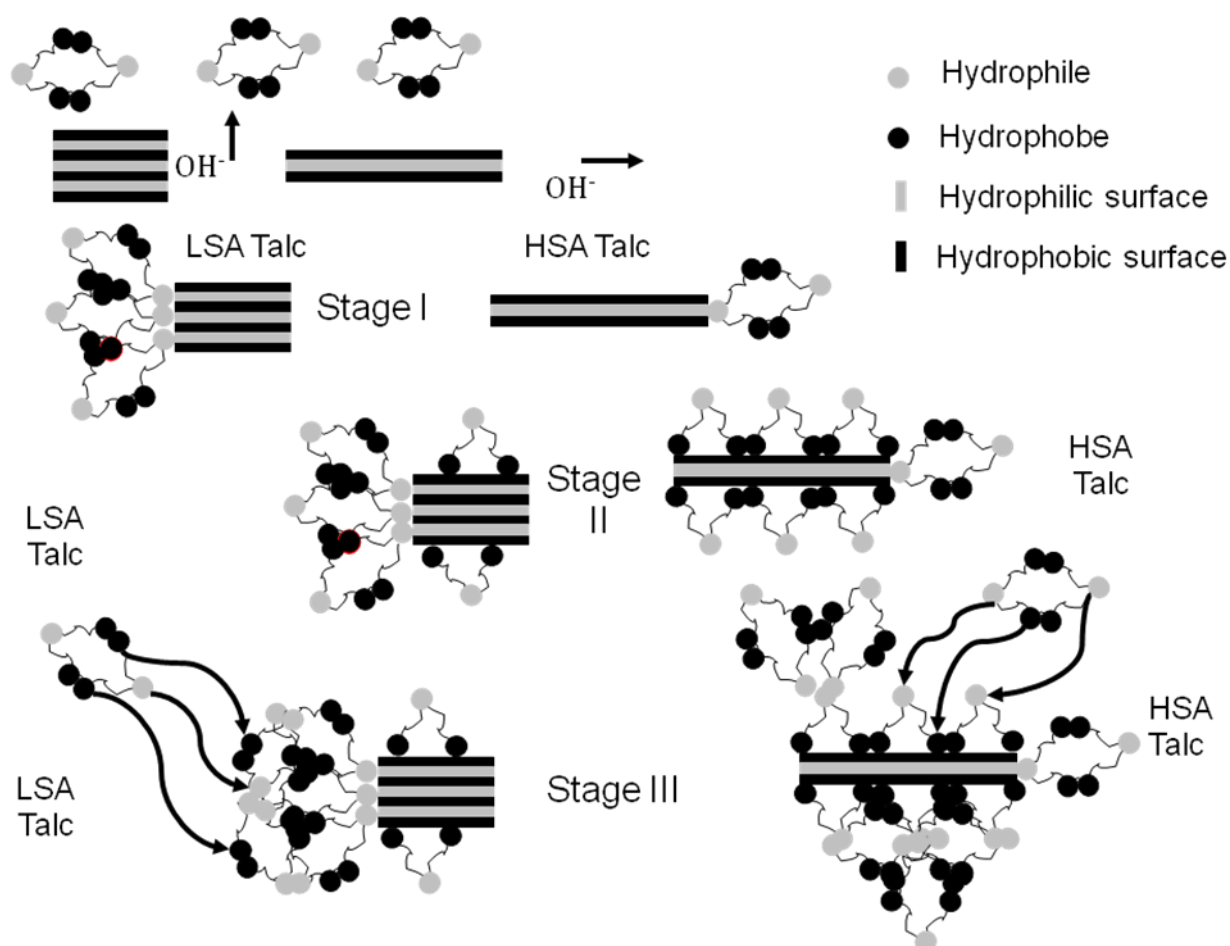


Figure 7-6 Schematic showing a possible mechanism for the adsorption of a fatty acid ester defoamer onto LSA and HSA surface area talc, respectively. For clarity, the size of the ester molecule has been enlarged relative to the talc.

The second stage involves the adsorption of the hydrophobic ends of single (undimerised) molecules onto the hydrophobic regions of the surface to form a sticky monolayer. As explained previously, the HSA talc has a higher aspect ratio and, therefore, a higher ratio of hydrophobic surface area relative to hydrophilic surface area for a given particle size (Wallqvist, Claesson *et al.*, 2006; Wallqvist, Claesson *et al.*,

2007). The higher stage II adsorption for HSA talc shown in Figure 7-4 supports the assertion that stage II is predominantly occurring at the hydrophobic surfaces, which dominate in terms of surface area, Figure 7-6. We suggest that the third adsorption stage involves the formation of an additional monolayer of appropriately orientated fatty acid ester defoamer molecules, as shown. We propose only one additional monolayer as the high relative permittivity of water would quench further adsorption (Jones and Or, 2002).

Figure 7-5 shows the adsorption isotherms for LSA MCC and HSA MCC. Adsorption onto the LSA MCC follows a single Langmuir isotherm, implying monolayer adsorption. The HSA MCC results show two distinct stages, which the data suggest is monolayer adsorption, Figure 7-7, followed by multi-layer adsorption and partial aggregation of the mineral-with-adsorbent species. The fatty acid ester molecules are supplied with surfactant, so will not aggregate with each other. The HSA MCC is dispersed using polyacrylate, and the carbon content of the polyacrylate is taken into consideration during data analysis. The LSA MCC has no surfactant, but the experiment could not be carried out at higher concentrations, as explained previously.

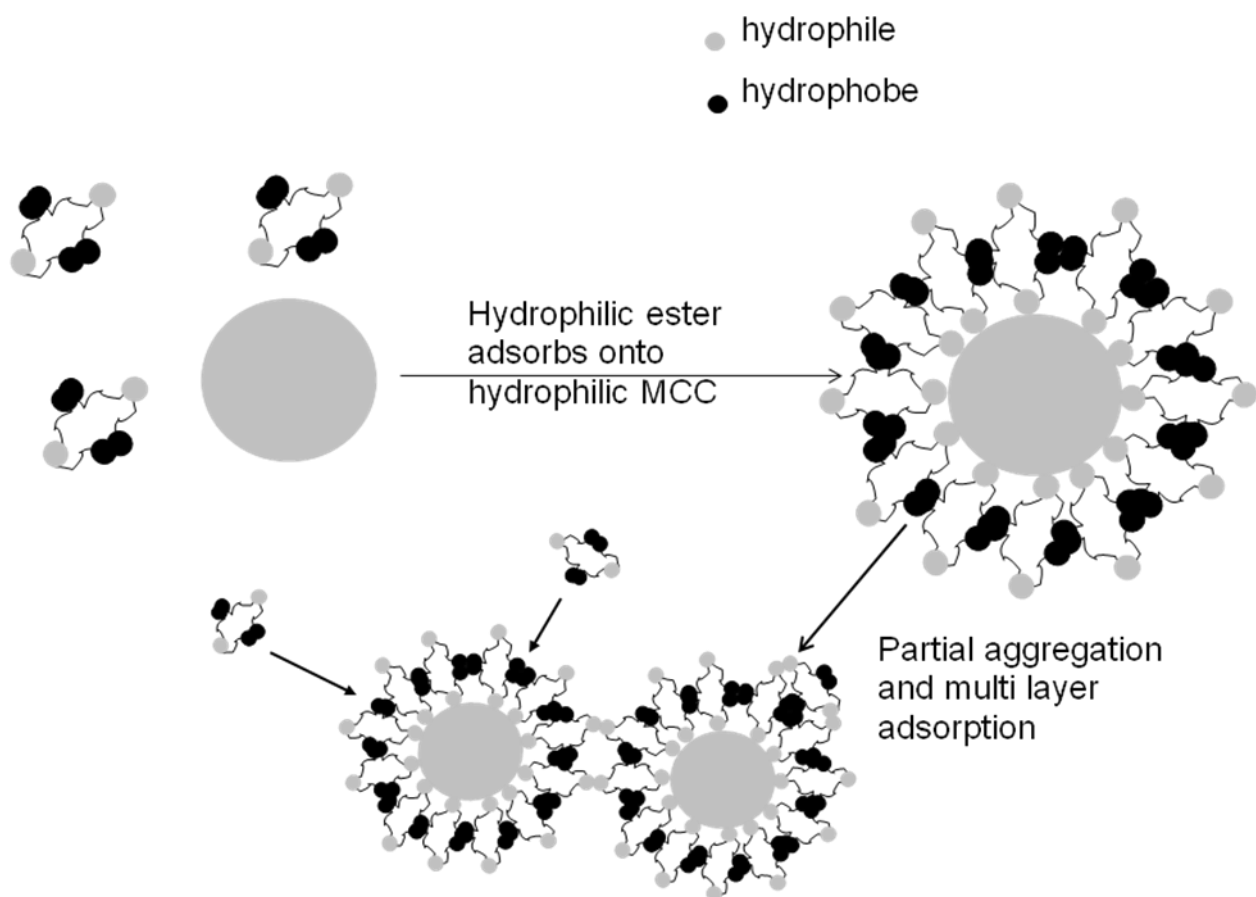


Figure 7-7 Schematic showing proposed adsorption mechanism for a fatty acid ester defoamer onto modified calcium carbonate (MCC) or a completely hydrophilic mineral. For clarity, the size of the ester molecule has been enlarged relative to the MCC.

#### 7.4.2 Adsorption of acrylic acid ester copolymer on mineral surfaces

Figure 7-8 shows the adsorption of the acrylic acid ester copolymer onto the LSA and HSA talc. As expected, the HSA talc is significantly better per unit mass of talc at adsorbing the acrylic acid ester copolymer than the LSA talc. Figure 7-9 shows the acrylic acid ester copolymer adsorption after correction for specific surface area. Figure 7-10 shows the adsorption of the acrylic acid ester copolymer onto the MCCs, with a greater adsorption per unit mass onto the LSA MCC.



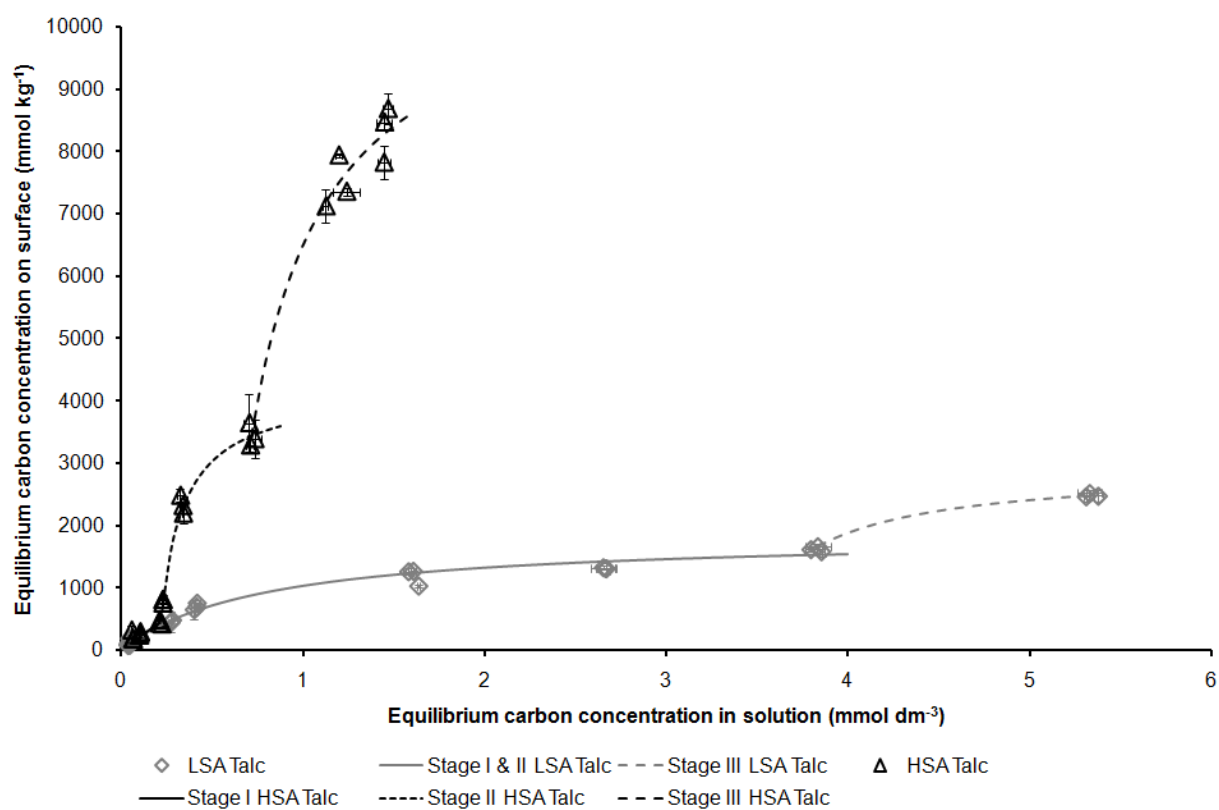


Figure 7-8 Adsorption of acrylic acid ester copolymer onto LSA and HSA talc.

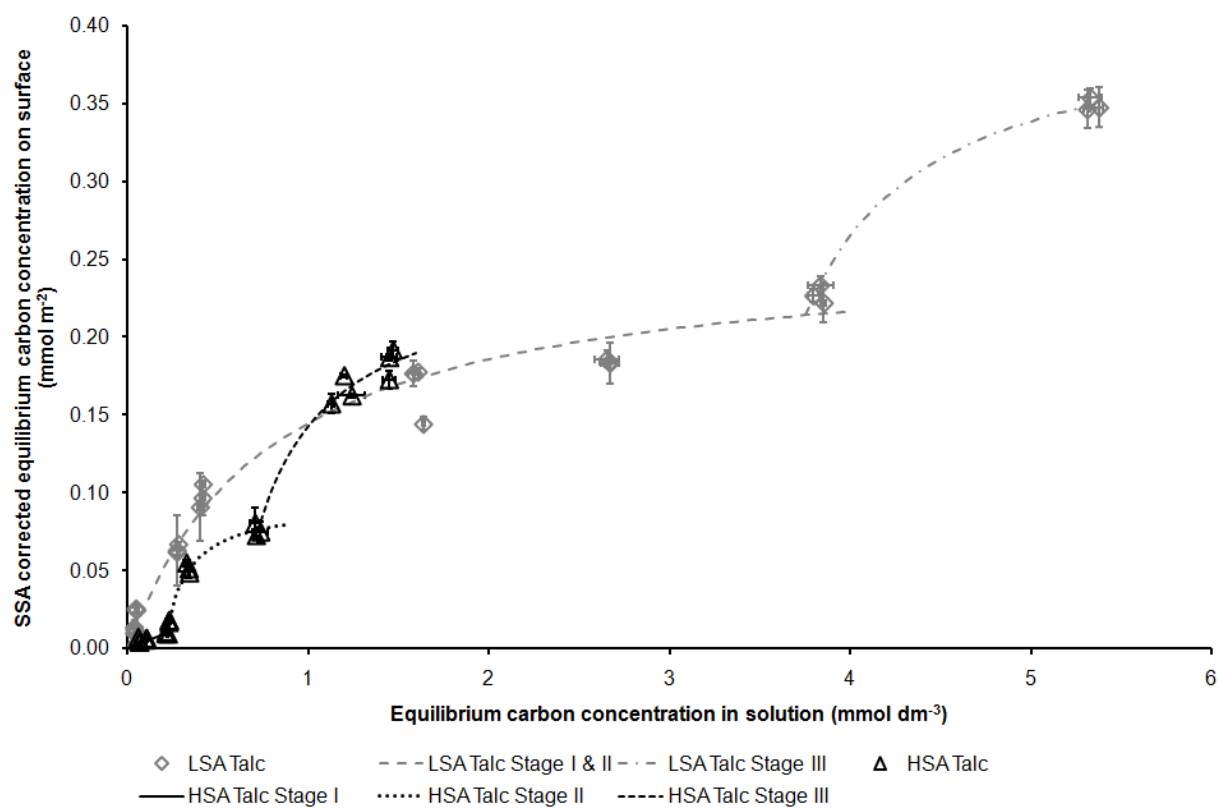
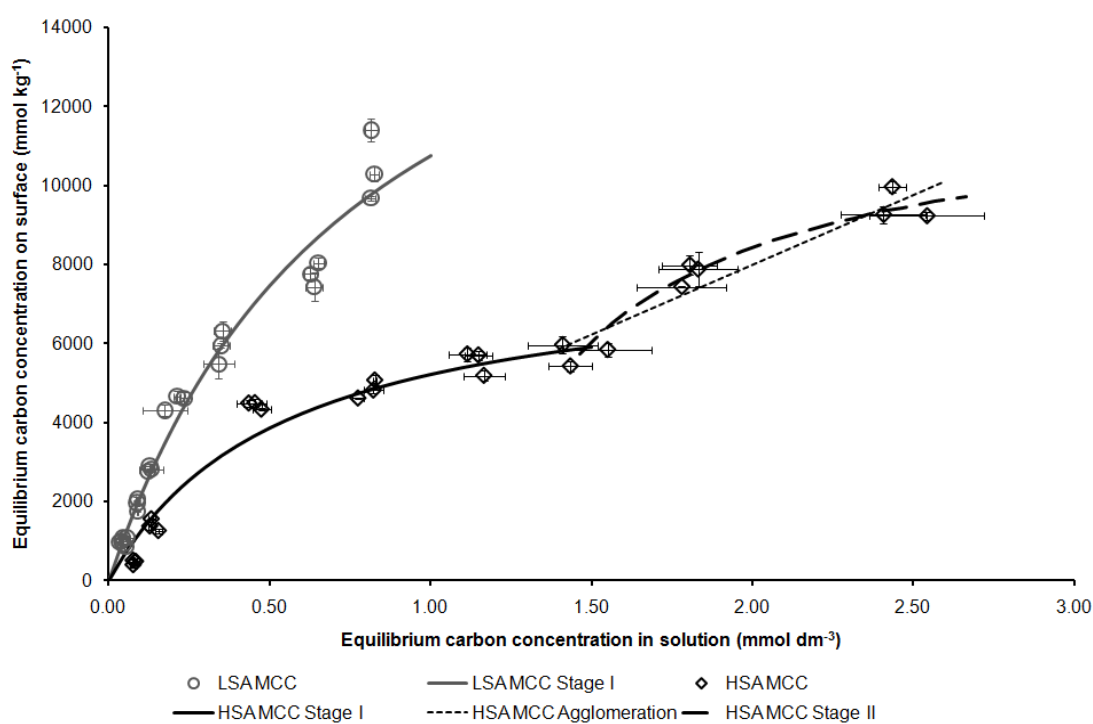
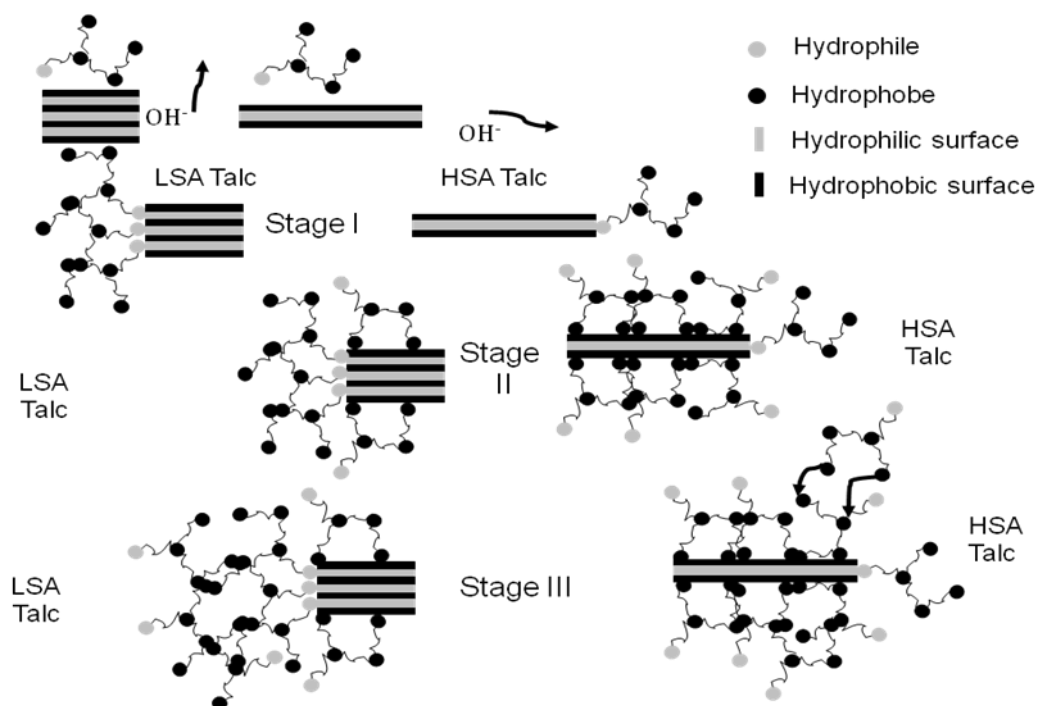


Figure 7-9 Adsorption of an acrylic acid ester copolymer onto LSA and HSA-talc corrected for the specific surface area of the talc.

In Figure 7-8 and Figure 7-9 the first stage results show that adsorption is greater for the LSA talc than HSA talc, suggesting that adsorption is occurring at the hydrophilic edges, Figure 7-11. The HSA talc results exhibit two distinct stages of adsorption; the first stage is hydrophilic adsorption, and the second stage is hydrophobic adsorption, because HSA talc adsorbs more than the LSA talc. The third stage is assumed to be adsorption of an additional monolayer of sticky.



**Figure 7-10** Adsorption of an acrylic acid ester copolymer onto LSA MCC and HSA MCC.



**Figure 7-11** Schematic showing proposed adsorption mechanism for an acrylic acid ester copolymer onto LSA and HSA talc. For clarity, the size of the ester molecule has been enlarged relative to the talc.

In Figure 7-10 the results show adsorption onto the LSA MCC, and the first and second stage of the adsorption onto HSA MCC can be usefully fitted using Langmuir relations. During the second HSA MCC stage, the turbidity increased, which implies partial aggregation. The Langmuir isotherm allows the calculation of the maximum adsorption values for each adsorption stage. The acrylic acid ester copolymer adsorbing onto HSA MCC gives maximum adsorption values of  $q_{\max,1} = 8\,050 \text{ mmol kg}^{-1}$  and  $q_{\max,2} = 12\,200 \text{ mmol kg}^{-1}$  for the 1<sup>st</sup> and 2<sup>nd</sup> stage, respectively. For both stages of adsorption to be following Langmuir behaviour,  $q_{\max,2}$  would need to be at least double  $q_{\max,1}$ . Some multi-layer adsorption does occur, but the absence of this clear relationship between  $q_{\max,1}$  and  $q_{\max,2}$  suggests that aggregation takes place during the 2<sup>nd</sup> stage, Figure 7-12.

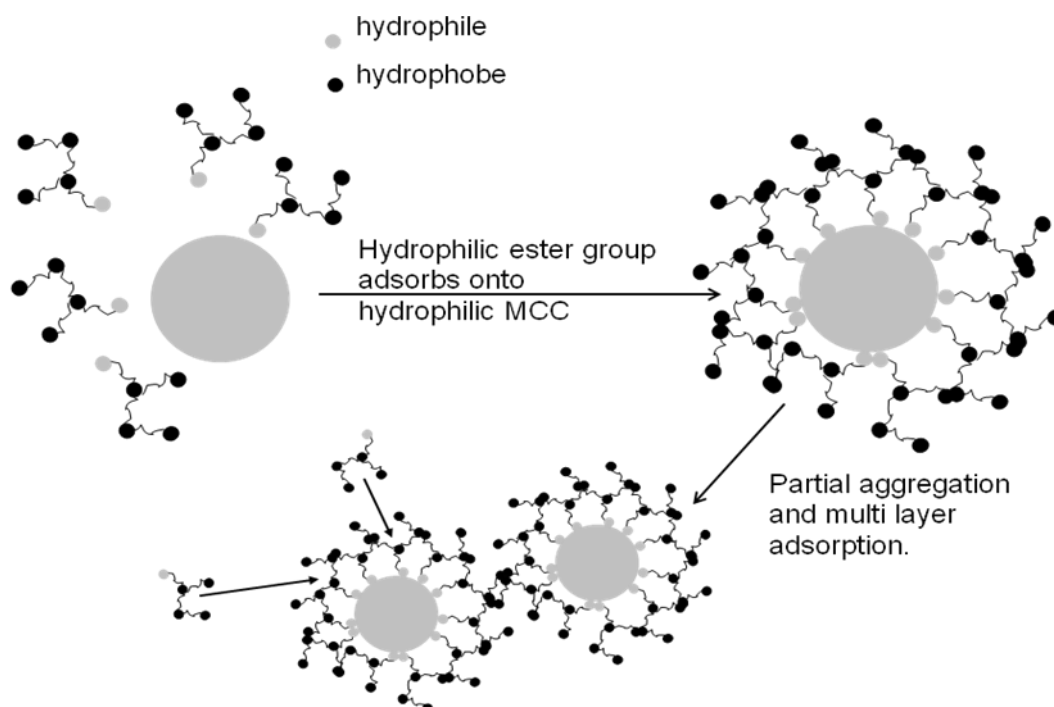


**Figure 7-12** Schematic showing proposed adsorption mechanism for acrylic acid ester copolymer onto modified calcium carbonate or a hydrophilic mineral. For clarity, the size of the ester molecule has been enlarged relative to the MCC.

Some of the differences between the LSA and HSA MCC can be explained by the differences in particle size. When a sticky particle is close to the size of the mineral particle the adsorption capacity decreases, as fewer sticky particles need to be adsorbed to reach saturation of the mineral particle. As the particle reaches saturation more quickly there will be more mobile sticky in suspension promoting aggregation at higher concentrations.

### 7.4.3 pH, conductivity, zeta-potential and turbidity

The pH of the suspension at the beginning of the experiment remained constant at 7.40, to within 0.51, on adsorption of the fatty acid ester defoamer. For adsorption of the acrylic acid ester copolymer, it remained constant to within 0.14 from the starting pH of 7.32. The conductivity decreased for both sticky suspensions after adsorption, in line with fewer charged particles remaining in suspension. For the fatty acid ester defoamer the conductivity decreased from  $1\,034\ \mu\text{S cm}^{-1}$  before adsorption to  $812 - 826\ \mu\text{S cm}^{-1}$  after adsorption, and the acrylic acid ester copolymer decreased from  $1\,133\ \mu\text{S cm}^{-1}$

before adsorption to  $958 - 984 \mu\text{S cm}^{-1}$  after adsorption. The reduction in the electrical conductivities of the solution after the adsorption supports the assumption that charged species were removed from solution or suspension.

The zeta potential results, Figure 7-13, for both sticky types show differences between the talc grades. For the fatty acid ester defoamer the zeta potential of the remaining unadsorbed species was more negative than the starting species, showing that the less charge-stable species have been adsorbed and the more charge-stable species left in suspension, as might be expected.

The zeta potential changes for the acrylic acid ester copolymer adsorptions were different for the two talc grades. The zeta potential of the supernatant above the LSA talc did not change significantly after adsorption. The zeta potential of the HSA talc is slightly less negative. This implies that, for the LSA talc, equal quantities of anionic and cationic species were removed by adsorption, whereas the HSA talc preferentially adsorbed more anionic species (i.e. species more negatively charged at their shear planes). This deduction is in accord with the differences in adsorption characteristics shown in Figure 7-8. HSA talc shows three distinct stages. However, because of the adsorption of both anionic and cationic species onto the LSA talc, stages I and II are merged.

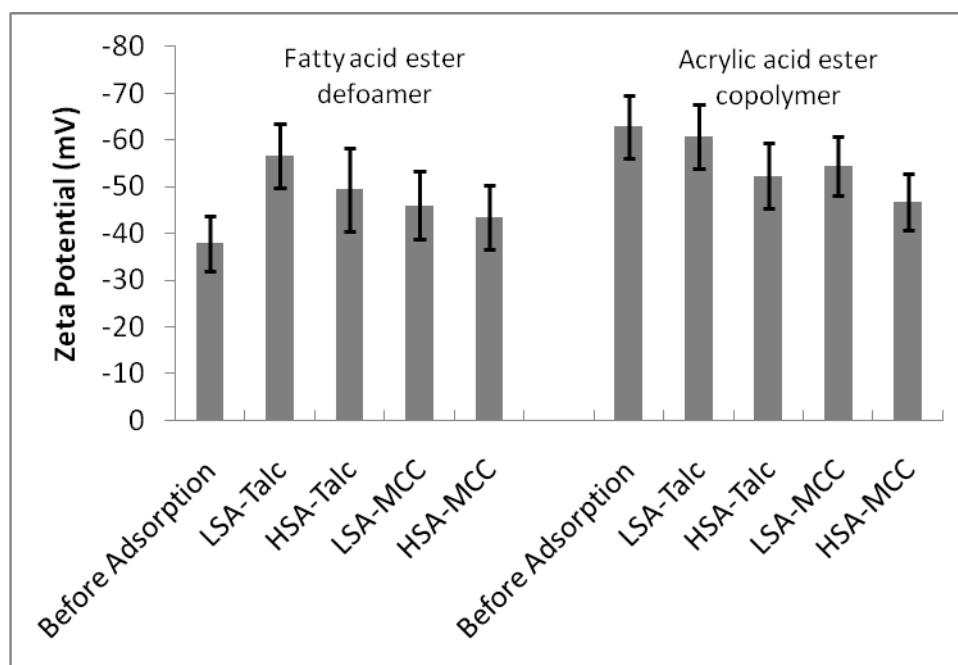


Figure 7-13 Mean zeta potentials of the supernatant suspensions before adsorption of a fatty acid ester defoamer and acrylic acid ester copolymer, and after adsorption onto the minerals shown and deposition of the mineral / adsorbate species by centrifuging. The sticky suspension being adsorbed was  $0.5 \text{ g dm}^{-3}$ , which saturates the mineral. The error bars indicate the standard deviation of the zeta potential distribution at 50 % of the maximum height of the distribution.

The interpretation of the adsorption onto the two modified calcium carbonate (MCC) grades is more complicated. It can be seen that they behave differently towards the defoamer (on the left of Figure 7-13) and the copolymer. The differences suggest that there must be both cationic and anionic adsorption sites on MCC. The defoamer adsorbs preferentially onto the anionic sites of LSA MCC, leaving the supernatant with a more negative zeta potential, whereas the copolymer adsorbs preferentially onto the cationic sites, leaving the supernatant with a lower (more positive) zeta potential than at the start of the experiment. Similarly, the defoamer adsorbs preferentially onto the anionic sites of HSA MCC, and the copolymer adsorbs even more preferentially onto the cationic sites of the HSA MCC. The conductivity changes confirm that charged species were removed from suspension during the experiment, but do not indicate whether the species are anionic or cationic.

The aggregation of mineral and sticky suspension is supported by turbidity changes during the adsorption experiment. For the higher sticky concentration experiments, the

turbidity for the HSA MCC with both model stickies increased during the thirty minutes the suspension was reaching equilibrium before it was centrifuged. During this time, by mass conservation, the term  $v_c$  in Equation 2-3 will remain constant. Therefore, an increase in turbidity must have been caused by an increase in the volume  $v$  of particles, indicating aggregation. However, this aggregation is slight, at only 1.3 – 1.4 %. By contrast, no turbidity change, and hence no aggregation, was observed for the LSA MCC. As stated previously, the LSA MCC experiment could not be carried out at the higher end of the sticky concentration because of adsorption onto the glassware. This provides a likely explanation of why no aggregation was seen.

## ***7.5 Conclusions***

This investigation used commercially available suspensions of model stickies, with undefined surfactants, in a laboratory system to determine adsorption onto mineral surfaces representing an in-situ industrial environment. The results suggest multistage adsorption. Multi-step Langmuir isotherms were used to describe adsorption onto different mineral systems, comparing the hydrophobic planar and hydrophilic edge surfaces of talc, and hydrophilic MCCs. Possible adsorption mechanisms have been proposed for sticky systems, which explain the results. The most efficient adsorbent of the fatty acid ester defoamer was the HSA talc per unit mass, due to the presence of a high surface area of hydrophobic surfaces. The most efficient at adsorbing the acrylic acid ester copolymer was the LSA-MCC. Additionally, the use of the chosen adsorbates enabled a description of the MCC surface charge balance to be derived in terms of coexisting anionic and cationic charge.

The results reported used a novel proxy method to allow the construction of adsorption isotherms of commonly found colloidal contaminants in a paper recycling environment,

which have significant implications in the industry. The proxy method has a wide applicability for the study of the complex adsorption systems.

#### **7.5.1 Highlights (Gribble, Matthews *et al.*, 2010a)**

- Stickies can be adsorbed onto the minerals within the recycled paper.
- Complex adsorption in paper mills can be studied using a proxy method.
- Fatty acid ester defoamer was best adsorbed by high surface area talc.
- Acrylic acid ester copolymer was best adsorbed by modified calcium carbonate.



## 8 Overview

The aim of this final chapter is to give a brief overview of the whole research project, and to suggest directions for future work. The research project involved characterisation of minerals, both porous and non-porous, and then using the minerals for the adsorption of model ‘stickies’ to improve the recycling of paper.

In chapter 3 different techniques were used to characterise the pore architecture of filter media. The techniques used included porometry, mercury porosimetry, scanning electron microscopy with two-dimensional image analysis. The chapter also included modelling of the porometry and mercury porosimetry data with Pore-Cor RS. The modelling results presented in chapter 3 included porometry measurements for the very first time. The filter media investigated had different structural characteristics, with some of the filter media being bimodal. Chapter 3 also characterised the different levels of pore architecture into four levels analogous to protein structure:

- Primary – distribution of void and throat sizes
- Secondary – connectivity of the voids
- Tertiary – relationship between the sizes of voids and the sizes of their immediate connecting neighbours
- Quaternary – size auto-correlations and gradations over the sample as a whole

The individual experimental techniques described in chapter 3 are suitable for characterisation of the primary architecture of voids, but it is very difficult to obtain information about the higher levels of structure. Chapter 3 showed that by using a combination of experimental and modelling techniques the higher level pore architecture is obtainable and the extra information obtained can then be used to improve simulations of other properties such as filtration or diffusion.

In chapter 4 three different grades of calcium carbonate were investigated using four types of technique; gas adsorption, absorption, SEM and porosimetry. The techniques were used to characterise the surface and porous structure of the calcium carbonates. The three grades of calcium carbonate were a ground calcium carbonate and two modified calcium carbonate grades. The absorption behaviour of the two modified calcium carbonate grades were different, and the additional experiments were to understand the differences between the wetting mechanisms. The ground calcium carbonate and dual porous modified calcium carbonate have a wetting mechanism divided into two stages, (short term and long term). The high surface area modified calcium carbonate only has a one stage wetting mechanism, which was abnormally fast when looking at the pore size distribution determined using mercury porosimetry.

Images of the calcium carbonate were obtained using SEM, an obvious difference is the lack of porosity of the ground calcium carbonate relative to the modified calcium carbonates. However, the SEM could not identify significant differences between the modified calcium carbonate grades. The three calcium carbonate grades were then analysed using the BJH algorithm to determine the pore sizes and to check for nano porosity. The ground calcium carbonate gas adsorption experiment showed no hysteresis for nitrogen or *n*-butane, so implied a non-porous material. The modified calcium carbonate results from both gas adsorption experiments showed hysteresis, with significant hysteresis identified for the high surface area modified calcium carbonate. The hysteresis implied the presence of nano features for both modified calcium carbonates. The BJH analysis of the desorption curve provided the pore volume and pore area of the nano features, and comparison of the BJH total pore area and BET specific surface area for the high surface area modified calcium carbonate implied the presence of ink-bottle pores (pores with only one connection). These ink-bottle pores provide additional nano rugosity that changes the wetting contact angle, thereby

improving the wetting performance of the high surface area modified calcium carbonate.

In chapter 5 a zero length column was developed to study the diffusion and desorption of benzene from a calcium carbonate stationary phase. The experiments used three grades of calcium carbonate to determine how desorption and diffusion changed when using a non-porous ground calcium carbonate and porous modified calcium carbonate. The experimental results were also compared with a simulation of diffusion from a unit cell generated in Pore-Cor RS from mercury porosimetry experimental data. A comparison of the gradients of the desorption curves showed that desorption was not the rate limiting step. The results also showed the dual porous modified calcium carbonate allowed benzene to diffuse more quickly than the high surface area modified calcium carbonate. The differences were attributed to greater steric hindrance from the nano features of the high surface area modified calcium carbonate. The comparison with the model showed that the model needs improvement to account for surface effects that affect the rate of diffusion, such as surface diffusion, and adsorption / desorption.

In chapter 6, different experimental techniques were compared to ascertain their suitability for determining the concentration of stickies in aqueous suspension or adsorbed onto a mineral surface, specifically the surfaces of talc, modified calcium carbonate and bentonite. A comparison was made of the advantages and disadvantages of the individual techniques. The work was then expanded by combining dissolved organic carbon analysis and elemental analysis results to construct adsorption equilibrium constants.

The techniques used to investigate the removal of stickies from aqueous suspension by adsorption were turbidity, chemical oxygen demand, gravimetric analysis, dissolved organic carbon analysis and total dissolved nitrogen analysis. Turbidity, chemical

oxygen demand and gravimetric analysis, were not able to cover the complete concentration range required, although are useful at higher sticky concentrations. Dissolved organic carbon analysis and total dissolved nitrogen analysis were applicable to the entire concentration range investigated, but the latter is not a universal technique as not all stickies have nitrogen atoms in their chemical formula. The technique used to investigate the adsorption of stickies onto the surface of the minerals was elemental analysis, which measured the carbon, hydrogen and nitrogen adsorbed. It is a universal technique providing very good quantitative results.

The dissolved organic carbon and elemental analysis results were combined to calculate the adsorption equilibrium constant for all the mineral and sticky systems. The results for the two talc grades were compared to provide qualitative inferences about the adsorption mechanism, such as preferential adsorbing onto hydrophilic sites instead of hydrophobic sites. Comparison of the equilibrium constants MCC and bentonite provided information about how the particle size affected the adsorption of the sticky systems, and a schematic was proposed with three different adsorption mechanisms; a sandwich, aggregation and a hybrid mechanism.

Chapter 7 concentrated on two of the sticky systems investigated in chapter 6, to determine if the techniques initially introduced in chapter 6 were able to construct proxy adsorption isotherms for adsorption of colloidal species. Two different grades of talc and modified calcium carbonate were studied. The results from the adsorption experiments were used to construct adsorption isotherms for the two sticky systems, which were modelled using a Langmuir and linear isotherm to describe the different stages of adsorption. For the talc systems, the isotherm was divided into three sections; an initial linear adsorption, followed by a Langmuir monolayer formation and finally a second adsorption layer. For the modified calcium carbonate systems, the adsorption

was simpler, with two stages: The first was Langmuir-like adsorption, which was followed by multilayer adsorption and aggregation of the sticky. A schematic representation of a possible adsorption mechanism was proposed for the sticky systems onto the two different mineral types. In the chapter it was concluded that the proxy technique is useful in generating adsorption isotherms for the study of complex colloidal systems, and the techniques used in chapters 6 & 7 have a wide applicability to the paper recycling industry.

### ***8.1 Future work***

During the research project interesting results have been found, which warrant further investigation. A brief summary of some of the future work that could be undertaken for Chapters 3 – 7 is detailed below.

In Chapter 3, the investigation of pore architecture was described using experimental and modelling techniques. The work should be continued by increasing the number of experimental techniques and by improving the capabilities of the model to allow data from all the experimental techniques to be used. The latter suggestion is currently being addressed within the research group by the development of a much more versatile replacement to Pore-Cor known as Porexpert.

In Chapter 4, five different experimental techniques were used for the characterisation of modified calcium carbonate, to understand why the absorption rate of high surface area modified calcium carbonate was similar to the absorption rate of dual porous modified calcium carbonate. The work in this chapter could be expanded to additional grades of modified calcium carbonates. The investigation of the surface chemistry and rugosity could usefully be investigated further. A characterisation of the crystal dimensions of the surface species would allow the calculation of how many gas

molecules can be adsorbed in each ink-bottle pore, as shown schematically in Figure 8-1.

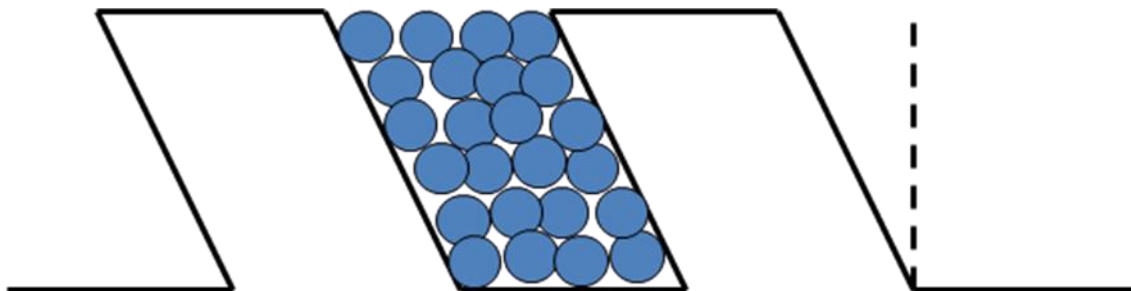


**Figure 8-1** Schematic of a possible packing arrangement for a gas adsorbing onto a modified calcium carbonate.

In Chapter 5, the diffusion and desorption behaviour of calcium carbonate was investigated. Further work for the zero length column should include changing the mobile phase, investigating different stationary phases, and deriving information about adsorption of the mobile phase.

In Chapter 6, the measurement of sticky concentration was performed using different analytical techniques. It is worth investigating the laboratory analytical techniques further to see if the technique can be adapted for use in a paper mill. Turbidity could be adapted for use in paper mills by using mixtures of stickies at different concentrations to construct a calibration curve, so that it would be possible to calculate an equilibrium constant for adsorption of stickies during a specific recycling process. The data from the modification may not be in the linear range, but could give semi quantitative information about removal of stickies. The measurement could be performed on line using a separate flow path. It is worth investigating whether a chemical oxygen demand measurement could be performed off-line in a paper mill, to assist in the control of stickies. The gravimetric technique can be used for measuring sticky residue successfully, but would also need to use a filtration step to remove remaining mineral prior to the gravimetric analysis, especially if used at low sticky concentrations. Instead of pipetting the suspension into the experimental vessel, the suspension could be

weighed in and the concentration of residue could then be corrected for any differences in initial suspension weight.

In Chapter 7, the adsorption isotherms and possible adsorption mechanisms were presented for two sticky systems. Future work for this chapter would aim to expand the range of minerals and stickies investigated, and search for synergistic combinations of minerals.

## Appendix A – Pore – Cor RS stochastic generation data for mercury porosimetry and porometry of filter media

Table A 1 Stainless steel mesh filter fitting parameters

Porometry	Throat Skew	Throat Spread	Connectivity	Pore Skew	Correlation Level
1	-45.911	0.78387	3.7001	1.0000	0.01
2	-42.353	0.69873	4.0148	1.0132	0.0130
3	-31.785	0.41560	5.6915	1.7724	0.30012
4	-16.688	0.37064	3.8384	5.6708	0.47534
5	-40.756	0.65355	4.2871	1.1692	0.03
Average	-35.499	0.58448	4.3064	2.1251	0.16569
Mercury Porosimetry	Throat Spread	Connectivity	Pore Skew	Correlation Level	Correlation Level
1	6.9810	0.66836	3.7736	2.3819	0.22180
2	-2.9870	0.99969	4.5952	1.0144	0.009
3	0.43388	0.72212	4.1231	1.2824	0.03
4	-0.07	0.81151	4.1130	1.1789	0.10613
5	-1.1408	0.60235	3.9536	5.8988	0.32329
Average	0.64342	0.76081	4.1117	2.3513	0.13804

Table A 2 Porvair Stainless steel sinter fitting parameters

Shielded Porosimetry	Throat Skew	Throat Spread	Connectivity	Pore Skew	Correlation Level
1	27.311	0.57642	4.7935	17.095	0.18528
2	-0.0008	0.57445	4.4037	1.8747	0.27230
3	-9.7243	0.63392	4.6912	1.2976	0.21786
4	-1.6130	0.48747	4.7848	2.2166	0.37324
5	0.40390	0.51228	5.3356	4.8224	0.37152
Average	3.2754	0.55691	4.8018	5.4613	0.28404
Mercury Porosimetry	Throat Skew	Throat Spread	Connectivity	Pore Skew	Correlation Level
1	45.152	0.64433	5.7012	9.2131	0.20961
2	48.872	0.65238	5.8220	1.1230	0.15047
3	40.931	0.61980	5.5570	14.195	0.22128
4	47.380	0.61522	5.2929	1.6471	0.0003
5	46.832	0.64041	5.4139	2.1061	0.14233
Average	45.833	0.63443	5.5574	5.6569	0.14480



Table A 3 Aegis stainless steel sinter fitting parameters

Mercury Porosimetry	Throat Skew	Throat Spread	Connectivity	Pore Skew	Correlation Level
1	4.0771	0.69595	5.4332	1.0205	0.53016
2	0.46305	0.41961	5.5496	2.1214	0.91216
3	2.3636	0.66358	5.5009	1.0001	0.50586
4	-1.3429	0.55414	4.9317	1.2075	0.70745
5	40.443	0.75630	5.9261	1.8344	0.11098
Average	9.2008	0.61792	5.4683	1.4368	0.55332

Table A 4 Glass fibre filter fitting parameters

Porometry	Throat Skew	Throat Spread	Connectivity	Pore Skew	Correlation Level
1	-45.532	0.59475	4.4817	1.5514	0.04
2	43.180	0.90920	3.1914	1.0764	0.06
3	-20.157	0.44267	3.2763	4.2060	0.47759
4	-32.532	0.55655	3.5709	3.8384	0.48483
5	-38.783	0.50447	5.5445	1.2884	0.009
Average	-18.7648	0.60153	4.0130	2.3921	0.214284
Mercury Porosimetry	Throat Skew	Throat Spread	Connectivity	Pore Skew	Correlation Level
1	12.024	0.23818	3.3890	284.27	0.82108
2	19.092	0.58841	4.7822	22.366	0.27394
3	33.674	0.84739	4.2427	3.0953	0.02
4	-5.9616	0.69575	4.3567	13.552	0.16328
5	-11.809	0.64309	4.9490	6.6950	0.12490
Average	9.4039	0.60256	4.3439	65.996	0.28064

Table A 5 Cellulose nitrate membrane filter fitting parameters

Porometry	Throat Skew	Throat Spread	Connectivity	Pore Skew	Correlation Level
1	-12.474	0.45391	3.3919	1.0018	0.26172
2	-26.397	0.50367	4.2569	1.1983	0.04
3	-12.059	0.27814	5.5228	1.2034	0.39138
4	-23.163	0.52040	3.3727	1.1751	0.02
5	-13.895	0.44763	3.3736	1.0602	0.31896
Average	-17.598	0.44183	3.9836	1.1278	0.20641
Mercury Porosimetry	Throat Skew	Throat Spread	Connectivity	Pore Skew	Correlation Level
1	-19.167	0.43079	3.2772	17.185	0.05
2	-28.252	0.51928	3.4002	33.494	0.16027
3	-24.256	0.42140	4.1057	23.020	0.11187
4	-26.017	0.47790	3.5376	12.182	0.09
5	-25.414	0.49782	3.4764	38.121	0.13226
Average	-24.621	0.46944	3.5594	24.800	0.10888

Table A 6 Grade 1 filter paper fitting parameters

Porometry	Throat Skew	Throat Spread	Connectivity	Pore Skew	Correlation Level
1	-28.943	0.54895	3.0580	1.9862	0.38812
2	-31.987	0.79711	3.3674	1.1684	0.24176
3	-44.511	0.58927	5.2530	1.0547	0.02
4	-47.814	0.42088	5.1328	1.1267	0.30652
5	-2.3544	0.92873	3.4256	1.0031	0.02
Average	-31.122	0.65699	4.0474	1.2678	0.19528
Mercury Porosimetry	Throat Skew	Throat Spread	Connectivity	Pore Skew	Correlation Level
1	-11.629	0.72592	3.1029	8.8447	0.34104
2	-28.769	0.84784	3.3019	2.2700	0.33592
3	-13.899	0.85758	3.6288	10.641	0.18073
4	-15.188	0.83954	3.6133	17.667	0.31114
5	-35.215	0.99597	3.8590	10.609	0.16663
Average	-20.940	0.85357	3.5012	10.006	0.26709

Table A 7 Track etch membrane fitting parameters

Porometry	Throat Skew	Throat Spread	Connectivity	Pore Skew	Correlation Level
1	-7.0992	0.46657	3.2113	1.0627	0.17162
2	-9.4505	0.26916	5.9142	1.0065	0.007
3	-8.7228	0.26332	5.9550	1.0005	0.006
4	-4.6938	0.41404	2.9205	1.1015	0.15605
5	-5.9038	0.37643	3.1252	1.0007	0.02
Average	-7.1740	0.35790	4.2252	1.0342	0.07213
Mercury Porosimetry	Throat Skew	Throat Spread	Connectivity	Pore Skew	Correlation Level
1	-5.1177	0.50945	2.9723	1.2398	0.25703
2	-33.809	0.61700	4.4360	1.0640	0.13159
3	-7.4634	0.41901	3.3285	1.9638	0.49211
4	2.0620	0.49365	2.9840	3.2816	0.18284
5	-0.9820	0.45120	2.8954	1.0400	0.22156
Average	-9.0620	0.49806	3.3232	1.7178	0.25703

## Appendix B – equilibrium constants for all systems in

### Chapter 6.

Table B 1 Fatty acid ester defoamer equilibrium constants

LSA Talc	0.5 g dm <sup>-3</sup>	0.1 g dm <sup>-3</sup>	0.05 g dm <sup>-3</sup>	0.01 g dm <sup>-3</sup>	0.005 g dm <sup>-3</sup>
$K_{eq} / g^{-1} dm^3$	0.34038	0.55654	0.61269	0.55701	0.54107
HSA Talc	0.5 g dm <sup>-3</sup>	0.1 g dm <sup>-3</sup>	0.05 g dm <sup>-3</sup>	0.01 g dm <sup>-3</sup>	0.005 g dm <sup>-3</sup>
$K_{eq} / g^{-1} dm^3$	0.33328	1.1518	1.3040	1.2558	1.2501
MCC	0.5 g dm <sup>-3</sup>	0.1 g dm <sup>-3</sup>	0.05 g dm <sup>-3</sup>	0.01 g dm <sup>-3</sup>	0.005 g dm <sup>-3</sup>
$K_{eq} / g^{-1} dm^3$	0.25479	0.24246	0.31953	0.30999	0.32757
Bentonite	0.5 g dm <sup>-3</sup>	0.1 g dm <sup>-3</sup>	0.05 g dm <sup>-3</sup>	0.01 g dm <sup>-3</sup>	0.005 g dm <sup>-3</sup>
$K_{eq} / g^{-1} dm^3$	0.63987	0.60558	0.56473	0.21966	0.61812

Table B 2 Acrylic acid ester copolymer equilibrium constants

LSA Talc	0.5 g dm <sup>-3</sup>	0.1 g dm <sup>-3</sup>	0.05 g dm <sup>-3</sup>	0.01 g dm <sup>-3</sup>	0.005 g dm <sup>-3</sup>
$K_{eq} / g^{-1} dm^3$	0.18643	0.53025	0.41274	0.54713	0.54517
HSA Talc	0.5 g dm <sup>-3</sup>	0.1 g dm <sup>-3</sup>	0.05 g dm <sup>-3</sup>	0.01 g dm <sup>-3</sup>	0.005 g dm <sup>-3</sup>
$K_{eq} / g^{-1} dm^3$	0.33934	0.48166	0.57203	0.70199	0.75252
MCC	0.5 g dm <sup>-3</sup>	0.1 g dm <sup>-3</sup>	0.05 g dm <sup>-3</sup>	0.01 g dm <sup>-3</sup>	0.005 g dm <sup>-3</sup>
$K_{eq} / g^{-1} dm^3$	0.33880	1.8343	1.9797	1.7785	2.001
Bentonite	0.5 g dm <sup>-3</sup>	0.1 g dm <sup>-3</sup>	0.05 g dm <sup>-3</sup>	0.01 g dm <sup>-3</sup>	0.005 g dm <sup>-3</sup>
$K_{eq} / g^{-1} dm^3$	0.45027	0.41897	0.36706	0.45617	0.45805

Table B 3 Mineral oil / Silicone defoamer equilibrium constants

LSA Talc	0.5 g dm <sup>-3</sup>	0.1 g dm <sup>-3</sup>	0.05 g dm <sup>-3</sup>	0.01 g dm <sup>-3</sup>	0.005 g dm <sup>-3</sup>
$K_{eq} / g^{-1} dm^3$	0.26462	0.33808	0.39602	0.34938	0.36057
HSA Talc	0.5 g dm <sup>-3</sup>	0.1 g dm <sup>-3</sup>	0.05 g dm <sup>-3</sup>	0.01 g dm <sup>-3</sup>	0.005 g dm <sup>-3</sup>
$K_{eq} / g^{-1} dm^3$	0.16228	0.61314	0.69727	0.72080	0.70073
MCC	0.5 g dm <sup>-3</sup>	0.1 g dm <sup>-3</sup>	0.05 g dm <sup>-3</sup>	0.01 g dm <sup>-3</sup>	0.005 g dm <sup>-3</sup>
$K_{eq} / g^{-1} dm^3$	0.42241	0.81361	0.89872	1.0234	1.0402
Bentonite	0.5 g dm <sup>-3</sup>	0.1 g dm <sup>-3</sup>	0.05 g dm <sup>-3</sup>	0.01 g dm <sup>-3</sup>	0.005 g dm <sup>-3</sup>
$K_{eq} / g^{-1} dm^3$	0.30852	0.29987	0.32863	0.34402	0.37054

Table B 4 Polyvinyl acetate equilibrium constants

LSA Talc	0.5 g dm <sup>-3</sup>	0.1 g dm <sup>-3</sup>	0.05 g dm <sup>-3</sup>	0.01 g dm <sup>-3</sup>	0.005 g dm <sup>-3</sup>
$K_{eq} / g^{-1} dm^3$	0.10096	0.10399	0.14907	0.17922	0.16227
HSA Talc	0.5 g dm <sup>-3</sup>	0.1 g dm <sup>-3</sup>	0.05 g dm <sup>-3</sup>	0.01 g dm <sup>-3</sup>	0.005 g dm <sup>-3</sup>
$K_{eq} / g^{-1} dm^3$	0.16639	0.35714	0.38445	0.37977	0.33836
MCC	0.5 g dm <sup>-3</sup>	0.1 g dm <sup>-3</sup>	0.05 g dm <sup>-3</sup>	0.01 g dm <sup>-3</sup>	0.005 g dm <sup>-3</sup>
$K_{eq} / g^{-1} dm^3$	0.22336	0.9918	1.1692	1.2113	1.4421
Bentonite	0.5 g dm <sup>-3</sup>	0.1 g dm <sup>-3</sup>	0.05 g dm <sup>-3</sup>	0.01 g dm <sup>-3</sup>	0.005 g dm <sup>-3</sup>
$K_{eq} / g^{-1} dm^3$	0.67428	0.71789	0.72146	0.67344	0.75932

Table B 5 Styrene-butadiene latex equilibrium constants

LSA Talc	0.5 g dm <sup>-3</sup>	0.1 g dm <sup>-3</sup>	0.05 g dm <sup>-3</sup>	0.01 g dm <sup>-3</sup>	0.005 g dm <sup>-3</sup>
$K_{eq} / g^{-1} dm^3$	0.03134	0.09151	0.09760	0.07976	0.08935
HSA Talc	0.5 g dm <sup>-3</sup>	0.1 g dm <sup>-3</sup>	0.05 g dm <sup>-3</sup>	0.01 g dm <sup>-3</sup>	0.005 g dm <sup>-3</sup>
$K_{eq} / g^{-1} dm^3$	0.05485	0.17335	0.17272	0.14079	0.15062
MCC	0.5 g dm <sup>-3</sup>	0.1 g dm <sup>-3</sup>	0.05 g dm <sup>-3</sup>	0.01 g dm <sup>-3</sup>	0.005 g dm <sup>-3</sup>
$K_{eq} / g^{-1} dm^3$	0.65639	1.3167	1.2890	1.3860	1.3803
Bentonite	0.5 g dm <sup>-3</sup>	0.1 g dm <sup>-3</sup>	0.05 g dm <sup>-3</sup>	0.01 g dm <sup>-3</sup>	0.005 g dm <sup>-3</sup>
$K_{eq} / g^{-1} dm^3$	0.02992	0.03157	0.02472	0.03790	0.03897

Table B 6 Colophonium resin equilibrium constants

LSA Talc	0.5 g dm <sup>-3</sup>	0.1 g dm <sup>-3</sup>	0.05 g dm <sup>-3</sup>	0.01 g dm <sup>-3</sup>	0.005 g dm <sup>-3</sup>
$K_{eq} / g^{-1} dm^3$	0.14623	0.13982	0.16551	0.16414	0.12522
HSA Talc	0.5 g dm <sup>-3</sup>	0.1 g dm <sup>-3</sup>	0.05 g dm <sup>-3</sup>	0.01 g dm <sup>-3</sup>	0.005 g dm <sup>-3</sup>
$K_{eq} / g^{-1} dm^3$	0.36033	0.34059	0.37399	0.35967	0.50257
MCC	0.5 g dm <sup>-3</sup>	0.1 g dm <sup>-3</sup>	0.05 g dm <sup>-3</sup>	0.01 g dm <sup>-3</sup>	0.005 g dm <sup>-3</sup>
$K_{eq} / g^{-1} dm^3$	0.23452	0.22766	0.22552	0.24760	0.23666
Bentonite	0.5 g dm <sup>-3</sup>	0.1 g dm <sup>-3</sup>	0.05 g dm <sup>-3</sup>	0.01 g dm <sup>-3</sup>	0.005 g dm <sup>-3</sup>
$K_{eq} / g^{-1} dm^3$	0.21012	0.23257	0.21456	0.21937	0.21066

**Table B 7 Alkyldiphenyloxide disulphonate equilibrium constants**

<b>LSA Talc</b>	<b>0.5 g dm<sup>-3</sup></b>	<b>0.1 g dm<sup>-3</sup></b>	<b>0.05 g dm<sup>-3</sup></b>	<b>0.01 g dm<sup>-3</sup></b>	<b>0.005 g dm<sup>-3</sup></b>
<b><math>K_{eq} / g^{-1} dm^3</math></b>	0.05451	0.08724	0.10253	0.08627	0.09378
<b>HSA Talc</b>	<b>0.5 g dm<sup>-3</sup></b>	<b>0.1 g dm<sup>-3</sup></b>	<b>0.05 g dm<sup>-3</sup></b>	<b>0.01 g dm<sup>-3</sup></b>	<b>0.005 g dm<sup>-3</sup></b>
<b><math>K_{eq} / g^{-1} dm^3</math></b>	0.35939	0.28441	0.31077	0.50129	0.37986
<b>MCC</b>	<b>0.5 g dm<sup>-3</sup></b>	<b>0.1 g dm<sup>-3</sup></b>	<b>0.05 g dm<sup>-3</sup></b>	<b>0.01 g dm<sup>-3</sup></b>	<b>0.005 g dm<sup>-3</sup></b>
<b><math>K_{eq} / g^{-1} dm^3</math></b>	0.27355	0.34253	0.38012	0.35512	0.34680
<b>Bentonite</b>	<b>0.5 g dm<sup>-3</sup></b>	<b>0.1 g dm<sup>-3</sup></b>	<b>0.05 g dm<sup>-3</sup></b>	<b>0.01 g dm<sup>-3</sup></b>	<b>0.005 g dm<sup>-3</sup></b>
<b><math>K_{eq} / g^{-1} dm^3</math></b>	0.04275	0.26792	0.28492	0.28476	0.28379

## Appendix C – Calibration curves for dissolved organic carbon data for Chapter 6

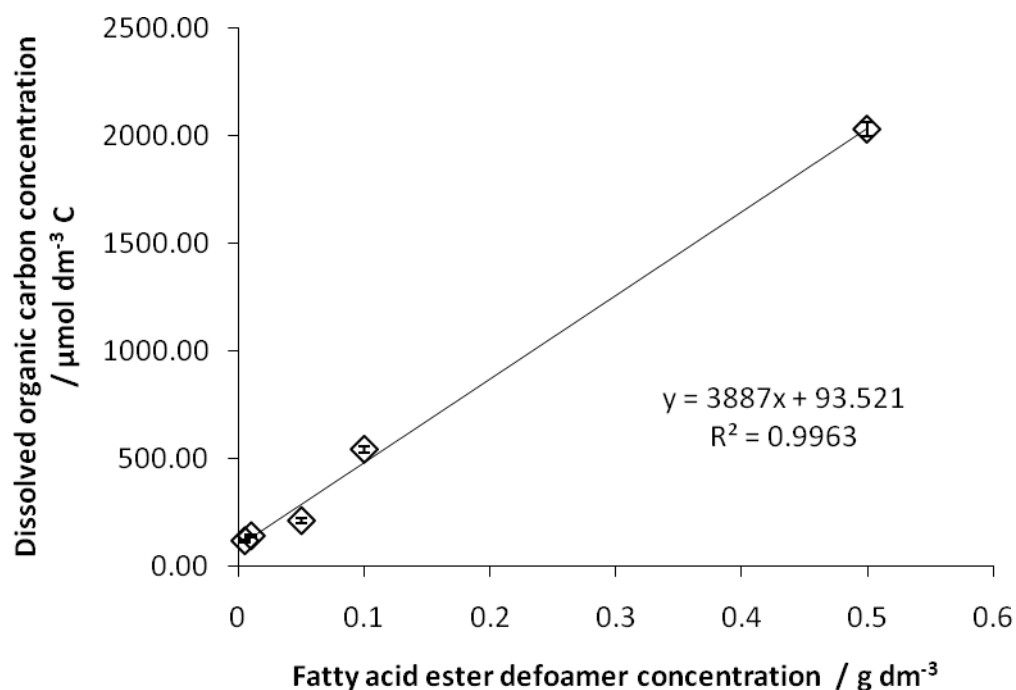


Figure C 1 Fatty acid ester defoamer dissolved organic carbon calibration graph. The error bars represent two times the standard deviation from three replicates.

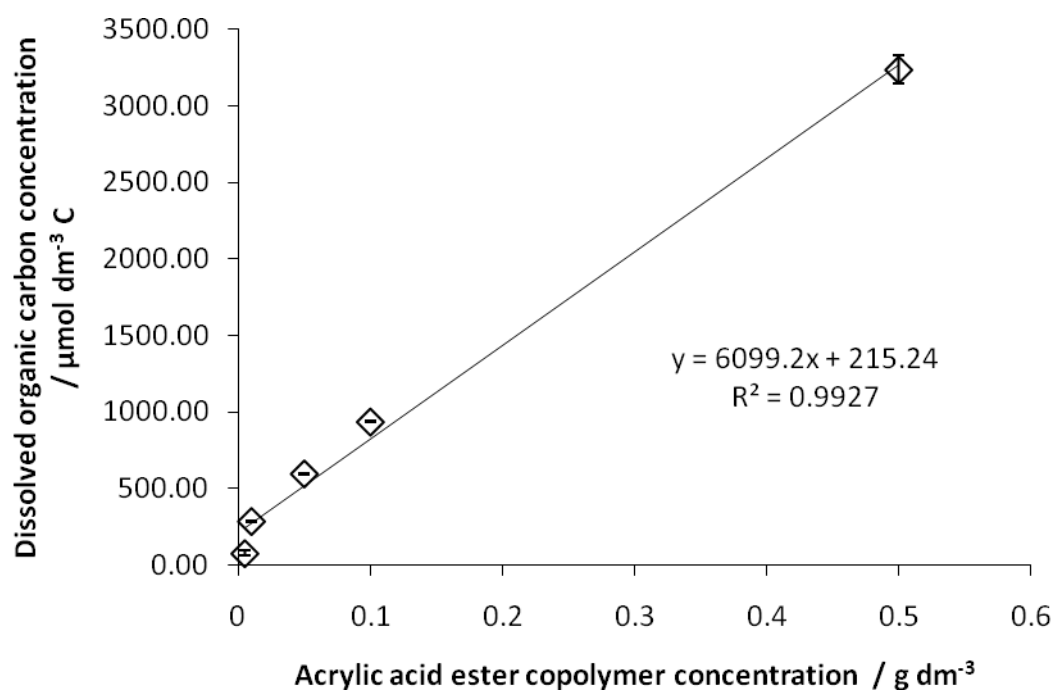


Figure C 2 Acrylic acid ester copolymer dissolved organic carbon calibration graph. The error bars represent two times the standard deviation from three replicates.

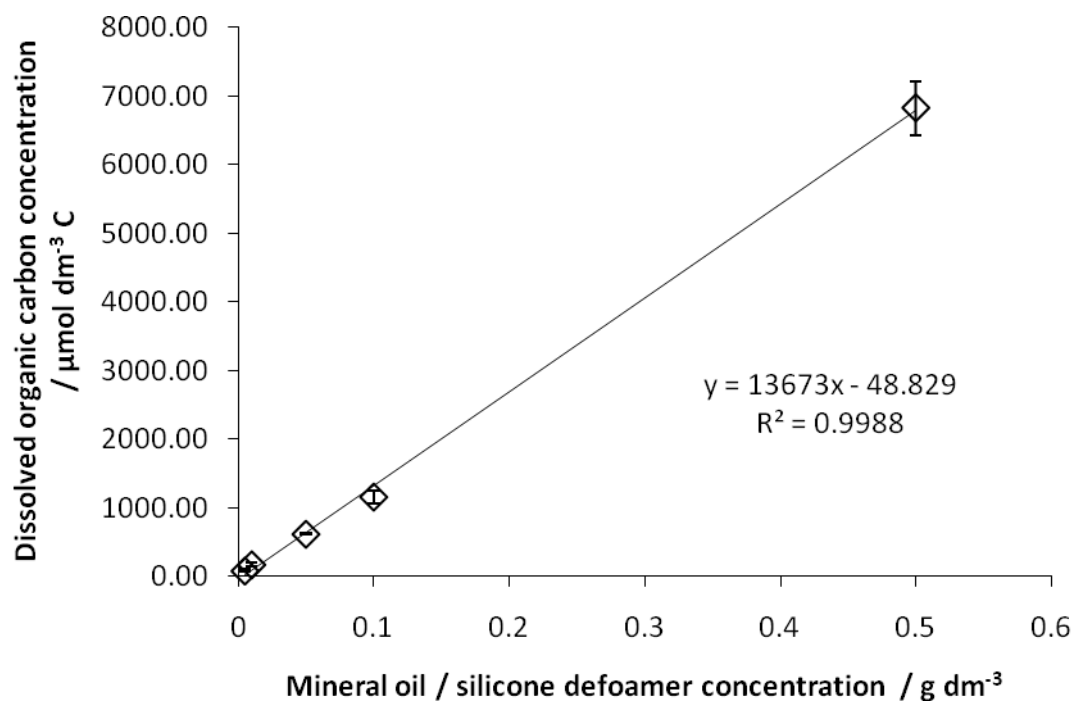


Figure C 3 Mineral oil / silicone defoamer dissolved organic carbon calibration graph. The error bars represent two times the standard deviation from three replicates.

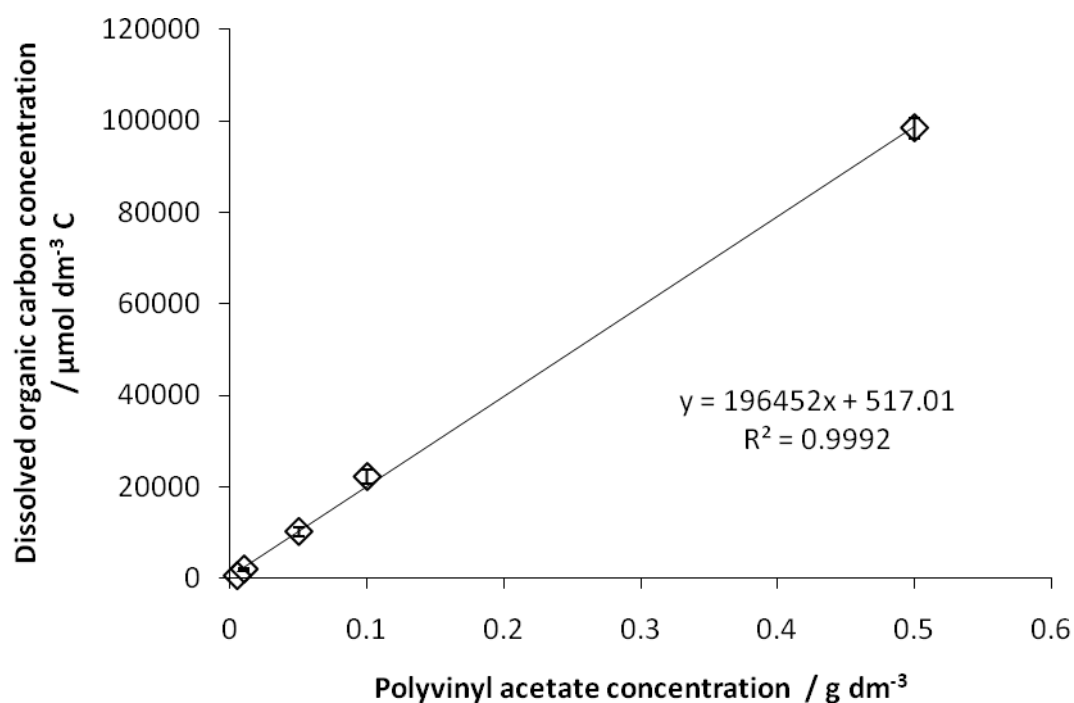


Figure C 4 Polyvinyl acetate dissolved organic carbon calibration graph. The error bars represent two times the standard deviation from three replicates.

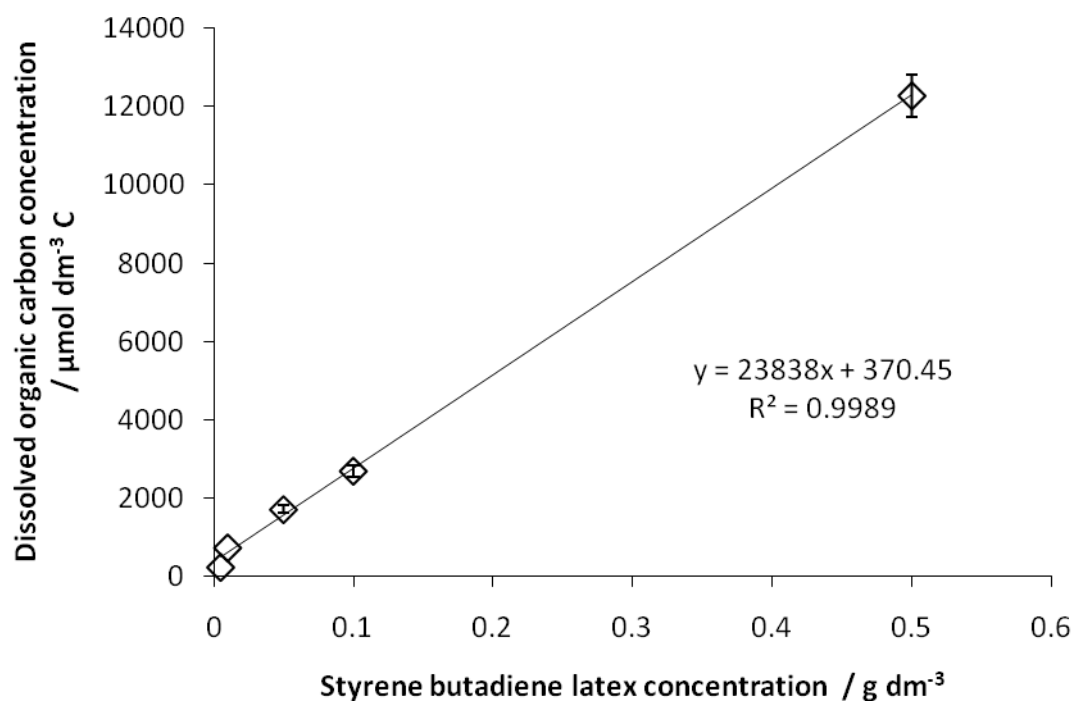


Figure C 5 Styrene butadiene latex dissolved organic carbon calibration graph. The error bars represent two times the standard deviation from three replicates.



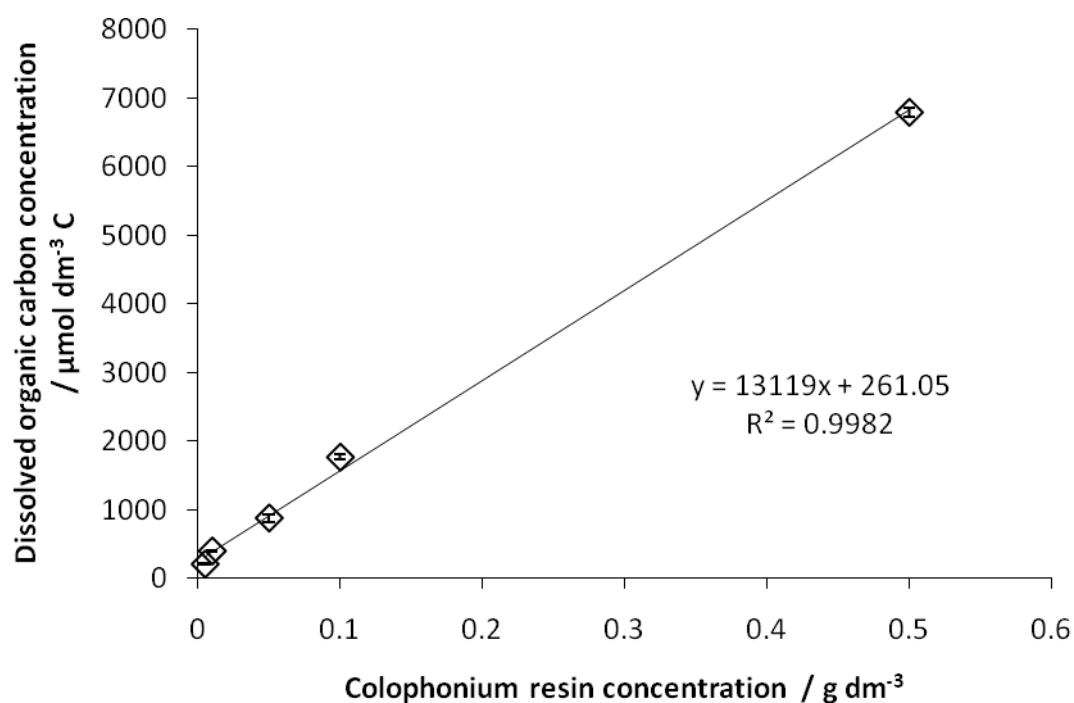


Figure C 6 Colophonium resin dissolved organic carbon calibration graph. The error bars represent two times the standard deviation from three replicates.

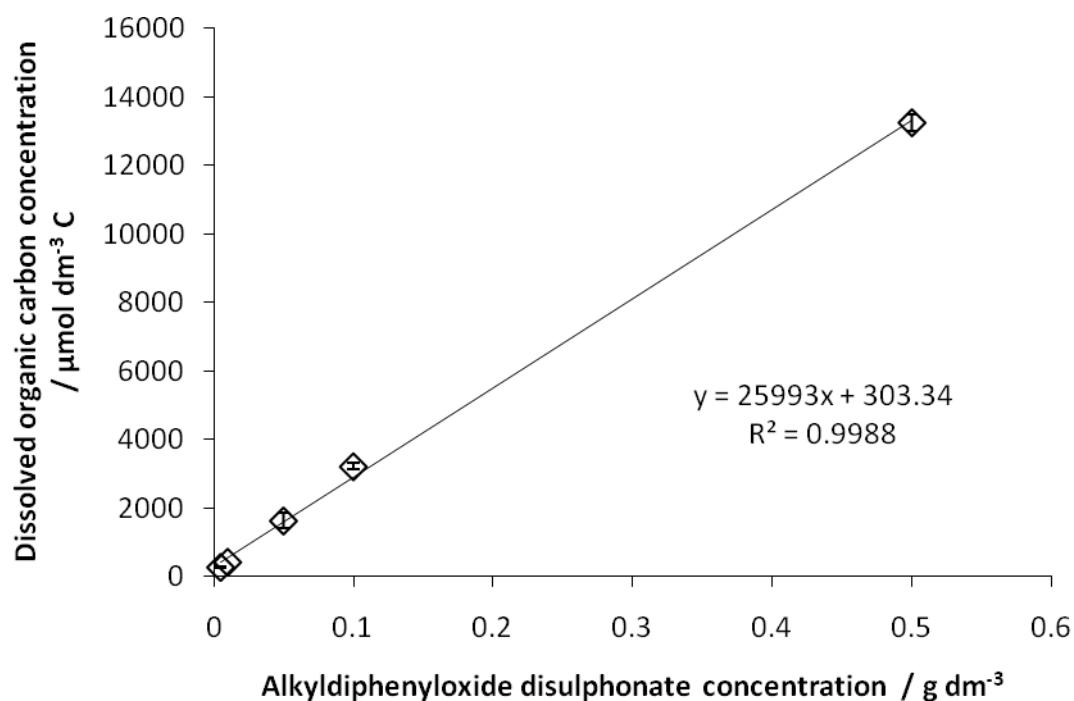


Figure C 7 Alkyldiphenyloxide disulphonate dissolved organic carbon calibration graph. The error bars represent two times the standard deviation.

## Appendix D – Fitting of ARIAN isotherm equations to raw adsorption isotherm data.

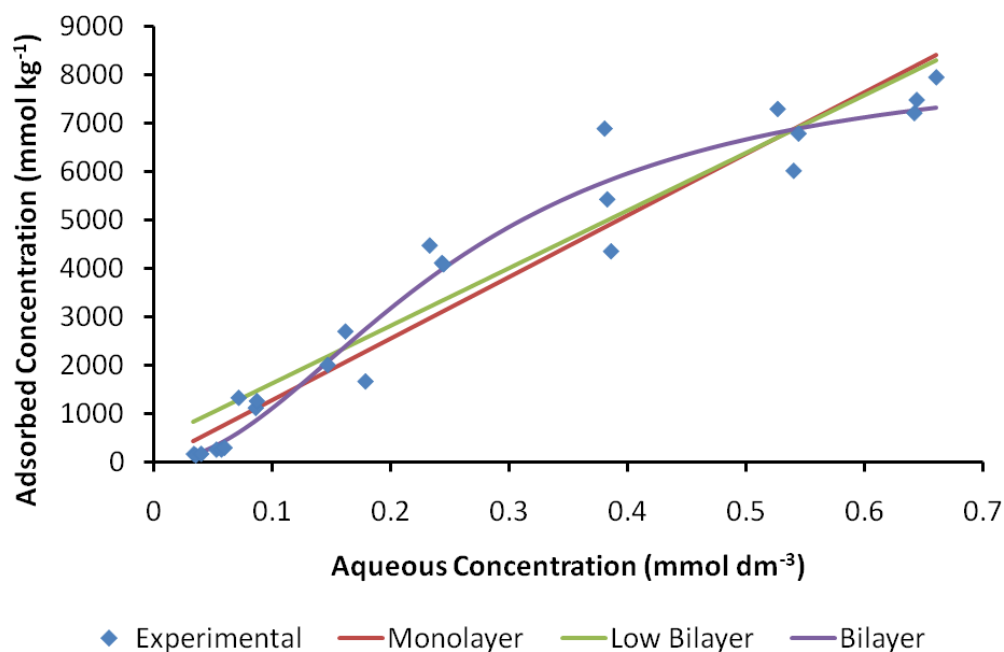


Figure D 1 Graph of ARIAN isotherms for LSA Talc adsorbing fatty acid ester defoamer

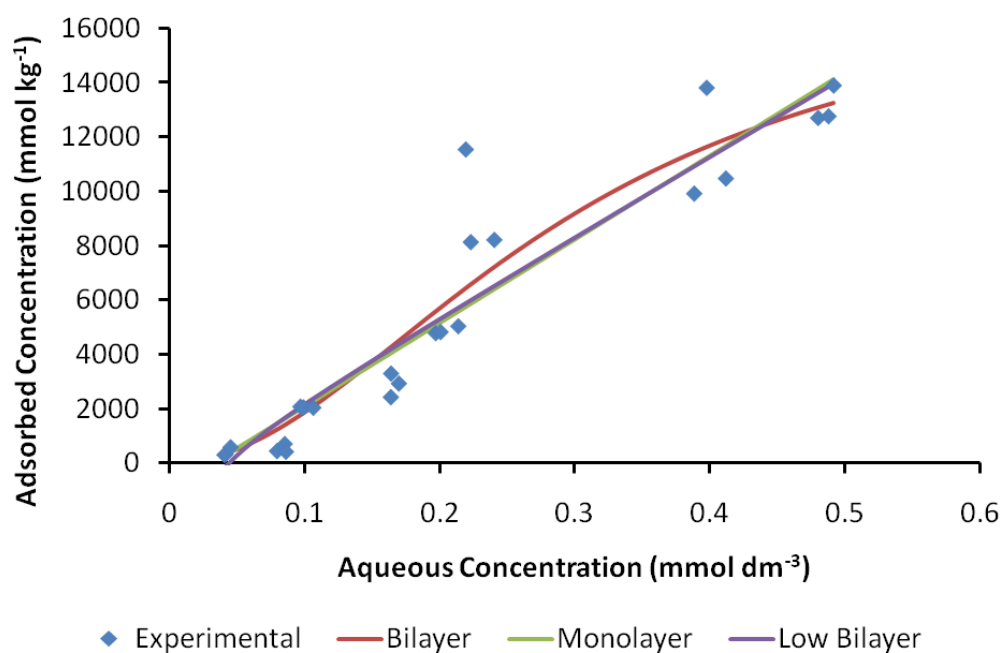


Figure D 2 Graph of ARIAN isotherms for HSA Talc adsorbing fatty acid ester defoamer

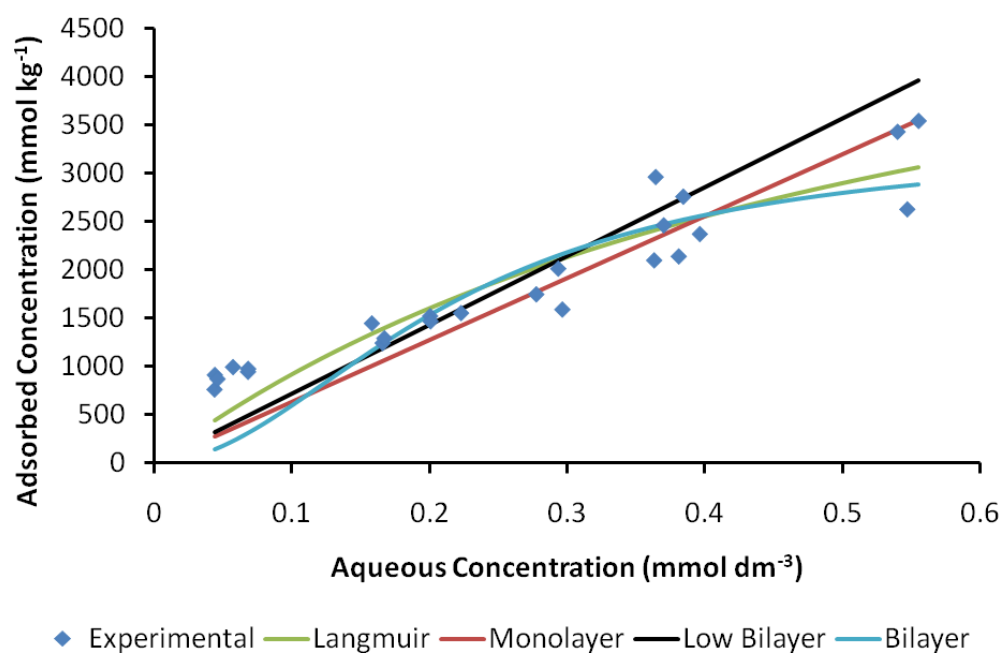


Figure D 3 Graph of Langmuir and ARIAN isotherms for LSA MCC adsorbing fatty acid ester defoamer

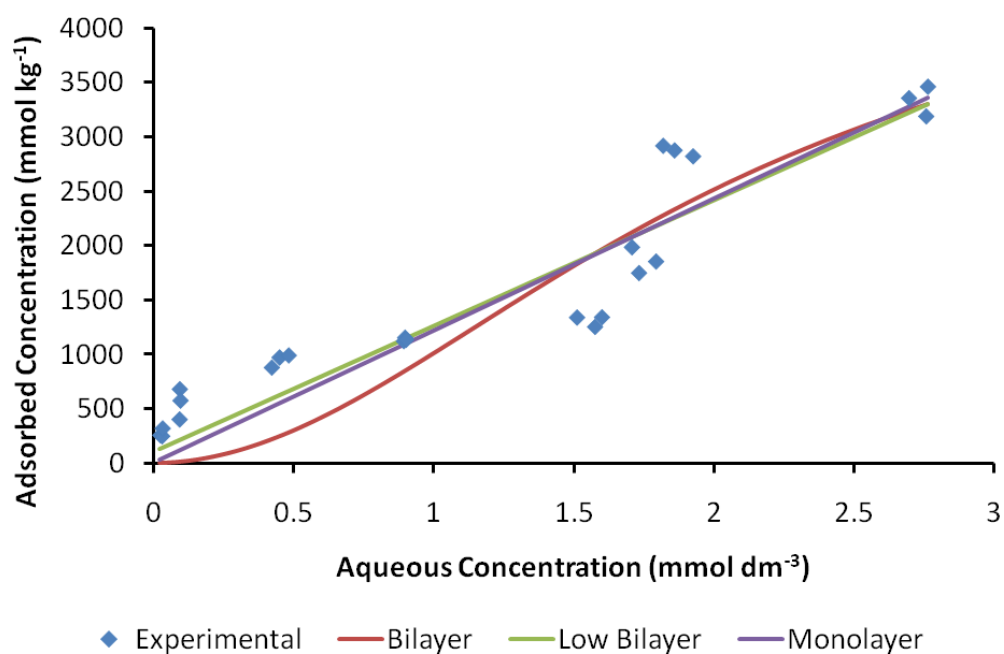


Figure D 4 Graph of ARIAN isotherms for HSA MCC adsorbing fatty acid ester defoamer

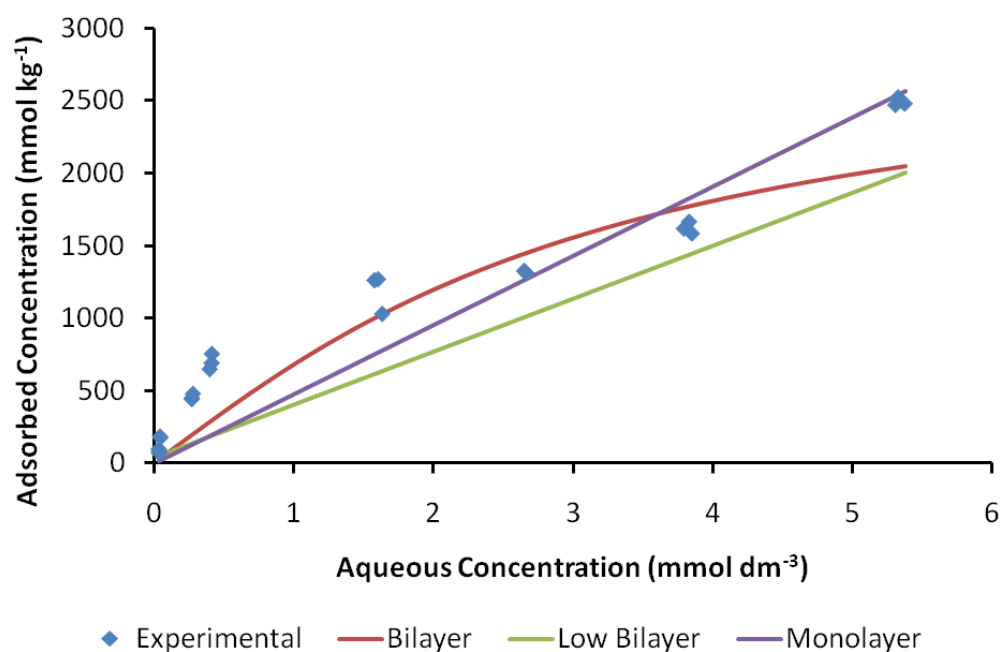


Figure D 5 Graph of ARIAN isotherms for LSA Talc adsorbing acrylic acid ester copolymer

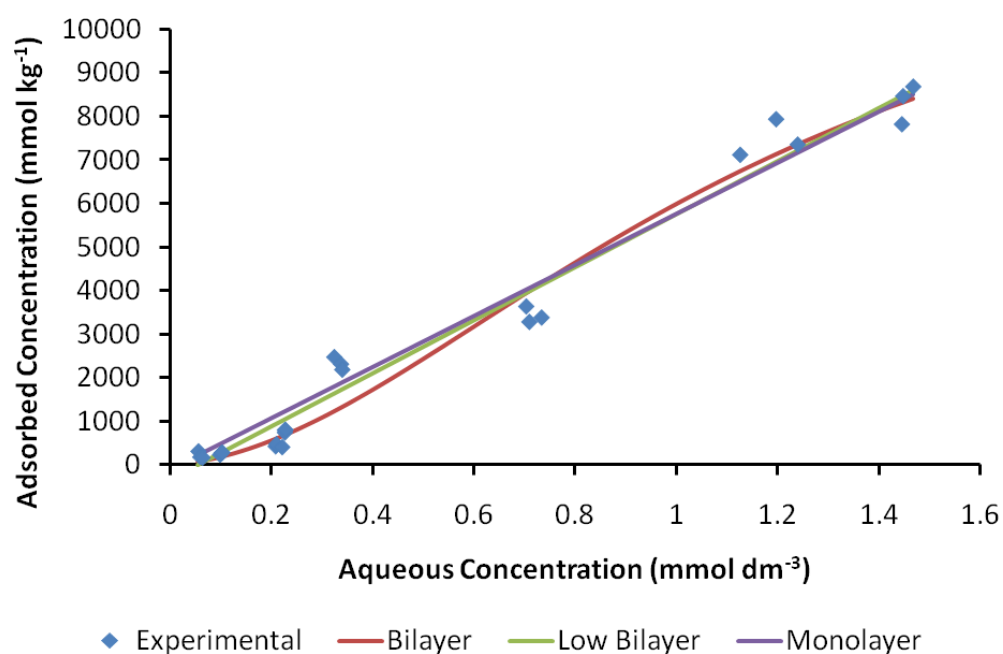


Figure D 6 Graph of ARIAN isotherms for HSA talc adsorbing acrylic acid ester copolymer

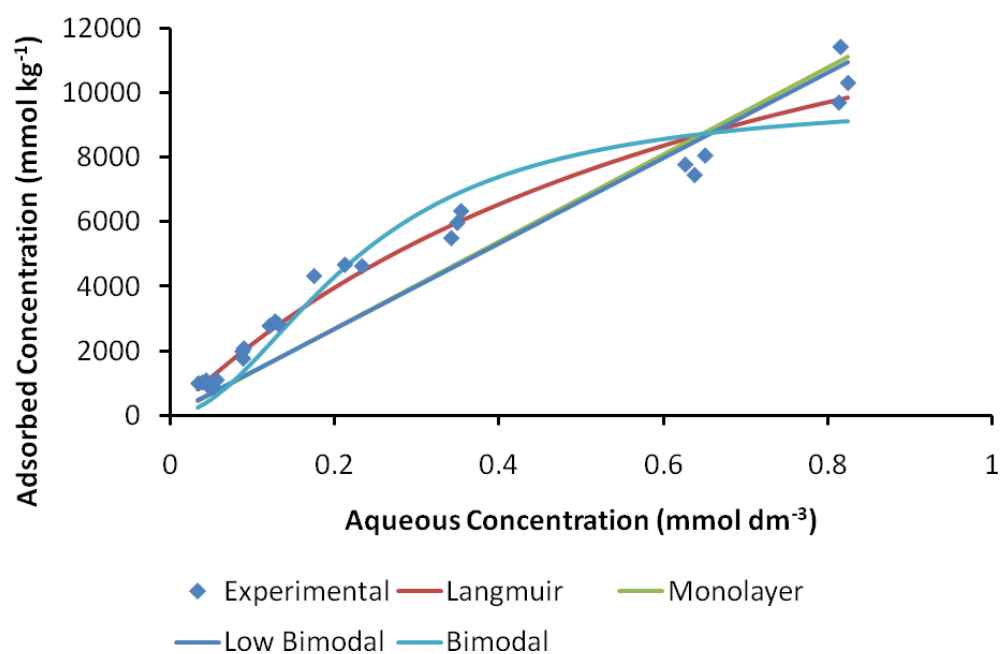


Figure D 7 Graph of Langmuir and ARIAN isotherms for LSA MCC adsorbing acrylic acid ester copolymer

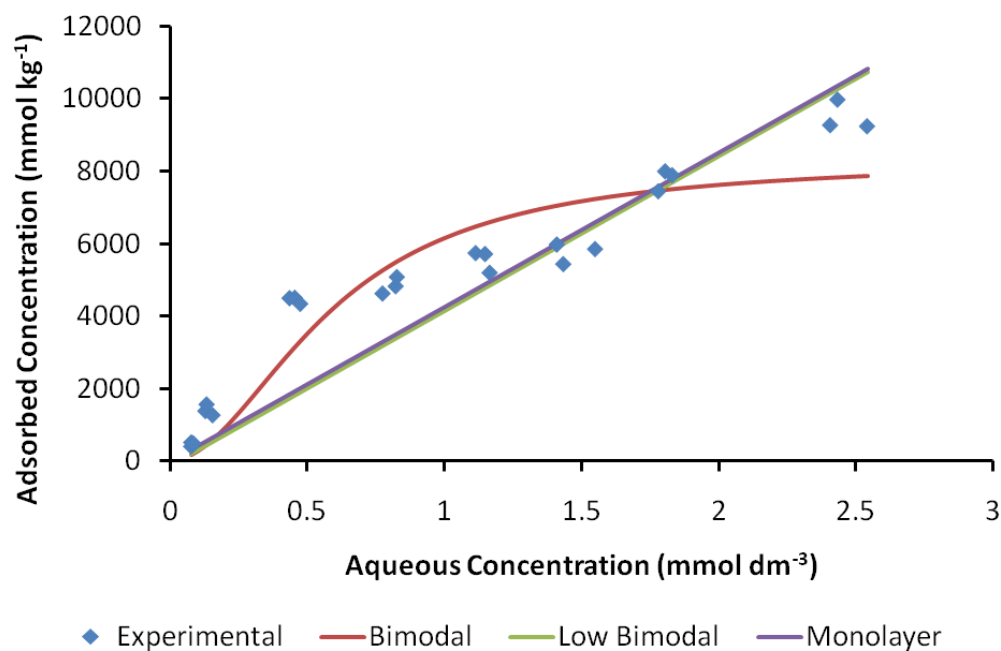


Figure D 8 Graph of ARIAN isotherms for HSA MCC adsorbing acrylic acid ester copolymer

## References

- Adamson, A. W. & Gast, A. P. 1997. *Physical Chemistry of Surfaces*, 6th ed. New York, Wiley-Blackwell.
- Allen, L. H. & Douek, M. 1993. Effectiveness of Talc for Pitch Control in Kraft Pulp Manufacture. *J. Pulp Pap. Sci.*, 19, J131-J136.
- Amey, J., Stott, T., Matthews, G. P., Laudone, G. M. & Lindop, J. W. 2008. *Porometer 4: Porous Media Analyser: User and Reference Manual*. Porvair Filtration Group Ltd.
- Asselman, T. & Garnier, G. 2000. Adsorption of model wood polymers and colloids on bentonites. *Colloids Surf. A.*, 168, 175-182.
- Atkins, P. & de Paula, J. 2002. *Atkins' Physical Chemistry*. Trento, Italy, Oxford University Press.
- Awum, F., Narayan, S. & Ruthven, D. 1988. Measurement Of Intracrystalline Diffusivities In NaX Zeolite By Liquid-Chromatography. *Ind. Eng. Chem. Res.*, 27, 1510-1515.
- Badr, E. S., Achterberg, E. P., Tappin, A. D., Hill, S. J. & Braungardt, C. B. 2003. Determination of dissolved organic nitrogen in natural waters using high-temperature catalytic oxidation. *TrAC, Trends Anal. Chem.*, 22, 819-827.
- Banaresmunoz, M. A. & Escribano, V. S. 1991. Adsorption-Isotherms of Nitrogen at 77 and 87-K and N-Butane at 236, 253, and 273-K Onto Tungsten Disulfide. *Langmuir*, 7, 1779-1783.
- Barrett, E. P., Joyner, L. G. & Halenda, P. P. 1951. The Determination of Pore Volume and Area Distributions in Porous Substances. I. Computations from Nitrogen Isotherms. *J. Am. Chem. Soc.*, 73, 373-380.
- Benecke, F., Gantenbein, D., Schoelkopf, J., Gane, P. A. C. & Gliese, T. 2009. Organic contaminants in recycled paper: a model study of the adsorbent properties of talc for idealised component suspensions. *Nord. Pulp Pap. Res. J.*, 24, 219-224.
- Bico, J., Thiele, U. & Quéré, D. 2002. Wetting of textured surfaces. *Colloids Surf. A.*, 206, 41-46.
- Binks, B. P., Fletcher, P. D. I., Price, A. & Hodge, P. 1992. Effects of subphase pH on surface pressure-area isotherms and monolayer deposition of preformed polymers with acid and ester hydrophilic groups. *Thin Solid Films*, 207, 273-278.

- Bodurtha, P., Matthews, G. P., Kettle, J. P. & Roy, I. M. 2005. Influence of anisotropy on the dynamic wetting and permeation of paper coatings. *J. Colloid Interf. Sci.*, 283, 171-189.
- Bosanquet, C. H. 1923. On the flow of liquids into capillary tubes. *Phil.Mag.Series 6*, 45, 525-531.
- Brandani, S. 1996. Analytical solution for ZLC desorption curves with bi-porous adsorbent particles. *Chem. Eng. Sci.*, 51, 3283-3288.
- Brandani, S. & Ruthven, D. M. 1995. Analysis of ZLC Desorption Curves for Liquid-Systems. *Chem. Eng. Sci.*, 50, 2055-2059.
- Brandani, S., Xu, Z. & Ruthven, D. 1996. Transport diffusion and self-diffusion of benzene in NaX and CaX zeolite crystals studied by ZLC and tracer ZLC methods. *Microporous Mater.*, 7, 323-331.
- Brunauer, S., Emmett, P. H. & Teller, E. 1938. Adsorption of Gases in Multimolecular Layers. *J. Am. Chem. Soc.*, 60, 309-319.
- Bryntesson, L. M. 2002. Pore network modelling of the behaviour of a solute in chromatography media: transient and steady-state diffusion properties. *J. Chromatogr. A*, 945, 103-115.
- Calvo, J. I., Hernandez, A., Pradanos, P., Martinez, L. & Bowen, W. R. 1995. Pore size distributions in microporous membranes .2. Bulk characterization of track-etched filters by air porometry and mercury porosimetry. *J. Colloid Interf. Sci.*, 176, 467-478.
- Choma, J., Jaroniec, M., Burakiewicz-Mortka, W. & Kloske, M. 2002. Critical appraisal of classical methods for determination of mesopore size distributions of MCM-41 materials. *Appl. Surf. Sci.*, 196, 216-223.
- Christian, G. D. 2004. *Analytical Chemistry*. USA, John Wiley & Sons, Inc.
- Crank, J. 1975. *The Mathematics of Diffusion*. Oxford, Oxford University (Clarendon) Press.
- Dawe, R. A. & Egbogah, E. O. 1978. Recovery of Oil from Petroleum Reservoirs. *Contemp. Phys.*, 19, 355-376.
- de Boer, R. 2003. Reflections on the development of the theory of porous media. *Appl. Mech. Rev.*, 56, R27-R42.
- Delagoutte, T. 2005. Management and control of stickies. *Prog. Pap. Recycl.*, 15, 31-41.
- Delagoutte, T. 2008. Stickies tackiness reduction with silanes. *Prog. Pap. Recycl.*, 17, 9-16.

- Derjaguin, B. & Landau, L. 1941. Theory of the stability of strongly charged lyophobic sols and of the adhesion of strongly charged particles in solutions of electrolytes. *Acta Physicochim. URS.*, XIV, 633-662.
- Doshi, M. R. 1991. Properties and Control of Stickies. *Prog. Pap. Recycl.*, 1, 54-63.
- Doshi, M. R. 2003. PAPTAC / TAPPI committee meeting on microstickies. *Prog. Pap. Recycl.*, 13, 44-53.
- Doshi, M. R. & Dyer, J. M. 1998. Management and Control of Stickies. *Paper Recycling Chal.* 3, 195-233.
- Douek, M. & Allen, L. H. 1991. Some Aspects of Pitch Control with Talc in Unbleached Kraft Pulps. *J. Pulp Pap. Sci.*, 17, J171-J177.
- Douek, M., Guo, X. Y. & Ing, J. 1997. An overview of the chemical nature of deposits stickies in mills using recycled fibre. *Recycling Symposium*, 313-330.
- Duncan, W. L. & Möller, K. P. 2000. A 'zero length' criterion for ZLC chromatography. *Chem. Eng. Sci.*, 55, 5415-5420.
- Eic, M. & Ruthven, D. M. 1988. New experimental technique for measurement of intracrystalline diffusivity. *Zeolites*, 8, 40-45.
- El Shafei, G. M. S. & Moussa, N. A. 2001. Adsorption of Some Essential Amino Acids on Hydroxyapatite. *J. Colloid Interf. Sci.*, 238, 160-166.
- Exner, H. E. & Hougardy, H. P. 1988. *Quantitative Image Analysis of Microstructures: A Practical Guide to Techniques, Instrumentation and Assessment of Materials*. Germany, Ir Pubns Ltd.
- Feng, X. J. & Jiang, L. 2006. Design and creation of superwetting/antiwetting surfaces. *Adv. Mater.*, 18, 3063-3078.
- Freundlich, H. 1926. *Colloid and Capillary Chemistry*. London, Methuen.
- Gane, P. A. C. Decoupling capillarity and permeability for rapid liquid absorption: Nanotechnology solution to super absorbers. In: *6th International Paper and Coating Chemistry Symposium*, 2006 Stockholm.
- Gane, P. A. C., Kettle, J. P., Matthews, G. P. & Ridgway, C. J. 1996. Void space structure of compressible polymer spheres and consolidated calcium carbonate paper-coating formulations. *Ind. Eng. Chem. Res.*, 35, 1753-1764.
- Gane, P. A. C., Ridgway, C. J., Lehtinen, E., Valiullin, R., Furo, I., Schoelkopf, J., Paulapuro, H. & Daicic, J. 2004. Comparison of NMR cryoporometry, mercury intrusion porosimetry, and DSC thermoporosimetry in characterizing pore size distributions of compressed finely ground calcium carbonate structures. *Ind. Eng. Chem. Res.*, 43, 7920-7927.



- Gane, P. A. C., Salo, M., Kettle, J. P. & Ridgway, C. J. 2009. Comparison of Young-Laplace pore size and microscopic void area distributions in topologically similar structures: a new method for characterising connectivity in pigmented coatings. *J. Mater. Sci.*, 44, 422-432.
- Gantenbein, D., Schoelkopf, J., Hunziker, P., Matthews, G. P. & Gane, P. A. C. 2009. Efficiency of colloidal pitch adsorption onto phyllosilicates: Comparing talc, chlorite and pyrophyllite. *Nord. Pulp Pap. Res. J.*, 24, 448-458.
- Gheorghiu, S. & Coppens, M. O. 2004. Optimal bimodal pore networks for heterogeneous catalysis. *AIChE J.*, 50, 812-820.
- Goldstein, J. I., Newbury, D. E., Echlin, P., Joy, D. C., Fiori, C. & Lifshin, E. 1981. *Scanning Electron Microscopy and X-ray Microanalysis : A Text for Biologists, Materials Scientists, and Geologists*. United States of America, Plenum Press.
- Gregg, S. J. & Sing, K. S. W. 1982. *Adsorption, Surface Area and Porosity*, 2nd ed. London, Academic Press.
- Gribble, C. M., Matthews, G. P., Gantenbein, D., Turner, A., Schoelkopf, J. & Gane, P. A. C. 2010a. Adsorption of surfactant-rich stickies onto mineral surfaces. *J. Colloid Interf. Sci.*, 352, 483-490.
- Gribble, C. M., Matthews, G. P., Laudone, G. M., Turner, A., Ridgway, C. J., Schoelkopf, J. & Gane, P. A. C. 2010b. Elucidation of Void Space Architecture of Filters by Comparison and Modelling of Porometry, Porosimetry and Microscopy. *AIChE J.* Submitted July 2010
- Groen, J. 2004. Critical appraisal of mesopore characterization by adsorption analysis. *Appl. Catal. A-Gen.*, 268, 121-125.
- Groen, J. C., Peffer, L. A. A. & Pérez-Ramírez, J. 2003. Pore size determination in modified micro- and mesoporous materials. Pitfalls and limitations in gas adsorption data analysis. *Micropor. Mesopor. Mat.*, 60, 1-17.
- Guera, N., Schoelkopf, J., Gane, P. A. C. & Rauatmaa, I. 2005. Comparing colloidal pitch adsorption on different talcs. *Nord. Pulp Pap. Res. J.*, 20, 156-163.
- Guyard, A., Daneault, C. & Chabot, B. 2006. Use of modified silica nanoparticle for fixation and elimination of colloidal and dissolved substances from white water. *Nord. Pulp Pap. Res. J.*, 21, 620-628.
- Halsey, G. 1948. Physical Adsorption on Non-Uniform Surfaces. *J. Chem. Phys.*, 16, 931-937.
- Heise, O. U., Kemper, M., Wiese, H. & Krauthauf, E. A. 2000. Removal of residual stickies at Haindl Paper using new flotation technology. *Tappi J.*, 83, 73-79.

- Hernández, A., Calvo, J. I., Prádanos, P., Palacio, L., Rodríguez, M. L. & de Saja, J. A. 1997. Surface structure of microporous membranes by computerized SEM image analysis applied to Anopore filters. *J. Membrane Sci.*, 137, 89-97.
- Hicyilmaz, C., Ulusoy, U. & Yekeler, M. 2004. Effects of the shape properties of talc and quartz particles on the wettability based separation processes. *Appl. Surf. Sci.*, 233, 204-212.
- Holmbom, B. & Sundberg, A. 2003. Dissolved and colloidal substances accumulating in papermaking process waters. *Wochenbl. Papierfabr.*, 131, 1305-1311.
- Holtham, D. A. L., Matthews, G. P. & Scholefield, D. S. 2007. Measurement and simulation of the void structure and hydraulic changes caused by root-induced soil structuring under white clover compared to ryegrass. *Geoderma*, 142, 142-151.
- Horsfall, M. J. & Spiff, A. I. 2004. Studies on the effect of pH on the sorption of  $Pb^{2+}$  and  $Cd^{2+}$  ions from aqueous solutions by *Caladium bicolor* (Wild Cocoyam) biomass. *Electron. J. Biotechnol.*, 7.
- Hunter, R. J. 1981. *Zeta Potential in Colloid Science: Principles and Applications*. East Kilbride, Academic Press Ltd.
- Hutten, I. M., Diaz, R., Roberts, M. K., Jeffrey, C. & Banerjee, S. 1997. Fiber to water distribution of stickies. *Tappi J.*, 80, 193-197.
- Igwe, J. C. & Abia, A. A. 2006. A bioseparation process for removing heavy metals from waste water using biosorbents. *Afr. J. Biotechnol.*, 5, 1167-1179.
- Johnson, A., Roy, I. M., Matthews, G. P. & Patel, D. 2003. An improved simulation of void structure, water retention and hydraulic conductivity in soil, using the Pore-Cor three-dimensional network. *Eur. J. Soil Sci.*, 54, 477-489.
- Jones, D. R. & Fitzhenry, J. W. 2003. Esterase-type Enzymes Offer Recycled Mills An Alternative Approach to Stickies Control. *Pulp Paper*, 77, 28-33.
- Jones, S. B. & Or, D. 2002. Surface area, geometrical and configurational effects on permittivity of porous media. *J. Non-Cryst. Solids*, 305, 247-254.
- Kemper, M. 1999. State-of-the-art and new technologies in flotation deinking. *Int. J. Miner. Process.*, 56, 317-333.
- Kumar, G. & Prabhu, K. N. 2007. Review of non-reactive and reactive wetting of liquids on surfaces. *Adv. Colloid Interfac.*, 133, 61-89.
- Kwok, D. Y. 1999. The usefulness of the Lifshitz-van der Waals/acid-base approach for surface tension components and interfacial tensions. *Colloids Surf. A.*, 156, 191-200.

- Langmuir, I. 1918. The Adsorption of Gases On Plane Surfaces Of Glass, Mica And Platinum. *J. Am. Chem. Soc.*, 40, 1361-1403.
- Laudone, G. M. 2005. *Environmentally friendly technology: The behaviour of natural and synthetic binder systems within paper coatings*. PhD Thesis, University of Plymouth, U.K.
- Laudone, G. M., Gregory, A. S., Price, J. C., Matthews, G. P. & Bird, N. R. A. 2009. A multi-property dual-porous model of soil. *Eur. J. Soil Sci.*, submitted July 3rd 2009.
- Laudone, G. M., Matthews, G. P. & Gane, P. A. C. 2008. Modelling diffusion from simulated porous structures. *Chem. Eng. Sci.*, 63, 1987-1996.
- Laudone, G. M., Matthews, G. P., Gane, P. A. C., Matthews, A. G., Ridgway, C. J., Schoelkopf, J. & Huggett, S. 2007. Estimation of structural element sizes in sand and compacted blocks of ground calcium carbonate using a void network model. *Trans. Por. Med.*, 66, 403-419.
- Laudone, G. M., Matthews, G. P., Gane, P. A. C., Ridgway, C. J. & Schoelkopf, J. 2005. Estimation of the effective particle sizes within a paper coating layer using a void network model. *Chem. Eng. Sci.*, 60, 6795-6802.
- Lawler, D. M. 1995. Turbidimetry and Nephelometry. In: Townshend, A. (ed.) *Encyclopedia of Analytical Science*. Academic Press.
- Li, D. P., Frey, M. W. & Joo, Y. L. 2006. Characterization of nanofibrous membranes with capillary flow porometry. *J. Membrane Sci.*, 286, 104-114.
- Lide (eds), D. R. 2004. *CRC Handbook of Chemistry and Physics*. Florida, USA, CRC Press, Inc.
- Liu, Y., Mu, L., Liu, B. & Kong, J. 2005. Controlled Switchable Surface. *Chem. Eur. J.*, 11, 2622-2631.
- Lowell, S., Shields, J. E., Thomas, M. A. & Thommes, M. 2004. *Characterization of Porous Solids and Powders: Surface Area, Pore Size and Density* Netherlands, Kluwer Academic Publishers.
- Luckham, P. F. & Rossi, S. 1999. The colloidal and rheological properties of bentonite suspensions. *Adv. Colloid Interfac.*, 82, 43-92.
- Malvern Instruments, L. 2005. Product Overview Brochure Mastersizer 2000.
- Matthews, G. P. 2000. Computer modelling of fluid interactions in porous coatings and paper - an overview. *Nord. Pulp Pap. Res. J.*, 15, 422-430.

- Matthews, G. P., Bodurtha, P. A., Price, J. C., Ridgway, C. J., Johnson, A., Roy, I. M. & Laudone, G. M. 2004. *Pore-Cor Research Suite User's Guide*. University of Plymouth Enterprise Ltd.
- Matthews, G. P., Canonville, C. & Moss, A. K. 2006. Use of a void network model to correlate porosity, mercury porosimetry, thin section, absolute permeability and NMR relaxation time data for sandstone rocks. *Phys. Rev. E*, 73, art 031307.
- Matthews, G. P., Laudone, G. M., Gregory, A. S., Bird, N. R. A., Matthews, A. G. & Whalley, W. R. 2010. Measurement and simulation of the effect of compaction on the pore structure and saturated hydraulic conductivity of grassland and arable soil. *Water Resour. Res.*, 46, W05501.
- McHale, G., Shirtcliffe, N. J. & Newton, M. I. 2004. Super-hydrophobic and super-wetting surfaces: Analytical potential? *Analyst*, 129, 284-287.
- Meyers, J. J., Crosser, O. K. & Liapis, A. I. 2001. Pore network modelling: determination of the dynamic profiles of the pore diffusivity and its effect on column performance as the loading of the solute in the adsorbed phase varies with time. *J. Chromatogr. A*, 908, 35-47.
- Meyers, J. J. & Liapis, A. I. 1998. Network modeling of the intraparticle convection and diffusion of molecules in porous particles packed in a chromatographic column. *J. Chromatogr. A*, 827, 197-213.
- Meyers, J. J. & Liapis, A. I. 1999. Network modeling of the convective flow and diffusion of molecules adsorbing in monoliths and in porous particles packed in a chromatographic column. *J. Chromatogr. A*, 852, 3-23.
- Micke, A., Kocirik, M. & Bulow, M. 1993. Theory of zero length column chromatography with the condition of a well-stirred sorbing zone. *Microporous Mater.*, 1, 373-381.
- Micromeritics 2006. *Gemini VI BET User Manual*. Norcross, GA, Micromeritics.
- Mie, G. 1908. Beiträge zur Optik trüber Medien, speziell kolloidaler Metallösungen. *Ann. Phys-Leipzig*, 330, 377-445.
- MiettonPeuchot, M., Condat, C. & Courtois, T. 1997. Use of gas-liquid porometry measurements for selection of microfiltration membranes. *J. Membrane Sci.*, 133, 73-82.
- Motoyuki, S. 1990. *Adsorption Engineering*. Japan, Elsevier.
- Neimark, A. V., Ravikovitch, P. I. & Vishnyakov, A. 2000. Adsorption hysteresis in nanopores. *Phys. Rev. E*, 62, R1493.

- Nguyen, D. T. 1998. Prevention of pitch and stickies deposition on paper-forming wires via adsorption of a cationic polymer associated with anionic species. *Tappi J.*, 81, 143-151.
- Olson, C. R. & Letscher, M. K. 1992. Increasing the Use of Secondary Fiber - An Overview of Deinking Chemistry and Stickies Control. *Appita J.*, 45, 125-130.
- Onusseit, H. 2006. The influences of adhesives on recycling. *Resour. Conserv. Recy.*, 46, 168-181.
- Pan, S. X., Davis, H. T. & Scriven, L. E. 1995. Modeling moisture distribution and binder migration in drying paper coatings. *Tappi J.*, 78, 127-143.
- Pan, X., Sanders, R., Tappin, A. D., Worsfold, P. J. & Achterberg, E. P. 2005. Simultaneous Determination of Dissolved Organic Carbon and Total Dissolved Nitrogen on a Coupled High-Temperature Combustion Total Organic Carbon-Nitrogen Chemiluminescence Detection (HTC TOC-NCD) System. *J. Autom. Method. Manag.*, 4, 240-246.
- Paria, S. & Khilar, K. C. 2004. A review on experimental studies of surfactant adsorption at the hydrophilic solid-water interface. *Adv. Colloid Interfac.*, 110, 75-95.
- Parida, S. K. & Mishra, B. K. 1998. Adsorption of styryl pyridinium dyes on polyethylene-glycol-treated silica. *Colloids Surf. A.*, 134, 249-255.
- Paturej, M. & El Fray, M. 2009. Syntheses of new poly(ester-carbonate-urethane)s based on trimethylene carbonate (TMC) and polyester polyol derived from dimerized fatty acid. *Polimery*, 54, 611-617.
- Peat, D. M. W., Matthews, G. P., Worsfold, P. J. & Jarvis, S. C. 2000. Simulation of water retention and hydraulic conductivity in soil using a three-dimensional network. *Eur. J. Soil Sci.*, 51, 65 - 79.
- Press, W. H., Flannery, B. P., Teukolsky, S. A. & Vetterling, W. T. 1986a. Evaluation of functions. In: Idem (ed.) *Numerical Recipes-The Art of Scientific Computing*. Cambridge: Cambridge University Press.
- Press, W. H., Flannery, B. P., Teukolsky, S. A. & Vetterling, W. T. 1986b. Minimization or Maximization of Functions. *Numerical Recipes-The Art of Scientific Computing*. Cambridge: Cambridge University Press.
- Press, W. H. & Teukolsky, S. A. 1991. Simulated Annealing Optimization Over Continuous Spaces. *Comput. Phys.*, 5, 426-429.

- Preston, A. R., Bird, N. R. A., Kinchesh, P., Randall, E. W. & Whalley, W. R. 2001. STRAFI-NMR study of water transport in soil. *Magn. Reson. Imaging*, 19, 561-563.
- Price, J. C., Matthews, G. P., Quinlan, K., Sexton, J. & Matthews, A. G. D. 2009. A Depth Filtration Model of Straining Within the Void Networks of Stainless Steel Filters. *AIChE J.*, 55, 3134-3144.
- Prins, M. W. J. 2001. Fluid Control in Multichannel Structures by Electrocapillary Pressure. *Science*, 291, 277-280.
- Rasband, W. S. 2008. ImageJ. 1.42o ed. Bethesda, Maryland, USA: U.S. National Institutes of Health.
- Ravikovitch, P. I., Haller, G. L. & Neimark, A. V. 1998. Density functional theory model for calculating pore size distributions: pore structure of nanoporous catalysts. *Adv. Colloid Interfac.*, 76-77, 203-226.
- Ravikovitch, P. I. & Neimark, A. V. 2002. Experimental confirmation of different mechanisms of evaporation from ink-bottle type pores: Equilibrium, pore blocking, and cavitation. *Langmuir*, 18, 9830-9837.
- Ravikovitch, P. I., Odomhnaill, S. C., Neimark, A. V., Schuth, F. & Unger, K. K. 1995. Capillary hysteresis in nanopores: Theoretical and experimental studies of nitrogen adsorption on MCM-41. *Langmuir*, 11, 4765-4772.
- Ridgway, C. J. & Gane, P. A. C. 2002. Dynamic Absorption into Simulated Porous Structures. *Colloids Surf. A.*, 206, 217-239.
- Ridgway, C. J. & Gane, P. A. C. 2003. Bulk density measurement and coating porosity calculations for coated paper samples. *Nord. Pulp Pap. Res. J.*
- Ridgway, C. J., Gane, P. A. C. & Schoelkopf, J. 2004. Modified calcium carbonate coatings with rapid absorption and extensive liquid uptake capacity. *Colloids Surf. A.*, 236, 91-102.
- Ridgway, C. J., Gane, P. A. C. & Schoelkopf, J. 2006. Achieving rapid absorption and extensive liquid uptake capacity in porous structures by decoupling capillarity and permeability: Nanoporous modified calcium carbonate. *Trans. Por. Med.*, 63, 239-259.
- Ridgway, C. J., Schoelkopf, J., Matthews, G. P., Gane, P. A. C. & James, P. W. 2001. The effects of void geometry and contact angle on the absorption of liquids into porous calcium carbonate structures. *J. Colloid Interf. Sci.*, 239, 417-431.
- Rigby, S. P. 2000. A hierarchical structural model for the interpretation of mercury porosimetry and nitrogen sorption. *J. Colloid Interf. Sci.*, 224, 382-396.

- Rigby, S. P. & Chigada, P. I. 2010. MF-DFT and Experimental Investigations of the Origins of Hysteresis in Mercury Porosimetry of Silica Materials. *Langmuir*, 26, 241-248.
- Rigby, S. P. & Daut, S. 2002. A statistical model for the heterogeneous structure of porous catalyst pellets. *Adv. Colloid Interfac.*, 98, 87-119.
- Rigby, S. P., Fletcher, R. S., Raistrick, J. H. & Riley, S. N. 2002. Characterisation of porous solids using a synergistic combination of nitrogen sorption, mercury porosimetry, electron microscopy and micro-focus X-ray imaging techniques. *Phys. Chem. Chem. Phys.*, 4, 3467-3481.
- Rigby, S. P., Watt-Smith, M. J., Chigada, P., Chudek, J. A., Fletcher, R. S., Wood, J., Bakalis, S. & Miri, T. 2006. Studies of the entrapment of non-wetting fluid within nanoporous media using a synergistic combination of MRI and micro-computed X-ray tomography. *Chem. Eng. Sci.*, 61, 7579-7592.
- Rogan, K. R. 1994. Adsorption of oleic acid and triolein onto various minerals and surface treated minerals. *Colloid Polym. Sci.*, 272, 82-98.
- Rohl, W., Vonrybinski, W. & Schwuger, M. J. 1994. Adsorption of Surfactants on Low-Charged Layer Silicates .2. Adsorption of Nonionic Surfactants. *Colloid Polym. Sci.*, 272, 324-331.
- Rouquerol, F. o., Rouquerol, J. & Sing, K. 1999. *Adsorption by Powders and Porous Solids Principles, Methodology and Applications*. Bodmin, Academic Press.
- Russell, T. P. 2002. Surface-Responsive Materials. *Science*, 297, 964-967.
- Ruthven, D. M. & Brandani, S. 1997. Measurement of diffusion in microporous solids by macroscopic methods. In: Fraissard, J. (ed.) *Physical adsorption: experiment, theory and applications*. Dordrecht: Kluwer Academic Publishers.
- Ruthven, D. M. & Stapleton, P. 1993a. Measurement of Liquid-Phase Counter-Diffusion in Zeolite Crystals by the ZLC Method. *Chem. Eng. Sci.*, 48, 89-98.
- Ruthven, D. M. & Stapleton, P. 1993b. Measurement of liquid phase counter-diffusion in zeolite crystals by the ZLC method. *Chem. Eng. Sci.*, 48, 89-98.
- Sakai, M., Yanagisawa, T., Nakajima, A., Kameshima, Y. & Okada, K. 2008. Effect of Surface Structure on the Sustainability of an Air Layer on Superhydrophobic Coatings in a Water-Ethanol Mixture. *Langmuir*, 25, 13-16. 10.1021/la802763h
- Samiey, B. & Golestan, S. 2010. Adsorption of Triton X-100 on silica gel: effects of temperature and alcohols. *Cent. Eur. J. Chem.*, 8, 361-369.
- Scheidegger, A. E. 1974. *The physics of flow through porous media*. Toronto, University of Toronto Press.

- Schoelkopf, J. 2002. *Observation and modelling of fluid transport into porous paper coating structures*. PhD Thesis, University of Plymouth, U.K.
- Schoelkopf, J., Gane, P. A. C., Ridgway, C. J. & Matthews, G. P. 2001. Influence of Inertia on Liquid Absorption into Paper Coating Structures. *Nord. Pulp Pap. Res. J.*, 15, 422-430.
- Schoelkopf, J., Ridgway, C. J., Gane, P. A. C., Matthews, G. P. & Spielmann, D. C. 2000. Measurement and network modelling of liquid permeation into compacted mineral blocks. *J. Colloid Interf. Sci.*, 227, 119-131.
- Sel, O., Sallard, S., Brezesinski, T., Rathouskì, J., Dunphy, D. R., Collord, A. & Smarsly, B. M. 2007. Periodically Ordered Meso- and Macroporous SiO<sub>2</sub> Thin Films and Their Induced Electrochemical Activity as a Function of Pore Hierarchy. *Adv. Funct. Mater.*, 17, 3241-3250.
- She, F. H., Tung, K. L. & Kong, L. X. 2008. Calculation of effective pore diameters in porous filtration membranes with image analysis. *Robot. Cim-Int. Manuf.*, 24, 427-434.
- Shirtcliffe, N. J., McHale, G., Atherton, S. & Newton, M. I. 2010. An introduction to superhydrophobicity. *Adv. Colloid Interfac.*, 161, 124-138.
- Silva, M. R., Sobral, A. J. F. N., Silva, J. A., Santos, A. C., Melo, S. M. & Beja, A. M. 2007. Dimer formation in 4-benzyl-5-methoxymethyl-3-methyl-1H-pyrrole-2-carboxylic acid benzyl ester. *J. Chem. Crystallogr.*, 37, 695-698.
- Skoog, D. A., Holler, F. J. & Crouch, S. R. 2006. *Principles of Instrumental Analysis*. Canada, Thomson Brooks / Cole.
- Solcova, O., Matejova, L. & Schneider, P. 2006. Pore-size distributions from nitrogen adsorption revisited: Models comparison with controlled-pore glasses. *Appl. Catal. A-Gen.*, 313, 167-176.
- Somasundaran, P. & Krishnakumar, S. 1997. Adsorption of surfactants and polymers at the solid-liquid interface. *Colloids Surf. A.*, 123-124, 491-513.
- Spiess, W. & Renner, K. 2004. Improving the efficiency of recovered paper screening or: How to effectively control stickies. *Wochenbl. Papierfabr.*, 132, 1002-+.
- Thommes, M., Skudas, R., Unger, K. K. & Lubda, D. 2008. Textural characterization of native and n-alky-bonded silica monoliths by mercury intrusion/extrusion, inverse size exclusion chromatography and nitrogen adsorption. *J. Chromatogr. A*, 1191, 57-66.



- Thommes, M., Smarsly, B., Groenewolt, M., Ravikovitch, P. I. & Neimark, A. V. 2006. Adsorption hysteresis of nitrogen and argon in pore networks and characterization of novel micro- and mesoporous silicas. *Langmuir*, 22, 756-764.
- Toivakka, M. & Nyfors, K. 2001. Pore Space Characterization of Coating Layers. *Tappi J.*, 84, 49.
- Tsakiroglou, C. D. & Ioannidis, M. A. 2008. Dual-porosity modelling of the pore structure and transport properties of a contaminated soil. *Eur. J. Soil Sci.*, 59, 744-761.
- Tsakiroglou, C. D., Ioannidis, M. A., Amirtharaj, E. & Vizika, O. 2009. A new approach for the characterization of the pore structure of dual porosity rocks. *Chem. Eng. Sci.*, 64, 847-859.
- Vähäsalo, L. J. & Holmbom, B. R. 2006. White pitch deposition and styrene-butadiene-rubber binder content in paper mill process waters. *Appita J.*, 59, 280-284.
- van Brakel, J., Modry, S. & Svata, M. 1981. Mercury Porosimetry: State of the Art. *Powder Technol.*, 29, 1-12.
- Van Oss, C. J., Good, R. J. & Chaudhury, M. K. 1986. The role of van der Waals forces and hydrogen bonds in "hydrophobic interactions" between biopolymers and low energy surfaces. *J. Colloid Interf. Sci.*, 111, 378-390.
- Van Oss, C. J., Good, R. J. & Chaudhury, M. K. 1988. Additive and nonadditive surface tension components and the interpretation of contact angles. *Langmuir*, 4, 884-891.
- Van Oss, C. J., Ju, L., Chaudhury, M. K. & Good, R. J. 1989. Estimation of the polar parameters of the surface tension of liquids by contact angle measurements on gels. *J. Colloid Interf. Sci.*, 128, 313-319.
- Verwey, E. J. W. & Overbeek, J. T. G. 1948. *Theory of the stability of lyophobic colloids*. New York, Elsevier.
- Wallqvist, V., Claesson, P. M., Swerin, A., Ostlund, C., Schoelkopf, J. & Gane, P. A. C. 2009. Influence of Surface Topography on Adhesive and Long-Range Capillary Forces between Hydrophobic Surfaces in Water. *Langmuir*, 25, 9197-9207.
- Wallqvist, V., Claesson, P. M., Swerin, A., Schoelkopf, J. & Gane, P. A. C. 2006. Interaction forces between talc and hydrophobic particles probed by AFM. *Colloids Surf. A.*, 277, 183-190.
- Wallqvist, V., Claesson, P. M., Swerin, A., Schoelkopf, J. & Gane, P. A. C. 2007. Interaction forces between talc and pitch probed by atomic force microscopy. *Langmuir*, 23, 4248-4256.

- Wang, S. T., Ying, Z., Xia, F., Xi, J. M., Wang, N., Feng, L. & Jiang, L. 2006. The preparation of a superhydrophilic carbon film from a superhydrophobic lotus leaf. *Carbon*, 44, 1848-1850.
- Wang, X., Yan, F., Li, Z., Zhang, L., Zhao, S., An, J. & Yu, J. 2007. Synthesis and surface properties of several nonionic-anionic surfactants with straight chain alkyl-benzyl hydrophobic group. *Colloids Surf. A.*, 302, 532-539.
- Watanabe, K., Badr, E.-S., Pan, X. & Achterberg, E. P. 2007. Conversion efficiency of the high-temperature combustion technique for dissolved organic carbon and total dissolved nitrogen analysis. *Int. J. Environ. An. Ch.*, 87, 387-399.
- Webb, P. A. & Orr, C. 1997. *Analytical Methods in Fine Particle Technology*. Norcross, GA, Micromeritics.
- Zabka, M. & Rodrigues, A. E. 2007. Measurement of pore diffusivity of R,S-[alpha]-Tetralol enantiomers in chiral adsorbent CHIRALPAK AD by zero length column method. *Sep. Purif. Technol.*, 57, 74-84.
- Zalc, J. M., Reyes, S. C. & Iglesia, E. 2003. Monte-Carlo simulations of surface and gas phase diffusion in complex porous structures. *Chem. Eng. Sci.*, 58, 4605-4617.
- Zhang, R. & Somasundaran, P. 2006. Advances in adsorption of surfactants and their mixtures at solid/solution interfaces. *Adv. Colloid Interfac.*, 123-126, 213-229.
- Ziel, R., Haus, A. & Tulke, A. 2008. Quantification of the pore size distribution (porosity profiles) in microfiltration membranes by SEM, TEM and computer image analysis. *J. Membrane Sci.*, 323, 241-246.